Measurement Biases in Weak Gravitational Lensing Surveys



Casey C D Cragg

Balliol College

University of Oxford

A thesis submitted for the degree of

Doctor of Philosophy

Michaelmas 2024

DECLARATION

I declare that no part of this thesis has been accepted, or is currently being submitted, for any degree or diploma or certificate or any other qualification in this University or elsewhere.

Casey Cragg	June 13, 2025

Acknowledgements

Enormous credit is due to my supervisors, Lance Miller and Chris Duncan. They have been exceptionally helpful and supportive scientific mentors throughout the duration of my DPhil, and their guidance and insight has been an invaluable resource. I must also thank all of the scientific colleagues, within the *Euclid* Consortium and at Oxford, who have been tremendous collaborators, and have provided a great deal of advice and support, including Konstantinos Tanidis, Jinhyub Kim, Imogen Whittam, David Alonso, Thomas Kitching, Alessio Spurio Mancini, Will Hartley, Federica Tarsitano, Francisco Javier Castander, Alex Hall, Andy Taylor, Jonathan Wong, Alex Maraio, Pedro Ferreira, and Chris Lintott; I deeply apologise to any whom I have missed. I must also acknowledge ESA and the *Euclid* Consortium as a whole, as well as the wider weak lensing community, without which none of the work presented in this thesis would have been conceivable. Emphatic thanks are also due to Ashling Gordon and Jonathan Patterson, without whom my DPhil activities would have been mired in chaos.

I must also extend my warmest thanks to all members of the Oxford Astrophysics sub-department with whom I have not interacted professionally, but who have nonetheless ensured that my time here has been enjoyable. In particular, I thank my esteemed compañeros of the OIPP, Alex, Mads, Jaime, Curro, Eric, and James, with whom I have shared a great deal of comradely discourse and treasured memories. I also sincerely thank all of the other Astrophysics DPhil students and postdocs at Oxford who have generated a level of banter that I never would have expected from the outset, including Rohan, Phil, Matthew, Fergus, Katie, Henry, Natalia, Lauren, and Matteo, along with many others, whose names are too many to mention here.

I also thank all of my friends in Oxford outside of my academic life, at Balliol and otherwise, who have contributed to my life immeasurably; Felicia, Arthur, Hermann, Noah, Calum, Grace, Tariq, Nikki, Rapha, Henrik, Mark, Ed, Pablo, Dario, Markella, Ben, Joey, Jack, Liv, Jenny, Andy, Lucia, Holly, Joe; and in particular Adam, Alex G, Boris, Momo, and Conan. Special thanks are due to my very dear friends Johny and Maike, without the unwavering love and support of whom the completion of this thesis would not have been possible. I must also acknowledge the Holywell Manor night porters, Mark and Steve, whose legendary status is well attested and deserved. I also very deeply thank my friends from

UCL, who have enduring support and care over the years; Dhruva, Raph, Nik, Aiham, Eva, Akash, Dorsa, Bokun, Sean, Anh; and especially Claude, who has been hugely supportive. I additionally acknowledge the support provided by Maike, Johny, and Boris in proofreading this manuscript.

I also give my sincerest thanks to my family, who have loved and supported me through thick and thin: Liza, Gareth, and Shristi; my sisters, Saoirse, Talulla, and Laoise; my mother, Alix; and my grandmother, Jenny. I would never have been able to reach the end of this journey without your unconditional belief and love. I would also like to extend my graitude to my school friends, Phillip, Chloë, Karifa, and John, as well as to Bruce Springsteen, and Elliott Smith.

Finally, I must express the deepest gratitude to those loved ones who have passed away; my grandpa John; Denis; and my father, Terry. I love and miss you all very much.

During my DPhil, I have been supported by an STFC Doctoral Studentship, in addition to financial support from Balliol College and the University of Oxford.

This work has made use of CosmoHub, developed by PIC (maintained by IFAE and CIEMAT) in collaboration with ICE-CSIC. It received funding from the Spanish government (grant EQC2021-007479-P funded by MCIN/AEI/10.13039/501100011033), the EU NextGeneration/PRTR (PRTR-C17.I1), and the Generalitat de Catalunya.

Statement of Originality

The conducted the work presented in this thesis as a DPhil student at the University of Oxford. The work presented in chapter 2 is based on the peer-reviewed research article Cragg et al., 2022 (MNRAS Volume 518, Issue 4, pp. 4909-4920), for which I am the lead author, and contributed all of the analysis and writing. This article was published in collaboration with Christopher A. J. Duncan, Lance Miller, and David Alonso, who provided software and technical comments; additional comments were provided by Thomas D. Kitching. The work presented in chapter 2 makes use of the NaMaster code presented in Alonso et al., 2019. The work presented in chapter 3, chapter 4, and chapter 5 was conducted as part of the activity of the *Euclid* Consortium, in part in collaboration with the efforts of the *Euclid* Consortium third Science Performance Verification exercise (SPV3), and involved collaboration with Lance Miller, Christopher A. J. Duncan, Konstantinos Tanidis, Jinhyub Kim, William Hartley, Federica Tarsitano, Francisco Javier Castander, and Alessio Spurio Mancini, who provided software, external data products, and technical comments. The work presented in these chapters forms the basis of a number of research articles in preparation. Except where otherwise stated or where reference is made to the work of others, I confirm that the work presented in this thesis is entirely my own; any work that has been conducted by collaborators is explicitly referenced in the text.

The copyright of this thesis rests with the author. The author asserts his moral rights.

Abstract

The ongoing and forthcoming weak gravitational lensing (WL) surveys of the 2020s, including the *Euclid* Wide Survey (EWS; Euclid Collaboration: Mellier et al., 2024), the *Rubin* Observatory Legacy Survey of Space and Time (LSST; (Dark Energy Science Collaboration: Mandelbaum et al., 2018)), and the *Roman* Space Telescope High-Latitude Imaging Survey (HLIS; Troxel et al., 2021), will measure the large-scale structure of the Universe with unprecedented depth, survey area, and image quality. The data collected by these surveys will allow the parameters of the ΛCDM cosmological model to be constrained with substantially greater precision than has been achieved previously. In order to meet the ambitious aims of these projects, of probing the nature of dark matter and dark energy, and investigating potential discrepancies between cosmological theory and observation, it will be vital to effectively characterise and mitigate systematic sources of error which impact the scientific analysis of data from these surveys, that are expected to dominate the error budgets (Albrecht et al., 2006).

WL surveys aim to measure the coherent distortion of galaxy images arising due to weak lensing induced by the tidal gravitational field of the inhomogeneous large-scale structure of the Universe (Kilbinger, 2015; Schneider et al., 2002). The distortion of galaxy images due to WL is referred to as the *shear*, and bias in the shear measurement is a major source of systematic error for WL surveys. In particular, sources of shear measurement bias must be well-characterised and mitigated in modern WL surveys. The aim of this thesis is to realistically forecast shear biases originating due to a number of sources of error that are expected to be relevant to Stage-IV WL surveys; and to estimate the impact of these on cosmological parameter inference.

In chapter 2, the impact of spatially-varying multiplicative shear bias on cosmological parameter estimation is forecast, for a general Stage-IV survey configuration. Based on the resulting bias in cosmological parameters, this analysis allows requirements to be placed on the properties of the residual spatial variations of the multiplicative shear bias for modern WL surveys.

In chapter 3, a methodology is developed to forward-model shear biases arising due to point-spread function (PSF) errors for the EWS. This provides a technique to allow realistic forecasting of shear biases arising due to PSF errors at the catalogue-level, that depend on galaxy properties including morphology and spectral energy

distribution (SED). This methodology is applied in chapter 4 to forecast shear biases arising due to galaxy SED errors for the EWS, and propagate these to cosmological inference; and in chapter 5, to forecast shear biases arising due to PSF modelling errors for the EWS.

Overall, the work presented in this thesis represents an advancement on previous work conducted in forecasting the impact of shear measurement biases on the analysis of data from modern WL surveys (in particular, with respect to the EWS; see e.g. Euclid Collaboration: Paykari et al., 2020; Massey et al., 2013). In this thesis, shear biases have been estimated with a higher degree of realism than in previous work, and a methodology has been developed to allow an end-to-end forecast of the cosmological impact of such biases, from pixels to parameters. This represents an important contribution to the characterisation of shear measurement biases, with applications to the mitigation of the impact of this source of systematic error; tasks which are essential to the realisation of the ambitious scientific aims of modern WL surveys.

There are decades when nothing happens; and there are weeks when decades happen.

— V. I. Lenin (apocryphal)

Contents

List of Abbreviations **xvii**

1 Introduction **1**
1.1 Cosmology with Weak Gravitational Lensing 1
1.1.1 The ΛCDM Cosmological Model 1
1.1.2 Testing ΛCDM with Cosmological Galaxy Surveys 9
1.1.3 Weak Gravitational Lensing 15
1.1.4 Projected Weak Lensing Observables 18
1.1.5 Measuring Cosmic Shear 20
1.1.6 Cosmic Shear Measurement Bias 24
1.2 Weak Gravitational Lensing with the *Euclid* Spacecraft 28
1.2.1 The *Euclid* Spacecraft 28
1.2.2 The *Euclid* Wide Survey 30
1.2.3 Shear Measurement with *Euclid* 33
1.2.4 The Point Spread Function for *Euclid* 34
1.2.5 Shear Measurement Biases Arising Due to Errors in the PSF for *Euclid* 37
1.3 Thesis Overview 38

2 Propagating Spatially-Varying Multiplicative Shear Bias to Cosmological Parameter Estimation for Stage-IV Weak Lensing Surveys **41**
2.1 Introduction 42
2.2 Methods 46
2.2.1 Pseudo-C_ℓ formalism 46
2.2.2 Survey model 50
2.2.3 Fisher matrix analysis 52
2.3 Results 57
2.3.1 Residual power spectra 57
2.3.2 Bias in cosmological parameters 61
2.3.3 Dependence of parameter bias on m-bias RMS 63
2.4 Discussion 67
2.4.1 Residual power spectra 67

2.4.2 Bias in cosmological parameters . . . 68
2.4.3 Dependence of parameter bias on m-bias RMS . . . 70
2.5 Conclusion . . . 71

3 Forecasting Shear Bias Arising Due to PSF Errors for the EWS 75
3.1 Introduction . . . 76
3.1.1 Relevance of PSF Errors to Shear Measurement for the *Euclid* Wide Survey . . . 76
3.1.2 Shear Bias Requirements for the *Euclid* Wide Survey . . . 77
3.1.3 Sources of PSF error for the *Euclid* Wide Survey . . . 86
3.1.4 Outline of the shear bias calculation method . . . 88
3.2 Shear Bias Estimation . . . 92
3.2.1 Description of PSF generation using the *Euclid* OU-SHE PSFTOOLKIT software . . . 92
3.2.2 Description of the Shear Bias Calculation . . . 94
3.2.3 Optimisation of PSF generation for shear bias calculation . . . 98
3.3 Estimation of Shear Bias at the Catalogue Level . . . 108
3.3.1 Description of the Method . . . 108
3.3.2 Optimisation and validation of SED matching . . . 115
3.3.3 Morphology and FoV Interpolation . . . 127
3.4 Conclusion . . . 132
3.4.1 Summary . . . 132
3.4.2 Applications and Future Work . . . 133

4 Forecasting the Impact of Galaxy SED Errors on PSF Estimation, Shear Measurement, and Cosmological Inference for the EWS 137
4.1 Introduction . . . 138
4.2 Forecasting Shear Bias Arising due to SED Errors . . . 139
4.2.1 SED Errors in the EWS . . . 139
4.2.2 Calculation of Shear Bias Arising Due to SED Errors for Mock Galaxies . . . 141
4.2.3 Results and Discussion . . . 144
4.3 Propagation of m-Bias to Parameter Estimation . . . 164
4.3.1 Propagation of SED Errors to Tomographic Cosmic Shear Angular Power Spectra . . . 166
4.3.2 Bias in Cosmological Parameters . . . 169
4.3.3 Discussion . . . 173
4.4 Conclusion . . . 176
4.4.1 Summary . . . 176
4.4.2 Future Work . . . 178

5 Tomographic Mapping of Spatially-Varying Shear Biases for the EWS 181
5.1 Introduction 181
5.1.1 Phase-Diversity Calibration Baseline PSF 184
5.2 Forecasting Shear Biases Due to PSF Modelling Errors 187
5.2.1 Sampling PSF Variations Using PCA 187
5.2.2 Propagating PSF Modelling Errors to Shear Biases 193
5.3 Mapping Tomographic Forecast Shear Biases 197
5.3.1 Tomographic Mock Galaxy Sampling 197
5.3.2 Constructing Tomographic Shear Bias Maps 198
5.3.3 Discussion 203
5.4 Conclusion 206
5.4.1 Summary 206
5.4.2 Future Work 208

6 Conclusions 211
6.1 Overview 211
6.2 Outlook 217

Bibliography 223

List of Abbreviations

LSS . . . . . Large-scale structure

WL . . . . . Weak gravitational lensing

EWS . . . . . *Euclid* Wide Survey

PSF . . . . . Point spread function

SED . . . . . Spectral energy distribution

FoV . . . . . Field of view

VIS . . . . . *Euclid* Spacecraft visible instrument

NISP . . . . . *Euclid* Spacecraft near-infrared spectrometer and photometer

OU–SHE . . . . *Euclid* Consortium shear measurement operational unit

OU–PHZ . . . . *Euclid* Consortium photometric redshift operational unit

SPV3 . . . . . *Euclid* Consortium 3rd science performance verification exercise

QE . . . . . Quadratic estimator

FT . . . . . Fourier transform

FD . . . . . Fourier domain

PTO . . . . . Propagate-to-object PSF requirements

SSC . . . . . Super-sample covariance

PDC . . . . . Phase-diversity calibration

PCA . . . . . Principal component analysis

STOP analysis Structural-thermal-optical analysis

WFE . . . . . Wavefront error

The empire, long divided, must unite; long united, must divide. Thus it has ever been.

— Luo Guanzhong, *Romance of the Three Kingdoms*

What do you think, Subhuti, is the extent of space in the Eastern Heavens easy to measure? [...] In like manner, is it easy to measure the extent of space in the Western, Southern, and Northern Heavens, upwards, downwards, in all the intermediate directions, in all the ten directions all around?

— *Vajracchedikā Prajñāpāramitā Sūtra*

1 Introduction

Contents

1.1 Cosmology with Weak Gravitational Lensing 1
1.1.1 The ΛCDM Cosmological Model 1
1.1.2 Testing ΛCDM with Cosmological Galaxy Surveys 9
1.1.3 Weak Gravitational Lensing 15
1.1.4 Projected Weak Lensing Observables 18
1.1.5 Measuring Cosmic Shear 20
1.1.6 Cosmic Shear Measurement Bias 24
1.2 Weak Gravitational Lensing with the *Euclid* Spacecraft 28
1.2.1 The *Euclid* Spacecraft 28
1.2.2 The *Euclid* Wide Survey 30
1.2.3 Shear Measurement with *Euclid* 33
1.2.4 The Point Spread Function for *Euclid* 34
1.2.5 Shear Measurement Biases Arising Due to Errors in the PSF for *Euclid* 37
1.3 Thesis Overview 38

1.1 Cosmology with Weak Gravitational Lensing

1.1.1 The ΛCDM Cosmological Model

One of the most significant astronomical developments of the 20$^{\text{th}}$ century was the discovery that the Universe is expanding, and the inference that this expanding Universe originated in a Big Bang. In the last ∼100 years, the project of physical

cosmology has been to theoretically develop, and observationally test, a cosmological model, that is able to consistently explain the observed expansion history of the Universe, its contents, and the evolution of cosmic structure.

The prevailing theoretical paradigm in modern cosmology consists of a model of an expanding spacetime described by the general theory of relativity (Friedmann, 1922; Lemaître, 1927; Robertson, 1935; Walker, 1937). In this model, the cosmic expansion originates with the Big Bang, and the subsequent expansion history is determined by the matter-energy content of the Universe, which is statistically homogeneous and isotropic (Dodelson, 2003). The cosmic expansion causes galaxies to recede from an observer, with recessional velocity proportional to their distance. This recessional velocity introduces a *redshift*, z, to the galaxy spectra[1]; the shift in spectral lines of galaxies was first observed by Slipher, 1914, and linked to recessional velocities by Slipher, 1918. The approximately proportional relationship at low redshifts between galaxy recessional velocities, inferred from redshifts, and distances, inferred from measurements of Cepheid variables within the galaxies, was discovered by Hubble, 1929, providing direct evidence of the expansion of the Universe that had been theoretically predicted by Friedmann, 1922 and Lemaître, 1927. The observed redshift of galaxies may therefore be used as a proxy of their distance, with a distance-redshift relation that depends on the cosmological model.

Early sources of evidence for the presence of a dark matter contribution to the matter-energy content of the Universe included observations of the radial profiles of the orbital velocities of stars in spiral galaxies (Rubin and Ford, 1970) and of velocity dispersions of stars in elliptical galaxies (Faber and Jackson, 1976). Observations of the formation of cosmic structure from galaxy clustering, as well as of the Faber-Jackson relation between elliptical galaxy velocity dispersions and luminosities, and the Tully-Fisher relation between spiral galaxy rotational velocities and luminosities, supported a model in which the dark matter is collisionless, i.e. composed of CDM (Blumenthal et al., 1984). Efstathiou

[1] In addition to a peculiar-velocity contribution to the observed galaxy redshifts.

et al., 1990 first suggested that measurements of the anisotropy of the cosmic microwave background (Bond et al., 1991; Meinhold and Lubin, 1991) and of galaxy clustering from the APM galaxy survey (Maddox et al., 1990) could be explained by a cosmological model dominated by a cosmological constant and cold dark matter. Subsequent observations of the recessional velocities of galaxies obtained using observations of type Ia supernovae (Perlmutter et al., 1999; Riess et al., 1998), and of the cosmic microwave background radiation (CMB, de Bernardis et al., 2001; Hanany et al., 2000), further supported the concordance ΛCDM cosmological model, in which the Universe has zero spatial curvature, and the matter-energy content at late times consists primarily of (i) the cosmological constant Λ, corresponding to a vacuum energy; (ii) cold dark matter, which is pressureless and does not interact via electromagnetism; and (iii) "baryonic" matter, consisting of protons, neutrons and electrons[2].

Constraints on Ω_{m} and Ω_{Λ} obtained from measurements of the distance-redshift relation of type Ia supernovae by Perlmutter et al., 1999 are shown in fig. 1.1; consistent results were obtained by Riess et al., 1998. These results significantly favour a non-zero contribution from a cosmological constant, providing strong evidence for the ΛCDM model. Constraints on the same parameters from measurements of anisotropies in the temperature of the CMB by de Bernardis et al., 2001 are shown in fig. 1.2, with 95% confidence region overlapping that obtained from measurements of type Ia supernovae by Perlmutter et al., 1999; Riess et al., 1998, also providing strong evidence for ΛCDM. Improved, consistent constraints supporting ΛCDM have been obtained by more recent cosmological experiments, including from measurements of type Ia supernovae (see e.g. Brout et al., 2022; Riess et al., 2022) and the CMB (e.g. Planck Collaboration: Aghanim et al., 2020).

In the ΛCDM model, the cosmic expansion begins with a period of exponential expansion referred to as *cosmic inflation*, during which perturbations in the curvature of spacetime with respect to the homogeneous background are sourced

[2]Relativistic species e.g. photons are also present, but these only represent a substantial contribution to the matter-energy content at early times, when the radiation temperature of the Universe (and hence the corresponding energy contribution) is much higher than at late times (Dodelson, 2003).

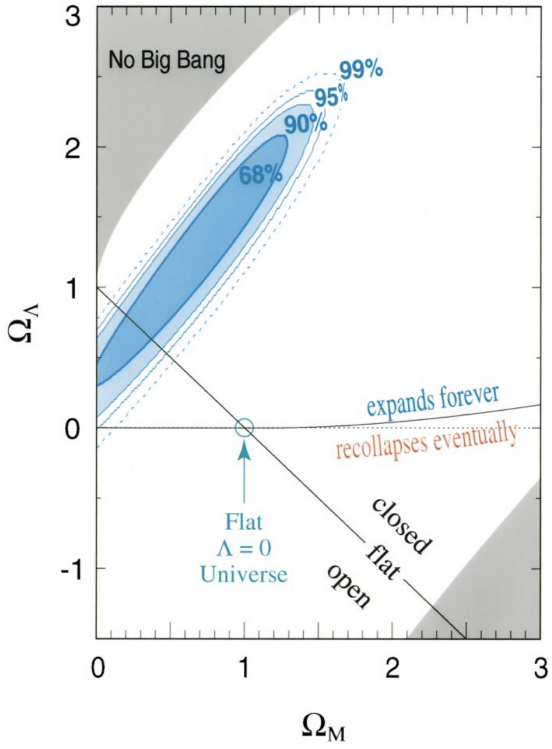


Figure 1.1: Constraints on Ω_m, Ω_Λ from observations of the distance-redshift relation of type Ia supernovae by Perlmutter et al., 1999. Blue contours show the confidence region with labelled confidence levels. The constraints favour a cosmological model consisting of a cosmological constant Λ and CDM.

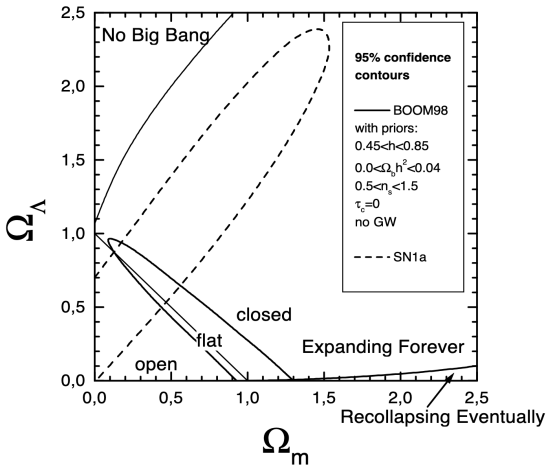


Figure 1.2: 95% confidence level on Ω_m, Ω_Λ from observations of anisotropies in the temperature of the CMB from de Bernardis et al., 2001 (solid contour), compared with the same confidence level contour for type Ia supernovae measurements by Perlmutter et al., 1999; Riess et al., 1998. The 95% confidence regions are consistent, providing evidence for ΛCDM.

by quantum-mechanical fluctuations (Linde, 2005). After inflation ends, these primordial curvature perturbations result in perturbations in the distribution of the matter-energy content of the Universe, which evolve through cosmic time, eventually giving rise to the large-scale structure (LSS) which is observed today (Dodelson, 2003). In particular, the evolution of these perturbations depends on the properties of the cosmological model, including the expansion rate of the Universe, the amplitude and distribution of primordial fluctuations, and the matter-energy content of the Universe, including the absolute and relative contributions of the different components. Measurements of the LSS may therefore be used to constrain the properties of the cosmological model.

The distribution and evolution of perturbations in the matter content of the Universe may be probed in various ways, including by observing anisotropies in the CMB (Ade et al., 2019; Bennett et al., 1996; de Bernardis et al., 2001; Hanany et al., 2000; Planck Collaboration: Aghanim et al., 2020; Spergel et al., 2003), which trace inhomogeneities in the baryon-photon medium at the epoch of last scattering in the early Universe, when the radiation temperature fell below the value corresponding to the ionisation energy of Hydrogen (Dodelson, 2003); as well as by observing the LSS at later times. Probes of the latter include measurements of the clustering of galaxies (Alam et al., 2017; Dark Energy Science Collaboration: Mandelbaum et al., 2018; DESI Collaboration: Adame et al., 2024; Euclid Collaboration: Mellier et al., 2024; Ross et al., 2007), redshifted Lyman-alpha absorption of light from high-redshift quasars by intergalactic neutral Hydrogen (Khaire et al., 2019; McDonald et al., 2006), and the distortion of galaxy images due to weak gravitational lensing (Dalal et al., 2023; Dark Energy Science Collaboration: Mandelbaum et al., 2018; Erben et al., 2013; Euclid Collaboration: Mellier et al., 2024; Heymans et al., 2021; Massey et al., 2007; The DES Collaboration: Abbott et al., 2022). The properties of the cosmological model may also be constrained using other probes, including measurements of the distance-redshift relation using standard candles (Brout et al., 2022; Perlmutter et al., 1999; Riess et al., 1998, 2022), or of the time-delay of high-redshift multiply-imaged periodic sources arising

due to strong gravitational lensing (Wong et al., 2020).

Perturbations in the matter content of the Universe are quantified by the fractional matter density contrast, $\delta(\boldsymbol{x}, t) = \big(\rho(\boldsymbol{x}, t) - \bar{\rho}(t)\big)/\bar{\rho}(t)$, with $\rho(\boldsymbol{x}, t)$ the matter density at three-dimensional position $\boldsymbol{x}$ and time t, and $\bar{\rho}(t)$ the mean matter density at time t. The time-dependence may be recast in terms of the cosmic scale factor a, which parametrises the expansion of the Universe and is normalised to unity at the present epoch; or the cosmological redshift $z = a^{-1} - 1$; this reparametrisation depends on the cosmological model (Dodelson, 2003).

In the ΛCDM cosmological model, the distribution of matter in the Universe is assumed to be statistically homogeneous and isotropic on large scales; together with the assumption of spatial ergodicity, such that spatial averages tend to ensemble averages on large scales (Peacock, 1999), this has the consequence that the spatial average of the overdensity $\langle \delta(\boldsymbol{x}; z) \rangle = 0$. However, homogeneity does not similarly constrain the higher moments of the overdensity field; in particular, the second moments of the overdensity field (also referred to as the *two-point statistics*) are frequently measured in cosmological observations of the LSS[3]. For example, given the Fourier transform of the overdensity field $\tilde{\delta}(\boldsymbol{k}, z)$, a commonly measured quantity is the *matter power spectrum* $P_{\delta\delta}(k, z)$ (Dodelson, 2003):

$$\langle \tilde{\delta}(\boldsymbol{k}_1, z) \tilde{\delta}(\boldsymbol{k}_2, z) \rangle \equiv (2\pi)^3 P_{\delta\delta}(k, z) \delta_D^3(\boldsymbol{k}_1 + \boldsymbol{k}_2), \tag{1.1}$$

with three-dimensional wave-vectors $\boldsymbol{k}_1, \boldsymbol{k}_2$, wave-vector magnitude k, and δ_D^3 is the three-dimensional Dirac delta function. Since $P_{\delta\delta}$ has units of volume, the corresponding dimensionless quantity may be defined as $\Delta_{\delta\delta}(k, z) \equiv \big(k^3/(2\pi)^2\big) P_{\delta\delta}(k, z)$. Since the two-point statistics and their evolution with cosmic time depend on the cosmological model, observations which are sensitive to the two-point statistics are a useful cosmological probe.

Cosmological experiments that aim to test the ΛCDM model do so by constraining a number of quantities which parametrise the model. For example,

[3] In the case of Gaussian perturbations, the higher moments are determined by the second moments and contain no additional information; in ΛCDM, this is the case for primordial perturbations, and for late-time perturbations on large scales; however, this is not the case on small scales, due to non-linearity of the growth of structure in this regime.

observations of the two-point statistics of the LSS are sensitive to the following parameters of the base ΛCDM model (Dodelson, 2003; Euclid Collaboration: Mellier et al., 2024; Planck Collaboration: Aghanim et al., 2020):

- The Hubble constant, H_0, which describes the fractional expansion rate of the Universe at the present epoch; this may also be parametrised by the dimensionless h, where $H_0 = 100h\ \mathrm{km\ s^{-1}\ Mpc^{-1}}$;
- The density parameters Ω_X; for matter-energy component X, the corresponding density parameter is the ratio of the density of that component to the critical density of the Universe, i.e. the total matter-energy density required for the spatial curvature to be zero, evaluated at the present epoch; that is, $\Omega_X = \rho_{X,0}/\rho_{\mathrm{crit},0}$, where the subscript 0 denotes evaluation at the present epoch. Observations of the LSS may constrain the cosmological-constant, cold dark matter, baryonic matter, and total matter density parameters, Ω_Λ, Ω_c, Ω_b, and Ω_m, respectively[4];
- n_s, the slope of the power spectrum of primordial curvature perturbations;
- σ_8, the root-mean-square amplitude of linear matter perturbations, averaged over a scale of $8h^{-1}\mathrm{Mpc}$; this parameter serves as a normalisation of the matter power spectrum.

Additional free parameters may be introduced as extensions to the base ΛCDM model, that might otherwise be assumed to be fixed. For example, observations of the two-points statistics are sensitive to the sum of masses of the three neutrino species, Σm_ν (Euclid Collaboration: Mellier et al., 2024; Planck Collaboration: Aghanim et al., 2020). If the assumption of vanishing spatial curvature is relaxed, then the contribution of the spatial curvature to the expansion and structure-formation history may enter the cosmological model via an additional spatial-curvature density parameter Ω_K, or a total density parameter Ω_tot that is not fixed

[4]Note that in a spatially-flat model, these sum to unity; because Ω_m is the sum of the baryonic and CDM density parameters, in the spatially-flat case it is hence necessary to measure only two density parameters, e.g. Ω_m and Ω_b.

at unity (Dodelson, 2003; Planck Collaboration: Aghanim et al., 2020). Additionally, in the standard cosmological model, the density and pressure of each matter-energy component X are related by an equation of state of the form $p_X = w_X \rho_X$. The equation of state parameter for component X determines the evolution of the density of that component ρ_X via the proportionality (Dodelson, 2003):

$$\rho_X \propto a^{-3(1+w_X)}. \tag{1.2}$$

The value of w_X for each component therefore dictates its effect on the expansion history of the Universe, and has a dominant impact on its effect on cosmic structure formation. Dark energy has the effect of suppressing the rate of growth of matter overdensities $\delta_m(a)$, with a higher dark energy density $\rho_{\rm DE}$ leading to more strongly-surpressed structure growth (Dodelson, 2003). The cosmological constant has equation of state parameter $w_\Lambda = -1$, although observations of the two-point statistics are sensitive to deviations from this. Additionally, in an extended model, the dark energy equation of state parameter may be allowed to evolve with cosmic time; this may be parametrised by (Chevallier and Polarski, 2001; Linder, 2003):

$$w_{\rm DE}(z) = w_0 + w_a \frac{z}{1+z}, \tag{1.3}$$

with w_0, w_a parametrising the redshift evolution of the equation of state. Note that this an arbitrary empirical parametrisation of the redshift-dependence of $w_{\rm DE}$, and the form of (1.3) is not physically-motivated by any particular dark energy model. Observations of the redshift evolution of the two-point statistics of the LSS are sensitive to these parameters (Dark Energy Science Collaboration: Mandelbaum et al., 2018; Euclid Collaboration: Mellier et al., 2024; Heymans et al., 2021; The DES Collaboration: Abbott et al., 2022). Measurements of baryon acoustic oscillations (BAO) obtained from galaxy clustering using spectroscopic redshifts with the Dark Energy Spectroscopic Instrument (DESI), combined with CMB data from Planck and type Ia supernovae (SNe) data from the Pantheon+, Union3, and DES data sets, have been claimed to prefer an evolving dark energy model with negative w_0, w_a; these constraints are shown in fig. 1.3 (DESI Collaboration: Abdul-Karim et al., 2025). On the other hand, this preference may be due to systematics

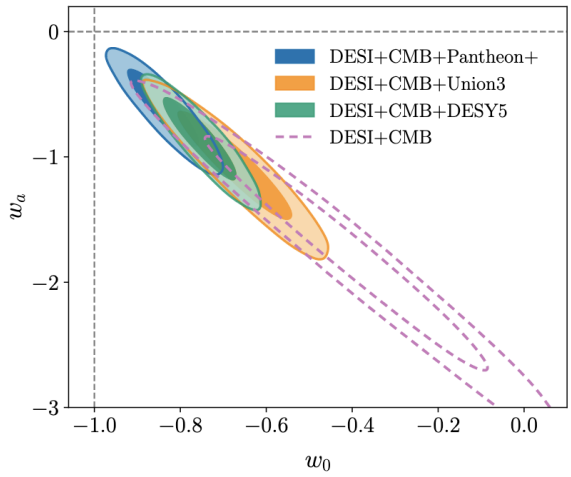


Figure 1.3: Constraints on w_0, w_a from BAO observations from DESI, combined with CMB measurements from Planck and SNe data from the DES, Union3, and Pantheon+ data sets (DESI Collaboration: Abdul-Karim et al., 2025). A joint analysis of these data sets favours an evolving dark energy model with the parametrisation of (Chevallier and Polarski, 2001; Linder, 2003), equation (1.3).

(particularly in the Ia supernovae datasets, see e.g. Efstathiou, 2025b) or issues with the prior expectations on the dark energy model (see e.g. Efstathiou, 2025a; Lewis and Chamberlain, 2025).

1.1.2 Testing ΛCDM with Cosmological Galaxy Surveys

A number of different probes of the two-point statistics of the LSS are employed in cosmological experiments. Many of these involve observations of large numbers of galaxies which trace the LSS. For example, if high-precision measurements of galaxy redshifts are available, i.e. from spectroscopic measurements of galaxies, then three-dimensional positions of galaxies may be estimated, and the two-point statistics (either the power spectrum or its real-space counterpart, the two-point correlation function) of the galaxy number-count distribution (referred to as *galaxy clustering*) may be measured (Alam et al., 2017; DESI Collaboration: Adame et al., 2024). Alternatively, if only lower-quality redshift estimates are available, e.g. from multi-band photometric observations of galaxies, then the *projected* angular two-point statistics may instead be measured by integrating the three-dimensional two-point statistics over the redshift-distribution of sources; radial information may be included by conducting such an analysis in multiple redshift

slices, a technique referred to as *cosmological tomography* (Euclid Collaboration: Mellier et al., 2024; Heymans et al., 2021; LSST Science Collaboration: Abell et al., 2009; The DES Collaboration: Abbott et al., 2022). An important source of systematic bias in measurements of galaxy clustering is that the two-point statistics of the distribution of galaxies are biased with respect to that of the underlying total matter distribution, in a way that depends on the highly non-linear and poorly-constrained physics of galaxy formation; this must be taken into account when constraining cosmological parameters using galaxy clustering measurements (Dodelson, 2003; Seljak et al., 2005).

Another important probe of the two-point statistics of the LSS is the *weak gravitational lensing* effect (Bartelmann and Schneider, 2001; Kilbinger, 2015; Mandelbaum, 2018; see section 1.1.3). Weak gravitational lensing (WL) results in the coherent distortion of galaxy images, arising due to the perturbation of the paths of light rays originating from source galaxies, as a result of the gravitational influence of the intervening matter comprising the LSS. This causes the observed shapes of galaxies, which are (approximately) intrinsically uncorrelated, to become correlated, in a way which depends on the two-point statistics of the LSS and hence on the cosmological model. This may be probed by measuring the two-point statistics of the shapes of galaxy images (typically quantified by their ellipticities, see section 1.1.3). The perturbation to galaxy ellipticities introduced due to WL is referred to as the *shear*; the statistical correlation of the galaxy shears arising due to WL by the LSS is referred to as *cosmic shear*. The signal-to-noise ratio of the perturbation to the shapes of individual galaxy images arising due to the WL effect is small, such that large sample sizes are required for competitive cosmological constraints (Kilbinger, 2015; see also section 1.1.3); since it is more expensive to conduct spectroscopic observations of galaxies than multi-band photometric observations to obtain redshift estimates, for WL it is thus typical to measure the projected two-point statistics in tomographic analyses (Euclid Collaboration: Mellier et al., 2024; Heymans et al., 2021; The DES Collaboration: Abbott et al., 2022; see also section 1.1.4).

WL is advantageous compared to galaxy clustering as a probe of the LSS because, to a first approximation, it does not depend on the bias of the distribution of galaxies with respect to the full matter distribution[5]; because it has a different sensitivity to the matter distribution than the galaxy clustering, WL therefore offers complimentary cosmological information to galaxy clustering. The cross-correlation two-point statistics of the galaxy shape and number-count distributions may also be measured in a tomographic analysis, a cosmological probe referred to as *galaxy-galaxy lensing* (Kilbinger, 2015; Mandelbaum et al., 2006; Pandey et al., 2022; Prat et al., 2022). In a photometric cosmological galaxy survey, all three of these probes — galaxy clustering, cosmic shear and galaxy-galaxy lensing — may be measured, and jointly used to constrain cosmological parameters, in what is referred to as a *3×2-point analysis* (Euclid Collaboration: Mellier et al., 2024; Heymans et al., 2021; Kilbinger, 2015; The DES Collaboration: Abbott et al., 2022).

Measurements of the 3×2-point statistics have been the principal objective of recent photometric cosmological galaxy surveys, including the Dark Energy Survey (DES; The DES Collaboration: Abbott et al., 2022), the Kilo-Degree Survey (KiDS; Heymans et al., 2021), and the Hyper Suprime-Cam Subaru Strategic Program (HSC; Dalal et al., 2023). These measurements have been conducted with the aim of constraining the parameters of the ΛCDM model, in order to detect possible tensions between measurements and the cosmological model, or between different probes, which may indicate the necessity of introducing extensions to the cosmological model. For example, 3×2-point measurements from e.g. KiDS have claimed a tension in the parameter $S_8 \equiv \sigma_8(\Omega_\mathrm{m}/0.3)^{0.5}$ of ∼2–3σ with respect to constraints on the same parameter obtained from observations of the CMB with the *Planck* spacecraft (Amon et al., 2023; DES and KiDS Collaboration: Abbott et al., 2023; Heymans et al., 2021). While such tensions may indicate the presence of physics beyond the ΛCDM model, they may also arise due to uncorrected systematic biases which impact 3×2-point analyses, including shear measurement biases (Euclid Collaboration: Paykari et al., 2020; Huff and Mandelbaum, 2017;

[5]The effect of the use of galaxies as biased tracers of the matter distribution in WL is referred to as *source-lens clustering*, see e.g. Bernardeau, 1998; Yu et al., 2015.

Kilbinger, 2015; Kitching et al., 2019; Sheldon et al., 2020), errors in the modelling of intrinsic alignments of galaxy shapes (Blazek et al., 2012; Hirata and Seljak, 2004; Joachimi and Bridle, 2010), errors in the modelling of the non-linear gravitational and baryonic physics that impact the matter distribution (Sánchez et al., 2022; Tröster et al., 2022), or bias in the estimation of galaxy redshifts from multi-band photometric measurements (Euclid Collaboration: Desprez et al., 2020; Li et al., 2023; Ma et al., 2006; Myles et al., 2021). Constraints on the cosmological parameters S_8 and Ω_m from a joint analysis of cosmic shear measurements from the year 3 data release of DES (DES Y3) and the fourth data release of KiDS (KiDS-1000) are shown in fig. 1.4, in comparison with constraints from the CMB measured with Planck, with constraints from the joint DES-KiDS analysis consistent with Planck at the level of 1.7σ (DES and KiDS Collaboration: Abbott et al., 2023). Constraints on the same parameters obtained from a re-analysis of KiDS-1000 cosmic shear data (KiDS-Legacy), with increased survey area and improved photometric redshift calibration, are shown in comparison with contraints from the year-3 data release of HSC (HSC-Y3), DES-Y3, and Planck in fig. 1.5, and are consistent with Planck at the level of $\sim 0.7\sigma$ (Wright et al., 2025), a substantially improved level of consistency. The impact of improved photometric calibration on the KiDS-Planck consistency in S_8 constraints highlights the importance of systematics to modern cosmological galaxy surveys.

The WL surveys of the 2010s and early 2020s mentioned above, namely DES, KiDS, and HSC, constitute the *Stage-III* WL surveys. These are being followed by the ongoing and forthcoming *Stage-IV* WL surveys (Albrecht et al., 2006), including the *Euclid* Wide Survey (EWS; Euclid Collaboration: Mellier et al., 2024) that is being conducted by the *Euclid* spacecraft (see section 1.2); the Legacy Survey of Space and Time (LSST; Dark Energy Science Collaboration: Mandelbaum et al., 2018) that will be conducted by the Vera C. Rubin Observatory; and the High Latitude Imaging Survey (HLIS; Doré et al., 2018) that will be conducted with the Nancy Grace Roman Space Telescope. The Stage-IV WL surveys will measure the 3×2-point statistics out to higher redshifts, with improved imaging quality,

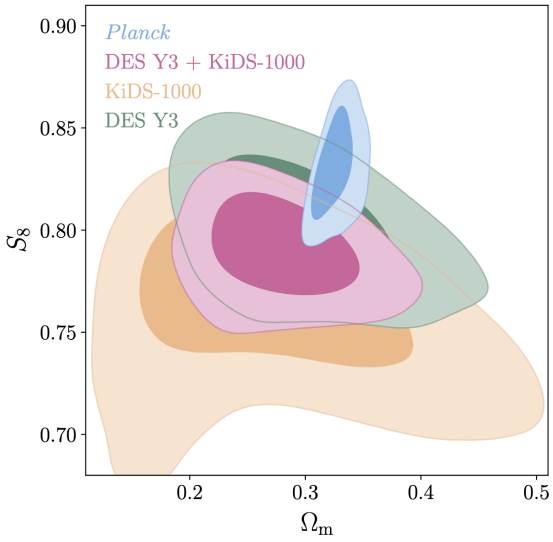


Figure 1.4: Constraints on parameters Ω_m, S_8 from DES Y3, KiDS-1000, a joint analysis of DES Y3 and KiDS-1000, and Planck (DES and KiDS Collaboration: Abbott et al., 2023).

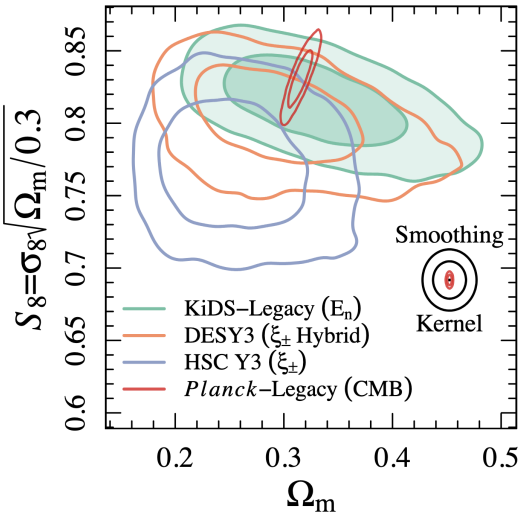


Figure 1.5: Constraints on parameters Ω_m, S_8 from KiDS-Legacy, DES Y3, HSC Y3,and Planck. The quantities E_n and $\xi_\pm$ respectively denote COSEBIs (Asgari et al., 2019) and cosmic shear two-point correlations Kilbinger, 2015 functions, which are different measures of the cosmic shear two-point statistics (Wright et al., 2025).

and with significantly larger sample sizes than the Stage-III WL surveys (Dark Energy Science Collaboration: Mandelbaum et al., 2018; Euclid Collaboration: Mellier et al., 2024); *Rubin* will have increased depth due to repeated observations, while *Euclid* and *Roman* will have high-quality imaging due to the stability of and lack of atmospheric contribution to the PSF (see section 1.1.5, section 1.2.4). This will result in increased cosmological constraining power compared with the Stage-III WL surveys, leading to increased significance of potential tensions with other probes, such as the reported tension in the S_8 parameter. Another cosmological parameter with respect to which data from Stage-IV surveys will be informative is H_0 (Euclid Collaboration: Mellier et al., 2024), for which there is tension of $\sim$4–6σ between CMB measurements and low-redshift probes including measurements of the distance-redshift relation with type Ia SNe (Riess et al., 2022), whereas Stage-III 3$\times$2-point data alone only provide a modest contribution to constraints on H_0 in combination with other probes (Heymans et al., 2021; The DES Collaboration: Abbott et al., 2022). Moreover, the increased signal-to-noise ratio of the WL measurement and deeper redshift sampling of Stage-IV WL surveys results in greater sensitivity to the evolution of the LSS with cosmic time (Dark Energy Science Collaboration: Mandelbaum et al., 2018; Euclid Collaboration: Mellier et al., 2024). This will result in increased precision in constraints on extensions to the dark energy model with respect to ΛCDM, such as an evolving dark energy equation of state parameter as parametrised in (1.3).

WL surveys are subject to many sources of systematic error, which bias the cosmological analysis conducted with data from these surveys. In order to take full advantage of the unprecedented cosmological constraining power of Stage-IV WL surveys (Dark Energy Science Collaboration: Mandelbaum et al., 2018; Euclid Collaboration: Mellier et al., 2024), it will be necessary to control the impact of such sources of systematic bias to an unprecedented degree. Bias in the measurement of the gravitational shear of galaxy images is one such source of systematic error in WL surveys. Forecasting the impact of such shear measurement biases for Stage-IV WL surveys – and in particular, the *Euclid* Wide Survey – is the topic of this work.

1.1.3 Weak Gravitational Lensing

Gravitational lensing is the general-relativistic effect in which the path of a light ray is deflected by the gravitational influence of matter, due to the curvature of spacetime (Schutz, 2009). In the context of cosmology, this may occur when the path of light emitted from distant source is perturbed on its path to an observer, due to the gravitational influence of the intervening matter. This results in distortion of the observed image of the source. In the case where there is an approximate line-of-sight alignment between the source object and a sufficiently concentrated lensing mass distribution, this will result in *strong gravitational lensing* of the observed source, in which the gravitationally-lensed image of the source is strongly distorted, i.e. the transformation of the image is non-linear (Treu, 2010). In the case of point sources e.g.. quasars, this results in the source being multiply-imaged (Wong et al., 2020); in the case of extended sources, in addition to multiple-imaging, this causes the image of the source to be distorted into arcs or rings (Postman et al., 2012).

However, such a line-of-sight alignment does not exist in most source-lens-observer systems. Such cases result in *weak* gravitational lensing. Indeed, all images of cosmological sources are weakly gravitationally-lensed to some finite degree, due to the perturbation of the paths of light rays by the gravitational influence of the LSS (Dodelson, 2003). Because the distortion of source images due to weak lensing depends on the mass distribution of the LSS, it carries cosmological information.

Given the angular position on the sky of a source in the absence of gravitational lensing $\boldsymbol{\theta}^S$ and the observed angular position of the image distorted due to gravitational lensing $\boldsymbol{\theta}^I(\boldsymbol{\theta}^S)$, the two are related by the lens equation (Bartelmann and Schneider, 2001; Kilbinger, 2015):

$$\boldsymbol{\theta}^S = \boldsymbol{\theta}^I - \boldsymbol{\alpha}(\boldsymbol{\theta}^S), \tag{1.4}$$

with $\boldsymbol{\alpha}$ the deflection angle, which depends on the source-lens-observer system. In the case of weak lensing, $\boldsymbol{\alpha}$ is determined by the cumulative effect of the gravita-

tional influence of the LSS along the line of sight. For non-relativistic perturbations δ on scales smaller than the horizon, the evolution of δ obeys Newtonian physics (Peebles, 1980), and δ is related to the Newtonian gravitational potential Φ by the Poisson equation (assuming a pressureless ideal fluid; Kilbinger, 2015):

$$\nabla^2\Phi(\boldsymbol{x},t) = 4\pi G a^2 \bar{\rho}(t)\delta(\boldsymbol{x},t). \tag{1.5}$$

The path of a light ray may be obtained by analogy with geometrical optics, by applying Fermat's principle to the light travel time $t = \int_0^r (n/c)dr'$, with r the radial coordinate, and the refractive index $n = 1 - (2\Phi/c^2)$ obtained from the perturbed FLRW metric in the Newtonian gauge (Dodelson, 2003) for a null geodesic, subject to the approximation that $\Phi/c^2 << 1$; Fermat's principle $\delta t = 0$ then yields the corresponding Euler-Lagrange equations. Integrating these along the line of sight leads to the following result for the deflection angle (Kilbinger, 2015):

$$\boldsymbol{\alpha} = -\frac{2}{c^2}\int_0^r \nabla_\perp \Phi dr', \tag{1.6}$$

with $\nabla_\perp\Phi$ the 2-dimensional gradient of Φ evaluated in the plane perpendicular to the light path. Then defining the *comoving* radial coordinate χ by assuming that the Universe has zero spatial curvature on large scales and factoring the cosmic scale factor out of the physical radial coordinate r such that $\chi(t) = a(t)r$, then the deflection angle $\boldsymbol{\alpha}$ is given by a fractional-comoving-separation-weighted line integral over $\nabla_\perp\Phi$. The lens equation then becomes, for a source at comoving radial coordinate χ (Dodelson, 2003; Kilbinger, 2015):

$$\boldsymbol{\theta}_S = \boldsymbol{\theta}_I - \frac{2}{c^2}\int_0^\chi d\chi' \frac{\chi - \chi'}{\chi}\nabla_\perp\Phi(\chi'), \tag{1.7}$$

where it has been assumed that the Universe has zero spatial curvature on large scales, and the *Born approximation* that applies in the WL regime has been applied, i.e. the line integral is evaluated along the path of the unperturbed light ray (Bartelmann and Schneider, 2001; Kilbinger, 2015).

Linearising the lens equation (1.4), the Jacobian matrix of the transformation from image coordinates $\boldsymbol{\theta}^I$ to source coordinates $\boldsymbol{\theta}^S$ may be written as (Bartelmann

and Schneider, 2001; Dodelson, 2003; Kilbinger, 2015):

$$\frac{\partial \theta_i^S}{\partial \theta_j^I} = \delta_{ij} - \frac{\partial \alpha_i}{\partial \theta_j^I} \equiv A_{ij}, \tag{1.8}$$

where the transformation matrix $\mathbf{A}$ has been defined; the inverse transformation matrix $\mathbf{A}^{-1}$ therefore describes the local mapping from source coordinates to image coordinates. The *convergence* κ and the two-component *shear* γ are defined such that (Bartelmann and Schneider, 2001; Dodelson, 2003; Kilbinger, 2015):

$$\mathbf{A} \equiv \begin{pmatrix} 1 - \kappa - \gamma_1 & -\gamma_2 \\ -\gamma_2 & 1 - \kappa + \gamma_1 \end{pmatrix}. \tag{1.9}$$

The convergence describes the isotropic change in size of a source due to lensing, and the shear describes the anisotropic stretching, distorting a circular source light distribution into an elliptical image light distribution (Dodelson, 2003; Kilbinger, 2015). The shear is a spin-2 quantity – i.e. it is symmetric under a rotation of π radians – and may be expressed as a complex number, $\gamma = \gamma_1 + i\gamma_2$. The shear is the principal observable of weak gravitational lensing, because the shear is estimated by measuring galaxy shapes (see section 1.1.5); however, the image transformation (1.9) also introduces a dependence of the galaxy shapes on the convergence, such that what is actually observed is the *reduced shear*: (Kilbinger, 2015):

$$g = \frac{\gamma}{1 - \kappa}. \tag{1.10}$$

In the weak gravitational lensing regime, both the shear and the convergence are of the order of at most a few percent, i.e. $|\kappa|, |\gamma| \ll 1$; in this case, the reduced shear is a good approximation of the shear to leading order (Kilbinger, 2015). However, for Stage-IV surveys, the inaccuracy of this approximation poses a non-negligible source of systematic bias in the WL analysis; additionally, the magnification of galaxy images due to the convergence impacts the observed angular number density of galaxies, biasing measurements of galaxy clustering. The contribution of the convergence to the cosmic shear and clustering measurements will therefore need to be corrected for or modelled (Duncan et al., 2022; Euclid Collaboration: Deshpande et al., 2020). The convergence may also be estimated from measurements of the magnification of galaxy number counts (Gillis and Taylor, 2016) and galaxy sizes and magnitudes (Freudenburg et al., 2020; Schmidt et al., 2012)

1.1.4 Projected Weak Lensing Observables

As discussed in section 1.1.2, cosmological experiments which study the LSS do so principally by measuring the two-point statistics. WL surveys are therefore primarily concerned with measuring the two-point statistics of the WL observables, in particular of the shear, γ. Because the measured shear is a projected quantity, i.e. is derived from an integral along the line-of-sight, it is of interest to measure the *projected* two-point statistics, i.e. angular two-point statistics of the 2-dimensional shear field projected onto the celestial sphere. This includes the angular two-point correlation function of the shear field that is a function of angular separation, $w(\theta)$ (Miralda-Escude, 1991), or its Hankel transform, the angular power spectrum (Peacock, 1999).

The projected convergence may be expressed as a line integral of the overdensity by subtracting the identity from the trace of the transformation matrix (1.9), inserting the line-integral definition of $\boldsymbol{\alpha}$ from (1.7), and applying the Poisson equation (1.5), using the fact that, for matter, $\bar{\rho} \propto a^{-3}$ (Kilbinger, 2015). This results in (Euclid Collaboration: Deshpande et al., 2024; Kilbinger, 2015):

$$\kappa(\theta) = \int_0^{\chi_{\rm lim}} d\chi \delta(\chi\boldsymbol{\theta}, \chi) W(\chi), \tag{1.11}$$

assuming that the Universe has zero spatial curvature on large scales, making a small angle approximation in the transverse separation $\chi\boldsymbol{\theta}$, and where $\chi_{\rm lim}$ is the limiting comoving distance of the observed galaxy sample. $W(\chi)$ is the *weak lensing projection kernel*:

$$W(\chi) = \frac{3\Omega_{\rm m} H_0^2 \chi}{2c^2 a(\chi)} \int_\chi^{\chi_{\rm lim}} d\chi' \frac{\chi' - \chi}{\chi'} n(\chi), \tag{1.12}$$

where $n(\chi)$ is the distribution of source galaxies as a function of comoving distance.

In the flat-sky approximation, the 2-dimensional Fourier transform of the convergence field $\tilde{\kappa}(\boldsymbol{\ell})$ may then be calculated (Kilbinger, 2015), with the 2-dimensional wave-vector $\boldsymbol{\ell}$ the Fourier conjugate of $\boldsymbol{\theta}$. Under the flat-sky approximation, the two-point correlation of $\tilde{\kappa}(\boldsymbol{\ell})$ is the angular power spectrum:

$$\langle \tilde{\kappa}(\boldsymbol{\ell}_1) \tilde{\kappa}^*(\boldsymbol{\ell}_2) \rangle \equiv (2\pi)^2 C_\ell^{\kappa\kappa} \delta_D^2(\boldsymbol{\ell}_1 - \boldsymbol{\ell}_2), \tag{1.13}$$

with the asterisk denoting complex conjugation, δ_D^2 is the 2-dimensional Dirac delta function, and $C_\ell^{\kappa\kappa}$ the convergence angular power spectrum. In 2-dimensional Fourier space, the convergence and shear are related by a factor of a complex exponential, $\tilde{\gamma}(\boldsymbol{\ell}) = e^{2i\beta}\tilde{\kappa}(\boldsymbol{\ell})$, with β the polar angle of the wave-vector $\boldsymbol{\ell}$; due to isotropy, the convergence and shear therefore have the same angular power spectrum, $C_\ell^{\kappa\kappa} = C_\ell^{\gamma\gamma}$ (Kilbinger, 2015). It should be noted that the flat-sky approximation made when defining angular power spectra in terms of 2-dimensional Fourier transforms of the κ and γ fields is not valid on large angular scales; the exact definition of the $C_\ell^{\gamma\gamma}$ depends instead on the spin-weighted spherical harmonic transform of the shear, $\gamma_{\ell m}$, and in this regime the identity $C_\ell^{\kappa\kappa} = C_\ell^{\gamma\gamma}$ does not hold. The exact curved-sky definition of the $C_\ell^{\gamma\gamma}$ in terms of spin-weighted spherical harmonics is provided in Taylor et al., 2018.

Defining a set of *tomographic* samples of source galaxies with distributions $n_i(\chi)$ from which tomographic shear fields γ_i are observed, then the angular power spectrum of the cross-correlated shear fields γ_i, γ_j in the flat-sky approximation is given by (Euclid Collaboration: Deshpande et al., 2024; Kilbinger, 2015):

$$C_\ell^{\gamma_i\gamma_j} = \int_0^{\chi_{\rm lim}} d\chi \frac{W_i(\chi)W_j(\chi)}{\chi^2} P_{\delta\delta}\Big(k = \frac{\ell - 1/2}{\chi}, \chi\Big), \tag{1.14}$$

also assuming that the Universe has zero spatial curvature on large scales, applying the *Limber approximation*, in which correlations along the line of sight are neglected, and where $W_i(\chi)$ are the lensing projection kernels (1.12) corresponding to the source distributions $n_i(\chi)$. The cosmic shear angular power spectra are therefore sensitive to the cosmological model, and hence the cosmological parameters listed in section 1.1.1, via its dependence on the matter power spectrum $P_{\delta\delta}$ (1.1) and its evolution, as well as via the lensing kernel functions W_i, which also depend on the redshift-scale factor-comoving-distance relation.

The galaxy clustering angular power spectra are defined by replacing the weak lensing kernels functions $W_i(\chi), W_j(\chi)$ in (1.14) with the corresponding galaxy clustering kernel functions, with each determined by the product of the source distribution $n_i(\chi)$ and a linear galaxy bias function $b_i(\chi)$ that describes the bias of the galaxy distribution with respect to the underlying matter distribution,

$\tilde{\delta}_{\rm gal}(\boldsymbol{k},\chi) = b_i(\chi)\tilde{\delta}_{\rm matter}(\boldsymbol{k},\chi)$, rather than the weighted integral over $n_i(\chi)$ as in (1.12) (Chisari et al., 2019). Similarly, the galaxy-galaxy lensing cross-correlation angular power spectra are defined by including a product of the corresponding WL and galaxy-clustering kernel functions in (1.14) (Chisari et al., 2019; Euclid Collaboration: Tutusaus et al., 2020). Joint cosmological parameter inference from combined tomographic measurements of cosmic shear, galaxy clustering, and galaxy-galaxy lensing angular power spectra, or alternatively, angular 2-point correlation functions, constitutes the 3×2-point analysis.

As described above, the shear is a complex, spin-2 quantity. The complex shear field therefore has three unique angular power spectra associated with it, e.g.. the auto-correlation and cross-correlation angular power spectra of the real and imaginary components $\tilde{\gamma}_1(\boldsymbol{\ell}), \tilde{\gamma}_2(\boldsymbol{\ell})$, defined analogously to (1.13). Alternatively, it is possible to decompose the shear field into curl-free *E-mode* and divergence-free *B-mode* components $\tilde{\gamma}^E(\boldsymbol{\ell}), \tilde{\gamma}^B(\boldsymbol{\ell})$, which are linear combinations of the components of the (spin-weighted) spherical-harmonic transforms of the complex shear field (Euclid Collaboration: Deshpande et al., 2024; Kitching et al., 2020, 2019). This has the advantage that, to leading order, only the E-mode auto-correlation angular power spectra $C_\ell^{\gamma_i^E\gamma_j^E}$ are expected to be introduced by WL, with the B-mode auto-correlation spectra $C_\ell^{\gamma_i^B\gamma_j^B}$ and the E-B cross-correlation spectra $C_\ell^{\gamma_i^E\gamma_j^B}$ vanishing in the absence of systematic effects, and neglecting B-modes induced due to source clustering (Euclid Collaboration: Deshpande et al., 2024; Kilbinger, 2015; Schneider et al., 2002). This separation of E- and B-mode angular power spectra therefore may be used as a diagnostic of the presence of systematic effects in WL surveys (see e.g. Kilbinger, 2015; Schneider et al., 2010).

1.1.5 Measuring Cosmic Shear

In WL surveys, the shear is estimated from measurements of the complex *ellipticity* of galaxy images $\boldsymbol{\epsilon}$, which is defined in terms of the major/minor axis ratio and position angle of the galaxy light profile; one definition is as follows (Schneider, 2006):

$$\boldsymbol{\epsilon} = \frac{1-a/b}{1+a/b}e^{2i\phi}, \tag{1.15}$$

with a, b the semi-major and semi-minor axes of the source light distribution, respectively, and ϕ the position angle. Another definition, referred to as the complex *polarisation*, is as follows (Schneider, 2006):

$$\boldsymbol{\chi} = \frac{1-(a/b)^2}{1+(a/b)^2} e^{2i\phi}. \tag{1.16}$$

Note that here $\boldsymbol{\chi}$ should not be confused with the comoving distance mentioned in previous sections.

Defining the intrinsic source ellipticity (in the absence of lensing) as $\boldsymbol{\epsilon}_{\rm int}$, then the observed ellipticity $\boldsymbol{\epsilon}$ as a function of the reduced shear g is (for $|g| \leq 1$, Seitz and Schneider, 1997):

$$\boldsymbol{\epsilon} = \frac{\boldsymbol{\epsilon}_{\rm int} + g}{1 - g^* \boldsymbol{\epsilon}_{\rm int}}. \tag{1.17}$$

Neglecting intrinsic alignments, $\langle \boldsymbol{\epsilon}_{\rm int} \rangle = 0$, the ellipticity definition (1.15) therefore has the convenient property that $\langle \boldsymbol{\epsilon} \rangle = g$. In the WL regime, $|g| \ll 1$ and the approximation $g \approx \gamma$ applies; hence, (1.17) reduces to $\boldsymbol{\epsilon} \approx \boldsymbol{\epsilon}_{\rm int} + \gamma$. The mean observed ellipticity $\langle \boldsymbol{\epsilon} \rangle$ is therefore an unbiased estimator of the shear:

$$\langle \boldsymbol{\epsilon} \rangle \approx \gamma. \tag{1.18}$$

If the polarisation definition of the ellipticity (1.16) is adopted, then, under the same approximations described above, the observed polarisation is approximated as $\boldsymbol{\chi} \approx \boldsymbol{\chi}_{\rm int} + P_\gamma \gamma$, with P_γ the *shear polarisability*. The polarisability is a matrix $P_{\gamma,ij} = \delta^{\rm K}_{ij} + \boldsymbol{\chi}_{{\rm int},i} \boldsymbol{\chi}_{{\rm int},j}$, such that $\langle P_{\gamma,ij} \rangle = (1 + \sigma^2_{\boldsymbol{\chi}}) \delta^{\rm K}_{ij}$, with $\delta^{\rm K}_{ij}$ the Kronecker delta and $\sigma^2_{\boldsymbol{\chi}}$ the variance of the (intrinsic) galaxy polarisation; in practice, this is approximated as a scalar $P_\gamma \approx 1.86$ (Paulin-Henriksson et al., 2008). The polarisation is therefore a biased estimate of the shear:

$$\langle \boldsymbol{\chi} \rangle \approx P_\gamma \gamma. \tag{1.19}$$

The polarisation definition (1.16) may be adopted because it has a simpler dependence on the second moments of the brightness distribution than the ellipticity definition (1.15).

The galaxy ellipticity (or polarisation) is measured from the source brightness distribution $I(\boldsymbol{x})$, with $\boldsymbol{x}$ the field-of-view position, obtained from noisy, pixelised data. The ellipticity may be measured directly, e.g.. from the second moments of the brightness distribution (see section 3.1.1; Bernstein and Jarvis, 2002; Hoekstra et al., 1998; Kaiser et al., 1995). Alternatively, the ellipticity may be estimated by fitting a model of the galaxy brightness profile parametrised by the ellipticity (e.g.. Euclid Collaboration: Congedo et al., 2024; Gentile et al., 2012; Miller et al., 2007; Zuntz et al., 2013). Bayesian model-fitting methods such as *lens*`fit` (Miller et al., 2007, 2013) and LENSMC (Euclid Collaboration: Congedo et al., 2024) jointly fit the model parametrised by the ellipticity to multiple exposures, while marginalising over nuisance parameters, including the galaxy size, position, flux, and radial profile (parametrised e.g. by Sérsic index, Sérsic, 1963).

Point-spread function correction

A critical component of shear measurement is the correction for the point-spread function (PSF) of the imaging system that is used to observe the galaxies. The PSF describes the response of the imaging system to a point source, and is convolved with the galaxy images; it depends on the response of the optical system, the detector response, and, for ground-based observations, the atmosphere; and in general, it is a function of FoV position, time, and wavelength. Convolution with the PSF acts to circularise galaxy images, reducing ellipticity correlations; on the other hand, anisotropy in the PSF may introduce additional spurious galaxy ellipticity correlations (Kilbinger, 2015).

In WL surveys, the PSF is modelled; this model may consist of an empirical parametrisation of the PSF, or be computed from a physically-realistic model of the optical system. For ground-based observations, the PSF is dominated by the atmospheric contribution, and has an approximately Gaussian profile (see e.g. Giblin et al., 2021), whereas for space-based observations, more detailed physical effects depending on the properties of the optical system must be considered (see e.g. Euclid Collaboration: Mellier et al., 2024). The PSF model is fit to

multiple stars in the FoV, and the PSF is then estimated for target galaxies, e.g. by interpolation. Since the PSF is in general wavelength-dependent, spectral information for the calibration stars is required to characterise the chromaticity of the PSF in order to accurately estimate the PSF for target galaxies (Kilbinger, 2015; Mandelbaum, 2018).

In direct shear measurement methods, the PSF must be deconvolved from the galaxy brightness distribution before the ellipticity is measured. For example, in the case of techniques which estimate the ellipticity from the second moments of the brightness distribution, (e.g. Kaiser et al., 1995), the PSF is deconvolved directly from the second moments of the brightness distribution[6]. On the other hand, in model-fitting shear-measurement methods (e.g. Miller et al., 2013), the PSF is convolved with the galaxy brightness distribution model before fitting to the data.

Weak gravitational lensing is a subtle effect, introducing distortions to observed galaxy ellipticities which are ~ 0.03 times the intrinsic ellipticity (Kilbinger, 2015). It is therefore necessary to average the ellipticity measurements over a large number of galaxies in order to obtain a shear measurement with a sufficiently high signal-to-noise ratio; in general, it is necessary to average ellipticity measurements over several hundred galaxies in order to obtain a signal-to-noise ratio of order unity (Kilbinger, 2015). Additionally, the bulk of the cosmological signal is carried by high-redshift source galaxies, with typical r- or i- band magnitudes $\sim$24, signal-to-noise ratios $\sim$10, and typically extending over $\sim$3–5 pixels, similar in size to the PSF (Kilbinger, 2015); accurate shear measurement and PSF estimation is therefore a central part of WL surveys.

Photometric redshifts

In addition to the shear measurement, another crucial component of the measurement the two-point statistics of the shear field is the estimation of galaxy redshifts, which provide the radial information which enters the source distri-

[6]For the case of space-based observations in which the PSF is diffraction limited, the procedure is more complicated; see chapter 3 for a discussion.

bution functions[7] $n_i(z)$, which enter e.g. the lensing projection kernels $W_i(\chi)$ (1.12) and the angular power spectra $C_\ell^{\gamma_i\gamma_j}$ (1.14). However, due to the large sample sizes required for WL surveys (Kilbinger, 2015), it is not feasible to obtain high-resolution spectroscopic observations that would be required for precise per-galaxy redshift estimates; instead, redshifts are estimated from broad-band photometric observations, resulting in *photometric redshifts* (Euclid Collaboration: Desprez et al., 2020; Ma et al., 2006). The main requirement on photometric redshift estimation is ensemble accuracy in the mean redshift and shape of the source redshift distribution functions $n_i(z)$, rather than accuracy on individual galaxy redshift estimates. Photometric-redshift estimation methods include SED-template-fitting-based techniques (e.g. BPZ, Benítez, 2000), machine-learning techniques utilising a spectroscopic training sample, such as self-organising maps, (SOMs; see e.g. Buchs et al., 2019), or techniques that make use of spatial clustering information of galaxies (see e.g. Rahman et al., 2015).

1.1.6 Cosmic Shear Measurement Bias

As described in section 1.1.5, cosmic shear is a very subtle effect, with distortions introduced of order a few percent of the intrinsic galaxy ellipticity. Shear measurement is therefore susceptible to observational systematic effects which induce *shear bias*. Since the shear is estimated by averaging over an ensemble of galaxy ellipticity measurements, what is required for WL is that the galaxy ellipticity measurements are unbiased on average. Bias in the measured shear can be approximated using a linear model (Heymans et al., 2006; Huterer et al., 2006):

$$\tilde{\gamma} = (1 + \boldsymbol{m})\gamma + \boldsymbol{c}, \tag{1.20}$$

with $\tilde{\gamma}, \gamma$ the measured and true shear, respectively, and $\boldsymbol{m}, \boldsymbol{c}$ are *multiplicative* and *additive* shear measurement biases, referred to as m- and c-biases, respectively. The additive and multiplicative shear biases are in general functions of angular position, redshift, and galaxy properties. Additive shear biases impact the $C_\ell^{\gamma\gamma}$

[7] Recasting the dependence on comoving distance χ to dependence on redshift, which is cosmology-dependent.

additively, via the angular power spectrum of the c-bias field; a spatially-constant additive bias has no impact on the $C_\ell^{\gamma\gamma}$ (Massey et al., 2013). A spatially-constant multiplicative bias introduces a constant multiplicative factor to the $C_\ell^{\gamma\gamma}$ (Massey et al., 2013); by comparison with (1.12), (1.14), it can be seen that this is degenerate with the source galaxy redshift distributions $n(z)$. Spatially-varying m-bias has a convolutive impact on the $C_\ell^{\gamma\gamma}$ (Kitching et al., 2019; this is the subject of chapter 2 (Cragg et al., 2022). It should be noted that since the shear is a spin-2 quantity, the spin-0 multiplicative bias m present in (1.20) is not fully general; in fact, in addition to the complex spin-0 multiplicative bias contribution, corresponding to a scaling and rotation of the shear field, Kitching et al., 2021 identified the possibility of a spin-4 multiplicative contribution to the shear bias, corresponding to a reflection of the shear field. Moreover, additional multiplicative bias terms with non-zero spin present in shear bias expansions to quadratic order are identified in Kitching and Deshpande, 2022. Only scalar spin-0 contributions to the multiplicative shear bias are considered in the work presented in this thesis.

Numerous effects introduce bias into shear measurement. For both model-fitting and direct shear measurement methods, the non-linear transformation from a noisy, pixelised brightness distribution to ellipticity estimates results in bias arising due to the imaging noise, *noise bias* (Hirata et al., 2004; Kilbinger, 2015; Refregier et al., 2012). Additionally, for model-fitting methods, an inappropriate galaxy brightness distribution model introduces *model bias*; for example, a model with too many or too few parameters will result in over- or under-fitting, respectively. Model bias can also be introduced if there is an ellipticity gradient across the galaxy brightness profile, e.g. due to bulge and disc components with different ellipticities (Bernstein, 2010; Voigt and Bridle, 2010). Ensemble shear biases can also be introduced due to source galaxy sample selection and detection effects, i.e. if the average shear of the selected source sample is not representative of the true shear field (Fenech Conti et al., 2017; Huff and Mandelbaum, 2017; Huff et al., 2014; Mandelbaum, 2018).

Shear bias arising due to PSF errors

An important source of shear bias arises due to error in the PSF assumed for shear measurement. In general, errors in the anisotropy of the PSF result in additive shear bias, whereas errors in the size of the PSF cause the galaxy ellipticity estimates to be diluted, resulting in multiplicative shear bias (Kilbinger, 2015; Mandelbaum, 2018; Massey et al., 2013; Paulin-Henriksson et al., 2008). Variations in PSF errors can result in spurious correlations in the measured shear field which can impact the cosmological analysis of WL data (Mandelbaum, 2018).

PSF error can originate from multiple sources. Just as with the shear measurement, the PSF estimation is susceptible to both noise and model biases (Kilbinger, 2015; Mandelbaum, 2018). The PSF model must accurately represent the spatial, temporal, and spectral variation of the PSF. If an empirical PSF model is insufficiently complex to capture these variations, or if a physically-motivated forward model neglects certain effects that impact the optical system, then the assumed PSF will be subject to model bias (Chang et al., 2012; Jarvis and Jain, 2008; Miller et al., 2013). Additionally, noise in the imaging data of stars used to fit the PSF model, as well as in spectral data used to characterise the chromaticity of the PSF, causes the assumed PSF to be subject to noise bias (see e.g. Melchior and Viola, 2012). Moreover, error can be introduced when estimating the PSF for galaxies from the model fit, which may be done e.g. by interpolation (see e.g. Paulin-Henriksson et al., 2008). Error in the assumed PSF for target galaxies may also arise due to systematic uncertainty in the chromaticity of the target galaxies themselves, for example due to imperfect knowledge of the spectral energy distribution (SED) of the galaxies (Cypriano et al., 2010; Meyers and Burchat, 2015), or due to colour gradients across the light profile of each target galaxy (Voigt et al., 2012). Forecasting the impact of shear biases arising due to PSF errors on the *Euclid* Wide Survey is the subject of chapter 3, chapter 4, and chapter 5.

Mitigation of shear biases

Various techniques have been proposed to detect or mitigate the impact of shear measurement biases in WL surveys. METACALIBRATION (Huff and Mandelbaum, 2017; Kannawadi et al., 2021; Sheldon and Huff, 2017) and METADETECTION (Sheldon et al., 2020) estimate the bias induced by the shape estimator, by applying an artificial shear to a galaxy image and measuring the response of the estimator, while taking into account selection and, in the case of METADETECTION, detection effects. Null tests have been proposed to detect the presence of residual PSF modelling errors in shear data, including by measuring correlations between measured star and model PSF sizes and shapes (see e.g. Jarvis et al., 2016; Rowe, 2010), as well as between higher moments of the PSF and galaxy shapes (Zhang et al., 2021, 2022). Techniques have also been proposed to measure the additive shear bias directly from shear maps, based on discrepancies between the statistics of the observed shear field from the fiducial cosmological expectation, including the expected vanishing of the shear signal when averaged over a sufficiently large area of the sky (Kitching et al., 2021; van Uitert and Schneider, 2016).

Due to the expected high statistical precision of Stage-IV WL surveys, systematic effects will need to be controlled to an unprecedented degree for these surveys. This is especially true for the shear measurement bias for these surveys, which will require accurate shear measurement for the high-redshift, low-magnitude, low-angular-size source galaxies which carry the bulk of the cosmological WL signal (Kilbinger, 2015). Forecasting the impact of shear measurement biases for Stage-IV WL surveys such as the LSST and the EWS is therefore an important task facing these surveys, and is the subject of the present work.

1.2 Weak Gravitational Lensing with the *Euclid* Spacecraft

1.2.1 The *Euclid* Spacecraft

Euclid is a medium-class mission in the Cosmic Vision 2015-2025 programme of the European Space Agency (ESA) (Euclid Collaboration: Mellier et al., 2024). The *Euclid* spacecraft, shown in fig. 1.6, is a space-based telescope, launched in 2023[8] with the primary aim of probing cosmology, and in particular constraining the properties of dark energy, by making observations of the LSS. *Euclid* will conduct the *Euclid* Wide Survey (EWS), a spectroscopic galaxy-clustering and photometric galaxy-clustering and WL cosmological survey.

The *Euclid* spacecraft consists of the telescope proper, instruments, and the service module, carrying the equipment supporting the spacecraft operations. The telescope is a 3-mirror anastigmat Korsch design (Korsch, 1977), with a 1.2-m primary mirror. The Korsch design consists of three curved mirrors; a further two flat mirrors are also present in the instrument cavity to guide the light beam to the instruments. A dichroic surface is present at the exit pupil of the telescope, that splits the visible and near-IR components of the beam, with each beam component directed to the corresponding instrument located in the payload module instrument cavity. A Sun-shield, part of the service module, is present, to protect the optical assembly and instruments from solar radiation, including to maintain thermal stability. *Euclid* is in orbit around the Earth-Sun Lagrange point L2, which is a thermally-stable environment (Euclid Collaboration: Mellier et al., 2024).

Euclid carries two scientific instruments: the Near-Infrared Spectrometer and Photometer (NISP; Euclid Collaboration: Jahnke et al., 2024), and the Visible instrument (VIS; Euclid Collaboration: Cropper et al., 2024). Both instruments share a $\sim$0.54 deg^2 field-of-view (Euclid Collaboration: Mellier et al., 2024).

[8] Following some delay in sourcing a launch vehicle, after the originally-planned Soyuz ST-2.1B rocket became unavailable, owing to concurrent geopolitical events (Euclid Collaboration: Mellier et al., 2024).

NISP is a near-IR (NIR) instrument capable of both spectroscopy (NISP-S) and multi-band imaging (NISP-P). The instrument consists of a filter wheel, a grism wheel, and the NIR detector. The filter wheel contains three photometric NIR passband filters, used for multi-band NIR imaging. The grism wheel contains 4 grisms which are used for NIR slitless spectroscopy; three "red" grisms which allow target spectra to be disentangled in the NISP images, and one "blue" grism which is used for observations that are ancillary to the EWS. The detector consists of a 4×4 array of Mercury-Cadmium-Telluride photodiode NIR detectors (Euclid Collaboration: Jahnke et al., 2024). NISP will conduct the spectroscopic galaxy clustering component of the EWS, as well as provide multi-band photometry to support the photometric redshift and PSF estimation for the photometric galaxy clustering and WL components of the EWS. NISP will also collect data for the *Euclid* Deep Survey (EDS), which provides auxillary data supporting the scientific analysis of the EWS, and is used for legacy science (Euclid Collaboration: Mellier et al., 2024).

The main purpose of the VIS instrument is to obtain accurate galaxy-shape measurements for the WL component of the EWS. VIS is a 6×6 array of charge-coupled device (CCD) detectors (Endicott et al., 2012), each with 4132×4096 $0.1''$ pixels in four quadrants. VIS has a single optical passband covering the wavelength range 530-920 nm, which is defined by the throughput of the optical system and detector, rather than a single photometric filter. This wide passband results in a highly chromatic PSF; see chapter 4 for a discussion of the impact of this on shear measurement. The CCD is kept at a temperature of $153\mathrm{K}$ to optimise the function of the instrument. The data from the CCDs is read out by 12 sets of read-out electronics (ROEs). In order to prevent image trailing arising due to continuous illumination of the detector during readout, a shutter is present; the operation of the shutter impacts the VIS PSF. The high pixel resolution, wide passband, and high throughput of the VIS detector are optimised for $S/N \geq 10$ detections of targets out to a limiting AB magnitude $m_{\mathrm{AB}} = 25$, sufficient for precise galaxy shape measurements for cosmological WL. Imaging data from



Figure 1.6: The *Euclid* spacecraft prior to launch. Top: telescope baffle; middle: payload module instrument cavity; bottom: service module; back: Sun shield (Euclid Collaboration: Mellier et al., 2024).

VIS will be used for the WL component of the EWS, as well as for the EDS and auxillary observations (Euclid Collaboration: Cropper et al., 2024; Euclid Collaboration: Mellier et al., 2024).

1.2.2 The *Euclid* Wide Survey

The *Euclid* Wide Survey (Euclid Collaboration: Scaramella et al., 2022) is the principal cosmological galaxy survey that is being conducted by *Euclid*. The currently ongoing EWS is planned to cover ∼14,000 deg^2 of extragalactic sky, avoiding the galactic plane, zodiacal background close to the ecliptic, solar system objects, and bright stars ($m_{\mathrm{AB}} < 4$), that contaminate the imaging. The EWS will consist of photometric imaging observations from VIS and NISP-P for ∼1.5 billion targets for the 3×2-point measurement, as well as spectroscopic observations from NISP-S for ∼35 million targets for the spectroscopic galaxy clustering measurement (Euclid Collaboration: Mellier et al., 2024). A space-based survey was chosen to allow a large survey footprint for cosmological LSS measurements, and to allow a highly stable, diffraction-limited PSF for precise shape measurement, with the

VIS imaging expected to have a limiting AB magnitude $m_{\rm VIS} \sim 26.7$ for 5σ point-source detection(Euclid Collaboration: Mellier et al., 2024), and with galaxies out to redshift $z \sim 2$ planned to be used in the 3×2-point analysis (Euclid Collaboration: Scaramella et al., 2022). The main aim of the EWS[9] is to investigate the origin of the accelerated expansion of the Universe, as well as to constrain the properties of dark matter (Euclid Collaboration: Mellier et al., 2024), and to investigate the origin of tensions in cosmological parameters present in data from Stage-III surveys, including H_0 and S_8 (DES and KiDS Collaboration: Abbott et al., 2023; Heymans et al., 2021; Riess et al., 2022). With respect to dark energy, the performance of the survey is quantified in terms of the dark energy *figure of merit* (FoM), defined in terms of the covariance matrix of the estimated values of dark energy parameters w_0, w_a, as follows (Euclid Collaboration: Mellier et al., 2024):

$$\mathrm{FoM_{DE}} = \frac{1}{\sqrt{\det[\mathrm{Cov}(w_0, w_a)]}}, \tag{1.21}$$

with w_0, w_a parametrising the redshift-evolution dark energy equation of state parameter w, as in (1.3). One of the main aims of the EWS is to constrain w_0, w_a such that FoM_{DE} >400 (Euclid Collaboration: Mellier et al., 2024; Euclid Collaboration: Paykari et al., 2020).

The nominal survey operations, including the EWS, were preceded by a period of commissioning, performance-verification, and calibration observations. Beginning in February 2024, the EWS is currently being conducted within a 6-year mission baseline length[10], and is planned to occupy 65.5% of the time spent conducting the routine spacecraft operations. The EWS coverage split by yearly progress is shown in fig. 1.7 (Euclid Collaboration: Mellier et al., 2024).

The spacecraft conducts EWS observations by tessellating the survey region of interest with non-overlapping tiles, arranged in rectangular patches, with four dithered exposures per tile. The observation sequence is planned subject to constraints on the allowed set of orientations of the spacecraft with respect

[9] As well as of the other Stage-IV WL surveys, the LSST (Dark Energy Science Collaboration: Mandelbaum et al., 2018) and the HLIS (Doré et al., 2018).

[10] The 6-year mission baseline is set by the amount of propellant carried by the spacecraft, that is required for maintenance of the unstable halo orbit around L2.

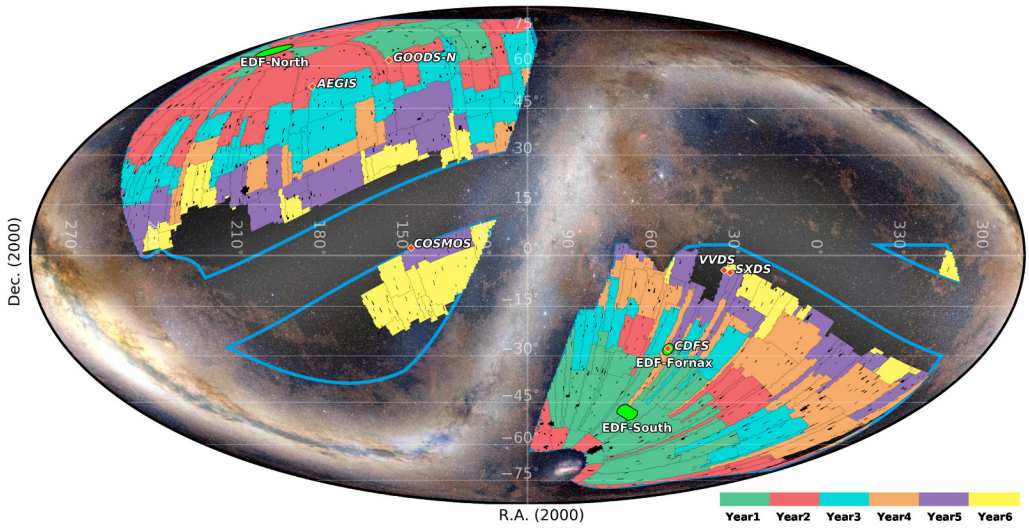


Figure 1.7: EWS footprint and coverage by year. Solid blue lines show the EWS region of interest with minimal non-extragalactic contamination. Light green regions correspond to EDS/auxillary fields; red diamonds indicate auxillary fields with overlapping external calibration data (Euclid Collaboration: Mellier et al., 2024).

to the Sun vector, to optimise thermal stability, and minimise the stray light that enters the optical system. Aside from the EWS, time is also allocated in the routine survey operations for EDS and auxillary field observations, calibration, and orbital maintenance. Approximately 9% of the nominal survey time is unallocated because target fields are not visible (Euclid Collaboration: Mellier et al., 2024; Euclid Collaboration: Scaramella et al., 2022).

In addition to the observations that are conducted by the *Euclid* spacecraft, the EWS also makes use of complimentary ground-based photometric and spectroscopic data, to supplement the photometry and spectroscopy carried out with NISP. This data is used for photometric redshift estimation, as well as to characterise the chromaticity of the VIS PSF. External multi-band photometry is required for the latter because the NIR NISP bands do not overlap the wavelength range of the VIS passband (Euclid Collaboration: Mellier et al., 2024). In the southern hemisphere, the EWS will make use of photometric data from the DES (Gatti et al., 2021), and the LSST (Guy et al., 2022); in the northern hemisphere, the external photometry will be provided by the UNIONS collaboration, consisting of data from CFHT, Pan-STARRS and HSC (Chambers et al., 2020). The EWS also makes

use of ground-based spectroscopic observations, which enters the photometric redshift and PSF calibration (Euclid Collaboration: Mellier et al., 2024).

1.2.3 Shear Measurement with *Euclid*

As described in section 1.1.6, the galaxy shape estimation is a crucial part of WL measurement. In the EWS, it is planned to use LENSMC, which is a Bayesian model-fitting shear measurement algorithm that involves marginalisation over nuisance parameters (Euclid Collaboration: Congedo et al., 2024). Work is also ongoing to integrate the METACALIBRATION algorithm (Huff and Mandelbaum, 2017; Sheldon and Huff, 2017) in the shear measurement pipeline for the EWS, to self-calibrate the response of the shear measurement algorithm (Euclid Collaboration: Mellier et al., 2024). Because *Euclid* is a space-based telescope, its PSF is diffraction-limited, and therefore has a complicated profile which is forward-modelled based on a physical model of the telescope, and fit to observations of stars (Euclid Collaboration: Mellier et al., 2024; see section 1.2.4). This approach is also motivated by the fact that the *Euclid* PSF is undersampled, and estimated from observations of stars which are shot-noise dominated.

In WL surveys, there are many observational systematic effects which impact the shear measurement. These include target detection and selection effects (Sheldon et al., 2020), the blending of galaxy images, including at different redshifts (MacCrann et al., 2022), detector effects including detector non-linearity, charge-transfer inefficiency (CTI; see e.g. Rhodes et al., 2010) and the brighter-fatter effect (BFE; see e.g. Antilogus et al., 2014), and other sources of error including cosmic rays, variations in star density, and various sources of background pixel noise (Euclid Collaboration: Martinet et al., 2019). For the EWS, the impact of CTI, the BFE, and detector non-linearity are corrected for in the data, while the impact of other instrumental effects are calibrated using simulated realistic *Euclid* mock data. This includes the high density of cosmic rays present in VIS images, which are flagged and affected pixels masked in the processing of the VIS imaging data. This process results in residual error that causes bias in the shear measurement, that

must be calibrated using image simulations. Because of the redshift-dependence of these effects, the calibration must be done separately for each tomographic bin, and the shear and photometric-redshift calibration must be done jointly (Euclid Collaboration: Mellier et al., 2024).

In order to satisfy the mission aims, in particular the requirement on $\mathrm{FoM_{DE}}$ discussed in section 1.2.2, requirements are placed on the precision of the calibration of EWS data. In the case of the shear measurement, this is expressed in terms of additive and multiplicative residual shear measurement biases, i.e. requirements on the uncertainty of the correction for bias in the shear measurement. These requirements are derived in Massey et al., 2013 as a requirement on the root-mean-square uncertainty on the residual additive bias $\sigma[\boldsymbol{c}] < 1.5{\times}10^{-4}$ and on the residual multiplicative bias $\sigma[m] < 2{\times}10^{-3}$. These requirements are discussed in more detail in section 3.1.2.

1.2.4 The Point Spread Function for *Euclid*

As discussed in section 1.1.6, a central component of shear measurement consists of the correction for the PSF. For the EWS, this is accomplished by forward-modelling the VIS PSF, taking into account the physical state of the spacecraft, in particular the optical system and VIS detector. This approach is chosen over empirical PSF estimation from stars and interpolation to the FoV positions of galaxies (as described in e.g. Kilbinger, 2015). This choice is made because, in the case of an empirical interpolation-based method, the density of stars across the VIS FoV of sufficiently high signal-to-noise ratio is too low to capture the spatial, temporal, and spectral variation of the *Euclid* PSF to an accuracy that is sufficient to satisfy the mission requirements. Instead, a parametric model of the optical system and detector is fit to observations of stars, and used to infer the PSFs for target galaxies (Euclid Collaboration: Mellier et al., 2024; Euclid Consortium: Miller et al., 2020a[11]). A sample model VIS PSF is shown in fig. 1.8.

[11]NB: references made in this thesis to Euclid Consortium: Miller et al., 2020a, as well as to other *Euclid* consortium technical notes (Euclid Consortium: Miller and Duncan, 2020; Euclid Consortium: Miller et al., 2022, 2019, 2020b), are not in the public domain.

The parametric PSF model used for the EWS assumes that non-convolutional detector effects, such as detector non-linearity and CTI (Massey et al., 2013; Rhodes et al., 2010), have been corrected for, and models the chromatic wavefront error (WFE) at the image plane, along with additional convolutional contributions arising from the telescope-detector system. The PSF model includes contributions due to the following effects (Euclid Collaboration: Mellier et al., 2024; Euclid Consortium: Miller et al., 2020a, Duncan et al. *in prep.*):

- Vignetting arising due to the projection of the telescope structure onto the entrance pupil;
- Optical path differences across the FoV arising due to the layout of the optical system;
- FoV-dependent WFE arising due to imperfections in the optical surfaces;
- Guiding error occurring during exposures;
- Detector charge diffusion (Niemi et al., 2015);
- Chromatic effects, including the polarisation-dependent telescope throughput, in particular the dichroic surface; detector quantum efficiency; and source SEDs;
- Undersampling of the detector; the PSF model is oversampled with respect to the native detector sampling in order to avoid bias due to aliasing in the model (Euclid Consortium: Miller et al., 2020a; see also section 3.2), and must be downsampled for the shear measurement.

Because of the broad passband of the VIS detector, the VIS PSF is highly chromatic. It is therefore necessary to take into account the SED of each target for which the PSF is estimated. In the chromatic *Euclid* VIS PSF model, the source SEDs act as spectral weightings (Schreiber et al., *in prep.*):

$$\boldsymbol{P}_{\rm gal}(\boldsymbol{p}) = \frac{\int d\lambda T(\lambda, \boldsymbol{p}) S_{\rm gal}(\lambda) \boldsymbol{P}_{\rm gal}(\lambda, \boldsymbol{p})}{\int d\lambda T(\lambda, \boldsymbol{p}) S_{\rm gal}(\lambda)}, \tag{1.22}$$

with $\boldsymbol{P}_{\rm gal}(\lambda, \boldsymbol{p})$ the monochromatic model PSF at wavelength λ and FoV position $\boldsymbol{p}$, $S_{\rm gal}$ the source SED, $T(\lambda, \boldsymbol{p})$ the throughput of the optical system and detector, and $\boldsymbol{P}_{\rm gal}(\boldsymbol{p})$ is the full chromatic PSF. Note that (1.22) neglects non-linear/non-convolutive effects. For the VIS PSF model, SED data from stars is used in the model fit to constrain the chromaticity of the model (Euclid Consortium: Miller et al., 2020a); to estimate the VIS PSF for target galaxies, photometric SED data from NISP-P and ground-based observations is used (Euclid Collaboration: Mellier et al., 2024). Shear measurement errors arising during the latter process are discussed in chapter 4.

Some of the effects listed above that impact the VIS PSF are expected to be constant over the operational lifetime of the *Euclid* spacecraft, including contributions from the optical surfaces and most detector contributions. Other contributions will induce temporal variation into the PSF model, in particular due to distortions in the optical structure of the telescope arising due to thermal variations in the spacecraft which depend on the orientation of the spacecraft with respect to the Sun vector; this effect will result in deformation of the layout of the optical system within the spacecraft, and hence in optical path variations which will impact the PSF. Shear measurement errors arising due to this effect are discussed in chapter 5. Because of this, it is necessary to periodically conduct in-orbit calibration of the VIS PSF (Euclid Collaboration: Mellier et al., 2024).

The VIS PSF is calibrated using a hierarchical process that consists of three steps. The first calibration stage occurred at the beginning of the nominal *Euclid* survey operations, during which a basis set of PSF variations as a function of orientation with respect to the Sun vector and across the FoV was constructed. This was conducted on phase-diverse observations, in which the PSF was measured with the telescope in a defocussed state, in order to lift degeneracies in the PSF model. This is referred to as the phase-diversity calibration (PDC; Euclid Consortium: Miller et al., 2019). Secondly, the PSF is calibrated using observations of specific calibration fields, with a monthly cadence, in order to detect long-timescale variations in the PSF. Thirdly, the calibrated PSF model basis set is fit to stars in each EWS

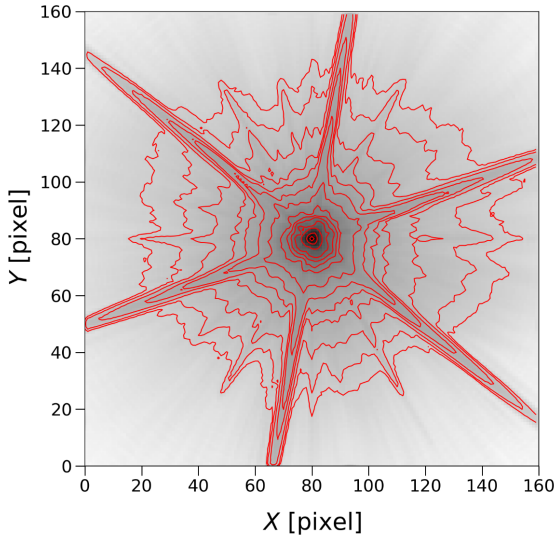


Figure 1.8: Stacked sample model VIS PSF. Pre-calibration PSF model fit to in-focus data, obtained during a small pre-survey phase-diversity calibration test. Red lines show PSF isophotes (Euclid Collaboration: Mellier et al., 2024).

science observation, to obtain an accurate, calibrated, FoV-dependent chromatic PSF model for each observation (Euclid Collaboration: Mellier et al., 2024).

1.2.5 Shear Measurement Biases Arising Due to Errors in the PSF for *Euclid*

As discussed in section 1.1.6, errors in the assumed PSF used for shear measurement result in shear measurement bias. This is particularly important for the EWS, which will constrain cosmological parameters with unprecedented precision, such that uncertainties in cosmological inference will be dominated by systematic errors (Euclid Collaboration: Mellier et al., 2024). The diffraction-limited PSF of a space-based telescope such as *Euclid* is highly sensitive to the physical system of the spacecraft, requiring a sophisticated model which is susceptible to errors that vary spatially, temporally, and spectrally. These introduce spurious correlations into galaxy shape measurement that are degenerate with the cosmological WL signal. The characterisation and mitigation of shear measurement biases arising due to PSF errors is therefore a crucial task for Stage-IV WL surveys, including the EWS (Albrecht et al., 2006).

A number of effects can introduce error into the VIS PSF that propagate

to shear measurement bias. These include mischaracterisation of the physical effects listed in section 1.2.4, including the chromatic or polarisation dependence, or FoV variation of errors in the optical surfaces; errors in the modelling of temporal variations of the PSF, including due to the finite cadence of the calibration observations; or errors in the characterisation of the chromaticity of the PSF, arising due to errors in the SED information that is used for the PSF estimation for source galaxies. The task of forecasting shear biases arising due to the latter two sources of PSF error for the EWS is described in chapter 3, chapter 4, and chapter 5, and outlined in more detail in section 1.3.

1.3 Thesis Overview

As discussed in this chapter, the ongoing and forthcoming WL surveys of the 2020s represent the era of "precision cosmology": due to the unprecedented depths, survey areas, and image quality, the error budgets of Stage-IV WL surveys such as the EWS, the LSST, and the HLIS are dominated by systematics (Albrecht et al., 2006). One important source of systematic error in WL surveys consists of bias in the shear measurement, and the characterisation and mitigation of such biases is a central task facing modern surveys.

The broad purpose of the work presented in this thesis is to forecast shear measurement biases for Stage-IV WL surveys, and the impact of such biases on cosmological parameter inference. This is a very large field of research, and the work presented in chapter 2–chapter 5 focuses on a small number of topics relevant to shear measurement for Stage-IV surveys. In particular, a large amount of the work presented in this thesis consists of the estimation of forecast shear biases arising due to PSF errors for the EWS, which is contained in chapter 3–chapter 5.

In chapter 2, the impact of spatial variations of the multiplicative shear bias on cosmological inference is forecast, for a general Stage-IV WL survey setting. The purpose of this work is to place requirements on the amplitude and characteristic scale of spatial variations of the m-bias. It is found that the impact of spatial variations of the m-bias is likely to represent a sub-dominant, but in some

circumstances potentially non-negligible, contribution to the shear measurement error budget for Stage-IV WL surveys.

In chapter 3, a method to forecast shear biases arising due to PSF errors at the catalogue-level for the EWS is described. This consists of efficiently defining a basis set of mock galaxy SEDs sampled from the *Euclid* Flagship 2 simulation (Euclid Collaboration: Castander et al., 2024), and estimating shear biases arising due to PSF errors for each of these SEDs, on a grid of mock galaxy morphology parameters and FoV position. Given the shear bias estimates for galaxies in this basis set, shear bias estimates are then inferred for the remaining galaxies in the Flagship 2 mock catalogue. The work presented in chapter 4 and chapter 5 consists of two applications of the methodology described in chapter 3, considering two different sources of PSF error for the EWS.

In chapter 4, the shear bias arising due to imperfect knowledge of galaxy SEDs is estimated, for mock galaxies in the Flagship 2 simulation. This results in PSF error because the galaxy SED information entering (1.22) is obtained from noisy, broad-band, ground-based photometric observations. The resulting shear biases are estimated as a function of galaxy redshift $z_{\rm obs}$, VIS magnitude $m_{\rm VIS}$, and spectral parameters, and broken down by galaxy sub-population., e.g. by "red" and "blue" galaxies. It is found that the SED-error-sourced m-bias is comparable in size to or larger than the relevant EWS requirements, and exhibits significant redshift-dependence. The multiplicative shear bias arising due to SED errors is then propagated to biases in cosmological parameter values, and the SED errors are found to induce parameter biases that are large compared to the forecast EWS statistical uncertainties, motivating the development of a scheme to mitigate or marginalise this systematic in the EWS analysis. In particular, w_0, w_a are found to be biased in the same direction that they are found to be discrepant from ΛCDM in DESI Collaboration: Abdul-Karim et al., 2025, which may result in spurious consistency between WL and other probes if this effect is not corrected for in the EWS analysis.

In chapter 5, the shear bias arising due to spatio-temporal variation of the

Euclid PSF which are not included in the VIS PSF model is estimated. These shear biases are estimated as a function of survey epoch, and it is found that the spatio-temporal variations of the c-bias components arising due to PSF modelling errors is comparable in size to or larger than the relevant EWS requirement. The survey epochs and FoV positions are projected to sky coordinates, and maps of shear bias variations are constructed. Because this work is subject to a number of caveats, it should be considered as an indicative proof-of-concept.

Finally, the thesis is concluded in chapter 6, including a discussion of potential directions for future research in this area.

At that time I was only 24 years old. My life then was already gloomy, disorderly, and solitary to the point of savagery.

— Fyodor Dostoyevsky, *Notes from the Underground*

2

Propagating Spatially-Varying Multiplicative Shear Bias to Cosmological Parameter Estimation for Stage-IV Weak Lensing Surveys

Contents

2.1 Introduction 42
2.2 Methods 46
2.2.1 Pseudo-C_ℓ formalism 46
2.2.2 Survey model 50
2.2.3 Fisher matrix analysis 52
2.3 Results 57
2.3.1 Residual power spectra 57
2.3.2 Bias in cosmological parameters 61
2.3.3 Dependence of parameter bias on m-bias RMS 63
2.4 Discussion 67
2.4.1 Residual power spectra 67
2.4.2 Bias in cosmological parameters 68
2.4.3 Dependence of parameter bias on m-bias RMS 70
2.5 Conclusion 71

Note: The work presented in this chapter makes use of the NaMaster code[1] developed by and presented in Alonso et al., 2019, to calculate the bias in cosmic

[1]In this work, the Python implementation of NaMaster is used, `pymaster` version 1.4 https://namaster.readthedocs.io/en/latest/

shear E-mode angular power spectra arising due to the mode-coupling effect of the spatially-varying multiplicative shear bias, as described in section section 2.1.

2.1 Introduction

As described in chapter 1, current and future weak lensing (WL) surveys aim to measure the spin-2 shear γ introduced to galaxy images due to WL by the large-scale structure, and estimated by the ellipticities of source galaxy images. The cosmic shear is one of the main cosmological probes that will be measured by ongoing and forthcoming stage IV surveys (Albrecht et al., 2006), including the *Rubin* Observatory's Legacy Survey of Space and Time (LSST) (Dark Energy Science Collaboration: Mandelbaum et al., 2018), and the *Euclid* Wide Survey (Euclid Collaboration: Mellier et al., 2024). Cosmic shear is a highly subtle effect, with distortions introduced on the order of a per cent of the intrinsic galaxy ellipticities (Kilbinger, 2015). As each successive survey contributes additional data, the resulting reduction in statistical uncertainty results in tighter requirements on the control of systematic errors. While previous WL surveys have accounted for systematic effects, forthcoming surveys will require understanding and mitigation of systematics to an unprecedented level of precision, including effects which have not previously been considered. One such effect consists of variations of bias in the shear measurement across the survey footprint. Such shear biases can result from multiple sources, including PSF variations, as described in section 1.1.6. Different systematic effects can separately introduce additive and multiplicative biases; for example, a c-bias can arise from errors in the anisotropy in the PSF, while an m-bias can result from PSF size errors (Huterer et al., 2006; Paulin-Henriksson et al., 2008); see also section 3.1.2.

While it is desirable to estimate and correct for these biases theoretically (e.g. from PSF modelling), it may also be possible to (at least partially) detect the presence of c-bias empirically, e.g. by using null tests (Kitching et al., 2021; van Uitert and Schneider, 2016). However, the latter is not possible for the m-bias, which must be predicted, e.g. from image simulations (Kannawadi et al., 2019;

Pujol et al., 2019), or inferred from self-calibration during the measurement process (Huff and Mandelbaum, 2017; Sheldon and Huff, 2017; Sheldon et al., 2020). For forthcoming stage-IV surveys such as the EWS, it is expected that the shape biases will need to be constrained to the level of $c \lesssim 1.5 \times 10^{-4}$, $m \lesssim 2 \times 10^{-3}$ in order to obtain the required sensitivity (Cropper et al., 2013; Euclid Collaboration: Mellier et al., 2024; Massey et al., 2013).

In this work, the effect of a spatially-varying multiplicative bias in the shear measurement on cosmological parameters estimated from the cosmic shear angular power spectrum, $C_\ell^{\gamma\gamma}$, is investigated. The analysis of Stage-IV WL surveys will be concerned with residual shear biases, i.e. biases arising due to imperfect calibration of systematics, as a result of uncertainties in systematics models. Such biases could arise e.g. when there are spatio-temporally varying errors in the PSF model. In particular, multiplicative bias is expected to occur due to errors in the assumed size of the PSF (Paulin-Henriksson et al., 2008). In optical weak-lensing surveys, the typical imaging field size is $\lesssim 1^\circ$, corresponding to multipole $\ell \gtrsim 200$, which provides a natural characteristic scale on which the m-bias may vary (Euclid Collaboration: Paykari et al., 2020). Additionally, there are expected to be PSF variations, and hence the possibility of PSF modelling errors, down to arcminute scales ($\ell \sim 10^3 - 10^4$), motivating study of the effect of a spatially-varying m-bias on a wide range of scales. There may also be spatially-varying m-bias arising from other effects in the shear measurement, such as may arise from variations in galaxy density leading to higher rates of image blending, which are correlated with the LSS.

Previous work has been conducted in this area, in particular by Kitching et al., 2020, 2019, in which it was found that a spatially-varying m-bias has a negligible effect on the shear power spectrum compared with the mean of the m-bias field, and should be negligible also when the m-bias field averages to zero across the sky. However, Kitching et al., 2019 did not extend the fully non-linear analytic calculation beyond a maximum multipole of $\ell_{\rm max} = 32$ (64 in Kitching et al., 2020). In Kitching et al., 2020, a linear approximation of the bias in $C_\ell^{\gamma\gamma}$

was also calculated up to $\ell_{\rm max} = 2048$ and compared with a forward model, with differences found ~ 4 orders of magnitude smaller than the cosmic variance. Kitching et al., 2020 also calculated the bias in the estimated amplitude of the shear power spectrum resulting from marginalisation over a prior on the mean m, and placed requirements on the bias and variance of that distribution with respect to the true mean m. That work did not consider the parameter bias arising due to the convolutive effect on the shear C_ℓ arising due to the spatial variations of the m-bias field.

Kitching et al., 2020, 2019 propagated shear biases into biases in the $C_\ell^{\gamma\gamma}$ using a fully general calculation which allowed for an m-bias field which was itself a complex-valued spin-2 field, resulting in a rapid scaling of the required computational time as $\ell_{\rm max}^5$. However, the resulting stringent upper limit on the range of multipoles that can be included in the analysis may result in an underestimation of the resulting bias in cosmological parameter estimates, because a spatially-varying m-bias with some characteristic angular scale (which may be large or small) will, due to mode coupling, bias the $C_\ell^{\gamma\gamma}$ down to small scales that will be included in the cosmology analysis for Stage-IV surveys. In this work, the analysis is restricted to a real-valued spin-0 m-bias, as is commonly assumed in shear analyses and is expected to result from realistic shear systematics such as PSF errors; the real part was predicted to be dominant compared to the imaginary part of the m-bias field by Kitching et al., 2019. The NaMaster code (Alonso et al., 2019), which implements a computationally-efficient pseudo-C_ℓ formalism, is applied, taking advantage of the resulting symmetries to determine the effect on the shear power spectrum of a spatially-varying m-bias. This method scales as $\ell_{\rm max}^3$ (Alonso et al., 2019). This allows the computation of the bias in the $C_\ell^{\gamma\gamma}$ down to scales corresponding to $\ell_{\rm max} \sim 10^3 - 10^4$. The calculation to such high ℓ is tractable in this case because orthogonality of the Wigner 3-j symbols involved in the calculation of the mode-coupling matrix reduces the dimensionality of the calculation. The effect of a random m-bias map is considered, generated according to an angular power spectrum with a characteristic scale

defined by a peak multipole $\ell_{\rm peak}$ and width σ_m. In the present analysis, the bias in the $C_\ell^{\gamma\gamma}$ arising due to a range of values for $\ell_{\rm peak}$ and σ_m is considered, and subsequently a Fisher-matrix analysis is utilised to predict the sensitivity of cosmological parameters to the spatially-varying m-bias for a typical stage-IV WL survey. While previous works have propagated shear biases into biases in cosmological parameters using a Fisher matrix analysis, these have either ignored the spatial variations of the m-bias (e.g. Amara and Réfrégier, 2008), relied on assumptions about the ℓ-coupling of the C_ℓs (e.g. Kitching et al., 2016; Massey et al., 2013), or did not carry out the full propagation of the shear bias from angular space (e.g. Taylor and Kitching, 2018, which propagated the shear bias power spectra into the dark energy figure of merit); this work is the first to calculate the full mode-coupling matrix corresponding to m-bias maps and propagate into biases in cosmological parameters. The BB power spectra which result from the mode-mixing effect arising due to the spatially-varying m-bias are also computed, and are compared to the bias in the EE power spectra. Note that the additive shear bias is not considered in the present work, as its form is expected to be strongly dependent on the particular systematics from which it results, whereas here a generic form for the m-bias is considered, that may be broadly relevant to stage-IV WL surveys; the principal subject of this work is the effect of the m-bias at high multipoles in the $C_\ell^{\gamma\gamma}$.

This chapter is organised as follows. In section 2.2 the methodology used is described, including the generation of the fiducial $C_\ell^{\gamma\gamma}$s, m-bias maps, the pseudo-C_ℓ formalism used to calculate the biased $C_\ell^{\gamma\gamma}$s, and the Fisher-matrix analysis used to forecast resulting biases in cosmological parameters. In section 2.3, the results are presented, including the residual $C_\ell^{\gamma\gamma}$s, and biases and the ratios of biases to the respective 1σ uncertainty in cosmological parameter estimates. In section 2.4 the results of the present analysis are discussed, and in section 2.5 the findings of the work presented in this chapter are summarised.

2.2 Methods

2.2.1 Pseudo-C_ℓ formalism

Consider a complex field $\boldsymbol{a}(\boldsymbol{\Omega})$ defined on the sphere, with spin s_a, where $\boldsymbol{\Omega} = (\theta, \phi)$ is the angular unit vector on the sphere. $\boldsymbol{a}$ can be considered as a 2-dimensional vector composed of its real and imaginary components, $\boldsymbol{a} \equiv (\mathrm{Re}(a), \mathrm{Im}(a))$. The spherical-harmonic transform of $\boldsymbol{a}$ is given by:

$$\boldsymbol{a}_{\ell m} = \int_{\boldsymbol{\Omega}} d\boldsymbol{\Omega} \mathsf{Y}^{s_a \dagger}_{\ell m}(\boldsymbol{\Omega}) \boldsymbol{a}(\boldsymbol{\Omega}), \tag{2.1}$$

where $\mathsf{Y}^{s_a}_{\ell m}$ is a 2×2 matrix, with columns given by 2-dimensional complex vectors with elements given by linear combinations of the spin-weighted spherical harmonics ${}_{s_a}Y_{\ell m}, {}_{-s_a}Y_{\ell m}$ of degree ℓ and order m, such that $\boldsymbol{a}_{\ell m}$ is also a vector with elements given by the decomponsition of the field into E and$B$-modes, $\boldsymbol{a}_{\ell m} \equiv (a^E_{\ell m}, a^B_{\ell m})$ (Alonso et al., 2019; Kitching et al., 2019; Zaldarriaga and Seljak, 1997); and superscript † here denotes conjugate transposition. If the field $\boldsymbol{a}$ is observed with a mask (or set of weights) $W_a(\boldsymbol{\Omega})$, such that the observed field $\widetilde{\boldsymbol{a}}(\boldsymbol{\Omega}) = \boldsymbol{a}(\boldsymbol{\Omega}) W_a(\boldsymbol{\Omega})$, then the spherical harmonic expansion coefficients of the masked field are calculated as follows (Brown et al., 2005; Hivon et al., 2002; Kogut et al., 2003):

$$\begin{aligned}
\widetilde{\boldsymbol{a}}_{\ell m} &= \int_{\boldsymbol{\Omega}} d\boldsymbol{\Omega} \mathsf{Y}^{s_a \dagger}_{\ell m}(\boldsymbol{\Omega}) \boldsymbol{a}(\boldsymbol{\Omega}) W_a(\boldsymbol{\Omega}) && (2.2)\\
&= \sum_{\ell' m'} \int_{\boldsymbol{\Omega}} d\boldsymbol{\Omega} W_a(\boldsymbol{\Omega}) \left(\mathsf{Y}^{s_a \dagger}_{\ell m}(\boldsymbol{\Omega}) \cdot \mathsf{Y}^{s_a}_{\ell' m'}(\boldsymbol{\Omega}) \right) \cdot \boldsymbol{a}_{\ell' m'} && (2.3)\\
&\equiv \sum_{\ell' m'} \mathsf{K}^{s_a}_{\ell m \ell' m'}[W_a] \cdot \boldsymbol{a}_{\ell' m'} \ , && (2.4)
\end{aligned}$$

where the 2×2 matrix $\mathsf{K}^{s_a}_{\ell m \ell' m'}[W]$ is the spin-s_a mode-mixing kernel describing the mode-mode coupling of a spin-s_a field due to W_a. If we consider a spin-s_b vector field $\boldsymbol{b}(\boldsymbol{\Omega})$ observed with mask $W_b(\boldsymbol{\Omega})$, then the 2×2 matrix of angular power spectra of vector fields $\widetilde{\boldsymbol{a}}(\boldsymbol{\Omega})$ and $\widetilde{\boldsymbol{b}}(\boldsymbol{\Omega})$ is estimated according to the following

pseudo-C_ℓ formalism (Alonso et al., 2019; Hivon et al., 2002; Kogut et al., 2003):

$$\begin{aligned}\mathrm{vec}\left[\langle\widetilde{\mathsf{C}}_\ell^{\tilde{a}\tilde{b}}\rangle\right] &= \frac{1}{2\ell+1} \\ &\times \sum_{\ell'}\sum_{mm'}\left(\mathrm{vec}\left[\mathsf{K}^{s_a}_{\ell m\ell' m'}[W_a]\right]\cdot\mathrm{vec}\left[\mathsf{K}^{s_b}_{\ell m\ell' m'}[W_b]\right]^\dagger\right) \\ &\cdot\,\mathrm{vec}\left[\langle\mathsf{C}_{\ell'}^{ab}\rangle\right] \qquad (2.5)\\ &\equiv \sum_{\ell'}\mathsf{M}^{s_a s_b}_{\ell\ell'}\mathrm{vec}\left[\langle\mathsf{C}_{\ell'}^{ab}\rangle\right]\ , \qquad (2.6)\end{aligned}$$

where the vectorisation operator $\mathrm{vec}[\mathsf{x}]$ maps from an $a\times b$ matrix to an ab-dimensional vector (Hamimeche and Lewis, 2008). Note that the angle brackets denote an ensemble average; these are henceforth omitted for brevity. The 2×2 matrix $\mathsf{M}^{s_a s_b}_{\ell\ell'}$ is the *mode-coupling matrix* which convolves the true power spectra $\mathsf{C}_{\ell'}^{ab}$ with the cross power spectrum of the masks, and is calculated from the spin-weighted spherical harmonic decompositions of $W_a(\mathbf{\Omega})$ and $W_b(\mathbf{\Omega})$. In this work, the NaMaster code (Alonso et al., 2019) is used to calculate (2.6). Considering equation (1.20), $1+m(\mathbf{\Omega})$ may be considered as a non-binary mask that is applied to the true shear field $\boldsymbol{\gamma}(\mathbf{\Omega})$, and can therefore be used to calculate the pseudo-C_ℓ of the biased shear field using equation (2.6). Note that for a spin-2 field such as the cosmic shear, the mode-coupling matrix also mixes E- and B-modes, generating BB-power which is otherwise expected to be subdominant in the intrinsic shear field.

As equation (2.5) includes a sum over three indices of a product that is integrated over the whole sphere, calculation of the mode-coupling matrix is, in the general case, computationally expensive. However, it is possible to express the mode-mixing kernels in terms of Wigner 3-j symbols (Edmonds, 1957; Hivon et al., 2002; Kogut et al., 2003), which obey an orthogonality relation that allows the summation in indices m_1, m_2 to be collapsed, greatly simplifying the calculation to a sum over the angular cross-power spectrum of the masks weighted by 3-j symbols (Kogut et al., 2003). NaMaster employs this method (and additionally, in the calculation of the mode-coupling matrix, replaces the C_ℓ of the masks with their pseudo-C_ℓ, which is more computationally efficient to calculate; see Alonso et al., 2019). This significantly reduces the computational cost of the calculation of

the angular power spectra of masked fields, reducing the scaling of the calculation by a factor of $\ell_{\rm max}^2$, thereby allowing calculation beyond the maximum multipoles that would be of interest for stage IV weak-lensing experiments, an improvement on the scaling found in the general calculation by Kitching et al., 2019.

The mode-coupling matrix $\mathsf{M}_{\ell\ell'}^{s_a s_b}$ depends only on the power spectrum of the mask (Alonso et al., 2019; Taylor and Kitching, 2018). As the clustering of the m-bias map considered here is by construction fully described by its angular power spectrum, it is not necessary to consider multiple realisations of the m-bias map for each of the values of $\ell_{\rm peak}$, σ_m and m-bias RMS considered in this work. It should be noted however that NaMaster takes as its input the mask and computes an estimate of the mask C_ℓ, which is used to compute the mode-coupling matrix. In the case considered here, this mask is a noisy realisation of the m-bias map, which is a random field. This results in a noisy estimate of the m-bias map C_ℓ which is used to calculate $\mathsf{M}_{\ell\ell'}^{s_a s_b}$. While this results in a loss of optimality of the $\mathsf{M}_{\ell\ell'}^{s_a s_b}$ estimate, this is not expected to have a significant effect when the smallest scales $\gtrsim 10^4$ are neglected, and so NaMaster was not modified to take the m-bias map C_ℓ as its input directly in order to avoid this effect. In a practical application, this modification would be trivial. Additionally, the m-bias W_ℓ will not be known in a real survey, and in a realistic case propagation from angular space (rather than ℓ-space) will be necessary; this work is also intended to serve as a proof of concept that the full propagation from angular space to m-bias maps to cosmological parameter biases is tractable.

Assuming a linear bias model for the shear measurement as in (1.20), and neglecting multiplicative bias contributions with non-zero spin, then for the case of a spatially-varying multiplicative bias $m(\mathbf{\Omega})$ as considered here, the biased shear field is given by:

$$\widetilde{\boldsymbol{\gamma}}(\mathbf{\Omega}) = \boldsymbol{\gamma}(\mathbf{\Omega})(1 + m(\mathbf{\Omega}))\,. \tag{2.7}$$

The quantity $1 + m(\mathbf{\Omega})$ is henceforth referred to as the *m-bias map*, where $m(\mathbf{\Omega})$ is real-valued and spin-0. A pseudo-C_ℓ approach may therefore be applied to describe the effect of a spatially-varying m-bias on the shear C_ℓs. This will allow

the computation of the bias in the cosmic shear angular power spectra due to $m(\mathbf{\Omega})$ with a weaker scaling with $\ell_{\rm max}$ than was obtained in previous work in this area (e.g. Kitching et al., 2020, 2019), enabling the impact of the spatially-varying m-bias to be probed out to much higher multipoles.

Note that here both the c-bias and any separate spatially constant m-bias have been neglected. While $m(\mathbf{\Omega})$ could in general contain a spatially constant term, the aim of this work is specifically to investigate the impact of the spatial variations that have previously been claimed to have negligible effect. Moreover, since the shear is a spin-2 vector field, in general it can be decomposed into E- and B-modes, and there are therefore in principle four power spectra, C_ℓ^{EE}, C_ℓ^{BB}, C_ℓ^{BE} and C_ℓ^{EB}; however, in the absence of certain systematic effects (including intrinsic alignments, selection effects and some PSF correction effects), the B-mode field is expected to be highly sub-dominant (Kilbinger, 2015) (though not vanishing, as source clustering is expected to introduce some B-modes (Schneider et al., 2002)). Any intrinsic B-mode field will therefore be neglected. In the analysis presented here, the biased EE power spectrum is calculated, as well as the BB power spectrum generated by the mode-coupling arising due to $m(\mathbf{\Omega})$. No E-B cross-correlation is expected to be generated in the presence of a spin-0 m-bias because the parity-odd (EB, BE) power spectra are not mixed with the parity even (EE, BB) power spectra (Alonso et al., 2019). As the shear field is expected to be approximately B-mode-free, any observed B-mode power may be used to detect the presence of and potentially calibrate residual systematic effects (Asgari et al., 2021). In particular, the BB power spectra contain information about the m-bias field which may in principle be used for self-calibration (Kitching et al., 2020). However, this is not considered in the present analysis due to uncertainty in the viability of self-calibration of the m-bias using the BB power, arising due to potential degeneracies in the B-modes generated by different systematics, according to the systematics-agnostic approach adopted in this work.

Redshift-dependence of the m-bias is not considered, with the same m-bias applied to all of the tomographic shear power spectra. In a real survey, there

will be a redshift-dependence of the m-bias, e.g. due to the decrease in observed galaxy size with redshift; as here a generic form for the m-bias is considered, without reference to a specific bias model, investigation of this effect is deferred to future work (see chapter 4). A full-sky analysis is also conducted, and so the mode-coupling effect due to any survey mask boundary is neglected.

A randomly-drawn m-bias map is considered, that is distributed according to an angular power spectrum W_ℓ with a Gaussian profile as a function of ℓ:

$$W_\ell \equiv A_m e^{-\frac{(\ell-\ell_{\rm peak})^2}{2\sigma_m^2}}, \tag{2.8}$$

with $\ell_{\rm peak}$ the peak multipole for W_ℓ, and σ_m the width in ℓ-space . W_ℓ is normalised by the factor A_m such that the resulting m-bias map has RMS value equal to 0.01, a nominal fiducial value which is a reasonable expectation for a forthcoming stage-IV survey. The way in which the results presented in this work vary with this value is also investigated, in order to allow requirements to be set on the amplitude of spatial variations of the m-bias. W_ℓ with $\ell_{\rm peak}$ in the range $50 - 5000$ and σ_m in the range $64 - 2048$ are considered.

2.2.2 Survey model

For the fiducial shear power spectra, redshift distribution of galaxies $n(z)$ of the following form is assumed (Smail et al., 1994):

$$n(z) \propto \left(\frac{z}{z_0}\right)^2 \exp\left[-\left(\frac{z}{z_0}\right)^{\frac{3}{2}}\right], \tag{2.9}$$

which is normalised to unity, and where $z_0 = z_m/\sqrt{2}$ with z_m the median redshift of the distribution (Euclid Collaboration: Blanchard et al., 2020). This distribution is divided into 10 equipopulated redshift bins up to a maximum redshift of 3, and convolved the distribution in each bin $n_i(z)$ with a probability density function with two slightly offset Gaussian terms, given by Euclid Collaboration: Blanchard et al. (2020), to account for the effect of photometric redshift errors with catastrophic outliers. The resulting $n_i(z)$ are shown in fig. 2.1. Fiducial shear auto- and cross- (EE) power spectra are calculated for each pair of bins using the

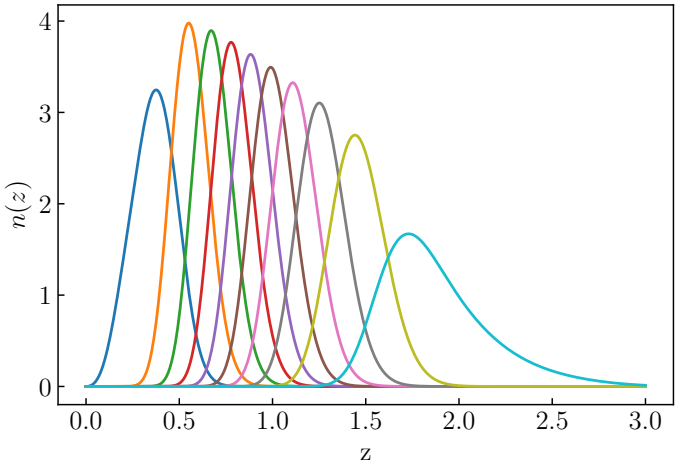


Figure 2.1: Gaussian-convolved $n(z)$ for the 10 tomographic redshift bins.

CORE COSMOLOGY LIBRARY (CCL)[2], a public standardized library of routines to calculate basic observables used in cosmology, (Chisari et al., 2019), denoted $C_\ell^{\gamma_i\gamma_j}$ for bin pair (i, j). A spatially-flat ΛCDM model is assumed, with the *Planck* 2018 best-fit cosmological parameter values as the fiducial values for cosmological parameters (see table 1, Planck Collaboration: Aghanim et al. (2020)). Massive neutrinos are not included in the fiducial cosmological model considered in this work. In the Fisher-matrix analysis, a dark energy model is considered with a dynamical equation of state, equation (1.3), in which the parameters w_0 and w_a are allowed to vary, with fiducial values of -1 and 0 respectively.

To each of the auto-power spectra $C_\ell^{\gamma_i\gamma_i}$ a constant shape-noise term n is added, given by (Euclid Collaboration: Blanchard et al., 2020) for the case of equipopulated redshift bins:

$$n = \frac{\sigma_e^2 N_z}{n_{\rm gal}}\,, \tag{2.10}$$

where σ_e^2 is the intrinsic ellipticity variance of source galaxies, N_z is the number of tomographic redshift bins and $n_{\rm gal}$ is the projected number density of source galaxies; following Euclid Collaboration: Blanchard et al., 2020, these are taken to be $\sigma_e^2 = 0.3^2 = 0.09$, $N_z = 10$ and $n_{\rm gal} = 30$ arcmin^{-2}. For each m-bias map

[2]In this work, the Python implementation `pyccl` version 2.5.0 is used, https://ccl.readthedocs.io/en/latest/

Table 2.1: Fiducial ΛCDM cosmological parameter values - cold dark matter density parameter Ω_c; baryonic matter density parameter Ω_b; reduced Hubble constant h; amplitude of the matter power spectrum σ_8; scalar spectra index n_s (values from Planck Collaboration: Aghanim et al. (2020), table 2, final column); dark energy equation-of-state parameters w_0 and w_a.

Cosmological parameter	Fiducial value
Ω_c	0.2607
Ω_b	0.0490
h	0.6766
σ_8	0.810
n_s	0.9665
w_0	-1
w_a	0

under study, NaMaster is used to compute the mode-coupling matrix $\mathsf{M}^{22}_{\ell\ell'}$; the mode-coupling matrix is then coupled with each $C_\ell^{\gamma_i\gamma_j}$ to obtain biased shear power spectra $\widetilde{C}_\ell^{\widetilde{\gamma}_i\widetilde{\gamma}_j}$. The *residual* C_ℓs are then calculated as:

$$\Delta C_\ell^{\gamma_i^E\gamma_j^E} = C_\ell^{\gamma_i^E\gamma_j^E} - \widetilde{C}_\ell^{\widetilde{\gamma^E}_i\widetilde{\gamma^E}_j} \,. \tag{2.11}$$

Residual shear C_ℓs are computed using NaMaster up to $\ell_{\rm cut} = 12288$; this is set by the resolution of the input HEALPix map, for which the corresponding parameter $N_{\rm side} = \ell_{\rm cut}/3 = 4096$ is chosen. The $\Delta C_\ell^{\gamma^E\gamma^E}$ are calculated up to higher multipoles than are considered in the subsequent Fisher matrix analysis, in order to obtain more accurate results for the mode-mixing at the scales of interest.

Example fiducial $C_\ell^{\gamma^E\gamma^E}$, generated using CCL using the stage-IV like survey configuration described in this section, are shown in fig. 2.2, with the auto-correlation $C_\ell^{\gamma_0^E\gamma_0^E}$ and cross-correlation $C_\ell^{\gamma_0^E\gamma_4^E}$ shown.

2.2.3 Fisher matrix analysis

A Fisher matrix analysis is conducted to forecast biases in cosmological parameters propagated from the bias in the shear C_ℓs due to the spatially-varying m-bias. Given a data vector $\boldsymbol{D}_\ell$ with non-zero mean consisting of angular power spectra at a particular ℓ and parameter-independent data covariance matrix $\mathsf{Cov}(\ell)$, the Fisher matrix can be approximated as (Duncan et al., 2014; Tegmark et al., 1997):

$$F_{\eta\tau} = \sum_\ell (\partial_\eta \boldsymbol{D}_\ell)(\mathsf{Cov}^{-1})(\ell)\partial_\tau \boldsymbol{D}_\ell \,, \tag{2.12}$$

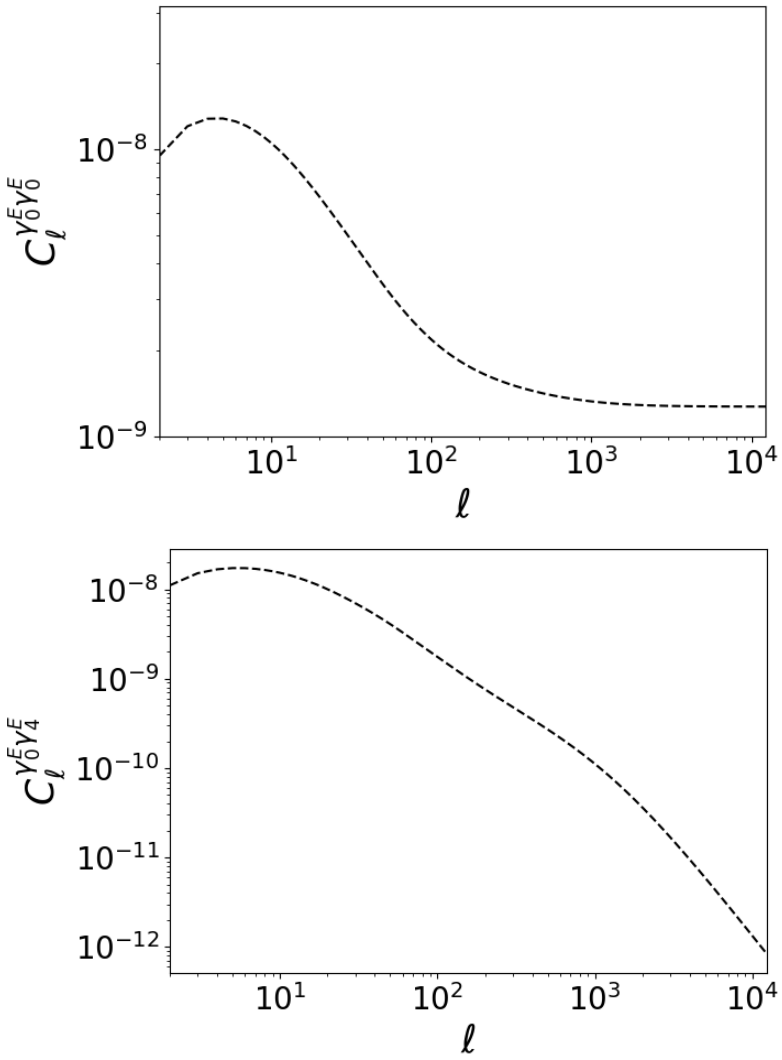


Figure 2.2: Top panel: fiducial $C_\ell^{\gamma_0^E\gamma_0^E}$ E-mode shearr auto-correlation angular power spectrum, generated using CCL (Chisari et al., 2019) using the stage-IV-like survey settings described in section 2.2.2. Bottom panel: fiducial $C_\ell^{\gamma_0^E\gamma_4^E}$ E-mode shearr cross-correlation angular power spectrum.

where $F_{\eta\tau}$ is the Fisher matrix and ∂_τ denotes partial differentiation with respect to parameter θ_τ. For the data vector at each ℓ, the vector composed of the fiducial $C_\ell^{\gamma_i^E\gamma_j^E}$s is taken, which are denoted as $\boldsymbol{C}_\ell$ for brevity; i.e. $\boldsymbol{C}_\ell = \{C_\ell^{\gamma_0^E\gamma_0^E}, C_\ell^{\gamma_0^E\gamma_1^E}, \cdots, C_\ell^{\gamma^E_{(N_z-1)}\gamma^E_{(N_z-1)}}\}$, where the redshift bin indices run from 0 to 9, and $\mathsf{Cov}(\ell)$ is the 55×55 covariance matrix of these power spectra at multipole ℓ, i.e. a submatrix of the $55N_\ell \times 55N_\ell$ full block-diagonal covariance matrix, with N_ℓ the number of ℓ-modes considered.

The derivatives of the data vector $\partial_\tau \boldsymbol{C}_\ell$ are approximated with a simple two-

step derivative:

$$\partial_\tau \boldsymbol{C}_\ell \approx \frac{\boldsymbol{C}_\ell(\theta_{\tau,\mathrm{fid}} + \delta\theta_\tau) - \boldsymbol{C}_\ell(\theta_{\tau,\mathrm{fid}} - \delta\theta_\tau)}{2\delta\theta_\tau} \,, \tag{2.13}$$

where $\theta_{\tau,\mathrm{fid}}$ is the fiducial value of parameter θ_τ and $\delta\theta_\tau$ is a small derivative step in θ_τ. The Fisher-matrix analysis is conducted with two sets of cosmological parameters for which cosmic shear is expected to be sensitive. In the base parameter set, the cold-dark-matter density parameter, Ω_c, that is the ratio of the density of cold dark matter to that of the critical density at the present epoch; σ_8, the amplitude of the linear matter power spectrum on scales of $8h^{-1}\mathrm{Mpc}$; and the constant dark energy equation-of-state parameter, w_0, are considered. In the extended parameter set, the base parameter set is considered, in addition to a parameter capturing the redshift-variation of the dark energy equation-of-state, w_a, where the evolution of the equation of state parameter is parametrised by w_0, w_a as in (1.3). The derivative steps in these parameters are chosen as $\{\delta\Omega_c = 0.01, \delta\sigma_8 = 0.005, \delta w_0 = 0.055, \delta w_a = 0.058\}$. These parameters are taken to be "free" in this analysis, considering the impact on their inference from the $C_\ell^{\gamma\gamma}$ due to bias in the shear power spectra, whereas the other parameters listed in table 2.1, h, Ω_b and n_s, are assumed to be well-known and fixed to their fiducial values.

In order to test the stability of the Fisher matrix calculation, the numerical stability of the derivatives was investigated, by perturbing values of the derivative steps, and selecting values such that all the Fisher matrix elements were stable with respect to perturbations in the region of the step choice. The contours (which are the same as those displayed in section section 4.3.2, though there with a bias offset from the fiducial values) are compared with the results f the Fisher forecast from Euclid Collaboration: Blanchard et al., 2020; while the precision of the forecast constraints obtained in this work is greater than that of the contours shown in Euclid Collaboration: Blanchard et al., 2020, due to the larger number of free parameters included in that analysis compared to that shown in this work, the directions along which the parameter constraints are degenerate is consistent.

In the results presented in this work, the bias in Ω_m, the total matter density parameter, is presented, which in ΛCDM is the sum of Ω_c and Ω_b (the density

parameter of baryonic matter). Since only Ω_c is varied, and the value of Ω_b is fixed to the Planck Collaboration: Aghanim et al. (2020) value, the Fisher matrix elements and the resulting biases that are obtained by varying Ω_c are also the correct results for Ω_m .

The covariance between a pair of shear power spectra $(C_\ell^{\gamma_i\gamma_j}, C_{\ell'}^{\gamma_p\gamma_q})$ in the Gaussian approximation is given by (Joachimi and Bridle, 2010):

$$\begin{aligned}\mathrm{Cov}[C_\ell^{\gamma_i\gamma_j}, C_{\ell'}^{\gamma_p\gamma_q}] \\ &= \delta_K^{\ell\ell'} \frac{2\pi}{(2\ell+1) f_{sky} \Delta\ell} \times \{C_\ell^{\gamma_i\gamma_p} C_\ell^{\gamma_j\gamma_q} + C_\ell^{\gamma_i\gamma_q} C_\ell^{\gamma_j\gamma_p}\} \\ &\equiv \mathrm{Cov}^{ijpq}(\ell)\,, \end{aligned} \quad (2.14)$$

where $\delta_K^{\ell\ell'}$ is the Kronecker delta, f_{sky} is the fraction of the sky covered by the survey, and $\Delta\ell$ is the width of multipole bandpowers. The parameter f_{sky} is taken to be 0.36, corresponding to a ∼15,000 deg^2 survey such as is the case for *Euclid* (Euclid Collaboration: Blanchard et al., 2020). The presence of f_{sky} in the denominator rescales every element of the covariance matrix, to account for the loss of information due to the cut sky, including the shot-noise contribution from the auto-spectra (2.10). In a real survey analysis, the sky mask will introduce off-diagonal covariance on scales corresponding to the mask window function. In this case, it is necessary to bin the power spectra and covariance matrix into bandpowers in order for the diagonal covariance assumption to hold. While the present analysis is not applied to the cut sky, its effect is incorporated at the Fisher level by binning the data vector and covariance into bandpowers with a nominal width of $\Delta\ell = 10$, and scaling the covariance by $1/f_{sky}$. A contribution due to the super-sample covariance (SSC, see e.g. Euclid Collaboration: Sciotti et al., 2024) is also included, calculated with `CCL` according to the prescription from Krause and Eifler, 2017. Due to computational limitations, the SSC is evaluated at the central multipoles of each pair of bandpowers, and taken as constant within the region of harmonic space corresponding to each pair.

Given the Fisher matrix, fiducial angular power spectra and bias in the power spectrum ΔC_ℓ^I corresponding to a tomographic bin pair $I \equiv (\gamma_i, \gamma_j)$, the result-

ing contribution to the bias in some cosmological parameter θ_η is given by the following (Amara and Réfrégier, 2008; Thiele et al., 2020):

$$\Delta\theta_\eta^I = \sum_\tau (\mathsf{F}^{-1})_{\eta\tau} \sum_J \sum_\ell (\partial_\tau C_\ell^J)(\mathsf{Cov}^{-1})^{J,I}(\ell)\Delta C_\ell^I \,, \tag{2.15}$$

where the covariance matrix $\mathrm{Cov}^{J,I}(\ell)$ is given by (2.14). The bias on parameter θ_η is then obtained by summing the contributions from each bin:

$$\Delta\theta_\eta = \sum_I \Delta\theta_\eta^I \,. \tag{2.16}$$

The marginalised 1σ uncertainty of parameter θ_α is given by:

$$\sigma_\alpha = \sqrt{(\mathsf{F}^{-1})_{\alpha\alpha}} \,, \tag{2.17}$$

and the ratio of the calculated bias in parameter θ_α to the corresponding 1-dimensional 1σ uncertainty is calculated as:

$$\mathrm{Sig}[\Delta\theta_\alpha] = \frac{\Delta\theta_\alpha}{\sigma_\alpha} \,. \tag{2.18}$$

Henceforth, the multipole at which the calculation of the mode-coupling matrix is truncated is referred to as $\ell_{\rm cut}$ and the maximum multipole considered in the Fisher analysis as $\ell_{\rm max}$. In the Fisher analysis, a low ℓ-cut of $\ell_{\rm min} = 10$ is used. A range of high ℓ-cuts in the range $\ell_{\rm max} = 1500 - 5000$ are applied at the Fisher level, in order to see the effect of including or excluding different scales on the Fisher matrix and parameter biases. At high multipoles, non-linear modes of the power spectrum contaminate the C_ℓs, biasing them with respect to the linear theory prediction and degrading the resulting cosmological parameter constraints; such a cut will be necessary, therefore, in any real survey. According to Euclid Collaboration: Blanchard et al., 2020, $\ell_{\rm max} = 1500$ corresponds to a pessimistic ℓ-cut, whereas $\ell_{\rm max} = 5000$ is expected to be optimistic. These cuts are applied both in the computation of the Fisher matrix (2.12), and of the parameter biases, (2.15). The analysis is applied to $\Delta C_\ell^{\gamma\gamma}$s computed with a range of values for the the peak multipole of the W_ℓ, in the range $\ell_{\rm peak} = 50 - 5000$, and σ_m, the width of the W_ℓ, is fixed to $\sigma_m = 64$. Additionally, the analysis is conducted keeping $\ell_{\rm max}$

fixed, and varying σ_m, in the range $64 - 2048$ and $\ell_{\rm peak}$ in the range $100 - 1100$, in order to test the validity of the choice of σ_m. In the Fisher matrix analysis first the parameter set $\{\Omega_m, \sigma_8, w_0\}$ (varying Ω_c with Ω_b fixed at the Planck Collaboration: Aghanim et al. (2020) value) is considered, in addition to the extended parameter set $\{\Omega_m, \sigma_8, w_0, w_a\}$, and the results are compared.

2.3 Results

2.3.1 Residual power spectra

Residual power spectra $\Delta C_\ell^{\gamma_i^E \gamma_j^E}$ arising due to the spatially-varying m-bias are computed by applying the pseudo-C_ℓ formalism described in section (2.1). Examples of the fractional residual power spectra $\Delta C_\ell^{\gamma_i^E \gamma_j^E} / C_\ell^{\gamma_i^E \gamma_j^E}$ are shown in fig. 2.3, with $\ell_{\rm peak}$ in the range $50 - 5000$. As illustrated in fig. 2.3, the residual power spectra are generally at least ~ 4 orders of magnitude below the fiducial C_ℓs. As can be seen, the structure of the residual C_ℓs is highly dependent on the characteristic scale of the W_ℓ, $\ell_{\rm peak}$. There is typically a minimum in the $\Delta C_\ell^{\gamma^E \gamma^E} / C_\ell^{\gamma^E \gamma^E}$ at $\ell \lesssim 10$ with an enhancement at higher ℓ. In the auto-spectra, this enhancement has a gentle gradient and plateau with increasing ℓ, whereas for the cross-spectra with high $\ell_{\rm peak}$ the enhancement is more sharply peaked. There is also a smaller drop at still higher ℓ, with this structure shifting to higher ℓ and increasing in strength with increasing $\ell_{\rm peak}$. The high-ℓ smaller minimum of the fractional residual C_ℓs is typically located at ℓ greater than $\ell_{\rm peak}$ by approximately 500. For lower values of $\ell_{\rm peak}$ the residual C_ℓs are enhanced across all ℓ, and they also vary more smoothly than for higher $\ell_{\rm peak}$.

BB power arising due to mode mixing

The BB power spectra arising due to the mode-mixing effect of the spatially-varying m-bias are also calculated, and examples of the BB power spectra are shown in fig. 2.4, for $\ell_{\rm max} = 5000$ and $\ell_{\rm peak} = 500$ and 5000, alongside the corresponding ΔC_ℓ^{EE}, divided by the fiducial C_ℓ^{EE}. For high $\ell_{\rm peak}$, the BB power spectra are of the same order of magnitude and follow closely the ΔC_ℓ^{EE}; for lower

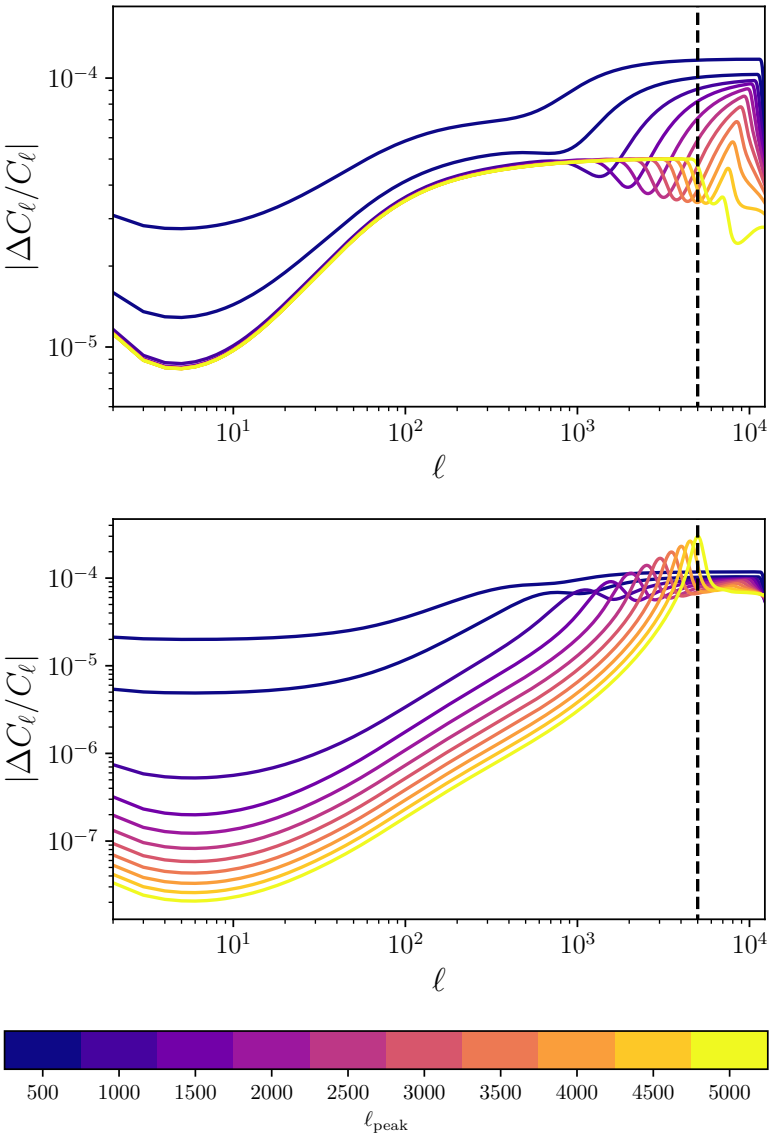


Figure 2.3: Ratio of residual to fiducial EE angular power spectra as a function of peak multipole of W_ℓ, with W_ℓ Gaussian profile width $\sigma_m = 64$ and m-bias RMS $= 0.01$. Black dashed line: Maximum value of $\ell_{\rm max}$ considered in the Fisher analysis. Top panel: autocorrelation of first tomographic redshift bin $\Delta C_\ell^{\gamma_0^E \gamma_0^E} / C_\ell^{\gamma_0^E \gamma_0^E}$. Bottom panel: cross-correlation of first and fifth tomographic redshift bins $\Delta C_\ell^{\gamma_0^E \gamma_4^E} / C_\ell^{\gamma_0^E \gamma_4^E}$.

$\ell_{\rm peak}$ the generated BB power spectra follow the ΔC_ℓ^{EE} less closely at high and low ℓ. The observed BB power spectra may therefore be a useful diagnostic of a residual spatially-varying m-bias, especially with a small characteristic scale. While this will be complicated by the fact that there are many systematics which may produce measurable shear B-modes, such that it will be difficult to isolate the signal arising due to any given systematic in the measured B-mode signal, it may be a useful diagnostic if different systematics result in different signature effects in the resulting BB power spectra. As a generic form for the m-bias map is considered, further conclusions about the viability of the measured B-mode signal as a systematics diagnostic cannot be made in this work.

Numerical effects in the $\Delta C_\ell^{\gamma^E\gamma^E}$

As a test of the methods presented in this work, the multipole at which the calculation of the mode-coupling matrix is truncated, $\ell_{\rm cut}$, is varied. In the top panel of fig. 2.3, at high ℓ and for high $\ell_{\rm peak}$, the fractional auto-ΔC_ℓ^{EE} curves can be seen to have sharp reductions at $\ell \sim 8 \times 10^3 - 10^4$. In order to determine whether this is a numerical effect arising due to the truncation of the calculation of the mode-coupling matrix at $\ell_{\rm cut} = 12288$, the calculation of the ΔC_ℓ^{EE}s was also carried out with $\ell_{\rm cut} = 6144$ (corresponding to $N_{\rm side} = \ell_{\rm cut}/3 = 2048$). In fig. 2.5, the effect of this on examples of the auto- and cross-power spectra for a range of values of $\ell_{\rm peak}$ is shown. As can be seen in the top panel, for the auto-ΔC_ℓ^{EE}s, the gentle minimum at intermediate ℓ followed by a rise and plateau at higher ℓ is robust against changes to $\ell_{\rm cut}$ and is therefore likely to be a real feature. The same is also true of the sharp peak in the cross-ΔC_ℓ^{EE}s. However, for $\ell_{\rm peak}, \ell \gtrsim 1.25 N_{\rm side}$, the auto-$\Delta C_\ell^{EE}$s contain a spurious sharp minimum due to the truncation of the calculation of the mode-coupling matrix. Indeed, when $\ell_{\rm peak}$ exceeds $\sim 1.25 N_{\rm side}$ by more than a factor of ~ 2, the calculated ΔC_ℓ^{EE}s are biased down to smaller ℓ (as can be seen in the highest $\ell_{\rm peak}$ curves in the disparity between the two $\ell_{\rm cut}$ cases). For $\ell_{\rm cut} = 12288$, $1.25 N_{\rm side}$ corresponds to $\ell \sim 5000$ (indicated with a vertical red dashed line in each panel). This justifies the maximum multipole $\ell_{\rm max}$

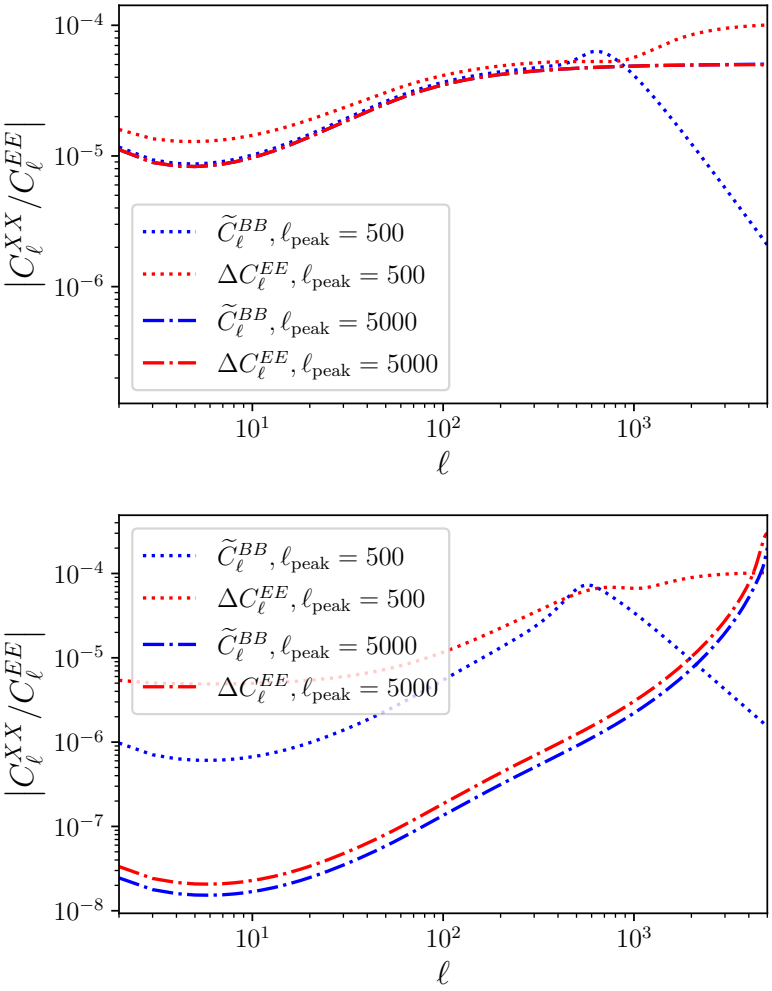


Figure 2.4: Comparison of BB power spectra generated by the mode coupling arising due to the spatially-varying m-bias $\widetilde{C}_\ell^{BB}$ with the residual EE power spectra ΔC_ℓ^{EE}, up to $\ell_{\rm max} = 5000$. Top panel: autocorrelation of first tomographic redshift bin $\Delta C_\ell^{\gamma_0^E\gamma_0^E}/C_\ell^{\gamma_0^E\gamma_0^E}$. Bottom panel: cross-correlation of first and fifth tomographic redshift bins $\Delta C_\ell^{\gamma_0^E\gamma_4^E}/C_\ell^{\gamma_0^E\gamma_4^E}$. W_ℓ Gaussian profile width $\sigma_m = 64$ and m-bias RMS $= 0.01$.

at which the residual power spectra are truncated in the Fisher-matrix analysis; in addition to corresponding to the optimistic *Euclid* setting (Euclid Collaboration: Blanchard et al., 2020), this also prevents contamination of the analysis by edge effects. Due to this effect, m-bias peak multipoles $\ell_{\rm peak} > 5000$ are also neglected in the Fisher-matrix analysis; this corresponds to scales of $\lesssim 2$ arcminutes, so that scales on which spatially-varying m-bias might be expected to arise due to PSF errors varying on the scale of the *Euclid* VIS FoV are still probed. This effect was also tested for the other tomographic power spectra with similar results.

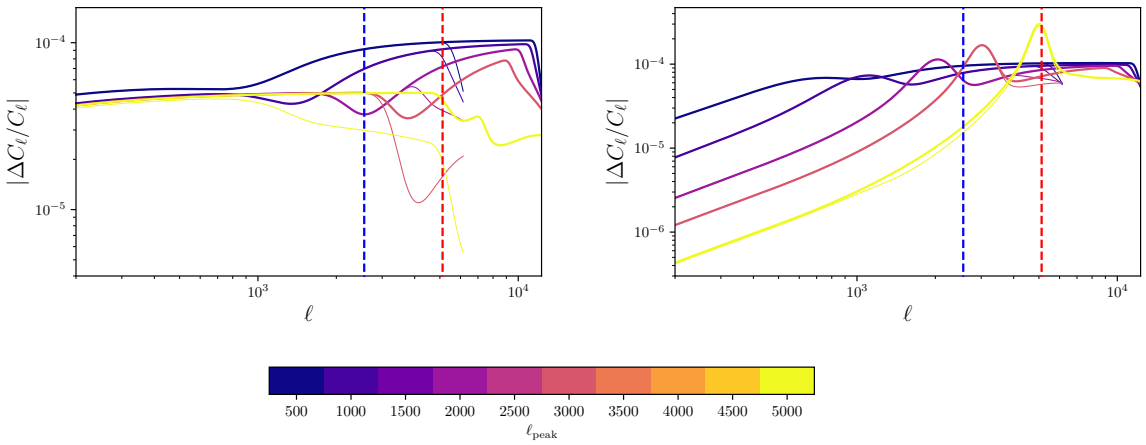


Figure 2.5: Ratio of residual to fiducial angular power spectra as a function of peak multipole of W_ℓ, with W_ℓ Gaussian profile width $\sigma_m = 64$ and m-bias RMS $= 0.01$, showing the effect of the truncation of the calculation of the mode-coupling matrix at a particular multipole $\ell_{\rm cut}$. Bold lines: $\ell_{\rm cut} = 3N_{\rm side} = 12288$. Thin lines: $\ell_{\rm cut} = 3N_{\rm side} = 6144$. Vertical dashed lines correspond to the maximum threshold values of $\ell_{\rm max}$ that could be considered in a subsequent Fisher analysis, equal to $1.25N_{\rm side}$; blue for the $\ell_{\rm cut} = 6144$ case and red for the $\ell_{\rm cut} = 12288$ case which are considered. Top panel: autocorrelation of first tomographic redshift bin $\Delta C_\ell^{\gamma_0^E\gamma_0^E}/C_\ell^{\gamma_0^E\gamma_0^E}$. Bottom panel: cross-correlation of first and fifth tomographic redshift bins $\Delta C_\ell^{\gamma_0^E\gamma_4^E}/C_\ell^{\gamma_0^E\gamma_4^E}$.

2.3.2 Bias in cosmological parameters

Using the Fisher matrix analysis described in section 2.2.3, biases due to shifts in the $C_\ell^{\gamma_i^E\gamma_j^E}$ are forecast for the base cosmological parameter set $\{\Omega_m, \sigma_8, w_0\}$ (varying Ω_c in the Fisher-matrix analysis, with Ω_b fixed at the Planck Collaboration: Aghanim et al. (2020) value). A high-ℓ cut $\ell_{\rm max}$ is applied in both the computation of the Fisher matrix (2.12) and of the parameter biases (2.15), and the analysis is repeated for a range of values of $\ell_{\rm max}$. In fig. 2.6 the ratio of the calculated parameter biases to the 1σ uncertainty as a function of $\ell_{\rm peak}$ and $\ell_{\rm max}$, with σ_m fixed at 64, is shown. Next, the extended parameter set $\{\Omega_m, \sigma_8, w_0, w_a\}$ is considered, and in fig. 2.7 the ratio of the parameter biases to the 1σ uncertainty as a function of $\ell_{\rm peak}$ and $\ell_{\rm max}$ with σ_m, the width of the W_ℓ, fixed at 64, is shown. Note that in some cases parameter biases are shown corresponding to values of $\ell_{\rm peak} > \ell_{\rm max}$; it should be recalled that $\ell_{\rm max}$ is the largest ℓ included in the *Fisher calculation*, but that values of $\ell \leq \ell_{\rm cut} = 12288$ are included in the calculation of the ΔC_ℓ^{EE} in all cases, as described in section 2.3.1; hence, even when the scale corresponding

to $\ell_{\rm peak}$ is not included in the Fisher analysis, the impact on the angular power spectra of W_ℓ with $\ell_{\rm peak} > e \ll_{\rm max}$ is accurately modelled on the scales entering the Fisher analysis in all cases. The analysis is also conducted keeping $\ell_{\rm max}$ fixed, and varying σ_m in the range $64 - 2048$, and $\ell_{\rm peak}$ in the range $100 - 1100$. It is found that for all parameters considered, the biases and their ratios to the 1σ uncertainty were insensitive to the value of σ_m for $\sigma_m \lesssim 500$, justifying the choice of $\sigma_m = 64$ for the main analysis. This is probably because the m-bias W_ℓ is normalised by A_m in equation (2.8), such that, by the integral-preserving property of convolution (Bracewell, 1965), the total power introduced due to the convolution with W_ℓ does not depend on σ_m for fixed A_m; changes in the shape of the residual C_ℓ^{EE}s due to variations in σ_m then have a sub-dominant impact on the resulting cosmological parameter biases. This in turn implies that changes in $\ell_{\rm peak}$ have a dominant effect on the shape of the residual C_ℓ^{EE} (measured by the resulting impact on parameters) compared with changes in σ_m. Larger values of σ_m for a given value of m-bias RMS resulted in reduced cosmological parameter bias; this is probably due to truncation of the tails of the W_ℓ resulting in reduced overall amplitude of the W_ℓ, and hence reduced over all power in the ΔC_ℓ^{EE}s.

In Table 2, the maximum absolute values of the bias-uncertainty ratios obtained in parameter biases are reported, for the base parameter set of $\{\Omega_m, \sigma_8, w_0\}$. The bias-uncertainty ratios for three values of $\ell_{\rm max}$ are reported, corresponding to pessimistic and optimistic settings for a *Euclid*-style survey (Euclid Collaboration: Blanchard et al., 2020) (note that for the 3-parameter case, the highest ratio of bias to 1σ uncertainty in σ_8 of 0.032 is achieved for $\ell_{\rm max} = 3000$). In table 3, the same are reported, for the extended parameter set of $\{\Omega_m, \sigma_8, w_0, w_a\}$.

For both parameter sets, there are two clear trends; firstly, that the parameter bias-uncertainty ratio is greater when higher multipoles ℓ are included in the Fisher analysis; and secondly, that the m-bias generally has a greater influence when it is peaked at smaller ℓ. Furthermore, the inclusion of the parameter w_a in the Fisher matrix has resulted in more significant biases for all parameters, due to the additional parameter degeneracy in the C_ℓs arising when more parameters

Table 2.2: Maximum absolute bias/1σ for pessimistic (1500) and optimistic (5000) values of $\ell_{\rm max}$, base parameter set (2 s.f.). W_ℓ Gaussian profile width $\sigma_m = 64$ and m-bias RMS $= 0.01$.

	Bias/1σ	
Parameter	$\ell_{\rm max} = 1500$	$\ell_{\rm max} = 5000$
Ω_m	0.0030	0.081
σ_8	0.023	0.022
w_0	0.035	0.089

are included in the Fisher analysis.

There is additionally a trend of subsidiary peaks – i.e. slopes with increasing $\ell_{\rm peak}$, followed by bumps –with bias-uncertainty ratios that are increasing in strength at higher $\ell_{\rm peak}$, for all parameters. These peaks are typically strongest where $\ell_{\rm peak}$ is less than $\ell_{\rm max}$ by ~ 500, though these peaks become suppressed for the highest values of $\ell_{\rm max}$. These occur because a given value of $\ell_{\rm max}$ will roughly coincide with the high-ℓ minimum of the $\Delta C_\ell^{\gamma^E\gamma^E}$ for which $\ell_{\rm peak} \sim \ell_{\rm max} - 500$. Therefore, for smaller values of $\ell_{\rm peak}$ than this, for which the structure in the $\Delta C_\ell^{\gamma^E\gamma^E}$ is shifted to lower ℓ, less of the $\Delta C_\ell^{\gamma^E\gamma^E}$ that is included in the bias calculation will consist of the low-ℓ plateau, and more will be in the higher-ℓ trough; whereas for larger values of $\ell_{\rm peak}$, the $\Delta C_\ell^{\gamma^E\gamma^E}$ is generally suppressed. In both cases, the resulting impact in the inferred cosmology is smaller, so a peak in parameter bias is obtained at this value of $\ell_{\rm peak}$. At the lowest values of $\ell_{\rm peak}$, the $\Delta C_\ell^{\gamma^E\gamma^E}$ is generally enhanced, resulting in the low-$\ell_{\rm peak}$ rise in parameter bias and bias-uncertainty ratio.

The Fisher-matrix analysis was also carried out without the inclusion of the super-sample covariance. It is found that the inclusion of the SSC increases the bias-uncertainty ratio by a factor of at most $\sim 25 - 30\%$ for $\ell_{\rm max} \sim 5000$.

2.3.3 Dependence of parameter bias on m-bias RMS

The variation of the forecast parameter biases with the amplitude of the variations of the m-bias map is also investigated. In fig. 2.8 the m-bias RMS which results in parameter bias-uncertainty ratios of $\Delta\theta/\sigma = 0.1$, 0.3 and 1 as a function of $\ell_{\rm peak}$ is shown, for the base parameter set of $\{\Omega_m, \sigma_8, w_0\}$, with $\ell_{\rm max} = 5000$. In fig. 2.9 this

Table 2.3: Maximum absolute bias/1σ for pessimistic (1500) and optimistic (5000) values of $\ell_{\rm max}$, extended parameter set (2 s.f.). W_ℓ Gaussian profile width $\sigma_m = 64$ and m-bias RMS $= 0.01$.

	Bias/1σ	
Parameter	$\ell_{\rm max} = 1500$	$\ell_{\rm max} = 5000$
Ω_m	0.0087	0.10
σ_8	0.0092	0.071
w_0	0.030	0.14
w_a	0.015	0.11

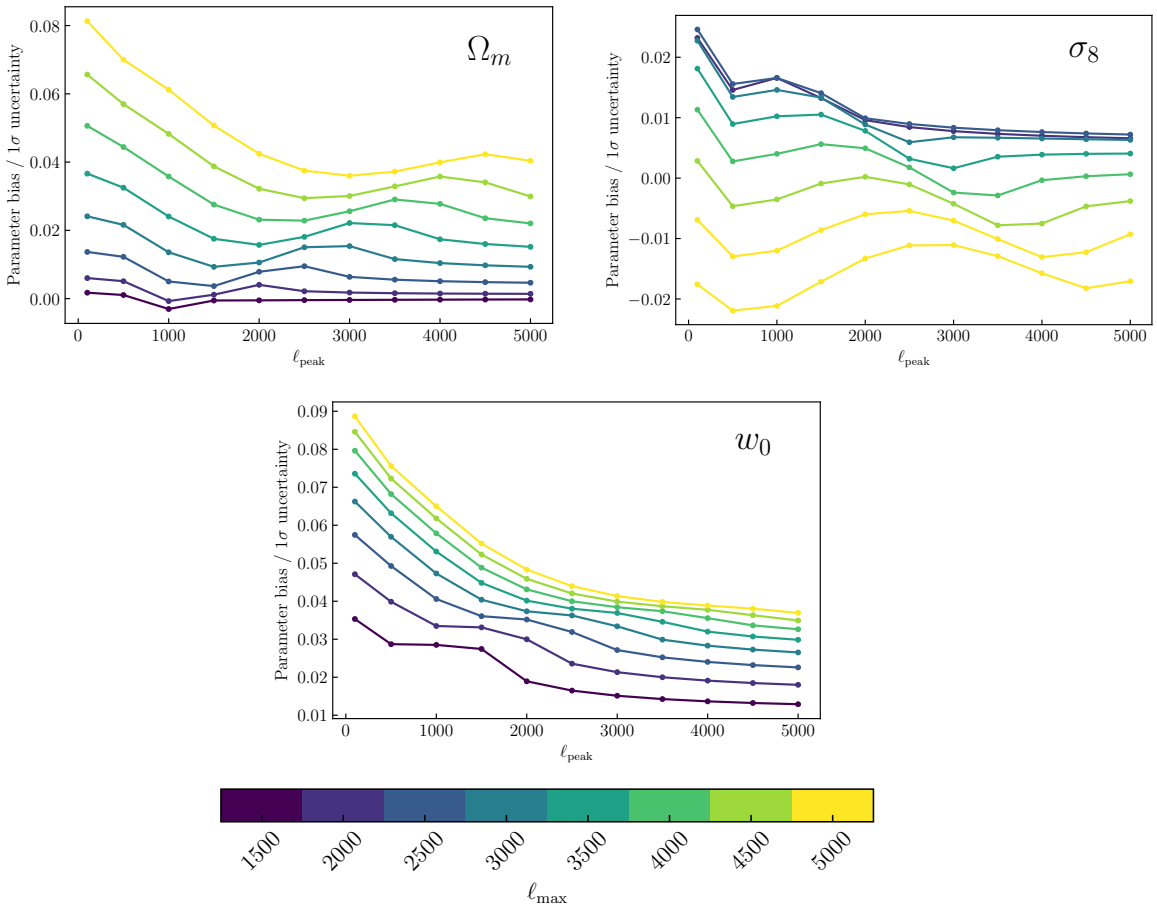


Figure 2.6: Parameter bias-uncertainty ratio in the case that $\{\Omega_m, \sigma_8, w_0\}$ are included in the Fisher matrix. W_ℓ Gaussian profile width $\sigma_m = 64$ and m-bias RMS $= 0.01$. **Upper-left panel:** Bias-uncertainty ratio for Ω_m as a function of $\ell_{\rm peak}$ and $\ell_{\rm max}$. **Upper-right panel:** Bias-uncertainty ratio for σ_8 as a function of $\ell_{\rm peak}$ and $\ell_{\rm max}$. **Lower panel:** Bias-uncertainty ratio for w_0 as a function of $\ell_{\rm peak}$ and $\ell_{\rm max}$.

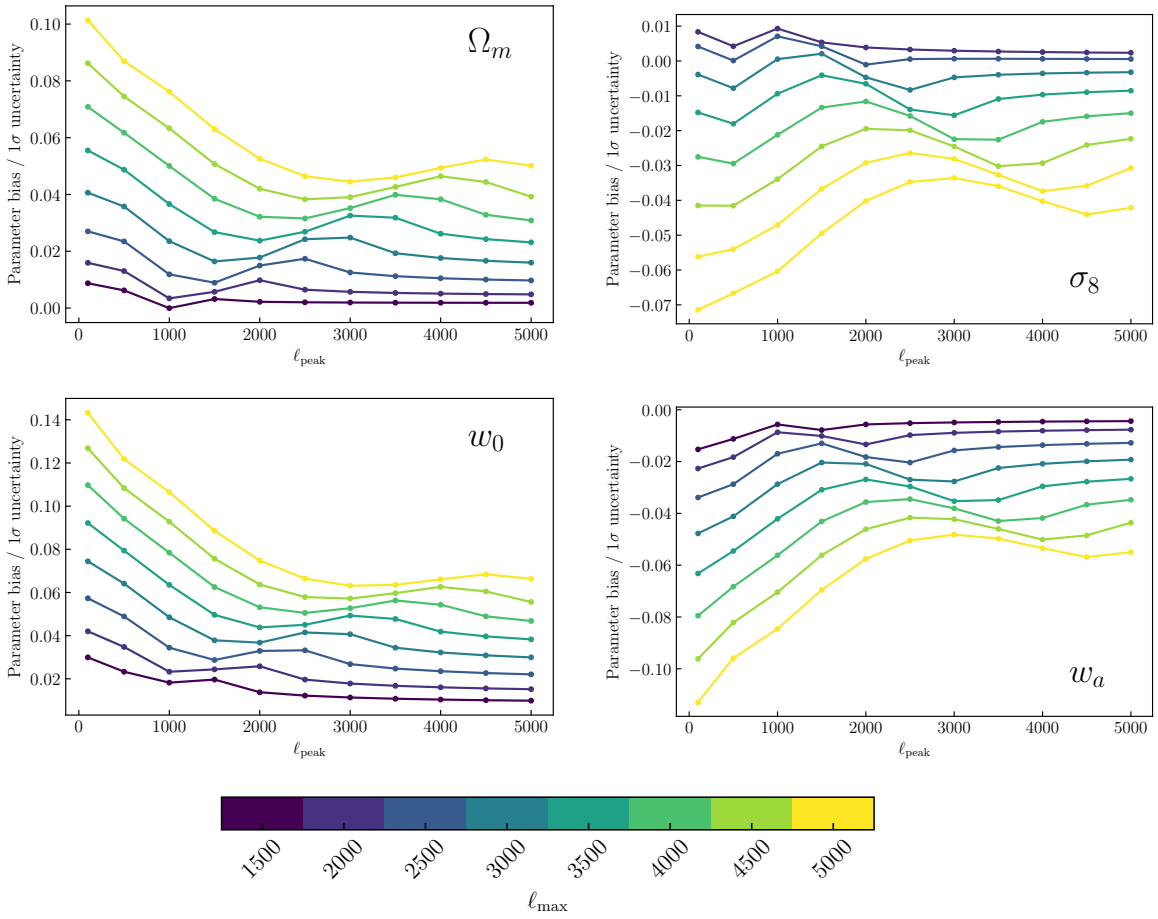


Figure 2.7: Parameter bias-uncertainty ratio in the case that $\{\Omega_m, \sigma_8, w_0, w_a\}$ are included in the Fisher matrix. W_ℓ Gaussian profile width $\sigma_m = 64$ and m-bias RMS $= 0.01$. **Upper-left panel:** Bias-uncertainty ratio for Ω_m as a function of $\ell_{\rm peak}$ and $\ell_{\rm max}$. **Upper-right panel:** Bias-uncertainty ratio for σ_8 as a function of $\ell_{\rm peak}$ and $\ell_{\rm max}$. **Lower-left panel:** Bias-uncertainty ratio for w_0 as a function of $\ell_{\rm peak}$ and $\ell_{\rm max}$. **Lower-right panel:** Bias-uncertainty ratio for w_a as a function of $\ell_{\rm peak}$ and $\ell_{\rm max}$.

is shown for the extended parameter set of $\{\Omega_m, \sigma_8, w_0, w_a\}$. As can be seen, a given bias-uncertainty ratio results from a smaller RMS for smaller values of $\ell_{\rm peak}$, and has a weakly increasing dependence on the number of parameters included in the Fisher matrix. For both parameter sets, the bias-uncertainty ratio is ~ 0.1 when the RMS$= 0.01$, ~ 0.3 when the RMS$= 0.02 - 0.03$, and the parameter biases reach the statistical errors when the RMS$= 0.03 - 0.06$, depending on $\ell_{\rm peak}$. It is found that the inclusion of SSC has a small effect on the RMS requirements that are recovered, with the case in which SSC is excluded resulting in the curves in fig. 2.8 and fig. 2.9 shifting up by at most 0.05 compared with the baseline case with SSC included.

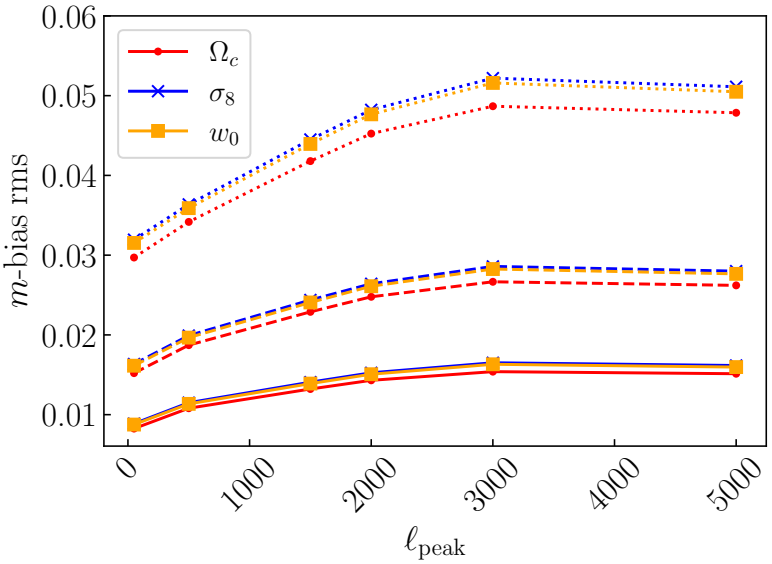


Figure 2.8: m-bias RMS which results in selected values of parameter bias-uncertainty ratio for the base parameter set $\{\Omega_c, \sigma_8, w_0\}$, as a function of $\ell_{\rm peak}$. W_ℓ Gaussian profile width $\sigma_m = 64$. Solid line: m-bias RMS which results in bias-uncertainty ratio of 0.1. Dashed line: m-bias RMS which results in bias-uncertainty ratio of 0.3. Dotted line: m-bias RMS which results in bias-uncertainty ratio of 1.

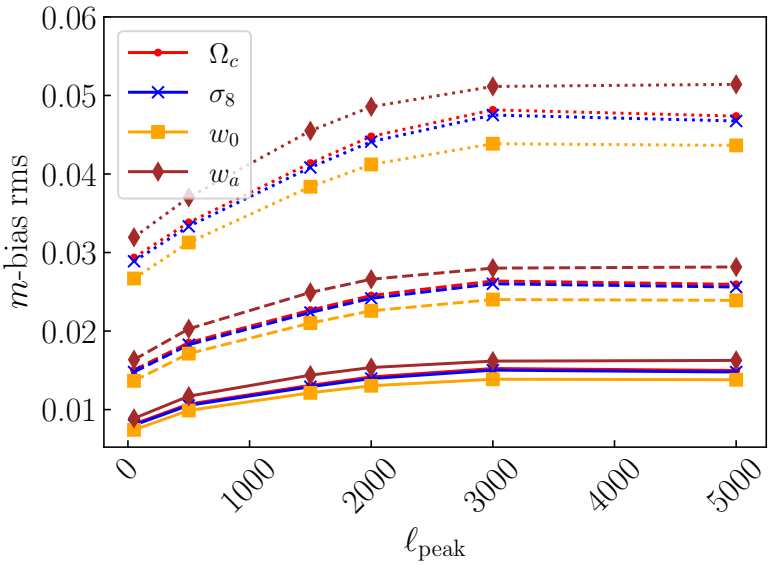


Figure 2.9: m-bias RMS which results in selected values of parameter bias-uncertainty ratio for the extended parameter set $\{\Omega_c, \sigma_8, w_0, w_a\}$, as a function of $\ell_{\rm peak}$. W_ℓ Gaussian profile width $\sigma_m = 64$. Solid line: m-bias RMS which results in bias-uncertainty ratio of 0.1. Dashed line: m-bias RMS which results in bias-uncertainty ratio of 0.3. Dotted line: m-bias RMS which results in bias-uncertainty ratio of 1.

2.4 Discussion

2.4.1 Residual power spectra

As can be seen in the fractional $\Delta C_\ell^{\gamma^E\gamma^E}$ shown in fig. 2.3, an m-bias with some particular $\ell_{\rm peak}$ can introduce a bias in the C_ℓs with generally consistent magnitude on a range of scales, due to mode-mode coupling; therefore, any analysis of the effect of an m-bias on the C_ℓs must not be limited only to the scales on which the m-bias varies. Note that as the effect of the spatially-varying m-bias on the power spectrum is more complicated than a constant scaling, the impact on the cosmological parameters due to marginalisation over a constant bias parameter will not be an effective means of mitigation. In a real survey, the C_ℓ of the m-bias map will not be known a priori, and will probably not be easily describable with a small number of parameters as in the case studied here. As a result, it will be difficult to marginalise over the effect of a spatially-varying m-bias in cosmological parameter estimation, because the number of required nuisance parameters will be too large. Due to this, the effect of m-bias marginalisation on cosmological parameter biases or figures of merit has not been considered in the present work.

The fractional residual shear angular power spectra reach a maximum of $\sim 10^{-4}$. Kitching et al., 2020, 2019 also calculated residuals between the full analytic shear C_ℓs, which included spatially-varying shear bias, and an analytic linear approximation, which only included mean and spatially-constant terms, up to a maximum multipole of 64. Kitching et al., 2020 also calculated residuals between forward-modelled shear C_ℓs, which included spatially-varying shear bias, and the linear approximation, up to a maximum multipole of 2048, and found differences which were also $\sim$4 orders of magnitude smaller than the fiducial power spectra. Similar results are therefore found in this work to that of Kitching et al., 2020, 2019 at the order-of-magnitude level, in the regions of ℓ-space in which the respective results overlap.

In Taylor and Kitching, 2018, the convergence angular power spectrum $C_\ell^{\kappa\kappa}$ is convolved with a sharp delta-like m-bias feature at $ell_{\rm spike} = 10^3$ (for a single tomographic bin); this results in a sharply peaked $\tilde{C}_\ell^{\kappa\kappa}$, with peak at $\ell_{\rm spike}$, with

excess power spread out on each side. This is similar to the results of this work for the tomographic cross-C_ℓ^{EE}s shown in the lower panel of fig. 2.3, in which there is a peak in the residual power centred at $\ell_{\rm peak}$. The maximum residual power found in this work for $\ell_{\rm peak}$ is higher than that found in Taylor and Kitching, 2018 ($\sim 10^{-4}$ in this work, vs. $< 10^{-5}$ in Taylor and Kitching, 2018); this depends on the value of the normalisation of the m-bias W_ℓ used in this work, A_m in (2.8), and if Taylor and Kitching, 2018 had chosen a normalisation of the spike feature consistent with the A_m chosen in this work, it follows that the integrated bias in the $C_\ell^{\kappa\kappa}$ would be consistent with that found in this work. Comparing the residual C_ℓ^{EE} in the lower panel of fig. 2.3 for $\ell_{\rm peak} = 10^3$ with the corresponding residual in $C_\ell^{\kappa\kappa}$ from Taylor and Kitching, 2018, the residial power spectra found in this work are smoothed out over a greater range of ℓ; this is due to the Gaussian profile of the m-bias W_ℓ adopted in this work, in contrast to the δ-like W_ℓ adopted in Taylor and Kitching, 2018. On the other hand, the profile of the auto-ΔC_ℓ^{EE}s shown in the upper panel in fig. 2.3 are in contrast to that obtained by Taylor and Kitching, 2018; the auto-ΔC_ℓ^{EE} contain power on a broad range of scales, in particular for low $\ell_{\rm peak}$, due to the Gaussian profile of the W_ℓ; additionally, they exhibit a minimum in power around the corresponding $\ell_{\rm peak}$, plus some lag, with enhancements in power rising asymmetrically on either side.

2.4.2 Bias in cosmological parameters

As shown in figs. 5 and 6, the parameter bias-uncertainty ratio generally increases with decreasing $\ell_{\rm peak}$ and increasing $\ell_{\rm max}$. The increase in bias-uncertainty ratio (and indeed in bias) with $\ell_{\rm max}$ occurs because the C_ℓs are biased on all scales and so including contributions from additional scales will increase the size of the parameter bias. Indeed, while including higher multipoles in the analysis results in a smaller parameter uncertainty, this effect is small compared with the increase in parameter bias with $\ell_{\rm max}$. The greater influence of an m-bias with small $\ell_{\rm peak}$ arises due to the generally larger $\Delta C_\ell^{\gamma^E\gamma^E}$ for smaller $\ell_{\rm peak}$. m-bias maps with different $\ell_{\rm peak}$ also affect each parameter differently; each parameter exhibits

different variation in the parameter bias with $\ell_{\rm peak}$ and $\ell_{\rm max}$, due to sensitivity of different parts of the shear power spectra to each parameter. The scale-dependence of the parameter biases which result from the spatial variations of the m-bias field, which come in through the $\ell_{\rm peak}$-dependence, demonstrates that the bias in shear power spectra and in cosmological parameters varies with the shape of the power spectrum of m-bias field. This shows that the impact of spatial variations of the m-bias on cosmological parameter estimation can not be fully mitigated by marginalisation, unless a parametric form of power spectrum of the m-bias field is known, which will be substantially non-trivial in practice.

Maximum values of parameter bias-uncertainty ratio obtained for the pessimistic and optimistic settings for $\ell_{\rm max}$ (Euclid Collaboration: Blanchard et al., 2020) are shown in tables 2 and 3, for the base and extended parameter sets respectively. Larger parameter bias-uncertainty ratios are obtained when more free parameters are included in the Fisher analysis. In the case of the optimistic cutoff multipole for a *Euclid*-style survey, corresponding to $\ell_{\rm max} = 5000$, the maximum bias-uncertainty ratios are at about 0.05 and 0.1 for the base and extended parameters sets, respectively. In the case of w_0, for which the maximum bias-uncertainty ratios for $\ell_{\rm max} = 5000$ is 0.12, this may still represent a non-negligible contribution to the total systematic error budget; this is potentially relevant in light of the fact that one of the main science goals of *Euclid* and other stage-IV surveys is the investigation of dark energy and the accelerated expansion (Albrecht et al., 2006; Dark Energy Science Collaboration: Mandelbaum et al., 2018; Euclid Collaboration: Laureijs et al., 2011; Euclid Collaboration: Mellier et al., 2024). In the pessimistic setting of $\ell_{\rm max} = 1500$, bias-uncertainty ratios do not exceed 0.025 in any case. In general, the systematic bias introduced by the spatially-varying m-bias on cosmological parameter estimates is expected to be sub-dominant, but not wholly negligible in certain cases. This is a refinement of previous work in this area, for example Kitching et al., 2020, 2019, which found that the impact on the shear angular power spectra of the spatially-varying m-bias should be small compared with the impact of the mean term; while in this

work the assumption is made of an m-bias with zero spatial mean and as such comparative conclusions with respect to (Kitching et al., 2020, 2019) are not made, it is quantified explicitly that the cosmological parameter bias induced by the spatially-varying m may be a non-negligible contribution to the error budget. While the mean m term may present the dominant contribution to the error budget from the m-bias, if this is well-constrained then the spatial variations may still result in a non-negligible bias in inferred cosmological parameter values.

2.4.3 Dependence of parameter bias on m-bias RMS

The amplitude of variations of the m-bias map which gives rise to parameter bias-uncertainty ratios of $0.1, 0.3$ and 1 is shown in figs. 7 and 8 for the 3-parameter and 4-parameter cases respectively, as a function of $\ell_{\rm peak}$, and for the optimistic high ℓ-cut of $\ell_{\rm max} = 5000$. It is also found that the dependence of bias-uncertainty ratio on m-bias RMS is close to quadratic, with the exponent departing from 2 (negatively, by a few per cent) for $\ell_{\rm peak} \lesssim 500$. The quadratic relationship is is expected as the mode-coupling matrix is proportional to the m-bias angular power spectrum which scales as the variance of the m-bias map. The parameter bias-uncertainty ratio obtained from an m-bias map with a given RMS depends on the scale of m-bias variations, and for an m-bias with a large characteristic scale the parameter bias can exceed the statistical uncertainty σ for RMS $\sim 0.04 - 0.05$; biases exceed 30% of the statistical uncertainty for RMS $\sim 0.02 - 0.03$ for m-biases peaked across the range of scales examined. This shows that the importance of the spatially-varying m-bias is sensitive to the RMS of the m-bias map, and hence that the potential impact of the spatially-varying m-bias on cosmological parameter constraints from cosmic shear cannot be neglected unless the expected amplitude of variations of the m-bias map is known from predicted constraints on the shear systematics which produce the spatially-varying m-bias. This allows requirements to be set on the allowed amplitude of variations of the spatially-varying m-bias, and hence on constraints of weak-lensing systematics from which the spatially-varying m-bias originates. In the case that the requirement on the amplitude

of spatial variations of the m-bias field is satisfied, such that the resulting bias on inferred cosmological parameters is deemed to be negligible, then it will be possible to neglect the convolutive effect of the spatial variations of the m-bias on the shear power spectra, and consider the effect of the m-bias on the shear C_ℓs as a constant scaling arising due to the mean m. In this case it will be acceptable to mitigate the effect of the m-bias on cosmological parameter estimation by marginalising over a prior on the mean m, and the dominant effect of the m-bias on parameter inference will be the marginalisation effect considered by Kitching et al., 2020.

It should also be noted that while requirements exist on the value of the mean m-bias (the requirement from Massey et al., 2013 is that $m \lesssim 2 \times 10^{-3}$), no such requirement has been placed on the amplitude of spatial variations of the m-bias (e.g. on the RMS of the m-bias field). In the analysis of data from forthcoming surveys such as the EWS, *residual* shear biases will be of interest, i.e. biases which result from uncertainties in the knowledge of the observational systematics that give rise to shear biases. Therefore, even if the mean m-bias is well calibrated subject to requirements, this does not by itself mean that the spatial variations of the residual m-bias must necessarily also be so; a key conclusion of this work is that it is separately necessary to place requirements on the amplitude of the spatial variations of the residual m-bias. This will allow requirements to be placed on models of the observational systematics that produce shear biases (e.g. requirements on the precision of PSF models) and on priors of these systematics.

2.5 Conclusion

In this work, the effect of a spatially-varying multiplicative shear bias on the estimation of cosmological parameters using the cosmic shear angular power spectrum has been considered. A computationally efficient pseudo-C_ℓ formalism has been applied to determine the bias in the cosmic shear power spectra $C_\ell^{\gamma^E\gamma^E}$ arising due to an m-bias field obeying a C_ℓ with a Gaussian profile, by considering the m-bias map as acting as a mask that introduces mode mixing into the shear

C_ℓs, and computing the mode-mixing matrix which convolves the $C_\ell^{\gamma^E\gamma^E}$ with the power spectrum of the m-bias map. This has allowed consideration of the effect of the m-bias at high ℓ, down to arcminute-scales corresponding to the expected field-of-view PSF variations in a Euclid-like photometric survey. The settings for a stage-IV style lensing survey such as *Euclid* (Euclid Collaboration: Blanchard et al., 2020; Euclid Collaboration: Mellier et al., 2024) have been considered, and fiducial tomographic shear C_ℓs have been computed using `CCL` (Chisari et al., 2019). Note that while in this work the EWS is considered as an example, the indicative results presented here are likely to be informative for other stage-IV weak-lensing surveys. This is repeated this for a number of different m-bias maps, characterised by different values for the mean and width of the m-bias W_ℓ, parametrised by $\ell_{\rm peak}$ and σ_m respectively. BB shear power spectra generated by the mode-coupling effect of the spatially-varying m-bias are also calculated, and are found to the residual EE shear power spectra closely, especially for a spatially-varying m-bias with a characteristic scale of arcminutes. It is concluded that it may in principle be possible to use the induced BB power to self-calibrate the spatially-varying m-bias, in agreement with previous work in this area (e.g. Kitching et al., 2020), though this will be complicated by the fact that the BB power induced by different systematics may be degenerate, and so this is not considered in this work.

Fractional residual C_ℓ^{EE}s are found that reach a maximum of $\sim 10^{-4}$. This is similar to the magnitude of fractional residuals found by Kitching et al., 2020, 2019 between analytic calculations involving the spatially-varying m-bias and only the constant and mean terms up to a maximum multipole of 64, and between a numerical forward model including the spatially-varying m-bias and an analytic calculation involving only the constant and mean terms up to a maximum multipole of 2048, though in this work the analytic calculation involving the spatially-varying m-bias has been extended to high ℓ.

A Fisher matrix analysis was then employed to forecast biases on cosmological parameters inferred from the $C_\ell^{\gamma^E\gamma^E}$ due to the bias in the power spectra $\Delta C_\ell^{\gamma^E\gamma^E}$ resulting from the spatially-varying m-bias, with no spatially constant term, i.e.

assuming perfect calibration of the shear field for the spatially invariant m-bias. It is found that the ratio of the parameter biases to the 1σ uncertainty depends strongly on $\ell_{\rm max}$ (a cut-off scale applied at the Fisher level) and $\ell_{\rm peak}$, with the parameter biases typically peaking both at high and low values of $\ell_{\rm peak}$, due to the dynamic nature of the $\Delta C_\ell^{\gamma^E\gamma^E}$ as a function of $\ell_{\rm peak}$ and $\ell_{\rm max}$. It is found that the parameter bias-uncertainty ratios are higher when more free parameters are included in the Fisher analysis. For realistic values of $\ell_{\rm max}$ for a *Euclid*-style survey, and for m-bias map RMS $= 0.01$, the bias in cosmological parameters resulting from a spatially-varying multiplicative shear bias reach a maximum of $\gtrsim 10\%$ of the forecast statistical error. It is found that the inclusion of super-sample covariance in the analysis increases the bias-uncertainty ratios that are recovered by modest amounts of at most a factor of $\sim 25 - 30\%$.

Whereas Kitching et al., 2020, 2019 concluded that the effect of a spatially-varying m-bias should be small compared with that of the mean m-bias, and negligible in the case of an m-bias field with zero mean, it is found that the effect of the spatially-varying m-bias can be neglected only subject to requirements on the properties of the m-bias field, in particular the RMS and characteristic scale of spatial variations. This caveat arises because the impact of the $\Delta C_\ell^{\gamma^E\gamma^E}$ up to significantly higher multipoles is considered, which allows the explicit calculation of the effect on the inference of cosmological parameters. This requires that the spatially-varying m-bias be a spin-0 field, though this is known to be a realistic assumption (for example, Kitching et al., 2019 found that the effect on the shear power spectra due to the imaginary part of the m-bias should be very small compared with the real part). This simplification allows an orthogonality relation to be taken advantage of in the computation of the m-bias mode-coupling matrix which significantly reduces the scaling of the calculation with the maximum multipole considered compared with the formalism of Kitching et al., 2019.

The variation of the parameter biases with the RMS of the m-bias map has also been investigated, and it is found that the relationship is close to quadratic. It is found that biases exceed 30% of the statistical error for RMS $\sim 0.02 - 0.03$

across the range of $\ell_{\rm peak}$ examined, and exceed the statistical error for RMS $\sim 0.04 - 0.05$ for small $\ell_{\rm peak}$. This allows requirements to be set on the permissible amplitude of variations of the m-bias, and hence on models of the relevant shear systematic effects that will be used for systematics control in forthcoming surveys. If the spatial variations of the m-bias field satisfy such a requirement, then it may be possible to mitigate the effect of the m-bias on parameter inference by marginalisation, as considered by Kitching et al., 2020.

In this work, a simple model for spatially-varying m-bias has been considered, in which the m-bias field exhibits power on a specific scale. This allows consideration of the sensitivity of inferred cosmological parameters to generic m-bias, arising due to systematics with power on a specific physical scale. However, a more realistic model may consider the potential redshift dependence of the m-bias, or a more realistic prescription for the statistics of the m-bias field, including the m-bias W_ℓ. In particular, it will be of interest to consider the effect of specific systematics which may contribute to the shear bias, including PSF and other instrumental effects, as well as effects relating to target selection, galaxy shape measurement, etc. In considering such effects it may also be of interest to consider the effect of the additive shear bias in a related analysis, which may potentially be considered in the pseudo-C_ℓ framework.

Forthcoming weak-lensing surveys will consider the combination of lensing and clustering 2-point statistics, referred to as a "3×2-point" analysis. Furthermore, a realistic parameter estimation analysis will utilise a complex but flexible nuisance parametrisation with ∼tens of additional parameters to characterise the various systematic effects present in the measurement. These additional terms will change the shape of the likelihood, impacting both parameter constraint precision and degeneracy, in a highly non-trivial way. The sensitivity of such an analysis to the spatial variations of the m-bias would represent a significant increase in the complexity of the problem that is considered, and is deferred to future work.

Leviathan was powerful and inevitable,
I fell in love with my fate as it crushed me to death...

— Will Toledo, *Famous Prophets (Stars)*

3

Forecasting Shear Bias Arising Due to PSF Errors at the Catalogue Level for the EWS

Contents

3.1 Introduction 76
3.1.1 Relevance of PSF Errors to Shear Measurement for the *Euclid* Wide Survey 76
3.1.2 Shear Bias Requirements for the *Euclid* Wide Survey 77
3.1.3 Sources of PSF error for the *Euclid* Wide Survey 86
3.1.4 Outline of the shear bias calculation method 88
3.2 Shear Bias Estimation 92
3.2.1 Description of PSF generation using the *Euclid* OU-SHE PSFTOOLKIT software 92
3.2.2 Description of the Shear Bias Calculation 94
3.2.3 Optimisation of PSF generation for shear bias calculation . 98
3.3 Estimation of Shear Bias at the Catalogue Level 108
3.3.1 Description of the Method 108
3.3.2 Optimisation and validation of SED matching 115
3.3.3 Morphology and FoV Interpolation 127
3.4 Conclusion 132
3.4.1 Summary 132
3.4.2 Applications and Future Work 133

3.1 Introduction

3.1.1 Relevance of PSF Errors to Shear Measurement for the *Euclid* Wide Survey

As discussed in section 1.1.3, weak gravitational lensing is a very subtle effect, typically introducing distortions in the measured ellipticities of galaxies at the percent level (Kilbinger, 2015). Accurate measurement of the shapes of galaxies is hence a core component of weak lensing surveys. The reduced shear (1.10) for a particular galaxy is estimated by its ellipticity. Neglecting the impact of intrinsic alignments (Crittenden et al., 2002), the ensemble average of ellipticity measurements of galaxies in a patch of the sky is an unbiased estimator of the reduced shear in that patch (Kilbinger, 2015). However, obtaining an unbiased estimate of the ellipticity of a galaxy image which is noisy, pixelated, has potentially complex morphology, and is subject to distortions due to the detector and optical system, including convolution with the point spread function (PSF), is a significant challenge. Various methods exist to measure ellipticities of galaxy images, including direct estimation from moments of the light distribution $I(\theta)$, such as the Kaiser-Squires-Broadhurst method (KSB, Kaiser et al., 1995), and model-fitting methods, in which a parametric light profile that includes the ellipticity is fit to the image, such as LensFit and LensMC (Euclid Collaboration: Congedo et al., 2024; Miller et al., 2007, 2013). Biases can be introduced at various stages in the galaxy shape measurement, for example due to the non-linear transformation of noisy pixel values to ellipticity, i.e. noise bias (Kacprzak et al., 2012); or, for model-fitting methods, due to an unrepresentative light profile model, i.e. model bias (Taylor and Kitching, 2018; Voigt and Bridle, 2010). Such biases may be corrected for using self-calibration methods such as MetaCalibration (Sheldon and Huff, 2017).

A crucial part of the galaxy shape measurement is correction for the PSF, which is convolved with galaxy images and introduces an additional perturbation to the galaxy shape originating from the optical system of the telescope. PSF correction generally consists of measuring the PSF from suitable stars observed in the field of view (FoV), which in the case of space-based observations, where

the PSF is diffraction-limited and has a complex profile, may involve fitting a PSF model to the selected stars, which is then used to estimate the PSF for target galaxies; see section 1.2.4 for a description of the procedure for the EWS. The convolution of the galaxy image with the PSF is then corrected for in the shear measurement (see e.g. Kilbinger, 2015 for a review of some approaches). Residual errors in the PSF may arise in this process, with errors in the anisotropy or size of the assumed PSF biasing the shear measurement and introducing spurious correlations to the galaxy shape distribution (Paulin-Henriksson et al., 2008). It is of interest to estimate the shear biases that are likely to arise due to residual PSF errors, for example to allow requirements to be placed on the accuracy of the PSF correction (Massey et al., 2013).

In this chapter, a method is described to estimate shear measurement biases arising due to errors in the assumed PSF for the EWS, for galaxies in the *Euclid* Flagship 2 mock catalogue (Euclid Collaboration: Castander et al., 2024). This is motivated in section 3.1.2. The calculation of shear measurement biases arising due to PSF errors is described in section 3.2, and the subsequent estimation of shear measurement biases for galaxies in the Flagship 2 mock is described in section 3.3. Applications and future propspects are described in section 3.4.

3.1.2 Shear Bias Requirements for the *Euclid* Wide Survey

The perturbation to the measured size and ellipticity of a galaxy due to residual PSF errors can be estimated using weighted quadrupole moments (Paulin-Henriksson et al., 2008):

$$Q_{ij} = \frac{\int d^2\boldsymbol{x}\, W(\boldsymbol{x}) x_i x_j I(\boldsymbol{x})}{\int d^2\boldsymbol{x}\, W(\boldsymbol{x}) I(\boldsymbol{x})}, \tag{3.1}$$

where $I(\boldsymbol{x})$ is the surface brightness distribution as a function of FoV position $\boldsymbol{x}$, $W(\boldsymbol{x})$ is a weighting function, and i, j index orthogonal directions in the image plane. The weighting function is used because the unweighted moments ($W = 1$) are divergent in the presence of noise (Kaiser et al., 1995). It is therefore desirable for $W(\boldsymbol{x})$ to be similar to the profile of the galaxy (Massey et al., 2013). A common

choice is a radial Gaussian function with scale matched to that of the galaxy (Massey et al., 2013).

In weak-lensing analyses, the reduced shear may be estimated by the ensemble average of the complex galaxy ellipticity, (1.15), or the polarisation, (1.16) (Schneider, 2006). It should be noted that the expectation value of the polarisation as defined in (1.16) is not an unbiased estimator of the reduced shear; in the weak lensing regime, the expectation value of $\boldsymbol{\chi}$ is biased with respect to the reduced shear by a factor of P_γ^{-1}, with $P_\gamma \approx 1.84$ the shear polarisability (Paulin-Henriksson et al., 2008; Schneider, 2006; see section 1.1.5). Then the size R^2 and 2 component ellipticity $\boldsymbol{\epsilon}$ and polarisation $\boldsymbol{\chi}$ can be estimated as (Schneider, 2006):

$$R^2 = Q_{11} + Q_{22}, \tag{3.2}$$

$$\chi_1 = \frac{Q_{11} - Q_{22}}{Q_{11} + Q_{22}}, \; \chi_2 = \frac{2Q_{12}}{Q_{11} + Q_{22}}, \tag{3.3}$$

$$\epsilon_1 = \frac{Q_{11} - Q_{22}}{Q_{11} + Q_{22} + 2\sqrt{Q_{11}Q_{22} - Q_{12}^2}}, \; \epsilon_2 = \frac{2Q_{12}}{Q_{11} + Q_{22} + 2\sqrt{Q_{11}Q_{22} - Q_{12}^2}}. \tag{3.4}$$

In this work, measurement biases on the polarisation $\boldsymbol{\chi}$ are considered.

For the case of unweighted, noise-free quadrupole moments, the size-squared and polarisation of an observed galaxy are given by (Paulin-Henriksson et al., 2008),

$$R^2_{\rm obs} = R^2_{\rm gal} + R^2_{\rm PSF}, \tag{3.5}$$

$$\boldsymbol{\chi}_{\rm obs} = \boldsymbol{\chi}_{\rm gal} + \frac{R^2_{\rm PSF}}{R^2_{\rm gal} + R^2_{\rm PSF}}(\boldsymbol{\chi}_{\rm PSF} - \boldsymbol{\chi}_{\rm gal}), \tag{3.6}$$

where $R^2_{\rm obs}, R^2_{\rm gal}$, and $R^2_{\rm PSF}$ are the observed and intrinsic squared RMS radius of the observed and intrinsic galaxy images and of the PSF, respectively, and $\boldsymbol{\chi}_{\rm obs}, \boldsymbol{\chi}_{\rm gal}, \boldsymbol{\chi}_{\rm PSF}$ are their ellipticities. Note that this neglects non-convolutive effects such as detector non-linearity (Plazas et al., 2016) or the brighter-fatter effect (Antilogus et al., 2014). Then, the intrinsic galaxy ellipticity is given by (Paulin-Henriksson et al., 2008),

$$\boldsymbol{\chi}_{\rm gal} = \frac{\boldsymbol{\chi}_{\rm obs} R^2_{\rm obs} - \boldsymbol{\chi}_{\rm PSF} R^2_{\rm PSF}}{R^2_{\rm obs} - R^2_{\rm PSF}}. \tag{3.7}$$

If the galaxy image is corrected for the PSF with some residual errors in the PSF size and ellipticity, $\delta(R^2_{\rm PSF})$ and $\boldsymbol{\delta\chi}_{\rm PSF}$, then the resulting biased estimate of the intrinsic ellipticity may be approximated with a first-order Taylor expansion (Paulin-Henriksson et al., 2008):

$$\begin{aligned}\widehat{\boldsymbol{\chi}}_{\rm gal} &\approx \boldsymbol{\chi}_{\rm gal} + \frac{\partial \boldsymbol{\chi}_{\rm gal}}{\partial\left(R^2_{\rm PSF}\right)}\delta\left(R^2_{\rm PSF}\right) + \frac{\partial \boldsymbol{\chi}_{\rm gal}}{\partial \boldsymbol{\chi}_{\rm PSF}}\boldsymbol{\delta\chi}_{\rm PSF} \\ &= \left(1 + \frac{\delta\left(R^2_{\rm PSF}\right)}{R^2_{\rm gal}}\right)\boldsymbol{\chi}_{\rm gal} - \left(\frac{R^2_{\rm PSF}}{R^2_{\rm gal}}\boldsymbol{\delta\chi}_{\rm PSF} + \frac{\delta\left(R^2_{\rm PSF}\right)}{R^2_{\rm gal}}\boldsymbol{\chi}_{\rm PSF}\right),\end{aligned} \tag{3.8}$$

from which we can identify multiplicative and additive bias terms.

The formalism of (3.5), (3.6), (3.7), and (3.8) is valid in the case of unweighted moments. However, for a space-based telescope such as *Euclid*, the PSF is diffraction-limited; this causes the unweighted moments (i.e. the moments (3.1) for which the weighting function is equal to unity) to become dominated by the wings of the surface brightness profile (Melchior et al., 2011). In this case, the bias model of (3.8) requires the inclusion of scalar correction factors to account for a weighting function in the definition of the moments (3.1) in order to prevent them from diverging (Massey et al., 2013). The resulting additive and multiplicative shear measurement biases are given by (Massey et al., 2013):

$$m = \frac{1}{P_R}\frac{\delta\left(R^2_{\rm PSF}\right)}{R^2_{\rm gal}}, \tag{3.9}$$

$$c = -\frac{1}{P_R P_\gamma P_\chi}\frac{R^2_{\rm PSF}}{R^2_{\rm gal}}\delta\chi_{\rm PSF} - \frac{1}{P_R P_\gamma}\frac{\delta\left(R^2_{\rm PSF}\right)}{R^2_{\rm gal}}\chi_{\rm PSF}, \tag{3.10}$$

where R^2, χ are now weighted moments, $P_\gamma \equiv \partial\chi_{\rm gal}/\partial\gamma$ is the shear polarisability, and the factors P_R and P_χ are scalar corrections to R^2 and χ respectively, which account for the use of weighted moments. Additionally, it is important to note that this formalism does not consider the biasing impact of any "non-convolutive" effects on the shear measurement, such as noise or model bias as described above, or other, non-convolutive instrumental effects. In effect, such additional sources of shear bias are considered to be decoupled from the shear bias arising due to PSF errors. From (3.9) and (3.10) it can be seen, in this approximation, that residual errors in the size of the PSF induce both multiplicative and additive biases in

the galaxy ellipticity measurement, while errors in the PSF ellipticity source only induce additive bias. These ellipticity measurement biases propagate to biases in the shear measurement when averaged over many galaxies.

The impact of such biases on angular power spectra may thence be calculated; for example, as discussed in chapter 2, a spatially-varying multiplicative bias is convolved with the shear C_ℓs via a mode-coupling matrix (Alonso et al., 2019; Cragg et al., 2022); and a spatially-varying additive bias results in an additive contribution to the power spectrum (Alonso et al., 2019). Constant m-bias just acts multiplicatively on the power spectrum, while constant c-bias has no effect (Kitching et al., 2019). Biased shear power spectra may then be propagated into biases in cosmological parameters by using a Fisher-matrix analysis, as in e.g. Euclid Collaboration: Paykari et al., 2020 and Cragg et al., 2022, by estimating the bias in posterior parameter estimates using Markov-chain Monte Carlo (MCMC)-based methods as in e.g. Cardone et al., 2014. Such analyses allow requirements to be placed on the acceptable size of additive and multiplicative biases in the shear measurement, which can be used to place requirements on the knowledge of and correction for specific systematics such as PSF errors, given some fraction of the error budget that is allocated to each systematic.

Massey et al., 2013 set requirements on the multipole-averaged additive and multiplicative biases on the shear angular power spectra for a Euclid-like shear survey configuration. This was conducted by propagating the corresponding biased tomographic C_ℓs into biases in the dark energy equation of state parameters w, w_a using a Fisher matrix formalism, marginalising over the rest of the cosmological parameter space and requiring that the bias in w, w_a be less than 0.31% of the 1-σ uncertainty on each respectively (in order to correspond with a 95% overlap with the unbiased PDF (Massey et al., 2013)), and assigning half the error budget to each of additive and multiplicative bias. The resulting requirements on the bias in the C_ℓs correspond to a requirement on the error of the additive shear bias of $\sigma[|c|] < 1.5 \times 10^{-4}$ and on the mean of the multiplicative shear bias of $\langle m \rangle < 2 \times 10^{-3}$ (Cropper et al., 2013). Using the formalism of (3.9), (3.10), Massey

et al., 2013 place requirements on the size and ellipticity of the PSF, and on the knowledge of these quantities for a space-based shear survey such as the EWS.

However, the analysis of Massey et al., 2013 is limited in a number of ways. Firstly, the scalar correction factors used to account for the use of weighted moments in the propagation of PSF error to shear bias in Massey et al., 2013 are a simple parametrisation which may not realistically reflect the true relationship between errors in the PSF and the resulting biases in the shear measurement. Furthermore, the allocation of error budget to knowledge of the PSF in this framework ultimately stems from requirements on the mean additive and multiplicative biases in the power spectra defined by Paulin-Henriksson et al., 2008, and therefore does not capture the full effect of the likely more complex form of the bias in the power-spectrum and degeneracies with cosmological parameters, and completely ignores the convolutive effect on the angular power spectra of spatially-varying shear biases. Additionally, as is relevant for forthcoming surveys such as the EWS, which may explore cosmological probes beyond 2-point statistics (Euclid Collaboration: Ajani et al., 2023), the impact of non-Gaussian position-dependence of the shear bias, or dependence on galaxy properties, is not incorporated in the approach of Massey et al., 2013. Moreover, it does not consider the joint impact of multiple systematics, which may be correlated or degenerate. Such systematics include sources of PSF error that may depend on galaxy properties, such as the PSF error arising due to imperfect galaxy SED information (see chapter 4), and photometric redshift errors (Euclid Collaboration: Desprez et al., 2020; Ma et al., 2006), or astrophysical systematics such as intrinsic alignments (Crittenden et al., 2002; Krause et al., 2015).

Motivation to Forecast Shear Bias at the Catalogue Level for the *Euclid* Wide Survey

The limitations of the analysis of Massey et al., 2013 motivate a more realistic forecast of the impact of PSF errors on cosmology. This is of particular interest for forthcoming weak lensing surveys such as the *Euclid* Wide Survey (EWS, Euclid Collaboration: Mellier et al., 2024; Euclid Collaboration: Scaramella et al., 2022)

and the Vera C. Rubin Observatory's Legacy Survey of Space and Time (LSST, Phillips Longley, 2021), due to the high number statistics resulting from large survey footprints and deep imaging; these surveys will require unprecedented control of systematics in order to obtain unbiased cosmological constraints. Robust performance verification, including the forecasting of the impact of systematic effects on the cosmological analyses of these surveys, is therefore an important task (Albrecht et al., 2006), in order to allow the identification of systematics that are likely to be important, and the definition of requirements on the accuracy of mitigation of such systematics.

It is desirable that such a forecast should include a calculation of the shear measurement biases induced by PSF error which does not rely on the potentially simplistic scalar-correction scheme of (3.9), (3.10). Additionally, the impact of PSF errors should be estimated *ab initio* at the level of individual galaxy shape measurements, i.e. at the catalogue-level, rather than the power spectrum level; this will allow a more realistic and versatile propagation to cosmology. In particular, this will allow the propagation of multiple systematics which may be correlated, such as shear measurement biases and photometric redshift errors, in a more realistic way. This will allow the evaluation of the impact of systematics on observables beyond 2-point statistics, such as higher-order statistics (Euclid Collaboration: Ajani et al., 2023) and mass mapping (Euclid Collaboration: Pires et al., 2020), which may be of interest for the rich data sets that forthcoming surveys such as the EWS will provide. Such an approach is also useful for the purposes of testing and validation of analysis codes in the presence of realistic systematics, such as methods to detect or mitigate systematics from the data (Kitching et al., 2021; van Uitert and Schneider, 2016) or cosmological inference pipelines (Euclid Collaboration: Paykari et al., 2020). A catalogue-level propagation of the impact of PSF errors on cosmological parameter estimation was conducted by Euclid Collaboration: Paykari et al., 2020, based on shear biases calculated from weighted moments. The work in this chapter is a development on that work, with more complexity in the PSF error models considered, a more accurate shear bias calculation, and

estimating shear biases for galaxies in an updated mock catalogue.

In this chapter, shear measurement biases arising due to PSF errors are estimated for individual galaxies in the Euclid Flagship 2 mock catalogue (Euclid Collaboration: Castander et al., 2024). If the same is done for other systematics, such as photometric redshift errors or intrinsic alignments, then the joint effect of such systematics may be propagated into cosmology in a full forecast. This work has been undertaken within the third Science Performance Verification exercise of the Euclid consortium (SPV3), which is currently undertaking the task of conducting such a catalogue-level forecast of the impact of expected realistic systematics into the cosmological inference pipeline for the EWS, in order to test the performance of the planned analysis. The development of a pipeline to forecast catalogue-level shear biases arising due to PSF errors is the focus of this chapter.

PSF Requirements

In addition to the total, high-level requirements on the bias on the shear measurement, a specific amount of shear measurement error budget is allocated to the allowed amount of error in the VIS PSF, that may then propagate to the shear measurement. These requirements are placed on the PSF metrics R^2 and ellipticity $\boldsymbol{\chi}$, defined in terms of weighted second moments, as in equations (3.5), (3.6) respectively.

The breakdown of the shear measurement error budget in terms of requirements on the PSF metrics originating from different contributions to the PSF error, for a general space-based stage-IV WL setting, is established in Cropper et al., 2013, and forms the basis for the calibration of the VIS PSF modelling and shear measurement. The EWS requirements on the uncertainty in the VIS PSF model are as follows (Euclid Collaboration: Mellier et al., 2024):

$$\frac{\delta R^2_{\rm PSF}}{R^2_{\rm PSF}} < 1 \times 10^{-3}, \tag{3.11}$$

$$\sigma[\boldsymbol{\chi}_{\rm PSF}] < 2 \times 10^{-4}. \tag{3.12}$$

Cropper et al., 2013 provides approximate formula relating the requirements on the PSF metrics to the corresponding requirements on shear biases, parametrised

by numerical weightings. Applying these relations, the requirements on the shear bias arising due to PSF modelling errors become:

$$\langle m_{\rm req}^{\rm model} \rangle < 3 \times 10^{-4}, \tag{3.13}$$

$$\sigma[|c_{\rm req}^{\rm model}|] < 6.3 \times 10^{-5}. \tag{3.14}$$

Additionally, a specific amount of the PSF error budget is allocated to the transfer of the PSF model, fit to observations of stars, to target galaxies. This *propagate-to-object* (PTO) budget allocated to the PSF for the EWS is as follows (Cropper et al., 2013; Euclid Consortium: Lorenzo Alvarez, 2014):

$$\frac{\delta R^2_{\rm obs}}{R^2_{\rm obs}} < 5 \times 10^{-4}, \tag{3.15}$$

$$\delta \boldsymbol{\chi}_{\rm obs} < 5 \times 10^{-5}, \tag{3.16}$$

for biases in the observed size-squared and ellipticity of galaxies, respectively, owing to the bias introduced due to lack of knowledge of the PSF. As is discussed in chapter 4, a significant use-case of the shear bias estimation methodology developed in this chapter consists of the estimation of shear biases arising due to imperfect knowledge of galaxy SEDs used in the transfer of the PSF to target galaxies. Therefore, the requirements of (3.15) and (3.16) will be used to benchmark the performance of the shear bias estimation discussed here. It should be noted that galaxy SED errors comprise a substantial source of error in the propagation of the PSF model to target galaxies; therefore, residual errors in the shear bias estimates need to be sub-dominant with respect to the PTO requirements, rather than negligible *per se*, since errors in the SED-error-sourced shear bias estimates which are sub-dominant with respect to the PTO requirement will by definition not have a significant impact on the EWS cosmology analysis.

In order to convert these requirements to approximate corresponding requirements on additive and multiplicative shear measurement biases, the formalism of (3.9) and (3.10) is adopted. Defining the propagate-to-object requirement on the PSF size $R^2_{\rm req,PTO}$ from (3.15), we have that $R^2_{\rm req,PTO} \equiv \delta\big(R^2_{\rm obs}\big)/R^2_{\rm obs}$. Then, if we define a corresponding moments-based requirement on the m-bias:

$$m_{\rm req}^{\rm PTO} = (1/P_R)\delta\big(R^2_{\rm PSF}\big)/R^2_{\rm gal}, \tag{3.17}$$

as per equation (3.9), and make use of equation (3.5), converting errors in $R^2_{\rm obs}$ to errors in $R^2_{\rm PSF}$ using the chain rule, and evaluate the ensemble average (since the performance of the shear bias calculation for an ensemble of galaxies is of interest), we obtain:

$$\langle m^{\rm PTO}_{\rm req}\rangle = \frac{R^2_{\rm req,PTO}}{P_R}\Big\langle 1+\frac{R^2_{\rm PSF}}{R^2_{\rm gal}}\Big\rangle. \tag{3.18}$$

Similarly, given the propagate-to-object requirement $\delta\boldsymbol{\chi}_{\rm obs} \equiv \boldsymbol{\chi}^{\rm PTO}_{\rm req}$, then we can define a moments-based requirement on the c-bias $c^{\rm PTO}_{\rm req}$ by comparing with equation (3.10). Then, making use of (3.6) to convert errors in $\boldsymbol{\chi}_{\rm obs}$ to errors in $\boldsymbol{\chi}_{\rm PSF}$ and $R^2_{\rm PSF}$, neglecting a term in $R^2_{\rm PSF}/R^4_{\rm obs}$, and substituting our $m^{\rm PTO}_{\rm req}$, we obtain:

$$c^{\rm PTO}_{\rm req} = -\frac{1}{P_\gamma P_{\boldsymbol{\chi}}}\Big(\frac{1}{P_R}\boldsymbol{\chi}^{\rm PTO}_{\rm req}\Big(1+\frac{R^2_{\rm PSF}}{R^2_{\rm gal}}\Big) - m^{\rm PTO}_{\rm req}\boldsymbol{\chi}_{\rm PSF}\Big) - \frac{1}{P_\gamma}m^{\rm PTO}_{\rm req}\boldsymbol{\chi}_{\rm PSF}. \tag{3.19}$$

Noting that Massey et al., 2013 find that values of $P_{\boldsymbol{\chi}} \sim 1$ are typical, terms in $m^{\rm PTO}_{\rm req}$ approximately cancel. Taking the ensemble average and taking the absolute value of the requirement, we find

$$\langle c^{\rm PTO}_{\rm req}\rangle = \frac{1}{P_\gamma P_{\boldsymbol{\chi}} P_R}\boldsymbol{\chi}^{\rm PTO}_{\rm req}\Big\langle 1+\frac{R^2_{\rm PSF}}{R^2_{\rm gal}}\Big\rangle. \tag{3.20}$$

Since the PSF-galaxy size-squared ratio is likely to be less than unity for most galaxies, the term in angle brackets in (3.19) and (3.20) will be of order unity. Hence we can approximate, in the most conservative case, $\langle m^{\rm PTO}_{\rm req}\rangle \approx R^2_{\rm req,PTO}/P_R$, and $\langle c^{\rm PTO}_{\rm req}\rangle \approx \boldsymbol{\chi}^{\rm PTO}_{\rm req}/P_\gamma P_{\boldsymbol{\chi}} P_R$. Therefore, through this and subsequent chapters, these approximations are taken as the (approximate) PTO component of the budget on the shear measurement bias requirements. As stated in section 1.1.5, $P_\gamma \approx 1.84$ (Massey et al., 2013); we also take $P_R \approx 2, P_{\boldsymbol{\chi}} \approx 1$ as in Massey et al., 2013. Based on this, we obtain for the PTO requirements:

$$m^{\rm PTO}_{\rm req} < 2.5\times10^{-4}, \tag{3.21}$$

$$c^{\rm PTO}_{\rm req} < 1.4\times10^{-5}. \tag{3.22}$$

Because these are more stringent than the PSF modelling requirements described above, they are used to validate the performance of the methodology developed in this chapter, under the strictest relevant scenario.

3.1.3 Sources of PSF error for the *Euclid* Wide Survey

There are many sources of PSF error that bias knowledge of the PSF. These are particularly problematic for cosmology if they spatially vary on angular scales similar to those on which the shear signal is coherent, such that they introduce spurious correlations into the shear signal, or are correlated with physical properties of galaxies or with other systematics. For example, the PSF has spatial (across the field of view), temporal (e.g. between exposures), and spectral variations that may be degenerate with the cosmological signal. For a description of the PSF modelling, measurement, and calibration for the EWS, see section 1.2.4. PSF error can be introduced at various stages of the PSF modelling, measurement and correction procedure. For Euclid, the PSF model is highly complex, taking into account many physical effects determining the optical state of the telescope (see section 1.2.4). Imperfect knowledge of such effects leads to errors in the PSF model. Furthermore, errors in the assumed PSF can be introduced in the interpolation of the PSF model parameters to the FoV-position and spectral energy distribution (SED) of each measured galaxy.

In this work, two effects that lead to PSF error for the EWS are considered, and shear biases that are expected to arise resulting from realistic mock forms of these sources of PSF error are forecast. Firstly, the PSF error that arises due to the imperfect SED information for target galaxies is considered. Since the calculation of the full chromatic PSF involves an integral over the monochromatic PSFs, weighted by the target SED (1.22) (Euclid Collaboration: Mellier et al., 2024), SED information is required to reconstruct the PSF for target galaxies. However, for the EWS, the galaxy SED information is estimated from noisy broad-band ground-based photometry. These noisy photometric SEDs result in bias in the assumed PSF shape (size and ellipticity), and hence shear bias, because the transformation from the SED space to the PSF profile space is nonlinear. Furthermore, as the Euclid VIS instrument has a wide passband, this is likely to be a significant contributor to the PSF-sourced shear bias for the EWS. Since SED errors correspond to errors in the assumed colours of galaxies, and considering the wavelength-dependence of the

diffraction limit of an optical system, it may be expected that SED errors primarily impact the size of the assumed PSF, and comparing to (3.9) and (3.10), that this may induce multiplicative and additive shear biases. This shear bias may also be correlated with other systematics that depend on the available spectral information of target galaxies, such as photometric redshift errors, which may increase its impact on cosmological inference. Since this effect enters the PSF estimation at the stage of the propagation of the PSF model, fit from observations of stars, to target galaxies, its maximum permitted contribution to the EWS shear measurement error budget is set by the PTO requirements listed in section 3.1.2 (see (3.15) and (3.16)).

Secondly, the error in the PSF model that arises due to thermal variations in the spacecraft is considered. As the spacecraft makes observations at different pointings, it has varying orientation with respect to the Sun vector. This results in thermal variations in the spacecraft that impact the structure of the optical system as a function of pointing, which result in PSF variations between pointings. While such variations can in principle be calibrated from measurements, the impact of neglecting this effect is investigated, to facilitate the aim of placing requirements on the cadence of calibration of the PSF variations. Owing to the potentially large angular scale of variation of the PSF across the survey footprint due to thermal variations, this effect may result in spurious shear bias correlations that may be significantly degenerate with the cosmological signal from the 2-point statistics. This effect impacts the PSF model, rather than the propagation of the PSF model to target galaxies as is the case for the galaxy-SED-sourced PSF errors, and therefore its contribution to the EWS shear measurement error budget is set by the PSF modelling requirements listed in section 3.1.2.

In this work, in order to evaluate the impact that these sources of PSF are likely to have on the cosmological analysis of the EWS, a forward-modelling approach is adopted. While the ideal case would consist of a full end-to-end propagation beginning from pixel-level simulations, a catalogue-level forecast is significantly more computationally tractable, while maintaining a high degree of physical realism compared with previous forecasts that started at the level

of summary statistics, e.g. Massey et al., 2013. Hence, in this work, the shear biases arising due to the above-described sources of PSF error are estimated for galaxies in the *Euclid* Flagship 2 mock catalogue (Euclid Collaboration: Castander et al., 2024). More details about the calculation of the PSF errors due to the two effects and the subsequent propagation to cosmological inference are given in chapter 4 and chapter 5 for the galaxy SED errors and thermal variations, respectively. In this chapter, the methodology used to forecast the shear bias due to general PSF errors at the catalogue-level for the EWS is described, including the calculation of shear bias arising due to some given PSF error (section 3.2), and the method used to estimate shear biases for mock galaxies in the *Euclid* Flagship 2 catalogue (section 3.3).

3.1.4 Outline of the shear bias calculation method

In this section, the methodology used to calculate the shear bias arising from error in the assumed PSF for the EWS, and the estimation of such shear biases at the catalogue level for the Euclid Flagship 2 mock catalogue (Euclid Collaboration: Castander et al., 2024) are discussed. Truth- and error-channel PSFs are generated using the *Euclid* OU-SHE (shear measurement operational unit) PSFTOOLKIT PSF modelling software (Euclid Consortium: Miller et al., 2020a, Duncan et al. *in prep.*) with the sources of systematic error in question (e.g. high-resolution mock galaxy SEDs vs. noisy photometric galaxy SEDs, see chapter 4) given as input. Next, the additive and multiplicative shear biases resulting from the PSF error are calculated. Note that, as described in section 3.1.2, the formalism of (3.9), (3.10) includes empirical scalar corrections to account for the use of weighted moments, which is necessary in the case of a diffraction-limited space-based telescope such as *Euclid*. The accuracy of such a correction scheme is not verified, and so instead, the shear bias resulting from some PSF error is calculated numerically, in order to obtain more accurate results. A calculation based on the LENSFIT shear-measurement algorithm (Miller et al., 2007, 2013), and adapted for this

purpose by Miller et al. (*in prep.*); Euclid Consortium: Miller et al., 2020b, is employed, and described in section 3.2.2.

It is not computationally feasible to explicitly calculate the shear biases for every galaxy in the mock catalogue. Therefore, a sub-sample of galaxies in the mock catalogue is defined, and shear biases for these galaxies are calculated. Galaxies in the sub-sample are then matched to similar galaxies in the mock based on their physical properties (colour indices, observed redshift, VIS magnitude), and galaxies in the mock are assigned the shear bias values corresponding to their matched galaxy in the sub-sample. This sub-sample of galaxies is sampled and matched to galaxies in the rest of the catalogue within cells in a grid of galaxy colour, redshift, and magnitude in the broad optical passband of the VIS instrument used for the EWS shear measurement (Euclid Collaboration: Cropper et al., 2024; Euclid Collaboration: Mellier et al., 2024).

The shear bias calculation is done on a grid of FoV positions, and for a number of values of galaxy size and ellipticity modulus. Once a galaxy in the catalogue has been matched to a neighbour in the basis sub-sample described above, the corresponding shear bias values are first interpolated over the 2-dimensional grid of galaxy size and ellipticity to the values of the galaxy in question at each FoV position, and then interpolated over the FoV grid to the position of the galaxy, in order to obtain the final estimates of the additive and multiplicative shear biases for the galaxy.

In section 3.2.1, the shear bias calculation is described, including the PSF generation using the *Euclid* PSFTOOLKIT software (Duncan et al., *in prep.*, Euclid Consortium: Miller et al., 2020a), the numerical maximum-likelihood calculation used to determine the shear bias (Miller et al. *in prep.*; Euclid Consortium: Miller et al., 2020b), and testing and optimisation of the code. In section 3.3, the method used to efficiently sample a basis set of galaxies from the catalogue, the matching scheme, and the interpolation over galaxy shape parameters and FoV position is described. The method is summarised in section 3.3.1. Chapter 4 and chapter 5 describe applications of this method in the case of imperfect knowledge of galaxy

SEDs and thermal variations in the spacecraft, respectively.

A flow chart summarising the shear bias estimation methodology described in section 3.2 is shown in fig. 3.1.

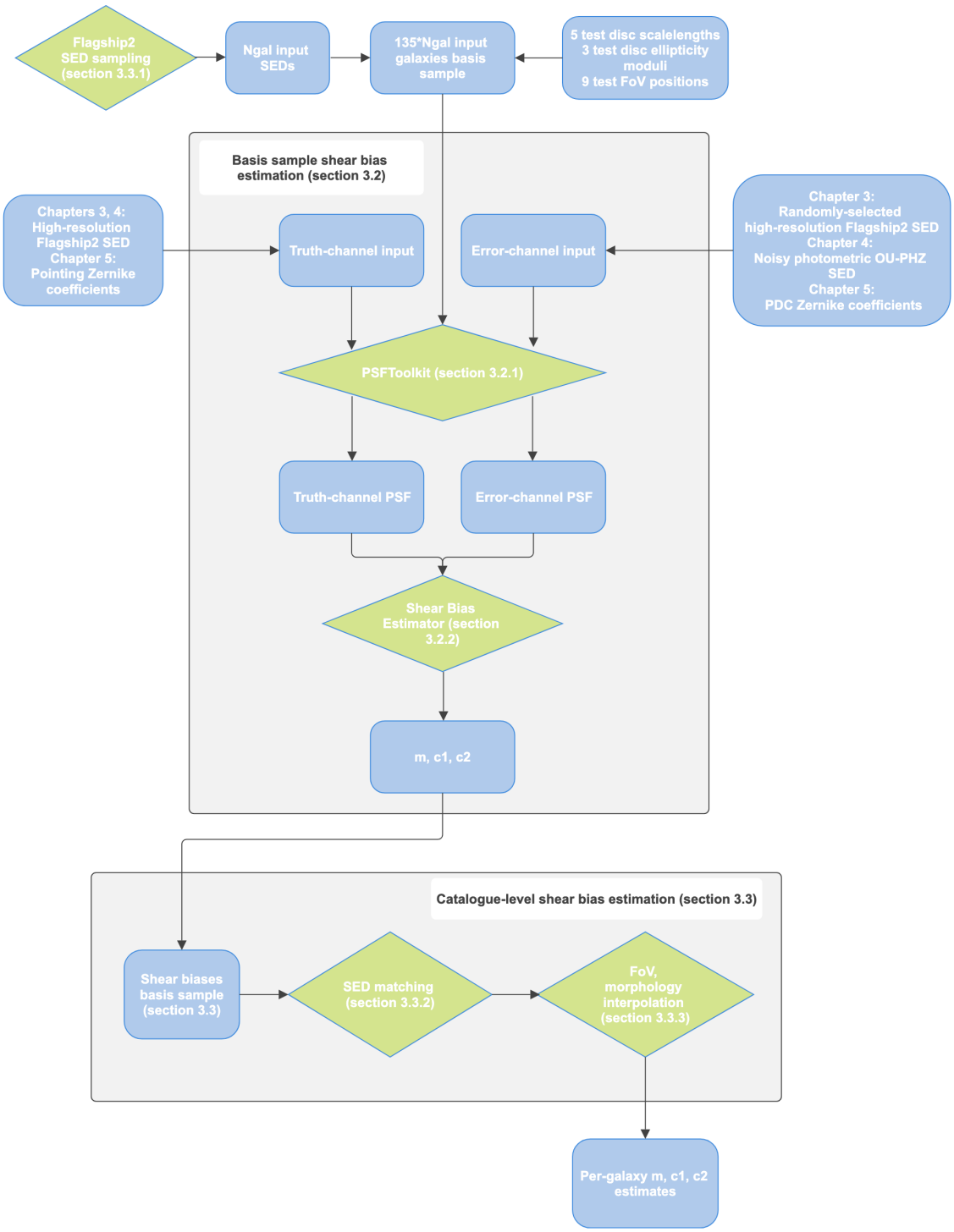


Figure 3.1: A flow chart outlining the shear bias calculation methodology described in section 3.2. See sections listed in flow chart elements for a description of the stages outlined.

3.2 Shear Bias Estimation

3.2.1 Description of PSF generation using the *Euclid* OU-SHE PSFTOOLKIT software

In the shear measurement for the EWS, the PSF is parametrically modelled using the *Euclid* PSFTOOLKIT software. For a description of the modelling, measurement, and calibration of the PSF for the EWS, see section 1.2.4.

In order to generate the broadband PSF for a particular target, the PSFTOOLKIT takes as input a telescope state object, which consists of a parametrisation of the telescope model, the target SED, and the FoV position of the target. In the present approach, "truth"- and "error"-channel configurations for the PSF generation inputs are considered; the PSFTOOLKIT is then used to generate corresponding truth- and error-channel PSFs, which are passed onto the shear bias calculation pipeline described in this chapter. The PSF is generated in a square postage-stamp array of some given dimensions, with some given integer oversampling factor with respect to the detector pixel size[1], in order to reduce the effect of aliasing in the generated PSF and galaxy images (see section 3.2.3). In this work, the impact of noisy photometric galaxy SEDs on the broadband PSF calculation for target galaxies is considered; moreover, the PSF model error arising due to time-dependent thermal variations in the spacecraft is considered.

For the propagation of SED errors into PSF errors, the truth-channel input SEDs are taken to be the high-spectral-resolution mock SEDs from the *Euclid* Flagship 2 mock catalogue (Euclid Collaboration: Castander et al., 2024). These consist of a linear combination of two template spectra, each with a template source-galaxy extinction curve applied, and a redshift. Corresponding mock noisy medium-band photometric SEDs are taken for the error-channel SEDs, generated from the corresponding truth-channel high resolution SEDs provided by the Euclid consortium photometric redshift operational unit (OU-PHZ). These consist of a noisy mock realisation of a broad-band observation of each truth-channel

[1]The default oversampling factor is $3\times$, with PSFs generated on an 480×480 oversampled-pixel array; given the native VIS pixel scale of $0.1''$, this corresponds to a default postage-stamp size of $16''\times16''$.

SED, interpolated to medium-band fluxes using a random-forest algorithm (F. Tarsitano and W. Hartley, *priv. comm.*). For each truth-channel SED, 10 noisy realisations of the corresponding error-channel SED are considered. The truth- and error-channel PSFs are calculated, corresponding to a basis set of galaxies sampled from the Flagship 2 mock catalogue with corresponding truth- and error-channel SEDs. To include the effect of FoV variation of the PSF, PSFs are generated on a 3×3 grid on the FoV, assuming the as-built telescope state (for more information on the sampling of galaxies from the Flagship 2 mock see section 3.3; for more information on the propagation of SED errors into shear bias and hence cosmology, see chapter 4).

For the propagation of thermal variations in the spacecraft into PSF errors, the WFE in the telescope state arising due to thermal variations in the spacecraft is considered. These thermal variations result in mechanical distortions in the optical system e.g. offsets of the optical path lengths between telescope components. These thermal variations arise due to differing orientations of the spacecraft with respect to the Sun vector for differing telescope pointings, resulting in an inhomogenous pattern of WFE across the survey footprint. The WFE as parametrised by Zernike coefficients is measured in the phase-diversity calibration conducted at the start of the survey and from observations of stars throughout the survey, but such calibration will be conducted with some finite cadence that will result in imperfect knowledge of the time-variation of the WFE. The worst-case scenario in which the time variation of the WFE is calibrated only at the start of the survey is considered. The error-channel model is therefore taken as the telescope state with Zernike coefficients equal to those measured at the start of the survey, with some defocus applied; for the truth-channel model, a prediction of the values of the Zernike coefficients at each pointing due to the thermal variations is considered, produced by Euclid Consortium: Miller et al., 2022; Ferrero et al., 2020. These truth- and error-channel configurations of the telescope model are passed into the PSF generation, for a sample of mock galaxies (including galaxy shapes and high-spectral resolution SEDs), on a 5×5 grid on the FoV (see chapter 5).

For more details on the estimation of Zernike mode variations as a function of pointing, the mock galaxy sampling, and of the propagation of this effect into shear bias and cosmology, see chapter 5.

Given the sets of truth- and error-channel PSFs generated for the various configurations of truth- and error-channel PSF inputs, the additive and multiplicative shear measurement biases corresponding to these PSF errors are then calculated.

3.2.2 Description of the Shear Bias Calculation

As discussed in section 3.1.2, the propagation of PSF errors from weighted moments described in Massey et al., 2013 requires the application of scalar corrections to the addditive and multiplicative shear biases to account for this, as in equations (3.9) and (3.10). However, such an approximation may not capture the full dependence on shear measurement method or choice of weighting function, which arises due to the mixing with higher-order moments that is introduced when weighted moments are calculated. This may result in inaccurate shear bias estimates. Indeed, Zhang et al., 2021 and Zhang et al., 2022 estimated the impact of moments up to 6th order on the additive and multiplicative bias due to PSF errors for HSC year 3 data, and found that they resulted in a $\sim 0.3\sigma$ bias on parameters S_8 and Ω_m, while a propagation based on second moments alone only accounted for a $\sim 0.1\sigma$ bias. This effect would likely be more significant for Euclid due to its expected higher constraining power. In this work, a numerical method due to Miller et al. (*in prep.*); Euclid Consortium: Miller et al., 2020b is therefore employed to calculate the shear bias due to PSF errors, rather than an approximate semi-analytic method based on weighted moments such as that of Massey et al., 2013.

The method that is used to calculate the shear bias due to PSF error is a maximum-likelihood estimator developed by Miller et al. (*in prep.*); Euclid Consortium: Miller et al., 2020b. In this scheme, the error-channel PSF is convolved with a simple parametric input galaxy surface brightness profile. The parameters of the surface-brightness model, convolved with the truth-channel PSF, are jointly fit, with the 2 ellipticity components being the parameters of interest. The resulting

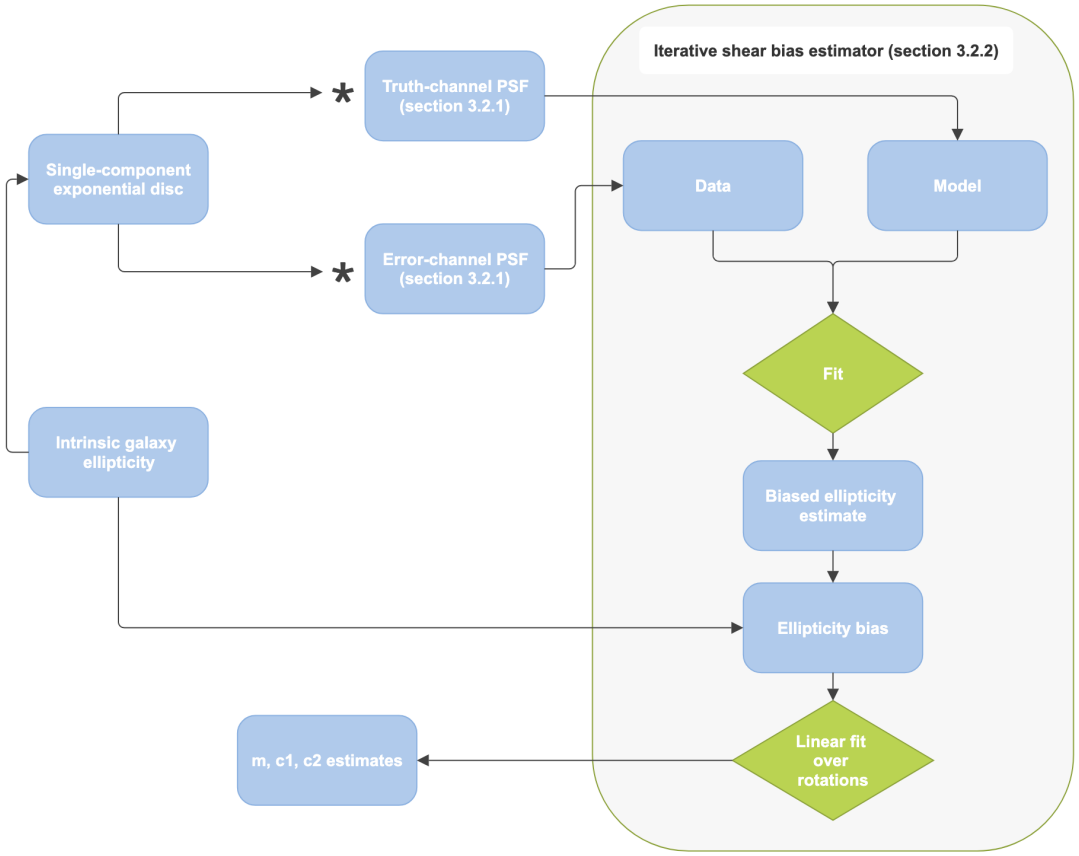


Figure 3.2: A flow chart outlining the shear bias calculation of Miller at al. *in prep.*, Euclid Consortium: Miller et al., 2020b. See the sections listed in the flow chart elements for a description of the stages outlined. The $*$ operator denotes convolution.

residual between the true and fitted ellipticity values is thus obtained, and a linear fit of the bias in the 2 ellipticity components as a function of input galaxy ellipticity is conducted, to estimate the resulting additive and multiplicative ellipticity measurement biases. A flow chart outlining the shear bias calculation described in this section is shown in fig. 3.2.

The shear bias calculation described proceeds as follows. A single-component exponential disc surface brightness profile is assumed for the test galaxy images, parametrised by a scalelength and ellipticity modulus. PSFs are generated by the PSFTOOLKIT in a postage-stamp array with elements representing oversampled pixels, with dimension $N \times N$. A pixel oversampling factor of 3 or 5 is used, depending on the test galaxy scalelength and the postage stamp size, set by the values of N, is varied with the galaxy scalelength for the purpose of code

optimisation; for more detail and justification, see section 3.2.3. To increase the speed of the calculation, the PSF image is fast-Fourier-transformed in order to carry out the convolution with the galaxy image, because according to the convolution theorem (McGillem and Cooper, 1984), in the Fourier domain (FD) the convolution becomes a multiplication. The exponential-disc galaxy image is generated on an oversampled postage-stamp in the FD, because the Fourier transform (FT) of the exponential disc is analytic (Rowe et al., 2015). The FD exponential-disc model, convolved with the truth-channel PSF, is then fit to the error-PSF-convolved Fourier-domain galaxy image, applying an iterative Newton-Raphson maximum-likelihood estimator to jointly fit the image centroid, scalelength-squared, and ellipticity; the 2 ellipticity components being the parameters of interest. The truth-PSF-convolved model is then fit to the error-PSF-convolved images, and the residuals between the true and fit model parameter values are calculated to obtain the bias in the model parameters arising due to convolution with the error-channel PSF, rather than the truth-channel PSF.

Given some set of parameters $\boldsymbol{q}$ (in the present case, the galaxy scalelength-squared r_s^2, ellipticity χ_1, χ_2 and centroid offset $\Delta x, \Delta y$) with some log-likelihood $\log \mathcal{L}(\boldsymbol{q})$, one aims to find the $\boldsymbol{q}$ which maximises the log-likelihood, such that $\nabla \log \mathcal{L} = 0$. The maximum-likelihood estimate $\hat{\boldsymbol{q}}$ may be found by iteratively taking Newton-like steps, solving:

$$\mathsf{H}(\boldsymbol{q}_n)\delta\boldsymbol{q}_n = -\nabla \log \mathcal{L}(\boldsymbol{q}_n), \tag{3.23}$$

for the step $\delta\boldsymbol{q_n}$, with H the Hessian, i.e. the matrix of second derivatives of $\log \mathcal{L}$ with respect to $\boldsymbol{q}$. In this scheme, the values of $\boldsymbol{q}$ are optimised such that $\nabla \log \mathcal{L} = 0$, which will be satisfied when $\delta\boldsymbol{q} = 0$. Starting with an initial guess $\boldsymbol{q}_n$, (3.23) is iteratively solved for the step $\delta\boldsymbol{q}_n = \boldsymbol{q}_{n+1} - \boldsymbol{q}_n$; $\boldsymbol{q}_{n+1}$ is then supplied as the subsequent guess, and the process is iterated until the magnitude of the step size $\delta\boldsymbol{q}_n$ converges to sufficiently close to 0 (i.e. up to some tolerance).

If the covariance is model-independent and a Gaussian likelihood is assumed for the error-PSF-convolved FD image $\boldsymbol{D}$ (described by model $\boldsymbol{M}(\boldsymbol{q})$), then the

gradient of the log-likelihood with respect to parameter q_m is (Euclid Consortium: Miller et al., 2020b):

$$(\nabla \log \mathcal{L})_m = -\frac{\partial \boldsymbol{M}^\dagger}{\partial q_m} \mathsf{C}^{-1} (\boldsymbol{M} - \boldsymbol{D}), \tag{3.24}$$

where † denotes Hermitian conjugation, and the Hessian of $\boldsymbol{M}(\boldsymbol{q})$ is approximated as the Fisher matrix F:

$$\mathsf{H}_{mn} \approx -\frac{\partial \boldsymbol{M}^\dagger}{\partial q_m} \mathsf{C}^{-1} \frac{\partial \boldsymbol{M}}{\partial q_n} = \mathsf{F}_{mn}. \tag{3.25}$$

In this work, images with zero pixel noise are considered, in order to isolate the impact of shear bias due to PSF errors; hence uncorrelated, constant-variance noise is assumed and C is set to the identity matrix. When calculating equations (3.24) and (3.25), the PSF-convolved model $\boldsymbol{M}$ by multiplying the exponential disc[2] and truth-channel PSF in the FD, for computational efficiency.

To solve (3.23), the truth-PSF-convolved galaxy model $\boldsymbol{M}$ and its first derivatives are initialised with the scalelength and ellipticity of the input surface brightness profile, with an initial guess of zero centroid offset. The resulting $\boldsymbol{M}$, together with the error-PSF-convolved $\boldsymbol{D}$, are used to calculate the gradient of the log-likelihood (3.24) and Fisher matrix (3.25), and (3.23) is solved for the step $\delta \boldsymbol{q}_n$. The step is added to the current iterate and the calculation is iterated until convergence is reached. The residuals between the true and fit ellipticity components are calculated. This is repeated for 4 galaxy position angles[3], and a least-squares linear fit of the ellipticity component residuals as a function of the true ellipticity components is carried out, to obtain multiplicative and additive biases in the polarisation $\boldsymbol{\chi}$. These are then converted to estimates for multiplicative and additive shear measurement biases by dividing by a factor of the shear polarisability P_γ.

The accuracy of the shear bias calculation described in this section is validated in Miller et al. (*in prep.*), by comparing the shear bias estimates with *lens*`fit`

[2]The Fouerier transform of the exponential disc is analytic (Rowe et al., 2015).

[3]This is done to reduce the shape noise contribution; such shape noise cancellation is also done in shear measurement algorithms, e.g. Massey et al., 2007.

measurements of the shear bias from simulated images. Results of these validation tests will be presented in forthcoming work.

For a given pair of truth- and error-channel PSFs, the resulting m, c-biases are calculated for a range of input brightness-profile scalelengths and ellipticity moduli. Shear biases are calculated for 5 values of galaxy major axis sampled logarithmically in the range $r_s = [0.1'', 0.5'']$ (see section 3.3.3); the typical scalelength at $i \simeq 24.5$, the approximate limiting magnitude of the EWS (Euclid Collaboration: Martinet et al., 2019; Euclid Collaboration: Racca et al., 2016) is expected to be $\simeq 0.3''$ (Simard et al., 2002). Three values of ellipticity modulus $|\chi| = [0.1, 0.3, 0.5]$ are considered. A PSF postage-stamp size is used, which is chosen to vary with galaxy major axis, and use a pixel oversampling factor of 3 or 5, depending on the input galaxy scalelength, corresponding to an oversampled pixel scale of $0.033'', 0.02''$ respectively (see section 3.2.3).

3.2.3 Optimisation of PSF generation for shear bias calculation

PSFs are generated in "postage-stamp" arrays with a finite size and pixel scale in the Fourier domain (FD). The Euclid VIS detector is undersampled with respect to the Nyquist sampling frequency of the PSF, i.e. the spatial sampling frequency (the reciprocal of the pixel scale) of the detector is less than twice that of the highest spatial-frequency structure in the PSF (Euclid Collaboration: Mellier et al., 2024; Euclid Consortium: Miller et al., 2020a). This undersampling results in aliasing i.e. mode-mixing between sampled and unsampled frequencies, in the generated PSF and PSF-convolved images. In order to mitigate this, PSFs are generated with a higher spatial sampling frequency than the detector (and FD galaxy images with the corresponding FD sampling frequency), i.e. they are oversampled, with an oversampled pixel scale that is an integer factor of the native VIS pixel scale (or the Fourier transform (FT) for the FD galaxy images). However, this oversampling substantially increases the computational time required to generate PSFs and estimate shear biases resulting from PSF errors, and as a result it is necessary to find a balance between acceptably low computational

cost, and acceptably small aliasing errors, by optimising the oversampling factor (and postage-stamp array size).

For the EWS, an oversampling factor of 3 is sufficient to Nyquist-sample the PSF (Kannawadi et al., 2021), which is band-limited (i.e. the support of its FT is bounded). However, aliasing is introduced due to the finite size of the postage-stamp FD PSF and galaxy image arrays, due to the loss of high-frequency Fourier modes resulting from the FD crop. Additionally, the crop in the image domain leads the corresponding FD PSF to no longer be band-limited, such that an oversampling factor of 3 may not sufficiently sample it (Euclid Consortium: Miller et al., 2020a). These effects cause the FD PSF-convolved galaxy images to be aliased, biasing the shear-bias estimates. On the other hand, the shear bias calculation will be faster if conducted using smaller postage-stamp arrays and oversampling factor. Hence, in order to optimise the speed of the shear bias estimation, the dependence of the output shear bias estimates on the postage-stamp size and pixel oversampling factor is investigated. For the shear bias calculation, the smallest oversampling factor and postage-stamp size for which the shear bias estimates have converged is selected.

In this section, the impact of the accuracy (with respect to a benchmark) and speed of the shear bias calculation are considered. This is accomplished by considering postage-stamp array sizes that vary with galaxy scalelength, because it is expected that the stamp size required to avoid aliasing increases with galaxy scalelength due to the presence of larger-scale modes. The shear bias calculation is therefore tested as a function of stamp size in integer multiples of the input galaxy scalelength. The benchmark case consisting of an oversampling factor of 5 and a postage-stamp size of $16'' \times 16''$ are chosen, which are the default settings in the PSFTOOLKIT (Duncan et al., *in prep*, Euclid Consortium: Miller et al., 2020a). Truth- and error-channel PSFs are generated, and the resulting additive and multiplicative shear biases for the benchmark case are calculated, as well as with an oversampling factor of 3, and a range of postage-stamp sizes, and the resulting error in the output shear estimates with respect to the benchmark

is calculated. For this test, this is repeated for the ranges of galaxy scalelengths in the range $r_s = [0.1'', 0.2'', 0.3'', 0.4'', 0.5'']$ and ellipticity moduli $|\chi| = [0.1, 0.5]$, because the modes present in the galaxy model, and hence the aliasing in the PSF-convolved surface-brightness profiles, will depend on the galaxy shape parameters. For the two cases of $3\times$ and $5\times$ oversampled PSFs, the PSF postage stamp is cut at a range of integer multiples of the input galaxy scalelength, $R_{\rm stamp}/r_s = [20, 30, 40, 50, 60, 80, 100]$, with $R_{\rm stamp}$ the postage-stamp size in arcseconds. Note that for larger galaxies, not all stamp size-scalelength ratio values correspond to $R_{\rm stamp}$ smaller than the benchmark stamp size, and these are excluded. Firstly, the residual errors in the output shear bias estimates between the benchmark postage-stamp crop of $32'' \times 32''$ and each value of $R_{\rm stamp}/r_s$ are calculated, for constant oversampling factor, as a function of $R_{\rm stamp}/r_s, r_s, |\chi|$, for the two cases of $3\times$ and $5\times$ oversampling. Also, the residual errors in the output shear bias estimates between the benchmark $5\times$ oversampling factor and the case of $3\times$ pixel oversampling are calculated, as a function of $R_{\rm stamp}/r_s, r_s, |\chi|$. This is repeated for 1000 truth- and error-channel PSF pairs, generated with corresponding truth- and error- channel high-resolution SEDs from the Euclid Flagship 2 mock catalogue, chosen by selecting SEDs corresponding to 2 randomly-selected galaxies from the mock catalogue. The residual errors in the shear bias calculation are evaluated with respect to the *Euclid* propagate-to-object requirements (see section 3.1.2). The aim of this comparison is to show that the errors introduced in the shear bias calculation due to aliasing are in general small compared with the magnitude of shear bias relevant for the EWS.

Results

The ratio between the residual errors in the output shear bias estimates and the PTO requirements, arising due to the postage-stamp crop with respect to the baseline postage-stamp size, for the two cases of $3\times$ and $5\times$ oversampling factor, galaxy scalelength and ellipticity moduli values listed above, as a function of $R_{\rm stamp}/r_s$, are shown in figs. 3.3 to 3.5 for the multiplicative bias m and two

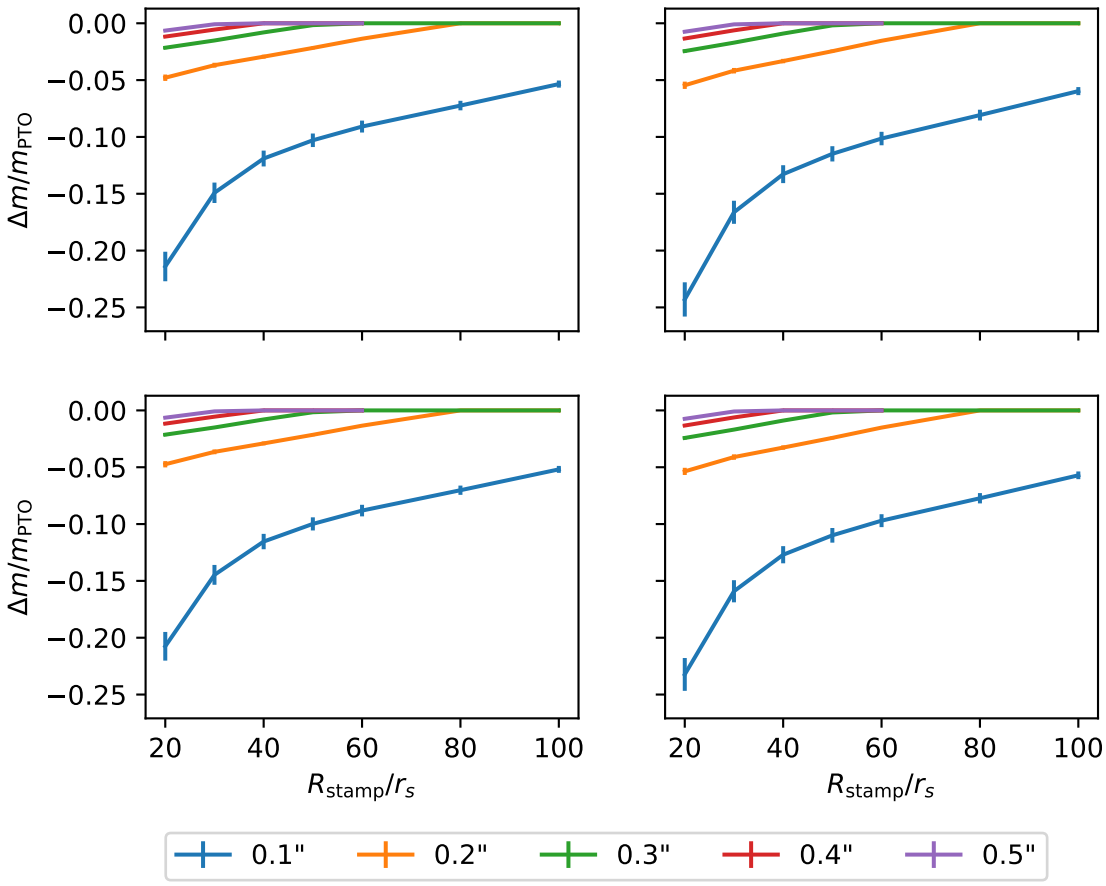


Figure 3.3: The ratio between the residual error in m-bias output from the shear bias calculation desribed in section 3.2.2 and the PTO requirement, arising due to cropped PSF postage-stamp size with respect to the baseline stamp size of $16'' \times 16''$, and plotted as a function of stamp size-galaxy scalelength ratio, $R_{\rm stamp}/r_s$. Residual biases are averaged over 1000 truth- and error-channel PSF pairs, generated from corresponding truth- and error-channel SED pairs randomly selected from the Euclid Flagship 2 mock catalogue. The coloured lines correspond to test galaxy scalelengths; $R_{\rm stamp}/r_s$ for which the corresponding $R_{\rm stamp}$ is larger than the baseline are excluded. Top/bottom panels: $3\times/5\times$ pixel oversampling factor respectively. Left/right panels: galaxy ellipticity modulus $|\chi| = 0.1, 0.5$ respectively. The error bars are estimated by the sample standard deviation of the m-bias from the sample of 1000 truth/error-PSF pairs.

components of the additive bias c_1, c_2, respectively. The residual shear biases are averaged over 1000 truth-/error-PSF pairs, and the error bars are the standard error on the mean, i.e. the sample standard deviation divided by $\sqrt{N_{\rm gal} - 1} = \sqrt{999} \approx 32$, with $N_{\rm gal}$ the number of galaxies in the sample; the standard error on the mean is considered because what is of primary interest is in the ensemble performance of the shear bias calculation.

The ratio between the residual errors in the output shear bias estimates and

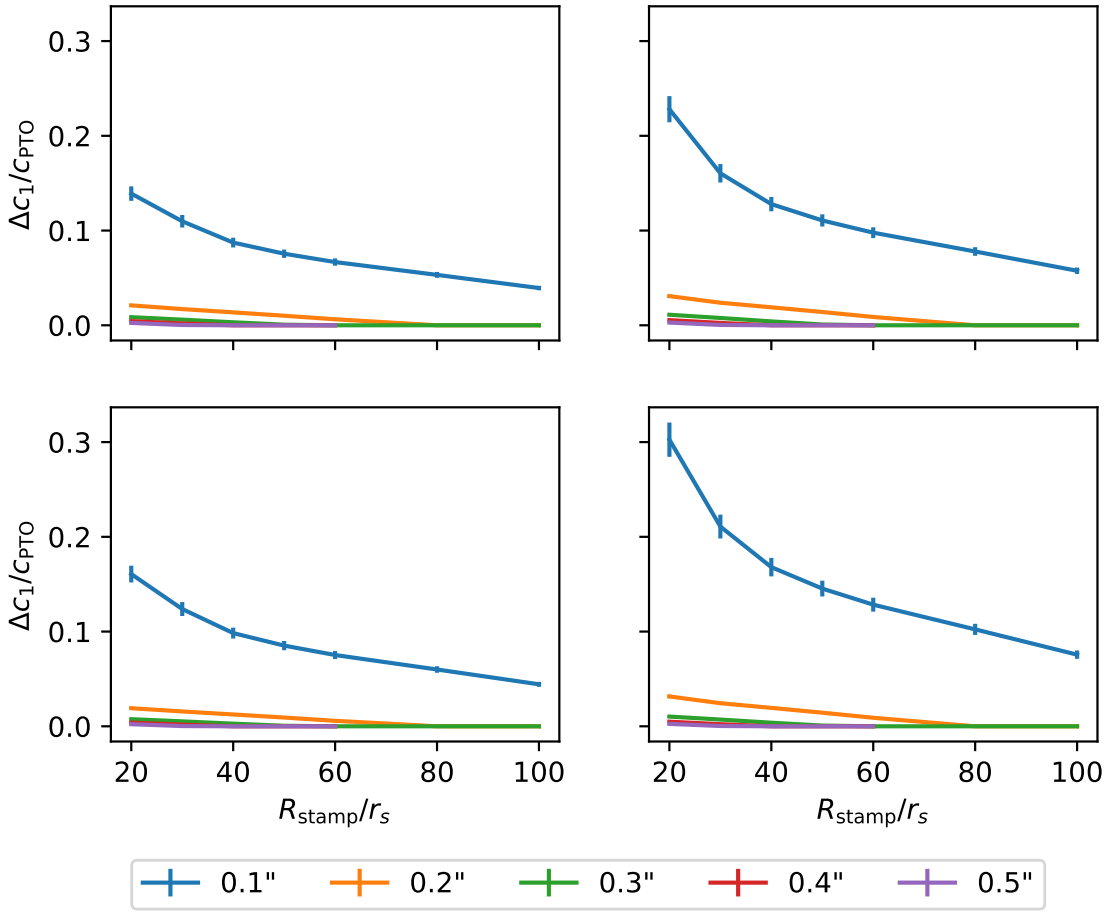


Figure 3.4: The same as fig. 3.3, for the additive bias component c_1.

the PTO requirements, arising due to the adoption of an oversampling factor of 3 versus 5, for galaxy scalelength and ellipticity moduli values listed above, as a function of $R_{\rm stamp}/r_s$, are shown in fig. 3.6 for the multiplicative bias m and two components of the additive bias c_1, c_2, respectively. In addition to accuracy, the speed of the computation is an important consideration. The mean time in seconds taken to calculate m, c_1, c_2 for an individual galaxy as a function of $R_{\rm stamp}/r_s$ is shown in fig. 3.7, for each tested oversampling factor $3\times, 5\times$, galaxy scalelength and ellipticity modulus.

Discussion

Figure 3.3, fig. 3.4, and fig. 3.5 show the residual shear bias arising due to truncation of the PSF postage-stamp, as a function of $R_{\rm stamp}/r_s$, for the tested values of oversampling factor and galaxy ellipticity. It can be seen that the residual error

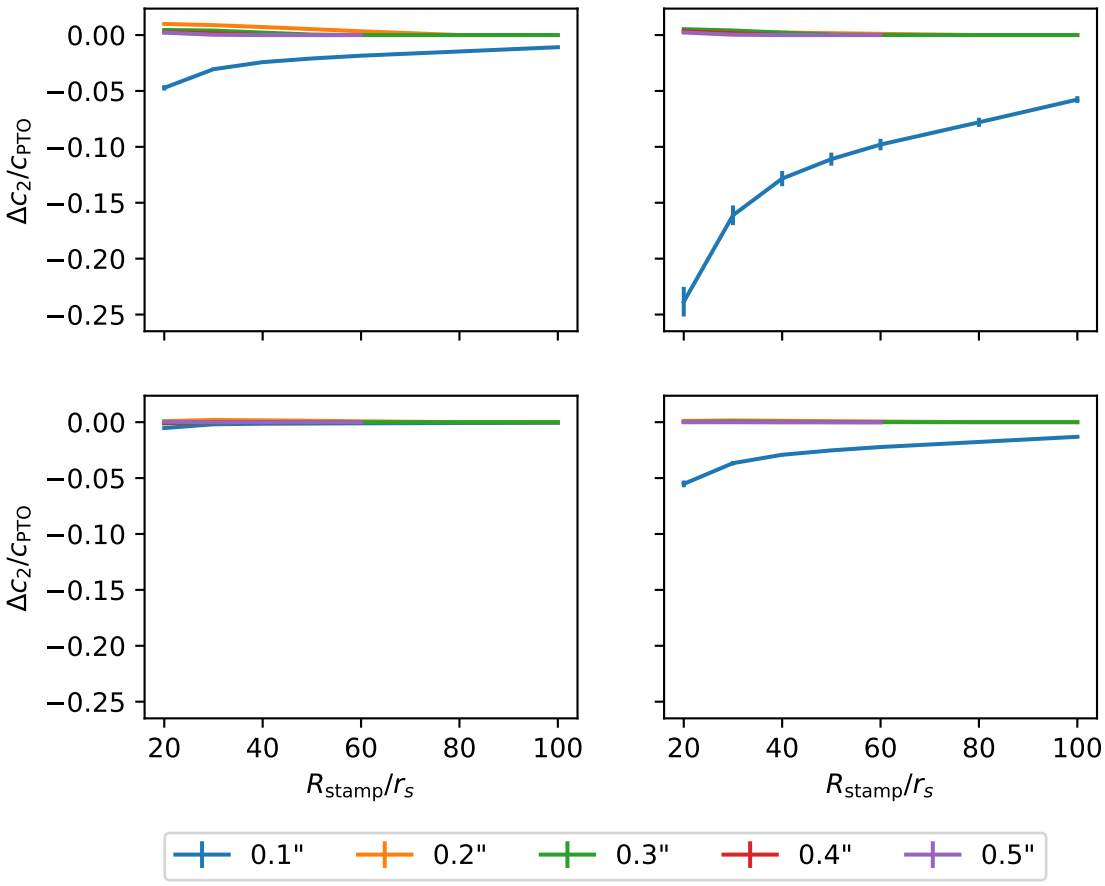


Figure 3.5: The same as fig. 3.3, for the additive bias component c_2.

in m, c_1, c_2 due to truncation of the stamp size is sub-dominant for galaxy sizes larger than $0.1''$, for both values of ellipticity moduli and oversampling factors tested. In general, the residual error is larger for larger ellipticity modulus, and decreases with increasing $R_{\rm stamp}/r_s$. In most cases the choice of oversampling factor does not have a dominant effect on the residual error in the output shear biases, apart from c_2 for $r_s = 0.1''$, shown in fig. 3.5; in this case, $3\times$ oversampling results in substantially larger residual shear bias compared with $5\times$ oversampling, particularly for $|\chi| = 0.5$. In contrast, for c_1 shown in fig. 3.4, the residual shear bias is actually slightly larger for $5\times$ oversampling than $3\times$ oversampling, though this effect is small compared to that on the c_2 component. This may arise because the $R_{\rm stamp}/r_s$ ratios correspond to different absolute array sizes for different values of oversampling factor. In most cases, for the most severe case of $r_s = 0.1''$, $|\chi| = 0.5$, the residual error becomes $\lesssim 10\%$ of the PTO requirement at $R_{\rm stamp}/r_s \sim 60$; this

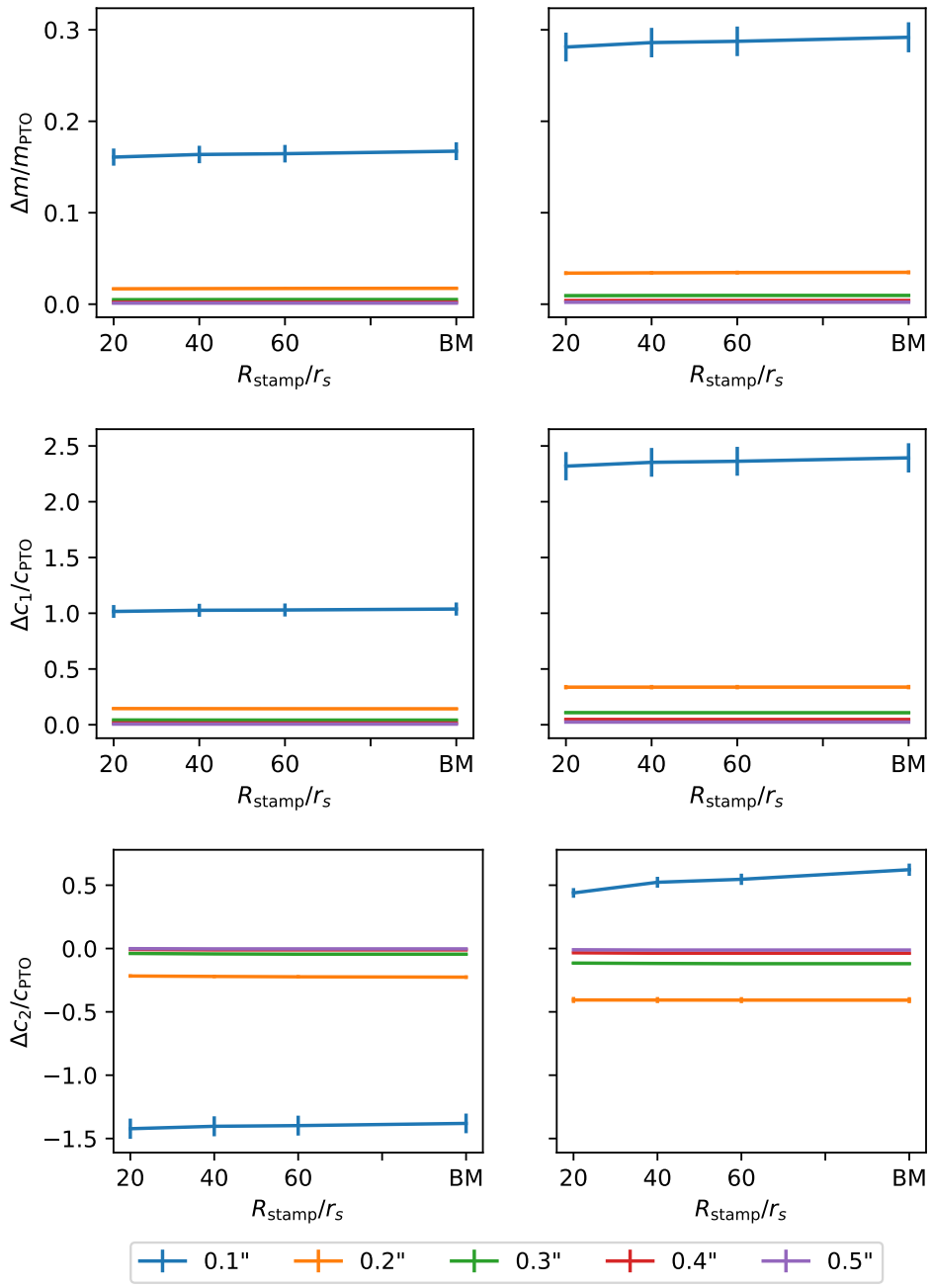


Figure 3.6: The ratio between the residual error in output from the shear bias calculation described in section 3.2.2 and the PTO requirements, arising due to adoption of $3\times$ oversampling factor, with respect to the case in which the baseline $5\times$ oversampling factor is adopted, as a function of stamp size-galaxy scalelength ratio, $R_{\rm stamp}/r_s$, averaged over 1000 truth- and error-channel PSF pairs, generated from corresponding truth- and error-channel SED pairs randomly selected from the Euclid Flagship 2 mock catalogue. The coloured lines correspond to test galaxy scalelengths; $R_{\rm stamp}/r_s$ for which the corresponding $R_{\rm stamp}$ is larger than the baseline are excluded. Top/middle/bottom panels: m-bias, c_1 additive bias component, and c_2 additive bias component respectively. Left/right panels: galaxy ellipticity modulus $|\chi| = 0.1, 0.5$ respectively. The error bars are estimated by the sample standard deviation of the m-bias from the sample of 1000 truth/error-PSF pairs.

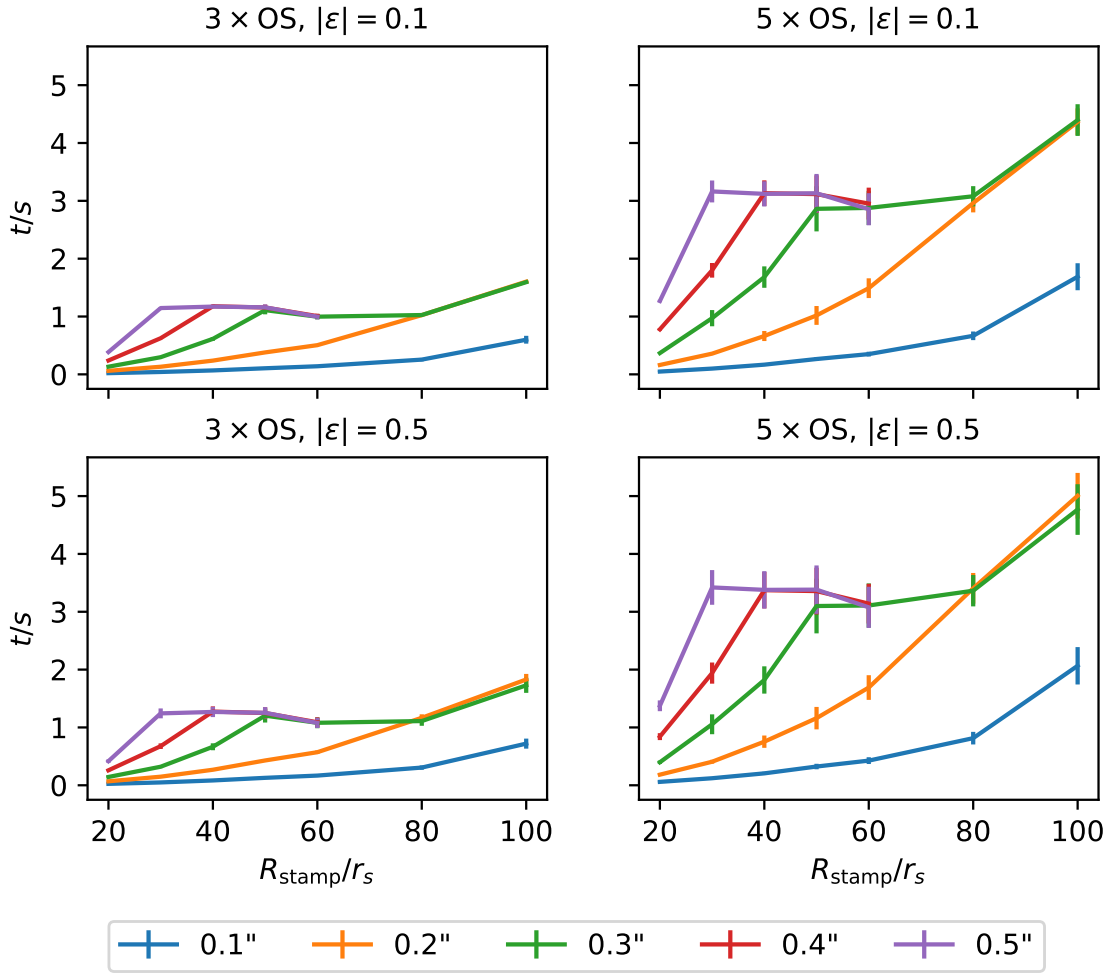


Figure 3.7: Time in seconds to calculate m, c_1, c_2 as a function of R_{stamp}/r_s. Left/right: $3\times/5\times$ oversampling factor, respectively. Top/bottom: $|\chi| = 0.1, 0.5$ respectively. Coloured lines correspond to different tested values of r_s.

is chosen as the minimum R_{stamp}/r_s for $r_s = 0.1''$.

Figure 3.6 shows the residual shear bias arising due to selecting $3\times$ oversampling, rather than the benchmark $5\times$ oversampling. In fig. 3.6, it can be seen that the additive bias is more heavily impacted by the choice of oversampling factor than the multiplicative bias. Additionally, the residual error in the output shear biases due to the oversampling factor with respect to the benchmark is largely independent of R_{stamp}/r_s, all the way out to the benchmark stamp size, though it has a strong dependence on r_s. From fig. 3.6, it can be seen that the impact of the choice of oversampling factor is significantly more important than the choice of postage-stamp size for galaxies with $r_s \leq 0.2\,\text{arcsecond}$, resulting in large residual

shear biases. For galaxies with $r_s \geq 0.3\,\mathrm{arcsecond}$, 3× oversampling results in sub-dominant residual shear biases with respect to 5× oversampling.

The systematically negative residual m-biases shown in fig. 3.3 imply that the truncation of the postage stamp causes the size of the PSF to be systematically overestimated, i.e. it causes the assumed contribution to the observed galaxy size of the PSF to be over-estimated, such that a smaller m-bias is obtained as a result of an incorrect galaxy SED (recall that in this test, the error in SED-error-sourced shear bias estimates arising as a result of the postage stamp truncation is being measured, rather than the shear bias due to the truncation); this implies that the aliasing arising due to the truncation is enhancing the wings of the PSF. The systematically positive residual c_1 and negative residual c_2, shown in figs. 3.4 and 3.5 respectively, similarly imply that the aliasing arising due to the postage-stamp truncation causes the PSF ellipticity components $\chi_1^{\mathrm{PSF}}, \chi_2^{\mathrm{PSF}}$ to be respectively under- and over-estimated. This implies that the truncation results in anisotropic aliasing of the PSF postage-stamps, which may arise due to intrinsic anisotropy in the *Euclid* PSF model. The reduction in oversampling factor from 5× to 3× has the opposite effect than the truncation on the m-bias, causing the PSF size to be systematically underestimated, as seen in fig. 3.6; whereas it has the same effect as the truncation for c_1, c_2 for $|\chi| = 0.1$. A high galaxy ellipticity modulus of $|\chi| = 0.5$ causes all three bias components to be relatively over-estimated due to the reduction in oversampling factor than for smaller $|\chi|$, implying greater sensitivity to underestimation of the PSF size and anisotropy for highly-elliptical galaxies.

From fig. 3.7 it can be seen that, for galaxies with $r_s \leq 0.2\,\mathrm{arcsecond}$, the time increases with R_{stamp}/r_s, up to the highest value considered, as expected due to the increasing array sizes. However, for larger galaxies, for which a given R_{stamp}/r_s corresponds to a larger stamp-size, the time plateaus at a r_s-dependent R_{stamp}/r_s, with a slight decrease in the time with increasing stamp size. Notably, for $r_s = 0.3\,\mathrm{arcsecond}$, for which the full range of tested R_{stamp}/r_s is within the benchmark stamp size, the time increases again after the plateau. The time taken also appears to become insensitive to r_s for sufficiently large stamp

sizes. Higher ellipticity modulus results in a modest increase in time taken to calculate the shear biases. The time taken increases with oversampling factor, by approximately a constant factor of $(5/3)^2$, again as expected. The higher time taken for galaxies with $r_s = 0.2'', 0.3''$ than for $r_s = 0.4'', 0.5''$ at high $R_{\rm stamp}/r_s$, despite the similar/smaller absolute stamp size, is likely because of the larger shear bias for the intermediate-size galaxies c.f. the large galaxies, due to the larger relative size of the PSF for smaller galaxies, resulting in an increased number of iterations in the shear bias solver.

From fig. 3.6, it can be seen that $3\times$ oversampling is insufficient for galaxies with $r_s = 0.1''$, and induces non-negligible residual error with respect to $5\times$ oversampling for $r_s = 0.2''$. On the other hand, for $R_{\rm stamp}/r_s \leq 40$, the calculation with $3\times$ oversampling for galaxies with $r_s \geq 0.3''$ dominates the time compared with the calculation with $5\times$ oversampling for galaxies with $r_s \leq 0.2''$ (see fig. 3.7). Additionally, the residual error in shear bias outputs due to the postage-stamp crop size with respect to the benchmark is negligible for galaxies with $r_s \geq 0.2''$ for all tested $R_{\rm stamp}/r_s \geq 20$, for both $3\times$ and $5\times$ oversampling factor (see fig. 3.3, fig. 3.4, and fig. 3.5). Hence postage-stamp sizes corresponding to $R_{\rm stamp}/r_s = 20$ for $r_s \geq 0.2''$ may be adopted, and PSFs and FD galaxy images may be generated with $3\times$ oversampling for galaxies with $r_s \geq 0.3''$ and with $5\times$ oversampling for galaxies with $r_s \leq 0.2''$. For $r_s = 0.1''$, the contribution to the time is largely subdominant compared with that of larger galaxies for $R_{\rm stamp}/r_s \lesssim 60$ (see fig. 3.7); since this value was also chosen as the minimum stamp size-scalelength ratio for these galaxies, the stamp size corresponding to $R_{\rm stamp}/r_s = 60$ for $r_s = 0.1''$ is hence selected. Notably this is larger than the absolute stamp size chosen for $r_s = 0.2''$, and equal to that for $r_s = 0.3''$. The calculation is further optimised by selecting postage stamp arrays that have prime factors strictly ≤ 5 in order to optimise the speed of the FFTs (Good, 1960); this increased the choice of postage-stamp size in the case of $r_s = 0.3''$ by $0.4''$, or 20 $5\times$-oversampled pixels.

It should be noted that, as discussed in section 3.1.2, it is sufficient that the residual shear bias errors discussed here be sub-dominant with respect to the

PTO requirements, rather than negligible. This is because errors in the SED-error-sourced shear bias estimates, such as are discussed here, which are sub-dominant with respect to the PTO requirement, will not have a significant impact on the EWS cosmology analysis.

The calculation is run for 1000 truth-/error-PSF pairs with (i) the same PSF postage-stamp cropped at $20 \times 0.5''$ and (ii) the PSF postage-stamp size varying with galaxy size as described above, and it is confirmed that (ii) is faster than (i) by a factor of ~ 2.1, despite the necessity of conducting the FFTs of the truth- and error-PSFs separately for each value of r_s in (ii). The calculation is also run (iii) generating only PSF postage-stamp arrays with $5\times$ oversampling, and (iv) generating PSFs with both $3\times$ and $5\times$ oversampling, and convolving galaxy images with $r_s \geq 0.3''$ with the $3\times$-oversampled PSFs and galaxy images with $r_s \leq 0.2''$ with the $5\times$-oversampled PSFs, as described above; it is confirmed that (iv) is faster than (iii) by a factor of ~ 2.0, despite the necessity of generating 2 sets of PSFs in case (iv). The generated $5\times$ PSFs were also downsampled to $3\times$ by interpolation using a bivariate spline, implemented using `scipy` (Ahlberg et al., 1967), and this was found to be slower than (iv) by a factor of ~ 1.4. Additionally, the calculation is run for 1000 truth-/error- SED pairs, solving (3.23) using both SVD and LU (Press et al., 2007) decomposition methods (implemented in `scipy`), and it is confirmed that the difference in contribution to the time taken for the shear bias calculation to run is negligible; the SVD solver is preferred because it is robust in the presence of ill-conditioning in the Fisher matrix, in contrast to the LU solver (Press et al., 2007).

3.3 Estimation of Shear Bias at the Catalogue Level

3.3.1 Description of the Method

As discussed in section 3.1.1, it is of interest to forecast shear biases for mock galaxies in the Euclid Flagship 2 catalogue. Having realistic forecast estimates for shear biases at the catalogue-level allows their impact on cosmological inference to be propagated more realistically than if their effect is approximately inserted at

the level of summary statistics, such as in Massey et al., 2013. This is because such a forward-modelling approach results in a more realistic estimate of the impact of the shear bias on the angular power spectra than a simple prescription such as in Massey et al., 2013. Additionally, it allows the propagation of the joint impact of systematics that may be correlated due to dependence on galaxy properties, such as PSF errors and photometric redshift errors.

From fig. 3.7 it can be seen, given the oversampling and postage-stamp size choices described in section 3.2.3, that the shear bias calculation takes $\sim$0.5s per galaxy. The Flagship 2 mock catalogue contains $\sim$4.8 billion galaxies (Euclid Collaboration: Castander et al., 2024), corresponding to $\sim$670,000 CPU-hours to calculate shear biases explicitly for all galaxies in the mock. It is therefore computationally unfeasible to calculate shear biases explicitly for all galaxies in the mock catalogue.

In order to overcome this issue, a sampling strategy is adopted, in which a sub-sample of galaxies from the Flagship 2 catalogue is defined, which is representative of the full population of galaxies in the mock. Galaxies in this sample are henceforth referred to as "sample galaxies", whereas galaxies in the catalogue that are not included in this sample are henceforth referred to as "catalogue galaxies". Shear biases are calculated for sample galaxies using the calculation described in section 3.2.2. Shear biases are then assigned to catalogue galaxies using a nearest-neighbour approach based on their proximity to sample galaxies in a space defined by an SED parametrisation (see section 3.3.2). However, it is also desirable to sample the regions of the space of galaxy parameters for which the density of galaxies present in the mock is low, in order to avoid systematically biasing the shear bias estimates for discrete sub-populations of galaxies that may result in biased cosmological forecasts. This is done by defining a grid in the space of galaxy $r-i, r-z, i-z$ colours and VIS magnitude, and ensuring that some minimum number of galaxies is sampled in each grid cell that is occupied in the full catalogue. While it is found that including the observed redshift $z_{\rm obs}$ of galaxies in the sampling grid does not significantly reduce the shear bias as a

function of $z_{\rm obs}$ arising due to the SED matching (see section 3.3.2), the observed redshift is included in the nearest-neighbour distance calculation.

The galaxy morphologies in the Flagship 2 mock are parametrised by an exponential-disc scalelength and ellipticity modulus. In this work the contribution from the bulges of galaxies is neglected. Each galaxy is also assigned a high-resolution SED $F(\lambda)$, with units of $\mathrm{erg\,cm^{-2}\,s^{-1}\,\mathring{A}^{-1}}$, which is a linear combination of 2 SEDs from a basis set of 31 template SEDs from the COSMOS survey (Ilbert et al., 2008). The 31 template SEDs are shown in fig. 3.8. 2 template SEDs are chosen for each galaxy in order to allow the space of possible SEDs to be continuously sampled, which would not be possible if only one template SED were sampled for each mock galaxy; additionally, this allows the model to incorporate the effect on the galaxy SEDs of galaxies that have both bulge and disc components. Each of the two template SEDs is also reddened according to one of five extinction curves $k(\lambda)$ from Ilbert et al., 2008, describing the extinction intrinsic to the galaxies with the same units as the template SEDs, one of which corresponds to no intrinsic extinction, and with a normalisation parameter that determines the amplitude of the extinction curve in the range $\alpha = [0, 0.5]$. An observed redshift $z_{\rm obs}$, i.e. with both cosmological and peculiar contributions, is also applied to the rest-frame SED. The galaxy flux is therefore given by:

$$F(\lambda) = \frac{1}{1 + z_{\rm obs}} \sum_{i=0}^{1} f_i F_i(\lambda) 10^{-0.4 k_i(\lambda)\alpha_i}, \tag{3.26}$$

with $F_i(\lambda), k_i(\lambda), \alpha_i$ the template SED, extinction curve and extinction normalisation parameter respectively for SED $i = 0, 1$, and f_i is an SED weight such that $f_0 + f_1 = 1$. The SEDs in the mock are therefore parametrised by template-SED and extinction-curve indices, as well as by the weights of the two template SEDs, colour excesses, and observed redshift. In the Flagship 2 catalogue, the corresponding VIS flux and fluxes in photometric filters for various external survey configurations are also provided, including for LSST (Phillips Longley, 2021), DES (Abbott et al., 2021), CFHTLens (Coupon et al., 2009), Subaru (Aihara et al., 2022) and Pan-STARRS (Flewelling et al., 2020) (see section 1.2.2), which will provide

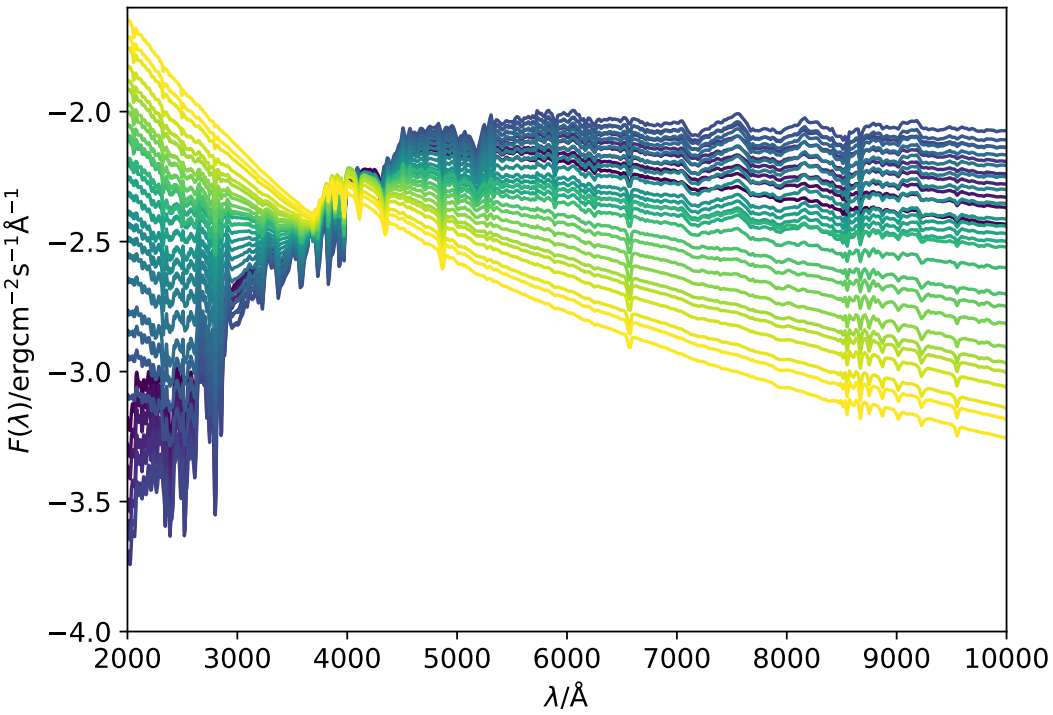


Figure 3.8: The 31 template SEDs used to calculate truth-channel high-resolution SEDs for mock galaxies in Flagship2. The colour mapping corresponds to the index of the galaxy SEDs, running from 0-30. The SEDs are multiplied by an arbitrary normalising factor (Euclid Collaboration: Castander et al., 2024).

colour information for the EWS for the galaxy PSF reconstruction and photometric redshifts (Euclid Collaboration: Mellier et al., 2024).

Galaxies are sampled in the space of galaxy colour $r-i, r-z, i-z$ and VIS magnitude $m_{\rm VIS}$, for a grid of values of galaxy disc scalelength, ellipticity modulus, and FoV x, y-position. Shear biases are calculated for these galaxies using the calculation described in section 3.2.2, and the remaining galaxies in the catalogue are matched to their nearest-neighbours in this sample, with distance measured in the $r-i, r-z, i-z, z_{\rm obs}, m_{\rm VIS}$ space. This is repeated separately for each position in the grid of galaxy disc scalelength, ellipticity modulus, and FoV position, and the SED-matched shear bias estimates are interpolated over the scalelength, ellipticity modulus, and over FoV position, using 1-dimensional linear interpolation to interpolate over each of the galaxy ellipticity modulus and scalelength, and a bilinear spline for the FoV interpolation (see section 3.3.3).

The performance of the SED sampling and matching is evaluated in section 3.3.2. The performance of the galaxy shape and FoV position interpolation is evaluated in section 3.3.3.

To sample the galaxies for which the shear bias calculation is done, the space of $r-i, r-z, i-z, m_{\mathrm{VIS}}$ is divided into a grid, from which galaxies in the mock catalogue are randomly sampled, with some minimum number of galaxies sampled from each grid cell that is represented in the catalogue. The grid covers the full range of $r-i, r-z, i-z$ and VIS magnitude values that exist in the catalogue, with cell size determined by the number of cells along each axis. The axis length in each of the 4 dimensions is chosen to minimise the shear bias introduced due to the SED matching as a function of each of the 4 dimensions, and the impact of varying the cell size is investigated in section 3.3.2. The colours are calculated from the mock LSST riz fluxes given in the Flagship 2 catalogue, after converting to magnitude m_r, m_i, m_z (Oke and Gunn, 1983):

$$m_a = -2.5 \log_{10}(F_{\nu,a}) - 48.6, \tag{3.27}$$

where m_a is the magnitude, and $F_{\nu,a}$ is the flux per unit frequency, in filter a. Equation (3.27) is also used to convert the VIS flux given in the mock catalogue to magnitude m_{VIS}. The galaxy colour indices (i.e. the differences between the riz magnitudes in (3.27)) are included in the grid parametrisation, instead of e.g. the SED-index parametrisation in equation (3.26), because there is a direct physical dependence between variations in the colour of target galaxies and variations in the PSF for the galaxy, since the size of the PSF for a diffraction-limited target depends on the colour of the target (Eriksen and Hoekstra, 2018). Sampling and matching galaxies in the colour-space should result in more accurate resulting shear bias estimates for the galaxies in the catalogue than sampling and matching in the space of the SED parametrisation (3.26), which contains arbitrary SED and extinction-curve indexing parameters, such that distance in this space does not directly physically correspond to variations in the PSF and hence the shear biases. The VIS magnitude is included in the grid parametrisation, because for the case of PSF error sourced by galaxy-PSF reconstruction using noisy photometry, the PSF

error depends on the photometric noise, and hence on the apparent magnitude of the target galaxy. The observed redshift is included in the grid parametrisation to explicitly track the redshift-dependence of the shear bias, because this may have a significant impact on cosmological parameter inference, in particular of the dark energy equation-of-state parameters w and w_a (Euclid Collaboration: Desprez et al., 2020).

The SED sampling proceeds as follows:

(i) Define the sampling grid by constructing histograms of $r-i, r-z, i-z, z_{\rm obs}, m_{\rm VIS}$-values of galaxies in the catalogue, with number of histogram bins in each dimension d set to the grid axis length $N_{{\rm axis},d}$ (chosen to optimise the accuracy of the SED matching), and taking the grid-cell boundaries as the histogram bin boundaries, such that the grid contains $N_{\rm cells} = \prod_d N_{{\rm axis},d}$ cells;

(ii) Bin the galaxies in the catalogue according to the grid;

(iii) Count the number of galaxies in the catalogue corresponding to each grid cell ν_i with $i = [0, .., N_{\rm cells} - 1]$;

(iv) Count the number of grid cells $N_{\rm occupied}$ for which $\nu_i > 0$;

(v) Define the maximum allowed number of galaxies in the sample corresponding to each grid cell, $n_{\rm max} \equiv \lfloor n_{\rm tot}/N_{\rm occupied} \rfloor$, where $n_{\rm tot}$ is the total number of galaxies desired for the sample; this choice prevents grid cells with large population ν_i from dominating the final sample;

(vi) For each grid cell for which $\nu_i > 0$, randomly sample a number of galaxies $n_i \equiv \min(n_{\rm max}, \nu_i)$ from the ν_i galaxies in the catalogue corresponding to each occupied grid cell;

(vii) If $\sum_i n_i < N_{\rm tot}$, sample randomly from the catalogue galaxies which have not already been sampled in step (vi) until $\sum_i n_i = N_{\rm tot}$.

The grid-cell size is defined by choosing $N_{\mathrm{axis},r-i,r-z,i-z,m_{\mathrm{VIS}}} = 8, 18, 12, 10$, respectively. See section 3.3.2 for a discussion of the impact of the choice of N_{axis} on the performance of the shear bias estimation method. Requiring that all grid cells which are occupied in the catalogue are sampled (step (vi)) ensures that there are no sub-populations of galaxies in the $r-i, r-z, i-z, m_{\mathrm{VIS}}$ grid-space that are present in the catalogue but not represented in the sample (on scales in the grid-space larger than the cell size). This is intended to reduce systematic bias in the shear bias estimates for such sub-populations, which may arise due to matching these galaxies to galaxies in the sample with significantly different SEDs. Additionally, it was necessary to sample an additional 1000 SEDs with the lowest values of $r-i$ in order to avoid significantly large SED-matching shear bias in this region of the sampling space, indicating that the PSF is highly sensitive to changes in $r-i$ at low values (see section 3.3.2).

In practice, most of the N_{cells} cells are not occupied, $(N_{\mathrm{occupied}} << N_{\mathrm{cells}})$, and there are a significant number of occupied grid cells with $\nu_i < n_{\mathrm{max}}$. Given step (vi), these grid cells are sampled, but when step (vi) is completed, the total number of sampled galaxies $\sum_i n_i < N_{\mathrm{tot}}$. Step (vii) samples up to N_{tot} galaxies by sampling randomly from the un-sampled galaxies in the catalogue; these are sampled from a given grid cell i with probability $(\nu_i - n_i)/(\sum_i(\nu_i - n_i))$, such that more densely-populated grid cells are more likely to be sampled, such that the distance between a sample galaxy to a catalogue galaxy in the $r-i, r-z, i-z, m_{\mathrm{VIS}}$ space is smaller in the more densely-populated grid cells, increasing the probability that a galaxy in a densely-populated grid cell will be matched to a galaxy with a similar SED, with the aim of reducing the mean bias on the shear biases estimated with the matching method.

To estimate the shear bias for a given galaxy in the catalogue, the galaxy SED is matched to its nearest-neighbour sample galaxy, with distance calculated in the $r-i, r-z, i-z, z_{\mathrm{obs}}, m_{\mathrm{VIS}}$ space, and with coordinates of SEDs standardised by subtracting the mean and dividing by the standard deviation of SEDs in the catalogue. Distances in this space are measured using a K-D tree algorithm

implemented in `scipy`. In section 3.3.2, the impact of conducting the matching by computing the distance in the space of parameters of equation (3.26), involving the SED and extinction-curve indices, α, SED weights and observed redshift, rather than the $r-i, r-z, i-z, z_{\rm obs}, m_{\rm VIS}$ space of the grid, is investigated, and found to result in substantially larger shear bias due to the SED matching than matching in the colour-redshift-VIS magnitude space. In section 3.3.2, the impact of matching catalogue-galaxy SEDs to a sample galaxies selected by randomly sampling SEDs from the full catalogue, rather than in grid cells, is investigated, and found to result in significantly higher shear biases due to the SED matching than the case in which SEDs are sampled in grid cells. In section 3.3.2, the impact of averaging the shear bias values for $k > 1$ neighbours to determine the shear bias estimate is investigated, i.e. generalising the method used to a k-nearest neighbours method, and it is found to have negligible effect. The subsequent interpolation of the shear bias estimates over the galaxy morphology parameters $r_s, |\chi|$ and the x, y FoV-position is discussed in section 3.3.3.

3.3.2 Optimisation and validation of SED matching

In the method described in section 3.3.1, the shear biases are estimated for catalogue galaxies by matching them to the nearest sample galaxy in the standardised space of $r-i, r-z, i-z, z_{\rm obs}, m_{\rm VIS}$, and assigning them the corresponding shear bias values. The space is standardised in each dimension by subtracting the values for each galaxy in the catalogue by the mean value over all galaxies in the catalogue, and dividing by the standard deviation of values for all galaxies in the catalogue. In order to evaluate the accuracy of this SED-matching technique, the shear biases which would result from taking for each catalogue galaxy its true Flagship 2 high-resolution SED, and the Flagship 2 high-resolution SED of the sample galaxy to which it is matched, are taken as the truth- and error-channel inputs to the shear bias calculation respectively. This approach is adopted partly because it is computationally unfeasible to re-define the sample many times, and compute e.g. error-channel noisy photometric SEDs for each new sample in order

to compute residual errors in corresponding realistic shear biases; additionally, this approach isolates the impact due to errors in the SED matching. The performance of the SED sampling and matching is not evaluated with respect to the shear bias arising due to the SED matching as a function of the VIS magnitude, because the high-resolution Flagship 2 SEDs parametrised by equation (3.26) do not depend on the normalisation of the flux, and hence $m_{\rm VIS}$ will not impact the SED-matching shear bias evaluated in this section.

The most naïve sampling and matching approach that might be applied consists of randomly sampling galaxies from the Flagship 2 catalogue (i.e. taking $N_{\rm cells} = 1$), and then estimating shear biases for catalogue galaxies by matching to nearest-neighbour sample galaxies in the space defined by the high-resolution SED-template parametrisation of equation (3.26). Because this parametrisation contains both continuous and discrete parameters — $z_{\rm obs}, f_{0,1}, \alpha_{0,1}$ and $F_{0,1}, k_{0,1}$ respectively — the approach adopted here is to first match galaxies to the nearest set of $F_{0,1}, k_{0,1}$ that is represented in the sample (with distance defined in the un-standardised space of $F_{0,1}, k_{0,1}$), and then match to the nearest neighbour which has those values $F_{0,1}, k_{0,1}$, in the space of $z_{\rm obs}, f_{0,1}, \alpha_{0,1}$, with values standardised by subtracting the mean catalogue values and dividing by the standard deviation of catalogue values.

The SED matching shear biases which arise when this random-sampling, SED-parameter-matching approach is adopted are shown in fig. 3.9, fig. 3.10, and fig. 3.11. The multiplicative bias arising due to the SED matching, $m_{\rm matching}$, is shown in fig. 3.9, with the $m_{\rm matching}$ in 30 bins in each of $z_{\rm obs}, r-i, r-z, i-z$ respectively shown in the sub-figures. In each bin, $m_{\rm matching}$ is averaged over 1000 catalogue-sample SED pairs. The error bars show the standard error on the mean, i.e. the standard deviation of the m-bias values for each redshift bin divided by $\sqrt{999}$, because for this test the presence of any coherent shear bias in the ensemble of galaxies as a function of redshift is of interest. The corresponding additive biases arising due to the SED matching, $c_{1,\rm matching}, c_{2,\rm matching}$ are shown in fig. 3.10 and fig. 3.11 respectively. SED-matching shear biases are evaluated as a function of galaxy shape, for $r_s = [0.1'', 0.3'', 0.5''], |\chi| = [0.1, 0.5]$. The SED-

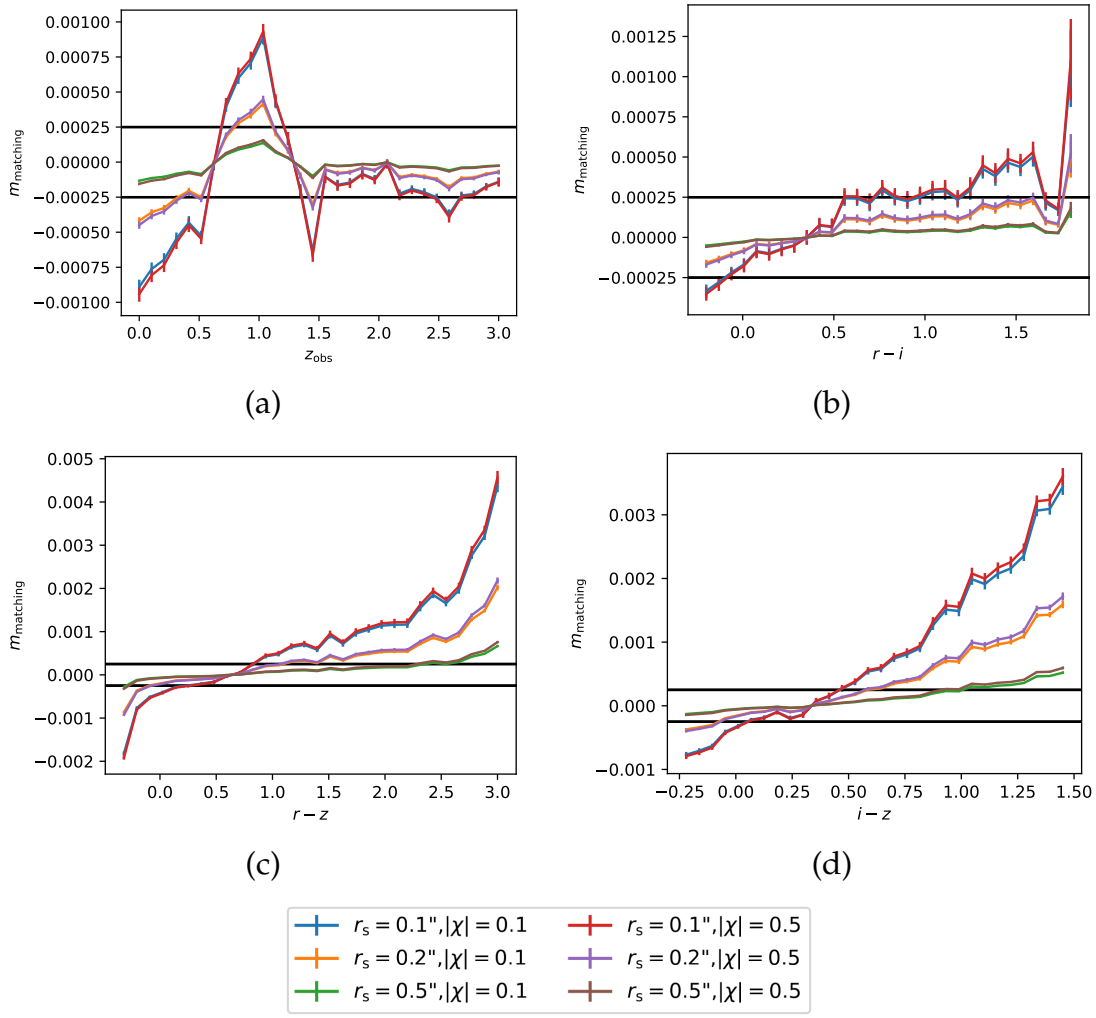


Figure 3.9: The multiplicative SED-matching shear bias m_{matching} arising when SED are randomly sampled with $N_{\mathrm{cells}} = 1$, and matched to catalogue galaxies in the SED-parametrising space of (3.26). m_{matching} calculated as a function of (a) z_{obs}, (b) $r - i$, (c) $r - z$, (d) $i - z$, on a grid of values of $(r_s, |\chi|)$. m_{matching} averaged over 1000 SEDs in each bin, with error bars showing the standard error on the mean. Black horizontal lines are the EWS PTO shear bias requirement (3.21) described in section 3.1.2.

matching shear biases are evaluated at the central point of a 3×3 grid on the FoV; it is verified that the SED-matching bias does not vary significantly with FoV-position, in the case considered here, in which the effect of the dichroic surface in the telescope is neglected.

As can be seen in figs. 3.9 to 3.11, the approach of randomly sampling galaxies from the sample, and then matching in the SED-parametrisation-space yields SED-matching biases that are comparable with, and in some cases exceeding, EWS PTO requirements. A more physically-motivated approach consists of matching

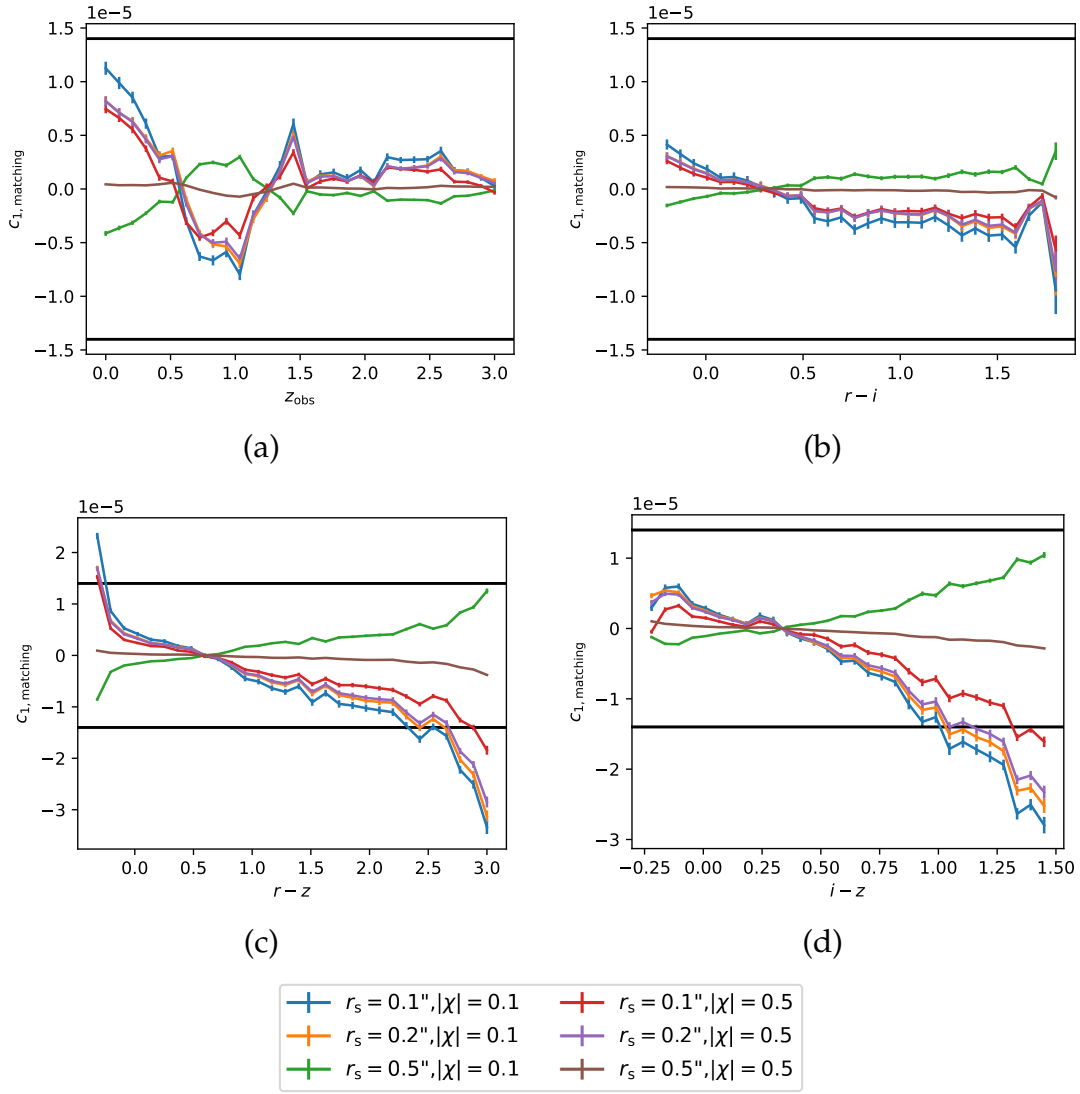


Figure 3.10: The same as fig. 3.9, showing the additive SED-matching shear bias component $c_{1,\mathrm{matching}}$. Black horizontal lines are the EWS PTO shear bias requirement (3.22) described in section 3.1.2.

SEDs in the space of colour indices $r-i, r-z, i-z$. Because of the colour-dependence of the PSF, SEDs which are close in the space of colour index values are likely to correspond to similar PSFs, and should therefore have low SED-matching shear biases as a result.

The observed redshift is also included in the nearest-neighbour distance calculation, in order to reduce bias in the shear bias estimates as a function of z_{obs} by construction. Additionally, for the investigation of shear bias arising due to noisy broad-band photometric SED information (see chapter 4), the VIS magnitude of galaxies is included in the nearest-neighbour distance calculation, because the

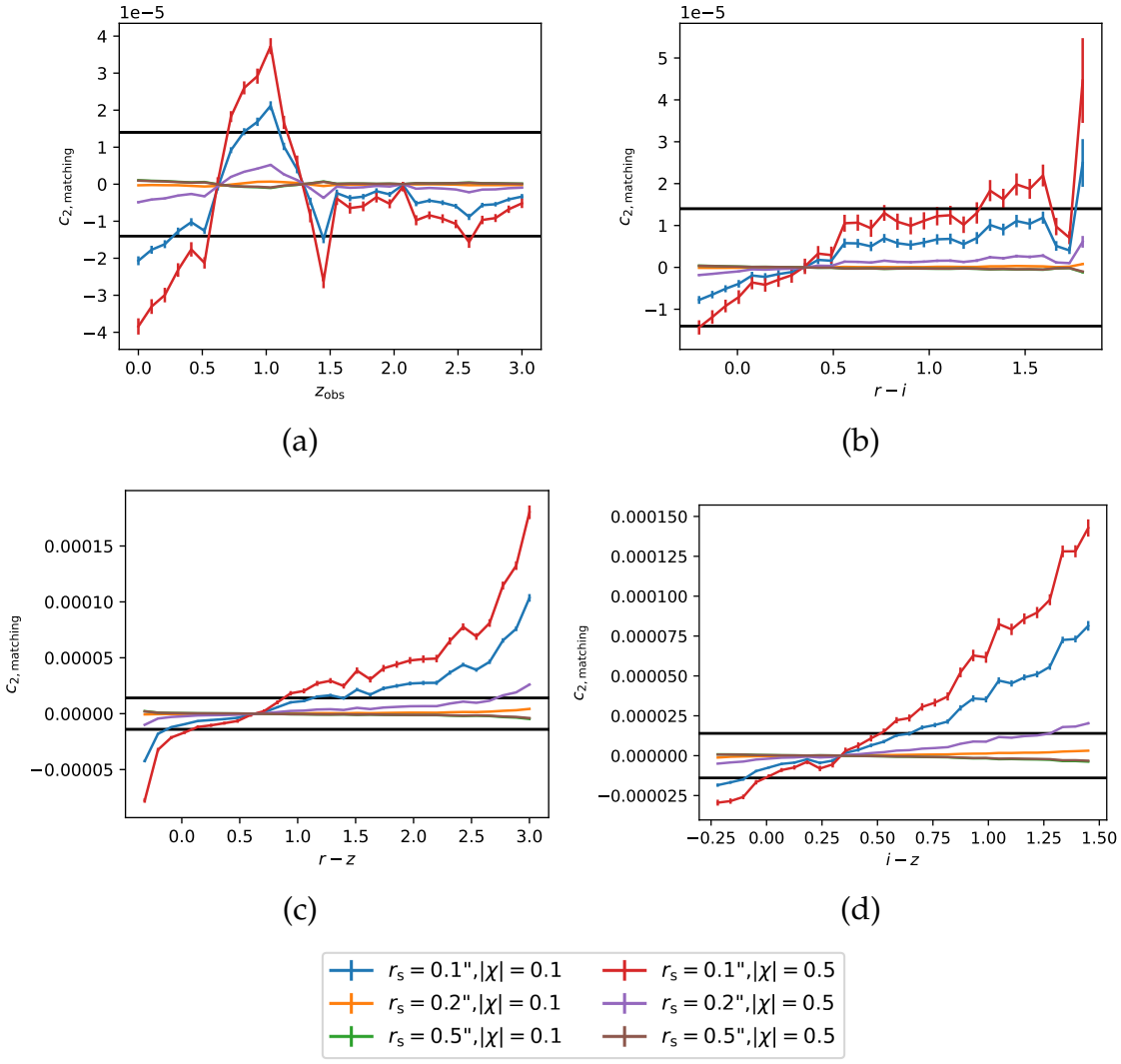


Figure 3.11: The same as fig. 3.9, showing the additive SED-matching shear bias component $c_{2,\mathrm{matching}}$. Black horizontal lines are the EWS PTO shear bias requirement (3.22) described in section 3.1.2.

shear bias due to this effect will be magnitude-dependent. The SED-matching shear bias m_{matching} as a function of $z_{\mathrm{obs}}, r-i, r-z, i-z$ for catalogue galaxies matched to nearest-neighbours in the $z_{\mathrm{obs}}, r-i, r-z, i-z, m_{\mathrm{VIS}}$-space is shown in fig. 3.12. For brevity, the additive matching biases are not shown for this case.

As can be seen in fig. 3.12, when galaxies are randomly sampled from the catalogue with $N_{\mathrm{cells}} = 1$, the SED-matching shear bias is still high compared with the EWS requirements, even when SEDs are matched in the $z_{\mathrm{obs}}, r-i, r-z, i-z, m_{\mathrm{VIS}}$-space. A further refinement to the method consists of also *sampling* within grid cells in the space of $r-i, r-z, i-z, m_{\mathrm{VIS}}$, as described in section 3.3.1. Various

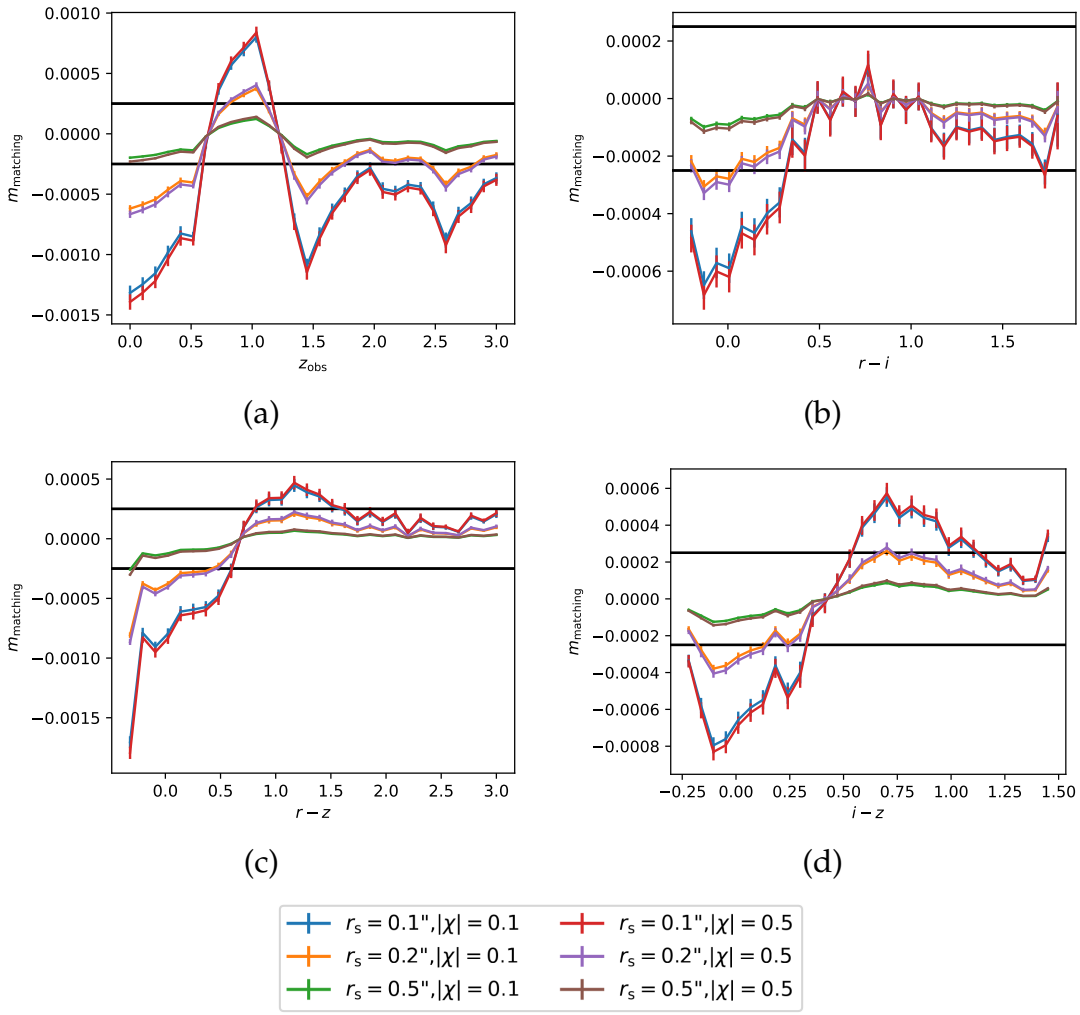


Figure 3.12: The multiplicative SED-matching shear bias m_{matching} arising when SED are randomly sampled with $N_{\mathrm{cells}} = 1$, and matched to catalogue galaxies in the space of $(z_{\mathrm{obs}}, r-i-r-z, i-z, m_{\mathrm{VIS}})$. m_{matching} calculated as a function of (a) z_{obs}, (b) $r-i$, (c) $r-z$, (d) $i-z$, on a grid of values of $(r_s, |\chi|)$. m_{matching} averaged over 1000 SEDs in each bin, with error bars showing the standard error on the mean. Black horizontal lines are the EWS PTO shear bias requirement (3.21) described in section 3.1.2.

configurations of $N_{\mathrm{axis},d}$ have been investigated, and it is found that the best results are produced for $N_{\mathrm{axis},d} = [8, 18, 12, 10]$ for $d = [r-i, r-z, i-z, m_{\mathrm{VIS}}]$, respectively. This also takes into account increasing computational time for the SED sampling with N_{cells}, and diminishing returns in accuracy with increasing N_{axis} in some cases. Note that, since the SED-matching bias does not depend on m_{VIS}, a fiducial value of $N_{\mathrm{axis},m_{\mathrm{VIS}}} = 10$ has been selected. It is also verified that including z_{obs} in the grid with $N_{\mathrm{axis},z_{\mathrm{obs}}} > 1$ does not significantly reduce the SED-matching shear bias. The m_{matching} arising when galaxies are sampled in this grid, and matched to catalogue

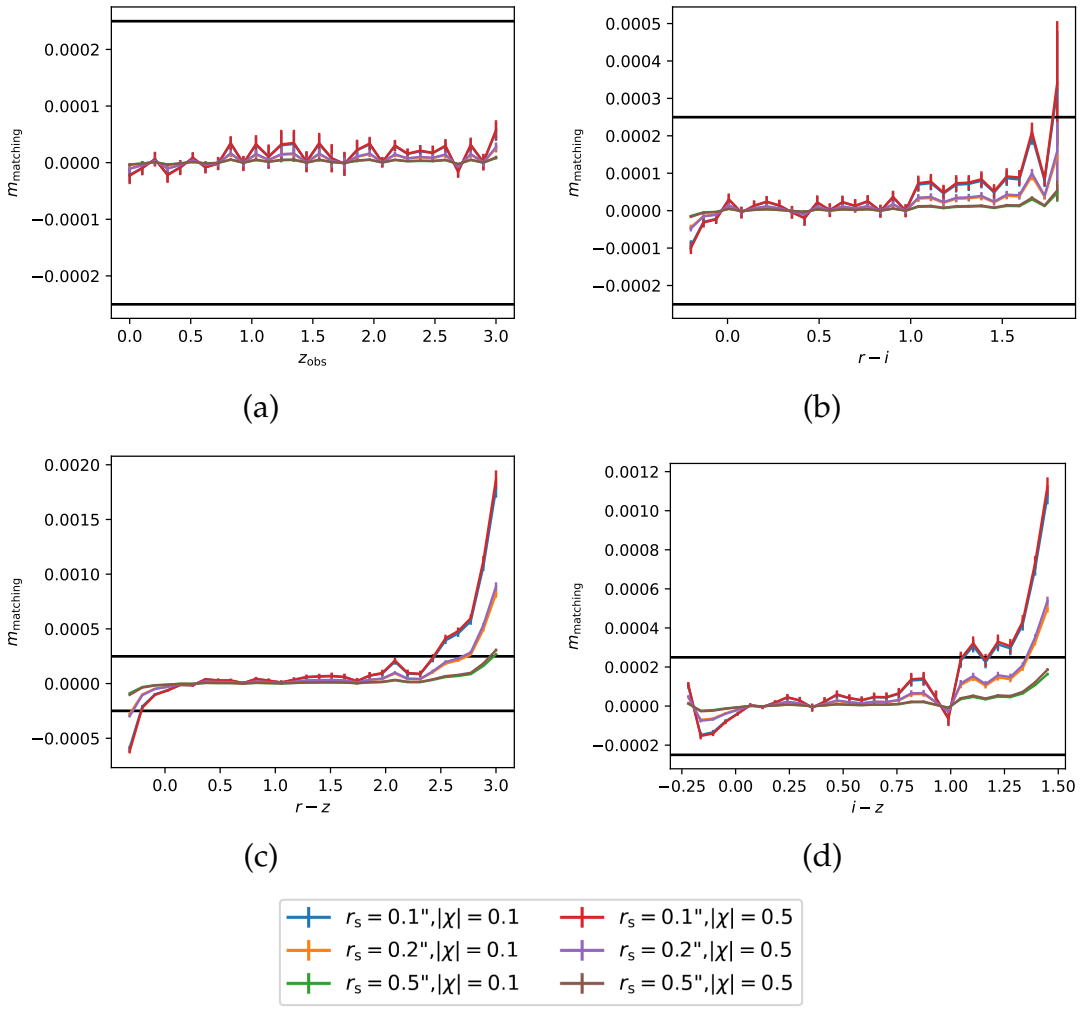


Figure 3.13: The multiplicative SED-matching shear bias m_{matching} arising when SED are sampled on a grid with $N_{\mathrm{axis},d} = [8, 18, 12, 10]$, for $d = [r-i, r-z, i-z, m_{\mathrm{VIS}}]$ respectively, and matched to catalogue galaxies in the SED-parametrisation-space of (3.26). m_{matching} calculated as a function of (a) z_{obs}, (b) $r-i$, (c) $r-z$, (d) $i-z$, on a grid of values of $(r_s, |\chi|)$. m_{matching} averaged over 1000 SEDs in each bin, with error bars showing the standard error on the mean. Black horizontal lines are the EWS PTO shear bias requirement (3.21) described in section 3.1.2.

galaxies in the SED-parametrisation-space, is shown in fig. 3.13.

The $m_{\mathrm{matching}}, c_{\mathrm{matching}}$ arising when galaxies are sampled in this grid, and matched to catalogue galaxies in the $z_{\mathrm{obs}}, r-i, r-z, i-z, m_{\mathrm{VIS}}$-space, is shown in fig. 3.14, fig. 3.15, and fig. 3.16.

As can be seen in fig. 3.13, the SED-matching m-bias is still exceeding the PTO requirement when SEDs are sampled in the $r-i, r-z, i-z, m_{\mathrm{VIS}}$ sampling grid, and matched to catalogue galaxies in the SED-parametrisation-space of (3.26). The SED-matching shear biases arising in the case in which galaxies are

sampled in the redshift-colour-magnitude grid, and matching in the same space of $z_{\rm obs}, r-i, r-z, i-z, m_{\rm VIS}$, are shown in figs. 3.14 to 3.16, in which it is shown that in this approach results in additive and multiplicative SED-matching shear biases that are within the PTO requirements for all values of redshift and colour index considered. It should be noted that a spike in $m_{\rm matching}$ was present at low values of $r-z$ which is comparable with the propagate-to-object m-bias requirement. This is resolved by sampling an additional 1000 SEDs in this region of $r-z$. The spike in SED-matching m-bias in the low-$r-z$ region implies that the PSF is particularly sensitive to small colour variations in this region of the colour space.

Discussion

As can be seen in fig. 3.9—fig. 3.16, the performance of the SED matching can be significantly improved by (i) sampling galaxies on a grid in the space of $(r-i, r-z, i-z, m_{\rm VIS})$, with additional sampling where necessary, and (ii) matching catalogue galaxies to sample galaxies in the space of $(z_{\rm obs}, r-i-r-z, i-z, m_{\rm VIS})$. Additionally, it may be noted that the SED-matching shear bias has quite significant inverse dependence on the galaxy size r_s, but only weakly increases with galaxy ellipticity modulus $|\chi|$. In the case of the additive bias component $c_{1,\rm matching}$, the polarity of the matching bias reverses for $r_s = 0.5''$ compared with smaller values of r_s, as seen in fig. 3.10 and fig. 3.15. There is substantial asymmetry in the SED-matching shear bias in the two additive components, with c_2 somewhat more affected than c_1; this arises due to intrinsic anisotropy of the PSF. It may also be noted from fig. 3.12 that the SED-matching shear bias as a function of $z_{\rm obs}$ is not significantly biased at any redshift even if the galaxies are sampled randomly, if the matching is done in the $(z_{\rm obs}, r-i-r-z, i-z, m_{\rm VIS})$-space rather than the SED-parametrisation space of (3.26). This is interesting given that $z_{\rm obs}$ is also included in the latter parametrisation, and implies that matching in the SED-parametrisation space of (3.26) introduces redshift-dependent SED-matching shear bias that is correlated with SED parameters other than $z_{\rm obs}$. That is, the SEDs are coherently matched such that shear bias is induced, in a way that is redshift-dependent, likely

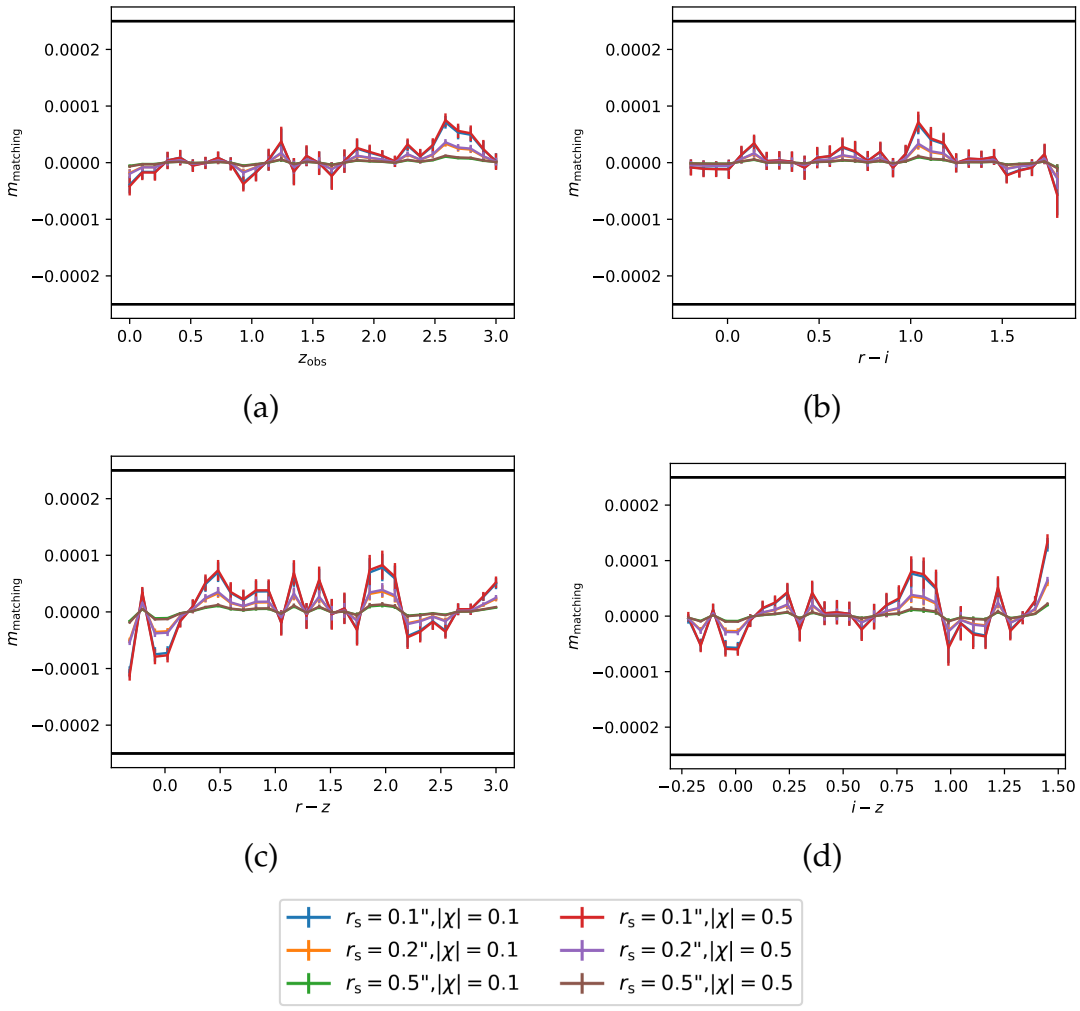


Figure 3.14: The multiplicative SED-matching shear bias m_{matching} arising when SED are sampled on a grid with $N_{\mathrm{axis},d} = [8, 18, 12, 10]$, for $d = [r-i, r-z, i-z, m_{\mathrm{VIS}}]$ respectively, with an additional 1000 low-$r-z$ SEDs sampled, and matched to catalogue galaxies in the space of $(z_{\mathrm{obs}}, r-i-r-z, i-z, m_{\mathrm{VIS}})$. m_{matching} calculated as a function of (a) z_{obs}, (b) $r-i$, (c) $r-z$, (d) $i-z$, on a grid of values of $(r_s, |\chi|)$. m_{matching} averaged over 1000 SEDs in each bin, with error bars showing the standard error on the mean. Black horizontal lines are the EWS PTO shear bias requirement (3.21) described in section 3.1.2.

due to the colour-redshift relation of galaxies in the Flagship 2 mock.

It should also be noted that the mean shear biases as a function of $z_{\mathrm{obs}}, r-i, r-z, i-z$ respectively do not have the same mean when averaged over all bins, because the samples are defined such that there are 1000 galaxies in each bin.

Finally, the impact of averaging the shear bias estimates over more than 1 nearest-neighbour is investigated. In this case, when distances in the $(z_{\mathrm{obs}}, r-i, r-z, i-z)$-space are calculated, neighbouring SEDs are assigned a weight, given by the reciprocal of their distance to the matched catalogue-galaxy. Distances

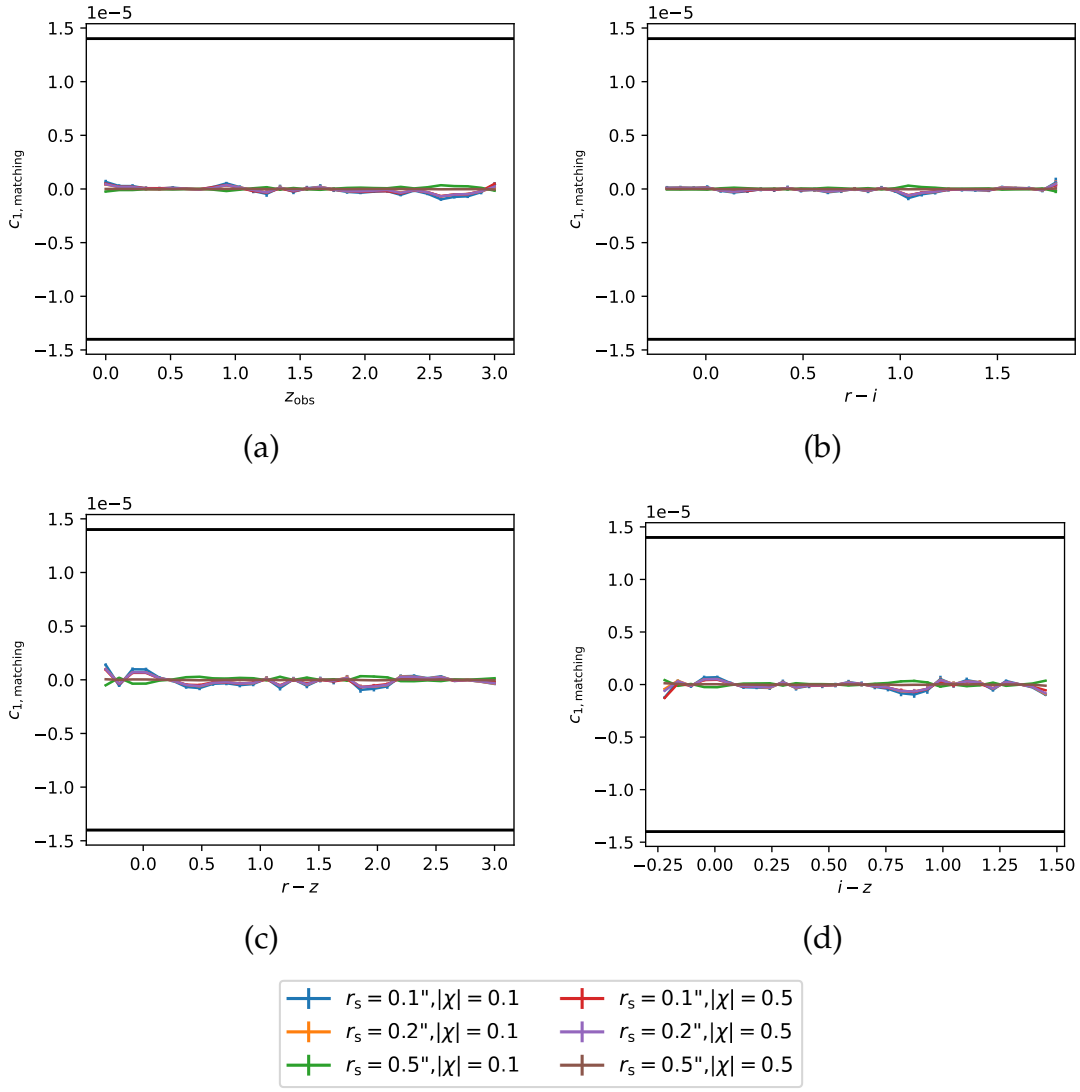


Figure 3.15: The same as fig. 3.14, showing the additive SED-matching shear bias component $c_{1,\mathrm{matching}}$. Black horizontal lines are the EWS PTO shear bias requirement (3.22) described in section 3.1.2.

are calculated in the coordinates standardised by subtracting from the catalogue mean, and dividing by the catalogue standard deviation. The catalogue galaxies are then assigned shear bias estimates by calculating a weighted mean over the k-nearest neighbours in the sample. This is tested for the benchmark case of matching catalogue SEDs to SEDs sampled on the grid of $r-i, r-z, i-z, m_{\mathrm{VIS}}$ with $N_{\mathrm{axis},d} = [8, 18, 12, 10]$, for $d = [r-i, r-z, i-z, m_{\mathrm{VIS}}]$ respectively, with distances calculated in the standardised $(z_{\mathrm{obs}}, r-i, r-z, i-z)$-space. The extreme case of $r_s = 0.1''$, $|\chi| = 0.5$ is adopted, with $k = [1, 2, 3, 4, 5]$ considered. The results for m_{matching} are shown in fig. 3.17, as a function of z_{obs}. The k-nearest-neighbour-

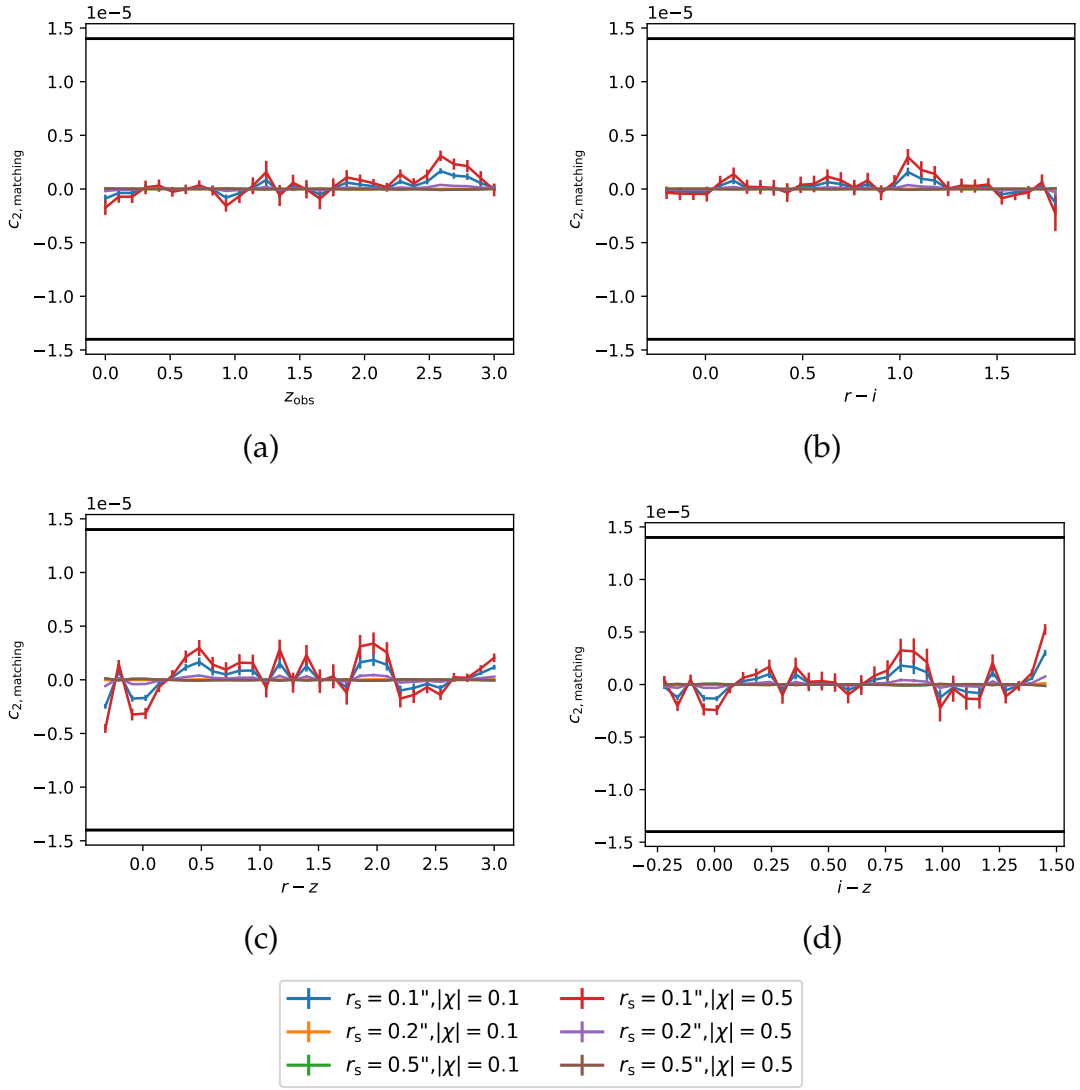


Figure 3.16: The same as fig. 3.14, showing the additive SED-matching shear bias component $c_{2,\mathrm{matching}}$. Black horizontal lines are the EWS PTO shear bias requirement (3.22) described in section 3.1.2.

averaged SED-matching bias is plotted without the requirements for clarity.

As can be seen in fig. 3.17, averaging over $k > 1$ nearest neighbours does not substantially affect the performance of the SED matching with respect to the EWS requirements, as evaluated by the multiplicated SED-matching shear bias m_{matching}. Increasing k may result in reduced variance of the shear bias estimates, though the significance of this effect is minor. At high and low redshifts the magnitude of the SED-matching m-bias is systematically larger when averaged over a larger number of neighbours. The sensitivity of the shear bias estimates to k is also tested as a function of $r-i, r-z, i-z$ and is verified to not have

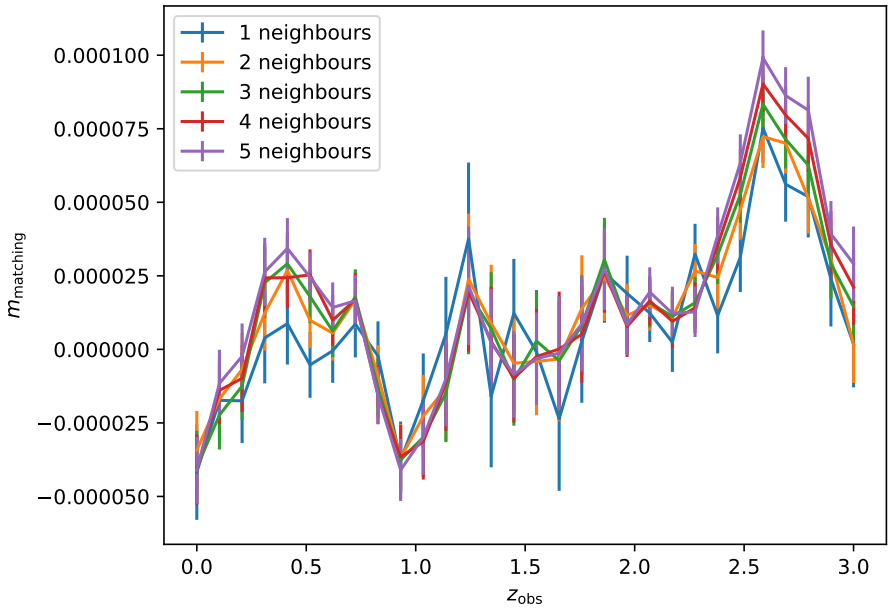


Figure 3.17: The multiplicative SED-matching shear bias m_{matching} as a function of z_{obs}, averaged over k nearest neighbours, arising when SED are sampled on a grid with $N_{\mathrm{axis},d} = [8, 18, 12, 10]$, for $d = [r-i, r-z, i-z, m_{\mathrm{VIS}}]$ respectively, with an additional low-$r-z$ SEDs sampled, and matched to catalogue galaxies in the $(z_{\mathrm{obs}}, r-i, r-z, i-z)$-space. m_{matching} calculated for $(r_s = 0.1'', |\chi| = 0.5)$. m_{matching} averaged over 1000 SEDs in each bin, with error bars showing the standard error on the mean. PTO requirement on the multiplicative bias is omitted for clarity.

a significant impact. It is verified that this is also true for the additive bias components $c_{1,\mathrm{matching}}$ and $c_{2,\mathrm{matching}}$.

The profiles of the redshift-variation of the shear bias components shown in the upper-left panels of figs. 3.9 to 3.16 are of note due to the dependence and impact on cosmology of this variation; in particular, it depends on the colour-redshift relation of galaxies in the catalogue. In particular, as can be seen in figs. 3.9 to 3.12, the shear bias components are strongly negative at low redshift, before rising to a peak at redshift $\sim$1, before plateauing at high redshift (this behaviour is mostly inverted for c_1, see fig. 3.10). This occurs when galaxy SEDs in the basis set are randomly sampled, and is largely alleviated when the basis set of SEDs is sampled using the colour grid method. In the former case, this causes galaxies with SEDs that are not well-represented in the catalogue to be matched with SEDs that are not likely to be close to them in the colour-space. If a galaxy is assigned an SED that is bluer than the galaxy is in realtity, then the corresponding PSF size will be

underestimaed (which may be argued e.g. based on Fraunhofer diffraction); as a result, the PSF will be under-corrected, leading to a suppression of the shear and negative SED-matching shear bias, dragging down the mean m-bias. By the inverse argument, galaxies which are assigned an SED that is redder than they are in reality will result in a positive SED-matching shear bias, dragging up the mean m-bias. This also impacts the additive bias components. If the error in the SED matching is strongly colour-dependent, then the strong redshift-dependence of the SED-matching shear biases therefore results from the redshift-dependence of the distribution of galaxy colours, which arises as a result of the evolution of the galaxy population. A similar effect is relevant to the shear biases arising due to SED errors discussed in chapter 4.

3.3.3 Morphology and FoV Interpolation

Having calculated shear biases for a sample of galaxies in the Flagship 2 catalogue, on a grid of galaxy size r_s, ellipticity modulus $|\chi|$, and x, y FoV-position, and having matched these sample galaxies to catalogue galaxies based on their SEDs, the final step in the catalogue-level shear bias estimation is to interpolate the shear bias estimates to the galaxy shape parameters and FoV position. This is done by firstly interpolating the shear bias estimates over r_s and $|\chi|$ in two 1-dimensional linear interpolations, followed by a bilinear spline interpolation over the x, y FoV position. To construct the interpolants for the galaxy shape interpolation, r_s is sampled in 5 points geometrically spaced in the range $[0.1'', 0.5'']$. The ellipticity modulus $|\chi|$ is sampled at $[0.1, 0.3, 0.5]$. For the FoV interpolation, the FoV is sampled on a uniform 3×3 grid, with the outer 8 grid points sampled at the boundary of the FoV. The 1-dimensional interpolation and bivariate splines are implemented using the `scipy.interpolate` package for `python`. It is verified that the `scipy RectBivariateSpline` routine runs similarly accurately and with somewhat shorter computational time than other 2-dimensional interpolation routines on a regular grid, in particular `RegularGridInterpolator`, also available in `scipy.interpolate`.

The interpolation scheme is tested by calculating shear biases on two grids of $r_s, |\chi|$ and x, y FoV-position; one on which to construct the interpolants, and one on which to evaluate the interpolants in order to test the accuracy of the interpolation. Shear biases are calculated for 500 mock galaxies at each point in the interpolation grids, by taking two random high-resolution ("truth-channel") Flagship 2 SEDs (see section 3.3.1) as truth- and error-channel inputs, respectively, for each galaxy, calculating the PSF error using the PSF toolkit (see section 3.2.1) and the resulting shear bias using the shear bias calculation described in section 3.2.2. To construct the interpolants, shear biases are calculated on a 3×3 grid on the FoV, and for 5 values of r_s and 3 values of $|\chi|$ sampled in the ranges described above. To test the interpolants, shear biases are calculated on a 6×6 grid on the FoV, 7 values of r_s within the above-stated range, and 5 values of $|\chi|$ within the above-stated range.

Initially, the first approach that was considered was to conduct a bivariate spline over r_s and $|\chi|$, followed by another bivariate spline over x, y. For both the $r_s - |\chi|$ and $x - y$ interpolation steps, the interpolants are constructed using (i) bilinear splines and (ii) bivariate splines of order 2, and the results are compared. Interpolation knots and test points are sampled uniformly (in this case, not geometrically for any parameter) in the ranges described above. It is found that the mean of the residual errors Δm, Δc_1, and Δc_2 are within the requirements of the EWS, though with substantial tails. Moreover, the order of the interpolation does not seem to significantly impact the residual errors in the resulting shear bias estimates. Averaging Δm over the 500 galaxy SEDs, with the corresponding histogram shown in the left panel of fig. 3.18, shows that the distribution of residual error in the shear bias as a function of the shape parameters are varied is multimodal. This behaviour arises because the bivariate spline interpolation over $r_s, |\chi|$ is substantially biased as a function of $|\chi|$, with galaxies with particular ellipticity-modulus values having systematically-biased interpolated m-bias estimates. Such a systematic bias in the shear bias estimates that is strongly correlated with the galaxy ellipticity modulus is an unacceptable bias in our method.

In order to reduce the bias in the shape-parameter interpolation, the bivariate

spline over r_s and $|\chi|$ was replaced by sequential 1-dimensional interpolations over each. In this case, interpolation knots and test points are sampled uniformly in the ranges described above, and the two cases of (i) all interpolation steps conducted at linear order, and (ii) a cubic interpolation over r_s, followed by a quadratic interpolation over $|\chi|$, followed by a bivariate spline of order 2 over x, y, are compared. Again, it is found that the order of the interpolations does not significantly change the residual errors in the resulting shear bias estimates. Replacing the bivariate spline over r_s and $|\chi|$ with two separate 1-dimensional interpolations over the galaxy shape parameters also results in reduced residual error in the m-bias estimates. Averaging over the 500 SEDs, as shown in the right panel of fig. 3.18, shows that replacing the bivariate spline over the shape parameters with two sequential 1-dimensional interpolations removes the systematic bias as a function of ellipticity. It should be noted that if the order of the r_s and $|\chi|$ interpolations is switched, then biased results as a function of $|\chi|$ as seen in the left panel of fig. 3.18 are reproduced.

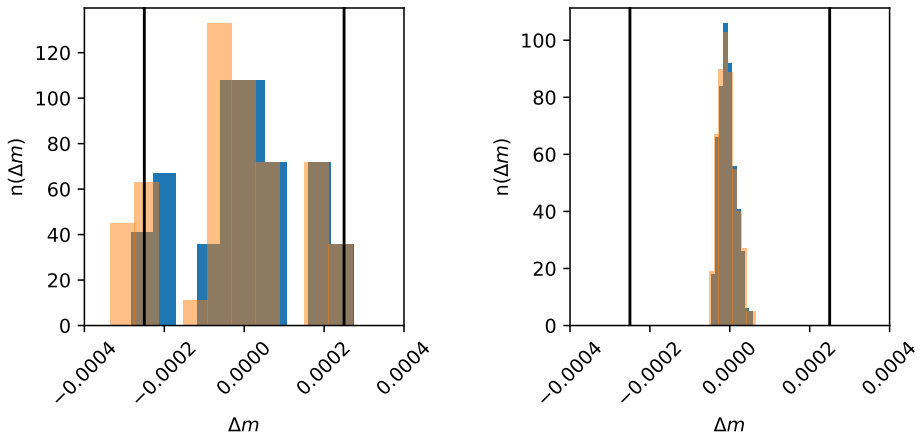


Figure 3.18: Histogram of residual error in multiplicative bias Δm arising when a bivariate spline is used to interpolate over the galaxy shape parameters, averaged over 500 SED pairs. Multimodality arises due to bias as a function of $|\chi|$. Blue: order 2 bivariate splines used. Orange: Bilinear splines used. Black vertical lines are the EWS PTO shear bias requirements (3.21), (3.22), as described in section 3.1.2.

The next refinement that was applied was to replace the sampling of r_s with uniformly spaced point, with sampling with points geometrically spaced in the same interval, and constructing the interpolant and conducting the interpolation

in the space of the natural logarithm of r_s. This is applied and tested with the same (uniformly-spaced) test points as described above. The final histograms of residual errors in the shear bias estimates arising due to the morphology and FoV interpolation are shown in fig. 3.19.

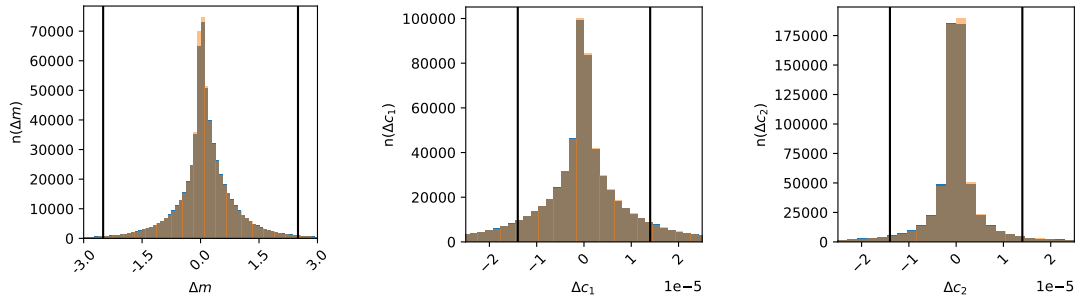


Figure 3.19: Histograms of residual error in shear bias arising when sequential 1-dimensional interpolation is used to interpolate over the galaxy size r_s and ellipticity modulus $|\chi|$, and the r_s interpolation knots are sampled geometrically in the range $[0.1'', 0.5'']$. Data points correspond to one of 500 SED pairs, and a point in the 5×3 shape-parameter sampling and 3×3 FoV sampling. Blue: order 3 and 2 1-dimensional interpolation used to interpolate of r_s,$|\chi|$ respectively, order 2 bivariate spline used for FoV interpolation. Orange: 1-dimensional linear interpolation used for the morphology interpolation, and a bilinear spline used for the FoV interpolation. Top: error in multiplicative bias Δm. Middle: error in additive bias component Δc_1. Bottom: error in additive bias component Δc_2. Black vertical lines are the EWS PTO shear bias requirements (3.21), (3.22), as described in section 3.1.2.

It is found that sampling r_s with geometric rather than uniform spacing does not substantially reduce the mean bias of the shear bias estimates, but it does make the histograms of residual error in the additive estimates more sharply peaked, reducing the tails, and is therefore more suitable than the uniform-sampling case. This is because the geometric r_s sampling more closely follows the distribution of galaxy sizes in the mock catalogue. This effect is particularly large for c_1. While this slightly increases the variance of the multiplicative bias compared with the uniformly-spaced r_s samples, this is modest compared with the gain for c_1. For this reason, this sampling of r_s is adopted. It is found, as seen in fig. 3.19, that the interpolation order does not significantly impact the accuracy of the resulting shear bias estimates; using linear interpolation at all steps results in a $\sim 40\%$ reduction in the computation time compared to the higher-order case, mostly due to reductions

in time in the 1-dimensional shape-parameter interpolation steps. Hence linear interpolation (including a bilinear spline for the x, y-interpolation) is adopted.

As shown in fig. 3.19, the mean residual errors in the shear bias estimates arising due to the morphology and FoV interpolation are small compared to the EWS PTO requirements described in section 3.1.2. However, the distributions of residuals have wide tails; this is especially the case for the c_1 additive bias component. As described in section 3.1.2, it is sufficient that errors in the mean shear bias estimates are sub-dominant, rather than negligible, with respect to the relevant requirements, for a source of shear measurement error that is expected to represent a significant fraction of the error budget. This is because sub-dominant shear bias errors are small compared to shear biases that are comparable with or larger than requirements, whereas for small shear biases, it is sufficient to show that they are within requirements, which is satisfied in the case of sub-dominant shear bias errors.

An additional note should be made about the variations of the additive bias, which in fig. 3.19 are shown to be comparable to the scale of the PTO requirement. In the case of the additive bias, the angular power spectra are impacted by variation in the additive bias $\sigma[\boldsymbol{c}]$, rather than its mean value (Massey et al., 2013)[4]. However, fig. 3.19 shows the distribution of *per-galaxy* shear bias residual errors, whereas the additive shear bias is by definition averaged over a large number of galaxies, of order $\sim 10^2$. Therefore, when the residual shear bias errors shown in fig. 3.19 are averaged over a sample of galaxies of size relevant to shear measurement, the variation in the residual errors will be reduced, such that the variations in these average additive-bias residual errors will satisfy the requirement described above, that they be sub-dominant with respect to the requirement. The performance of the morphology and FoV interpolation is hence considered to be satisfactory for the purposes of this work.

It has also been verified that increasing the resolution of the sampling of galaxy shape parameter and FoV position interpolation knots does not significantly

[4]However, this does not hold for the 2-point correlation function.

change the performance of the interpolation scheme. This was tested by replacing the test samples with the interpolation samples (the former chosen to have higher resolution in both galaxy shape parameters and FoV position), and vice-versa.

3.4 Conclusion

3.4.1 Summary

In this chapter, a method for estimating the cosmic shear measurement biases that are expected to arise in the EWS due to errors in the assumed PSF, for mock galaxies in the Flagship 2 simulated catalogue, is described. Due to the high dimensionality of the space which galaxies inhabit, and which the PSF (and hence the resulting shear bias) depends on, combined with the computational cost of estimating the PSF error and propagating this through to estimated shear bias, it is a significant challenge to efficiently estimate such shear biases for a large number of galaxies in the mock. The general approach taken has been to calculate shear biases for a subset of points in this space, and devise an interpolation scheme to infer shear bias estimates for mock galaxies in the catalogue.

The dimensions over which the shear bias needs to be interpolated includes the space of galaxy spectra, morphology, and FoV-position. In general it also includes position on the survey footprint (or equivalently, epoch), and this will be discussed in chapter 5. The interpolation over this space has been achieved by defining a sub-sample of galaxy SEDs from the Flagship 2 mock, for which shear biases will be calculated on a grid of galaxy exponential-disc scalelength r_s, ellipticity modulus $|\chi|$, and FoV-position x, y. In order to reduce the risk of coherent sub-populations of galaxies with systematically biased shear bias estimates, the SED sampling was conducted on a grid defined in the space of observed redshift $z_{\rm obs}$, colour indices $r-i, r-z, i-z$ and Euclid VIS magnitude $m_{\rm VIS}$ (section 3.3.1).

Given the sub-sample of SEDs selected, shear biases may then be calculated from a given source of PSF error, by passing truth- and error-channel inputs to the *Euclid* OU-SHE PSFTOOLKIT, which outputs corresponding truth- and error-channel PSFs (section 3.2.1). A likelihood-maximisation technique based on an

iterative quadratic estimator is used to estimate the additive and multiplicative shear biases that result from this PSF error (section 3.2.2). The PSF generation and shear bias calculation have been optimised to ensure speed and accuracy of the estimation (section 3.2.3).

Having calculated shear bias estimates for the sample of SEDs and on the grid of $r_s, |\chi|$ and FoV x, y, catalogue galaxies are matched to sample galaxies in order to estimate shear bias values for the former. Multiple SED sampling and matching schemes were considered, and it was found that the highest accuracy in the estimated shear biases was achieved by finding the nearest-neighbour of each catalogue SED in the sample, with distance defined in the space of $z_{\rm obs}, r-i, r-z, i-z, m_{\rm VIS}$, standardised by subtracting the catalogue mean and dividing by the catalogue standard deviation, and assigning the corresponding shear bias values (on the galaxy shape, FoV-grid) to the catalogue galaxy (section 3.3.1). The shear biases are then finally interpolated over the shape parameters, with sequential 1-dimensional linear interpolations over $r_s, |\chi|$, and a bilinear spline over FoV x, y (section 3.3.3). Each step of this pipeline has been tested and validated in order to optimise its speed and accuracy.

3.4.2 Applications and Future Work

The methodology presented in this chapter may be used the propagate realistic sources of PSF error into per-galaxy additive and multiplicative shear bias estimates, for galaxies in the Euclid Flagship 2 mock catalogue. In chapter 4, this method is applied to the PSF error that arises due to noisy, broad-band SEDs that are used to reconstruct the chromatic broadband VIS PSF for Euclid. High-resolution SEDs from Flagship 2, and corresponding noisy mock photometric fluxes, are passed to the PSFTOOLKIT and used to generate resulting shear bias estimates. This is used to forecast the dependence of the shear bias on galaxy properties, including redshift and VIS magnitude. Sampling from tomographic redshift distributions $n_i(z)$ defined for the Flagship 2 simulation, provided by I.

Tutusaus (*priv. comm.*), mean m-biases per tomographic redshift bin are estimated, and propagated to biases in cosmological parameters.

In chapter 5, the methodology is applied to the case of PSF modelling errors arising due to thermal variations in the spacecraft which are not included in the PSF model, and induce temporal variation into the PSF. The PSF takes as input variations in the Zernike coefficients (i.e. coefficients of a basis set describing the wavefront that reaches the exit pupil of the telescope) with respect to a baseline determined by in-orbit calibration data. This varies as a function of pointing, introducing an additional degree of freedom in the shear bias estimation. From the estimated temporal variation of the PSF, shear bias HEALPIX maps are produced.

The methodology presented in this chapter provides a forward-modelling approach to forecasting the impact that PSF error may have on cosmic shear measurement and cosmology with a greater degree of realism than has been previously available. A significant advantage is that it allows the realistic propagation of various sources of PSF error through the Euclid science pipeline to cosmology, rather than simpler prescriptions for such systematics inserted at an intermediate stage, such as at the 2-point level, which may not propagate in such a realistic way (Cropper et al., 2013; Massey et al., 2013). Additionally, propagating the impact of systematics to the catalogue-level, rather than e.g. considering only the impact of systematics on summary statistics, allows the impact of such systematics on other observables e.g. higher-order statistics to be investigated. This is of particular benefit for the analysis of stage-IV surveys such as the EWS, for which expected large data volumes are expected to drive interest in novel observables (Euclid Collaboration: Ajani et al., 2023; Euclid Collaboration: Pires et al., 2020). Forward-modelling the impact of systematics at the catalogue level provides the flexibility to propagate them to a wide variety of observables.

Another benefit is that, if other observational systematics can be forward-modelled in the catalogue in a similar way, then this approach allows a realistic investigation of the correlations and degeneracies between such systematics, and whether they may warrant further study. For example, the PSF error arising due

to imperfect galaxy SED information that will be investigated in chapter 4 will be correlated with photometric redshift error, because for Euclid, the same noisy broad-band ground-based photometry will be used to reconstruct the PSF, as well to infer photometric redshifts (Euclid Collaboration: Desprez et al., 2020; Euclid Collaboration: Mellier et al., 2024; Ma et al., 2006). It is difficult to forecast the full joint impact of both systematics without a detailed forward-modelling-based approach as described in this chapter, and future work will focus on this issue specifically.

They say more money more problems
Bring on the problems
Bring on the problems
Bring on the [...] problems...

— Drake & 21 Savage

4

Forecasting the Impact of Galaxy SED Errors on PSF Estimation, Shear Measurement, and Cosmological Inference for the EWS

Contents

4.1 Introduction 138
4.2 Forecasting Shear Bias Arising due to SED Errors 139
4.2.1 SED Errors in the EWS 139
4.2.2 Calculation of Shear Bias Arising Due to SED Errors for Mock Galaxies 141
4.2.3 Results and Discussion 144
4.3 Propagation of m-Bias to Parameter Estimation 164
4.3.1 Propagation of SED Errors to Tomographic Cosmic Shear Angular Power Spectra 166
4.3.2 Bias in Cosmological Parameters 169
4.3.3 Discussion 173
4.4 Conclusion 176
4.4.1 Summary 176
4.4.2 Future Work 178

4.1 Introduction

While the *Euclid* spacecraft will conduct an imaging survey using the VIS instrument in order to measure galaxy shapes, the *Euclid* Wide Survey will also take in complementary photometric measurements from ground-based observations, which are also essential to the weak lensing measurement (Euclid Collaboration: Mellier et al., 2024). Spectral information (in the form of multi-band photometry) is required to obtain photometric redshifts (Euclid Collaboration: Desprez et al., 2020), as well as to estimate the PSF for each target galaxy, which is highly chromatic, owing to the the broad passband of the VIS instrument (Euclid Collaboration: Cropper et al., 2024). While the *Euclid* spacecraft obtains space-based multi-band photometric measurements using the NISP instrument (Euclid Collaboration: Jahnke et al., 2024), this is a near-IR instrument and does not cover the VIS passband, and does not provide enough information to estimate SEDs (or photometric redshifts) for galaxies within the redshift range of the WL sample and the wavelength range of the VIS passband (Euclid Collaboration: Mellier et al., 2024).

As described in section 1.2.4, for the EWS, the PSF for a given target galaxy is estimated by an integral over the monochromatic PSFs, weighted by the throughput of the telescope and the SED of the target galaxy (1.22). Error in the assumed SED of a given galaxy therefore presents a source of PSF error that may impact the shear measurement for that galaxy. In particular, because it is unaffordable to obtain high-resolution spectra of all of the $\sim$1.5 billion galaxies that will be used for shear measurement (Euclid Collaboration: Mellier et al., 2024), the EWS relies on ground-based photometric measurements in broad photometric bands (see section 1.2.4); this results in a loss of spectral information due to the coarse wavelength sampling, and also introduces a noise bias into the PSF estimation due to the non-linear transformation between the galaxy SED and the profile of the PSF. This introduces bias in the shear measurement. Because this shear measurement bias depends on the SED of each measured galaxy, it is likely to be correlated with errors in the photometric redshift estimates (Eriksen and Hoekstra, 2018;

Euclid Collaboration: Desprez et al., 2020), as well as with other astrophysical systematics impacting the two-point statistics that are correlated with the galaxy colours such as intrinsic alignments (Crittenden et al., 2002), and as a result may have a substantial impact on the cosmological analysis. It is therefore of interest to forecast the impact of this source of PSF error for the EWS. Eriksen and Hoekstra, 2018 forecast the bias in the PSF size resulting from imperfect SED information for the EWS; the present work builds on previous work by estimating resulting shear biases and propagating to biases in cosmological parameters. Forecasting the impact of SED errors on the EWS shear measurement, and the propagation of this to biases in cosmological parameter estimates, is the focus of this chapter.

In this chapter, the methodology described in chapter 3 is used to estimate shear measurement biases arising due to SED errors for mock galaxies in the *Euclid* Flagship 2 catalogue (Euclid Collaboration: Castander et al., 2024). Mock photometric error-channel SEDs are obtained for a basis sub-sample of galaxies in the mock, and corresponding shear biases are calculated for this sub-sample, and then estimated for a test sample of galaxies in the rest of the catalogue, using the technique described in section 3.3. The calculation of shear biases arising due to SED errors for galaxies in the Flagship 2 mock is described in section 4.2. The dependence of the resulting shear bias on physical properties of the galaxies is investigated in section 4.2.3, and the impact of the shear biases arising due to SED errors on cosmological parameter estimation is investigated in section 4.3. The results and future prospects are summarised in section 4.4.

4.2 Forecasting Shear Bias Arising due to SED Errors for the EWS

4.2.1 SED Errors in the EWS

As described in section 1.2.4, the EWS will make extensive use of ground-based multi-band photometric galaxy data, both for the photometric redshift estimation (Euclid Collaboration: Desprez et al., 2020) and the PSF estimation. This will be obtained from a number of ground-based surveys covering the footprint of the

EWS, including LSST (Phillips Longley, 2021), DES (Abbott et al., 2021), CFHTLens (Coupon et al., 2009), Subaru (Aihara et al., 2022) and Pan-STARRS (Flewelling et al., 2020). The coarse-grained, noisy spectral information provided by this data results in error in the assumed SED of each target galaxy. In order to propagate the impact of this SED error to the shear measurement, it is necessary to pass mock truth- and error-channel SEDs for each galaxy as inputs to the shear bias calculation described in chapter 3 that is used to calculate the corresponding shear measurement biases.

The high-resolution, truth-channel mock SEDs that are assigned to galaxies in the *Euclid* Flagship 2 mock catalogue are described in section 3.3.1. To summarise, they each consist of a weighted linear combination of two template SEDs from the COSMOS survey (Ilbert et al., 2008), each with some extinction curve (one of five from (Ilbert et al., 2008)) together with an extinction coefficient, and with a redshift applied to the linear combination. Corresponding noisy photometric error-channel SEDs are provided by the *Euclid* Consortium Photometric Redshift Operational Unit (OU-PHZ). For each truth-channel SED, mock broad-band fluxes are generated by integrating the truth-channel SED over 7 photometric passbands (in this case, the DES *griz* bands (Flaugher et al., 2015) and the NISP *yjh* bands (Euclid Collaboration: Mellier et al., 2024) that are used for the EWS SED estimation at southern declinations), with noise added. The resulting broad-band SEDs are then matched to 12-band fluxes from the COSMOS survey (Ilbert et al., 2008), with mock COSMOS fluxes for the error-channel SED estimated by a weighted average of the 32 nearest-neighbours in the COSMOS sample. These medium-band fluxes are then upsampled to 100 narrow-band fluxes covering the entire VIS bandpass using Gaussian-process regression. This upsampling includes some extrapolation, because the COSMOS bands do not cover the red end of the VIS bandpass, up to $\sim 930\ \mathrm{nm}$ (Euclid Collaboration: Mellier et al., 2024). The generation of the mock error-channel SEDs is carried out by OU-PHZ and supplied by (W. Hartley & F. Tarsitano, *priv. comm.*). In order to incorporate the uncertainty arising due to photometric noise in the analysis conducted in this work, 10 realisations of each

noisy error-channel SED are generated per corresponding truth-channel SED.

Inhomogeneity of the photometric configurations between different ground-based surveys that will provide SED data for the EWS is neglected. Spatial variation of the photometry within each ground-based survey configuration, arising due to e.g. dependence on elevation via airmass, is also neglected. Additionally, the effect of polarisation of light from the observed galaxies, including the contribution of the dichroic surface within the *Euclid* spacecraft (see section 1.2.4), is also neglected.

The SED errors described in this section result in error in the assumed PSF and hence bias shear measurement. The propagation of these SED errors to shear measurement biases is described in section 4.2.2.

4.2.2 Calculation of Shear Bias Arising Due to SED Errors for Mock Galaxies

The methodology described in chapter 3 is used to estimate the shear biases arising due to SED errors, for galaxies in the *Euclid* Flagship 2 mock catalogue. To summarise, this takes as input truth- and error-channel SEDs, which are passed to the OU-SHE PSFTOOLKIT software to generate corresponding truth- and error-channel PSFs. A model-fitting method (Euclid Consortium: Miller et al., 2020b) is then used to estimate corresponding additive and multiplicative shear measurement biases (see section 3.2). This is done for a basis sub-sample of SEDs sampled from the Flagship 2 mock catalogue, on a grid of values of galaxy exponential-disc scalelength, ellipticity modulus, and FoV position; shear bias estimates are then obtained for galaxies in the mock using a combination of (i) nearest-neighbour matching galaxy truth-channel SEDs to those in the sub-sample, and (ii) interpolation over the galaxy shape parameters and FoV position (see section 3.3).

The basis sub-sample of 30,100 truth-channel SEDs is defined as described in section 3.3.1. For each of these, 10 noisy realisations of narrow band photometric error-channel SEDs are provided by OU-PHZ (W. Hartley & F. Tarsitano, *priv.*

comm.). These are passed to the shear bias calculation pipeline described in section 3.2, and additive and multiplicative shear biases are calculated for each SED in the basis sub-sample, on a grid of five galaxy scalelength r_s values geometrically spaced in the range $[0.1'', 0.5'']$, and three ellipticity modulus $|\boldsymbol{\chi}|$ values linearly spaced in the range $[0.1, 0.5]$; this is repeated for each central point on a regular 3×3 grid on the FoV (see section 3.2.2 and section 3.3.3).

The focus of this work is to investigate the dependence of the shear measurement bias arising due to SED errors on the physical properties of mock galaxies in the Flagship 2 mock, including VIS magnitude m_{VIS}, observed redshift z_{obs}, and galaxy colour. In order to achieve this, the approach taken in this section is to sample galaxies from the mock in equipopulated bins in these physical parameters, and estimate the mean shear bias values for galaxies in these bins. For each sampled galaxy, the shear bias is estimated as described in section 3.3.1, with the galaxy SED matched to its nearest-neighbour in the basis sub-sample, and the shear bias values interpolated over the corresponding grid of shape parameters and FoV position, as described in section 3.3.3.

In the Flagship 2 mock catalogue, the distribution of galaxy scalelengths and ellipticity moduli extends beyond the bounds of the shape parameter grid on which the basis sample of shear bias values is calculated. A selection is therefore imposed on the sampled galaxies, masking out galaxies with scalelength lying outside the interpolation range. For the galaxy ellipticity moduli, in order to avoid introducing a shear-dependent selection which might bias an end-to-end analysis, the shear bias estimates are linearly extrapolated for ellipticity moduli lying outside the interpolation range. It is verified that errors in the shear bias estimates introduced due to the extrapolation are subdominant compared with the PTO shear bias requirements (3.21) and (3.22), with respect to which the results of this chapter are compared, satisfying the requirement on the shear bias estimation discussed in section 3.1.2, and it is also verified that the $|\boldsymbol{\chi}|$ extrapolation has a sub-dominant impact on the results presented in this chapter.

Mean per-bin additive and multiplicative shear biases are estimated, as a

function of VIS magnitude $m_{\rm VIS}$, observed redshift $z_{\rm obs}$, and colour index $r-i$ (with r, i magnitudes defined as described in section 3.3.1). Additionally, the mean effective wavelength of an SED $\mathcal{M}_\lambda$ is defined as follows:

$$\mathcal{M}_\lambda = \frac{\int d\lambda T(\lambda) S_{\rm gal}(\lambda) \lambda}{\int d\lambda T(\lambda) S_{\rm gal}(\lambda)}, \tag{4.1}$$

with $T(\lambda)$ the VIS instrument optical throughout (see section 1.2.4), and $S_{\rm gal}(\lambda)$ the galaxy SED; the denominator is equivalently the VIS flux $F_{\rm VIS}$. Mean per-bin shear bias estimates are also calculated as a function of the effective mean wavelength $\mathcal{M}_\lambda^{\rm truth}$ corresponding to each truth-channel SED, as well as for the bias in effective mean wavelength between truth- and error-channel SEDs (averaged over the 10 noise realisations per SED pair), $\Delta\mathcal{M}_\lambda = \mathcal{M}_\lambda^{\rm truth} - \langle \mathcal{M}_\lambda^{\rm error} \rangle$.

For each of the galaxy properties $m_{\rm VIS}$, $z_{\rm obs}$, $r-i$, $\mathcal{M}_\lambda^{\rm truth}$, $\Delta\mathcal{M}_\lambda$, mean shear bias estimates are calculated for 15 bins in each parameter; shear biases are averaged over 10 noise realisations per SED-pair, and over 1000 galaxies randomly drawn from the corresponding bin in the Flagship 2 mock catalogue. If fewer than 1000 galaxies exist in the catalogue in any particular bin, the total number of galaxies in that bin are sampled.

Moreover, because the EWS total requirement on the additive bias is on its statistical uncertainty (Massey et al., 2013, see section 3.1.2), the standard deviation of the absolute value of the additive shear bias $\sigma[|\boldsymbol{c}|]$ arising due to SED errors is also calculated, for 15 bins as a function of the galaxy properties $m_{\rm VIS}$, $z_{\rm obs}$, $r-i$, $\mathcal{M}_\lambda^{\rm truth}$, $\delta\mathcal{M}_\lambda$.

For all galaxy properties except $m_{\rm VIS}$, when sampling mock galaxies from the Flagship 2 catalogue to build selections that are binned in galaxy property, a limiting VIS magnitude selection cut is imposed on the galaxy sample of $m_{\rm VIS} \leq 24.5$. This is the nominal limiting magnitude of the EWS (Euclid Collaboration: Mellier et al., 2024) that is expected to be set by the noise in the VIS imaging as well as in the complimentary ground-based photometry.

In chapter 3, the sensitivity of the SED-matching to the choice of SED-sampling and matching grid axis parameter $N_{{\rm axis},m_{\rm VIS}}$ was not investigated, owing to the

insensitivity of the errors in the SED sampling and matching algorithm to photometric noise. This parameter is set as $N_{\mathrm{axis},m_{\mathrm{VIS}}} = 10$; the analysis is repeated with values $N_{\mathrm{axis},m_{\mathrm{VIS}}} = 8, 12$ and it is verified that the results presented in section 4.2.3 are not sensitive to the choice of the value of this parameter.

In section 4.2.3, shear biases as a function of the Flagship 2 galaxies properties described above are presented. Dependence of the SED effective mean wavelength on the other galaxy properties m_{VIS} and z_{obs} is also shown for illustrative purposes. The spatial variation of the shear biases on the FoV is presented and discussed in section 4.2.3.

The results presented in section 4.2.3 demonstrate that the shear measurement biases that arise due to PSF error resulting from imperfect knowledge of galaxy SEDs in many cases exceeds the propagate-to-object requirement on the knowledge of the PSF (see section 3.1.2), and in some cases the total EWS shear bias requirements (section 3.1.2). This effect therefore poses a substantial source of systematic bias in the EWS cosmological analysis. In section 4.3, the impact of the multiplicative shear bias arising due to SED errors is propagated to cosmological parameter inference. In section 4.4, possible mitigation approaches are discussed.

4.2.3 Results and Discussion

It should be noted that, in the shear bias plots presented in fig. 4.1–fig. 4.12, mean shear biases averaged over all bins will not necessarily be consistent, because the bins are sampled to be equipopulated (or populated with the total number of galaxies present in the catalogue in each bin, if fewer). This corresponds to a selection that is not necessarily representative of the catalogue population, or consistent between binning schemes.

Dependence of Shear Bias on Galaxy Properties

The multiplicative and 2-component shear biases as functions of VIS magnitude m_{VIS}, averaged over galaxies from the *Euclid* Flagship 2 mock catalogue in 15 bins in m_{VIS}, are respectively shown in fig. 4.1, with sub-plots showing breakdowns of

the sample by (i) "central" and "satellite" galaxies, and (ii) "red sequence", "green valley", and "blue cloud", as identified in the Flagship 2 mock. The multiplicative and 2-component additive shear biases are respectively shown as functions of $z_{\rm obs}$ in fig. 4.2; as functions of $r-i$ in fig. 4.3; as functions of $\mathcal{M}_\lambda^{\rm truth}$ in fig. 4.4; and as functions of $\Delta\mathcal{M}_\lambda$ in fig. 4.5. As in chapter 3, shear biases are plotted along with the total EWS shear bias requirements (Euclid Collaboration: Mellier et al., 2024) (see section 3.1.2), as well as the propagate-to-object requirements that are relevant to the PSF (see section 3.1.2). When shear bias values are typically sub-dominant with respect to the corresponding PTO requirement, the total EWS shear bias requirement has been omitted for clarity. The error bars for each bin are given by the standard error on the mean, estimated using the law of total variance (Weiss et al., 2005), by adding contributions from the variance of the mean shear bias estimated for the 10 noise realisations each galaxy SED, and from the variance of the shear bias estimates for the (up to) 100 galaxies sampled in each bin, and calculating the corresponding standard error $SE(\bar{b})$ for shear bias estimate $\bar{b}$ (Montgomery, 2019):

$$\mathrm{SE}(\bar{b}) = \sqrt{\frac{\sigma^2_{\rm gal}}{N_{\rm gal}} + \frac{\sum_i^{N_{\rm gal}} \sigma^2_{{\rm realis},i}}{N_{\rm gal} N_{\rm realis}}}, \tag{4.2}$$

where $\sigma^2_{\rm gal}$ is the variance of the noise-averaged shear bias estimates $\bar{b}$ for the $N_{\rm gal}$ galaxies sampled in each bin, and $\sigma^2_{{\rm realis},i}$ is the variance of the shear bias values estimated for each of the $N_{\rm realis} = 10$ noise realisations for galaxy i, such that the galaxy-averaged variance of the noise-averaged shear bias estimates is $\sum_i^{N_{\rm gal}} \sigma^2_{{\rm realis},i}/N_{\rm realis}$.

Discussion of dependence on galaxy properties

The shear measurement biases arising due to SED errors as a function of $m_{\rm VIS}$ are shown in fig. 4.1. The m-bias (panels (a),(b)) remains roughly stable until $m_{\rm VIS} \gtrsim 26$, at which point it sharply increases in magnitude. The same is true for the c_1 additive bias component (panels (c), (d)). This magnitude dependence of the shear biases is as expected, because photometric observations of galaxies at fainter

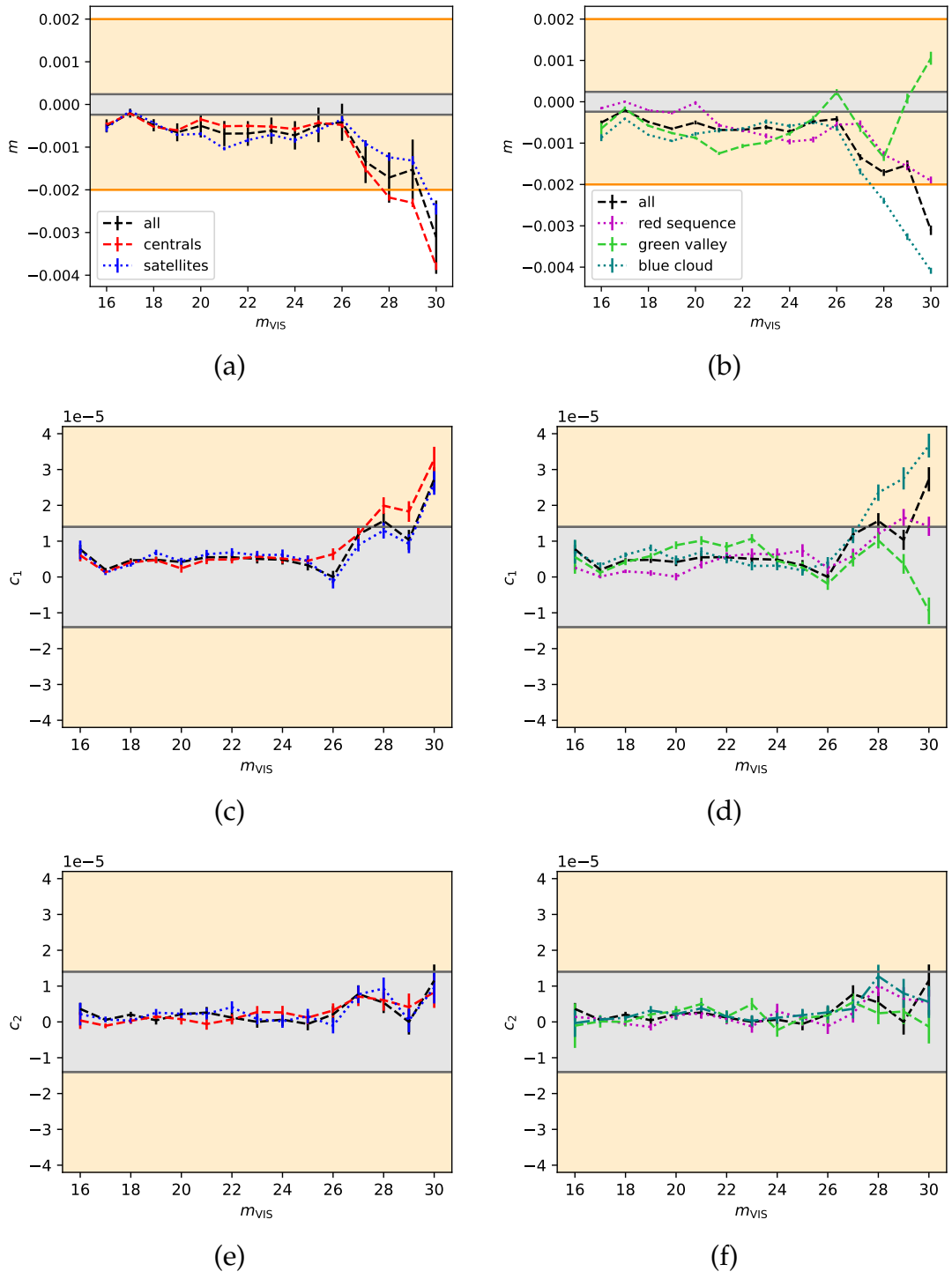


Figure 4.1: Mean shear bias components m, c_1, c_2 as functions of VIS magnitude $m_{\rm VIS}$. Averaged over 1000 galaxies from the *Euclid* Flagship 2 mock in each bin (or the total number present in the mock in each bin if fewer). Top row, (a), (b): m component. Middle row, (b), (c): c_1 component. Bottom row, (c), (d): c_2 component. Left column, (a), (c), (e): galaxy sample broken down into centrals and satellites. Right column, (b), (d), (f): galaxy sample broken down into red sequence, green valley, and blue cloud galaxies. The orange shaded region corresponds to the range within the EWS total requirement (see section 3.1.2); the grey shaded region corresponds to the range within the PSF propagate-to-object requirements (see section 3.1.2).

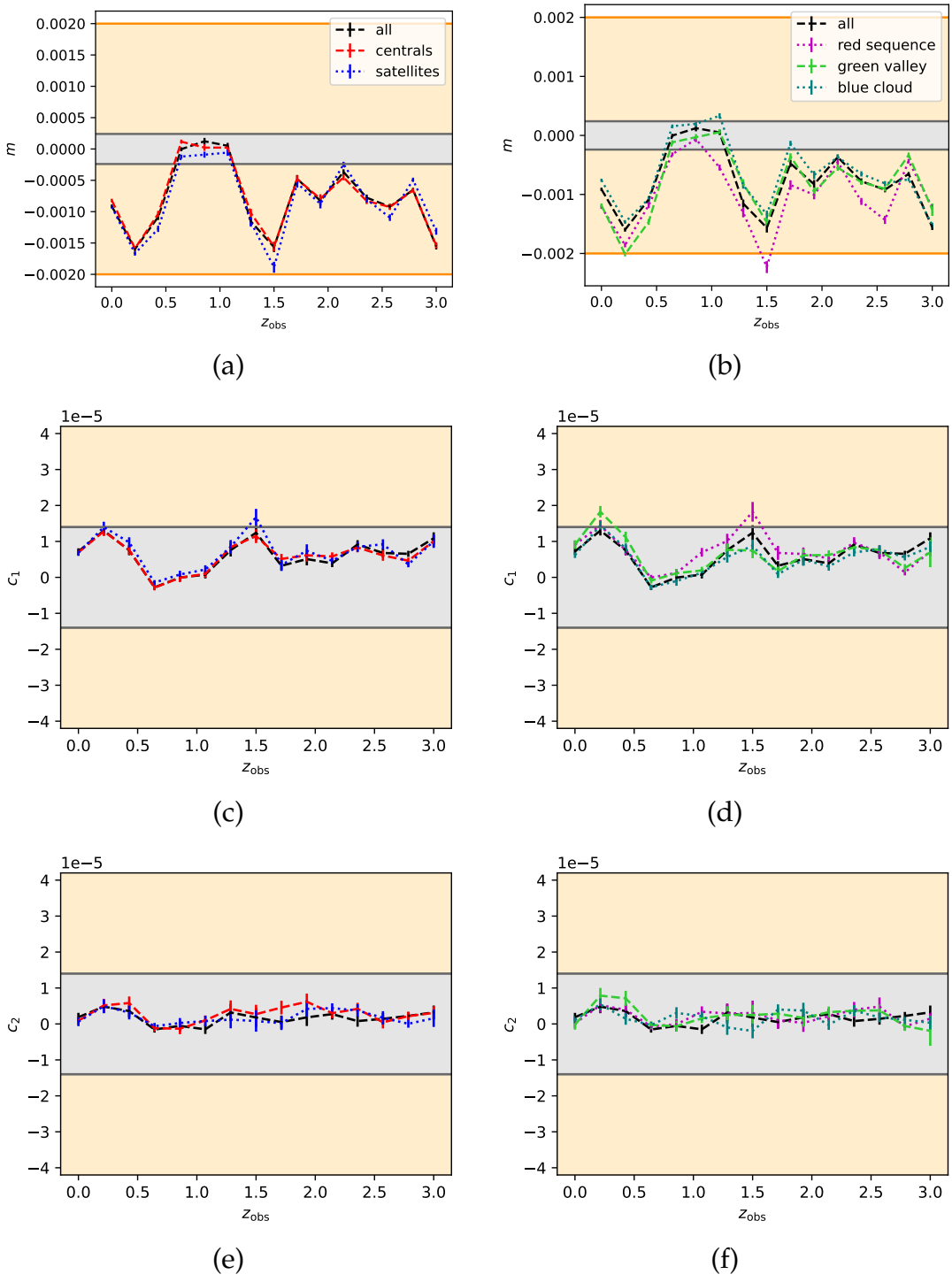


Figure 4.2: Mean shear bias components m, c_1, c_2 as functions of observed redshift $z_{\rm obs}$. Averaged over 1000 galaxies from the *Euclid* Flagship 2 mock in each bin (or the total number present in the mock in each bin if fewer). Top row, (a), (b): m component. Middle row, (b), (c): c_1 component. Bottom row, (c), (d): c_2 component. Left column, (a), (c), (e): galaxy sample broken down into centrals and satellites. Right column, (b), (d), (f): galaxy sample broken down into red sequence, green valley, and blue cloud galaxies. The orange shaded region corresponds to the range within the EWS total requirement (see section 3.1.2); the grey shaded region corresponds to the range within the PSF propagate-to-object requirements (see section 3.1.2).

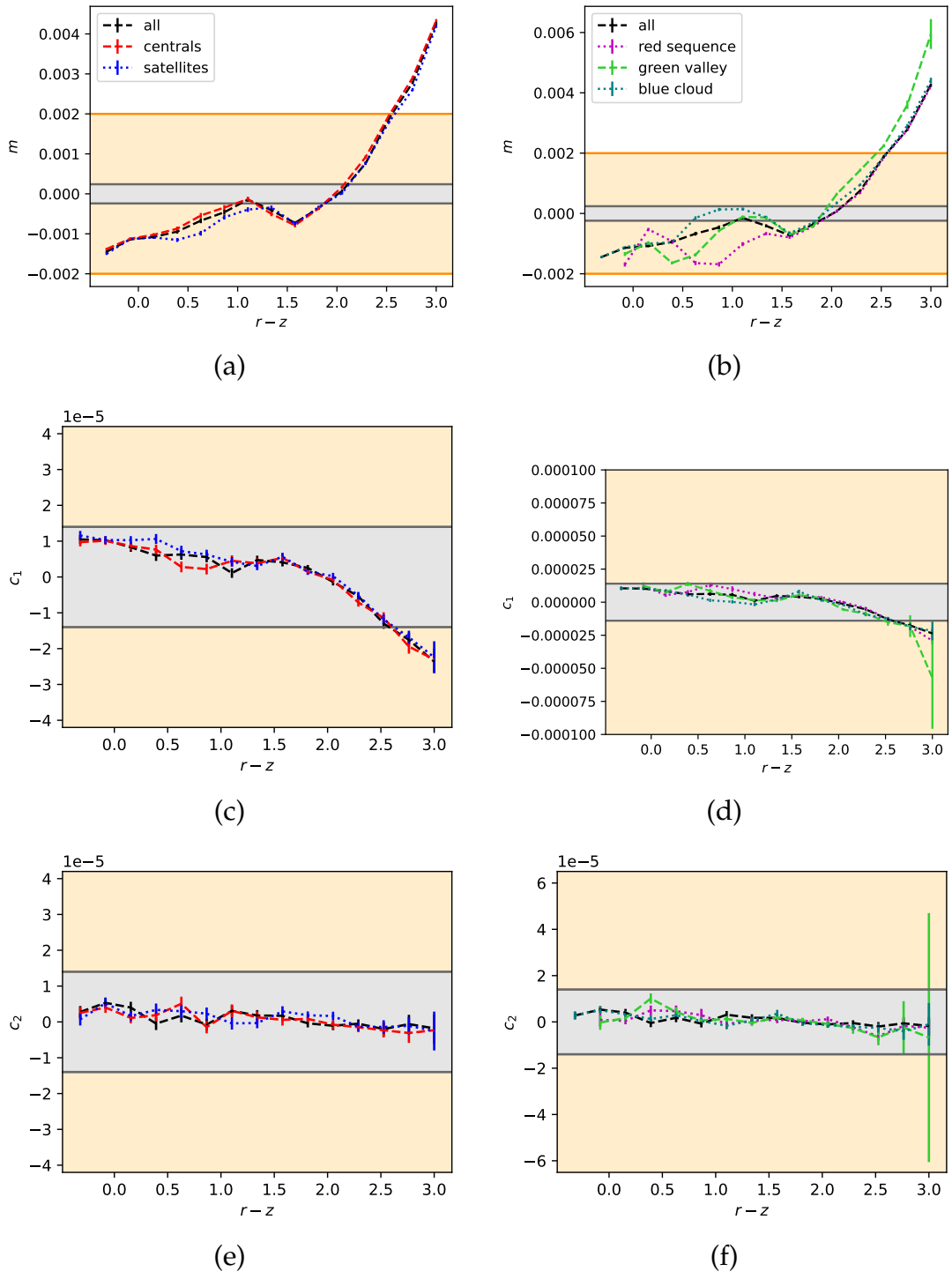


Figure 4.3: Mean shear bias components m, c_1, c_2 as functions of colour index $r - z$. Averaged over 1000 galaxies from the *Euclid* Flagship 2 mock in each bin (or the total number present in the mock in each bin if fewer). Top row, (a), (b): m component. Middle row, (b), (c): c_1 component. Bottom row, (c), (d): c_2 component. Left column, (a), (c), (e): galaxy sample broken down into centrals and satellites. Right column, (b), (d), (f): galaxy sample broken down into red sequence, green valley, and blue cloud galaxies. The orange shaded region corresponds to the range within the EWS total requirement (see section section 3.1.2); the grey shaded region corresponds to the range within the PSF propagate-to-object requirements (see section 3.1.2).

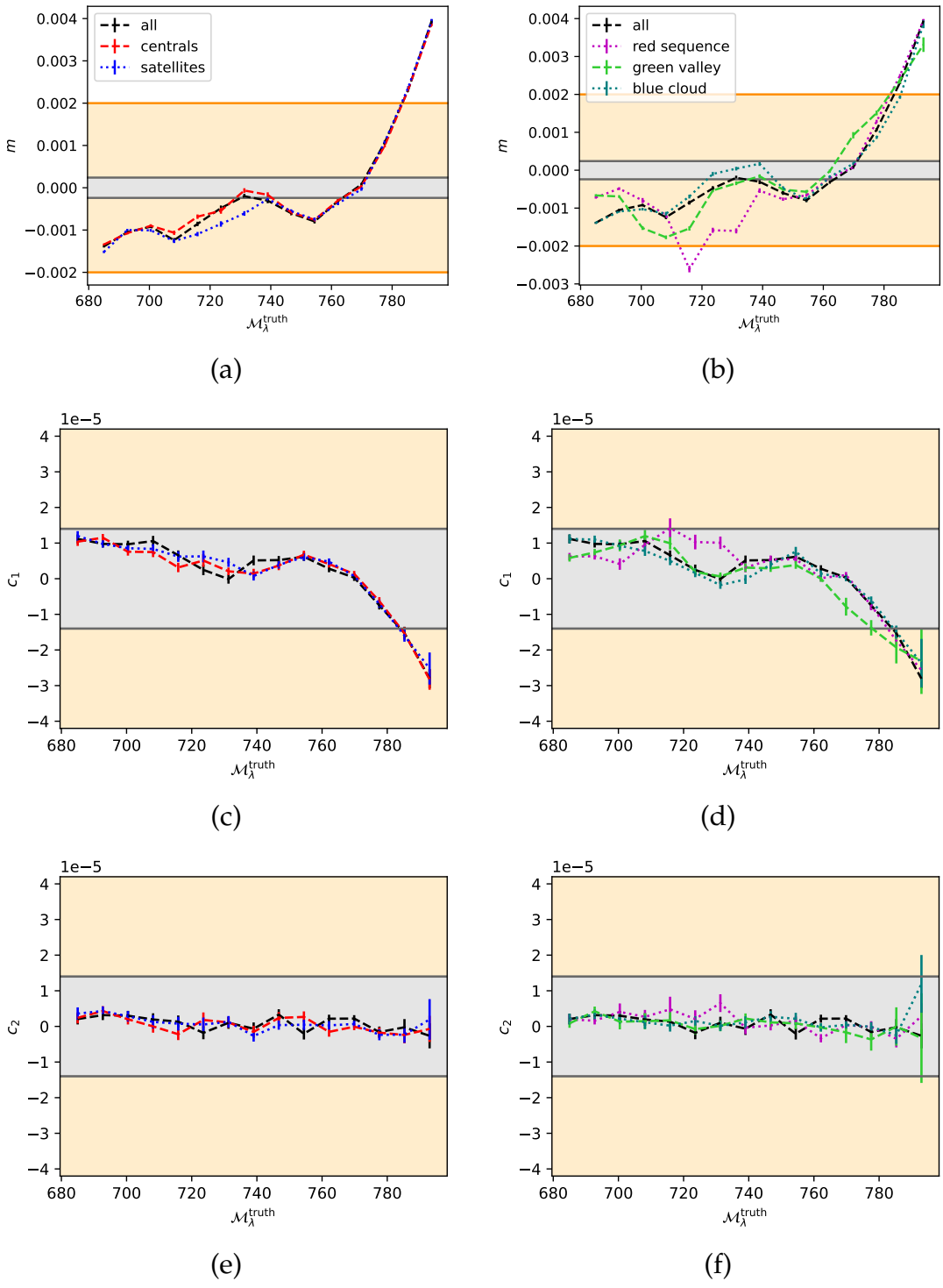


Figure 4.4: Mean shear bias components m, c_1, c_2 as functions of truth-channel SED mean effective wavelength $\mathcal{M}_\lambda^{\mathrm{truth}}$. Averaged over 1000 galaxies from the *Euclid* Flagship 2 mock in each bin (or the total number present in the mock in each bin if fewer). Top row, (a), (b): m component. Middle row, (b), (c): c_1 component. Bottom row, (c), (d): c_2 component. Left column, (a), (c), (e): galaxy sample broken down into centrals and satellites. Right column, (b), (d), (f): galaxy sample broken down into red sequence, green valley, and blue cloud galaxies. The orange shaded region corresponds to the range within the EWS total requirement (see section 3.1.2); the grey shaded region corresponds to the range within the PSF propagate-to-object requirements (see section 3.1.2).

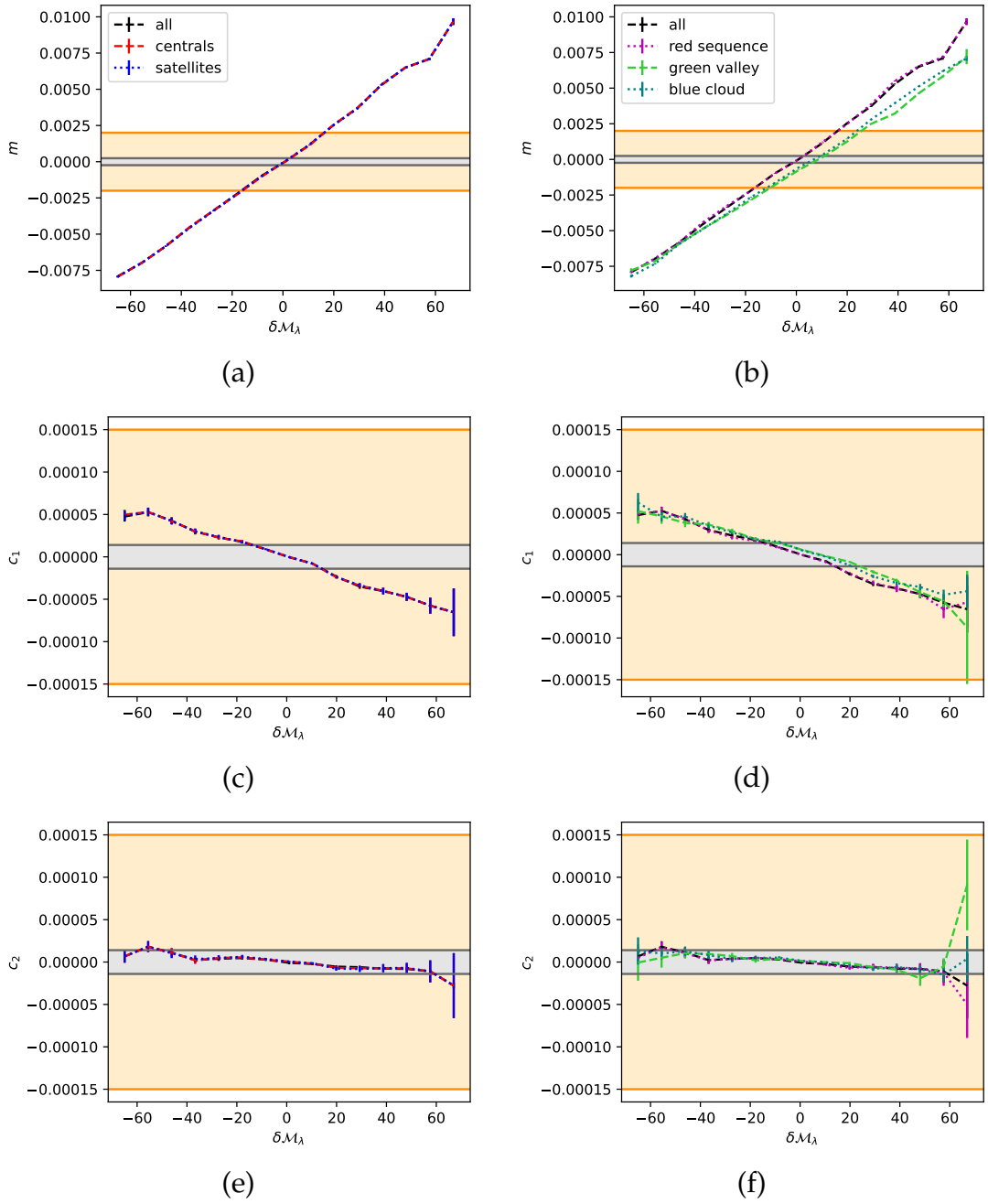


Figure 4.5: Mean shear bias components m, c_1, c_2 as functions of bias in SED mean effective wavelength $\delta\mathcal{M}_\lambda$. Averaged over 1000 galaxies from the *Euclid* Flagship 2 mock in each bin (or the total number present in the mock in each bin if fewer). Top row, (a), (b): m component. Middle row, (b), (c): c_1 component. Bottom row, (c), (d): c_2 component. Left column, (a), (c), (e): galaxy sample broken down into centrals and satellites. Right column, (b), (d), (f): galaxy sample broken down into red sequence, green valley, and blue cloud galaxies. The orange shaded region corresponds to the range within the EWS total requirement (see section 3.1.2); the grey shaded region corresponds to the range within the PSF propagate-to-object requirements (see section 3.1.2).

magnitudes will have lower signal-to-noise ratios, making the PSF estimation for these galaxies more susceptible to photometric noise bias. This also results in the increasing size of the error bars with m_{VIS} seen in fig. 4.1. There is also a contribution arising due to decreasing galaxy size with magnitude that also results in increasing shear biases with magnitude. In general, the c_1 additive bias component is more sensitive to SED errors than the c_2 component (panels (e), (f)), likely due to anisotropy in the PSF.

Because the EWS will apply a limiting magnitude of $m_{\mathrm{VIS}} < 24.5$[1] (Euclid Collaboration: Mellier et al., 2024), galaxies fainter than this will have negligible impact on the cosmological analysis, and it is the stable shear biases at magnitudes below the limiting magnitude that are of interest. For subsequent plots and in the cosmology propagation in section 4.3, a hard magnitude cut of $m_{\mathrm{VIS}} < 24.5$ is applied; it should be noted that this is likely not representative of any non-binary weighting scheme that will be applied in the EWS analysis.

The dependence of the shear biases on observed redshift z_{obs} is shown in fig. 4.2. Varying shear bias with redshift is of substantial importance to cosmological analysis, because in the definition of the tomographic angular power spectra (1.14) it is degenerate with both the redshift source distribution $N(z)$ and the underlying matter power spectrum (section 1.1.4, Kilbinger, 2015). In fig. 4.2, it can be seen that in particular the multiplicative shear bias arising due to SED errors (panels (a), (b)) exhibits rapid variations with z_{obs} on scales comparable to the total EWS requirements (and substantially larger than the error bars), and can therefore be expected to have a substantial impact on the cosmological analysis. The precise dependence of the shear bias on redshift depends on both the dependence of the shear bias on the galaxy SEDs, and the relation between the galaxy SEDs and z_{obs} in the survey. This effect is similar to the strongly redshift-dependent SED-matching shear bias described in section 3.3.2, and the m-bias has a qualitatively similar profile; that effect also occurs as a result of the colour-redshift relation in

[1] In particular, rather than a hard magnitude cut, the EWS cosmological analysis may employ a shear/photometric redshift weighting scheme that will down-weight galaxies with higher uncertainty in the shear and photometric redshift measurements; this is expected to be relevant for galaxies fainter than $m_{\mathrm{VIS}} \sim 24.5$ (Euclid Collaboration: Mellier et al., 2024).

the catalogue; the redshift-dependence of the SED-error-sourced shear bias has a large impact on cosmological inference, as discussed in section 4.3. As can be seen in panels (c)-(f) of fig. 4.2, the mean additive bias is approximately within the PSF propagate-to-object requirement at all redshifts.

In order to understand the redshift dependence of the multiplicative shear bias, the dependence of the truth-channel SED mean effective wavelength $\mathcal{M}_\lambda^{\rm truth}$ on $z_{\rm obs}$ is shown in fig. 4.6, as a proxy for the colour-redshift relation in the catalogue. This may be compared with panels (a) and (b) of fig. 4.4, which show a generally increasing dependence of the m-bias on $\mathcal{M}_\lambda^{\rm truth}$. This may drive the apparent correlation between the $z_{\rm obs}$ profiles of the m-bias (fig. 4.2 (a,b)) and of $\mathcal{M}_\lambda^{\rm truth}$ (fig. 4.6), with the profiles of each displaying a peak at $z_{\rm obs} \sim 0.8$, with a lower average m-bias at higher redshifts. Indeed, the increasing trend of the m-bias with $\mathcal{M}_\lambda^{\rm truth}$ shown in fig. 4.4 (a), (b) may be explained by chromaticity of the error in the SED reconstruction and the transformation to shear measurement biases, by a similar mechanism as described in section 3.3.2 – i.e. that, if the SED reconstruction causes galaxies to be interpreted as bluer than they are in reality, this will result an under-correction for the PSF size, suppression of the shear, and negative shear biases; and vice-versa for galaxies that are interpreted as redder than they are in reality. It may also be noted that the redshift-dependence of $\mathcal{M}_\lambda^{\rm truth}$ (fig. 4.6) exhibits a correlation with the total forecast $N(z)$ for the EWS, as shown in figure 4 of Euclid Collaboration: Mellier et al., 2024, with a corresponding correlation between the m-bias redshift profile and the $N(z)$ that may have a significant impact on the cosmological analysis.

In addition to the combination of chromaticity of the error in the SED reconstruction and the transformation to shear measurement biases, the strong dependence on $\mathcal{M}_\lambda^{\rm truth}$ o the m-bias may also be connected to the colour-magnitude relation in the catalogue. To investigate the latter contribution, the dependence of $\mathcal{M}_\lambda^{\rm truth}$ on $m_{\rm VIS}$ is shown in fig. 4.7, from which it can be seen that fainter galaxies have on average *shorter* mean effective wavelengths than galaxies brighter than the magnitude cut of $m_{\rm VIS} < 24.5$. In contrast, fig. 4.4 (a), (b) demonstrates

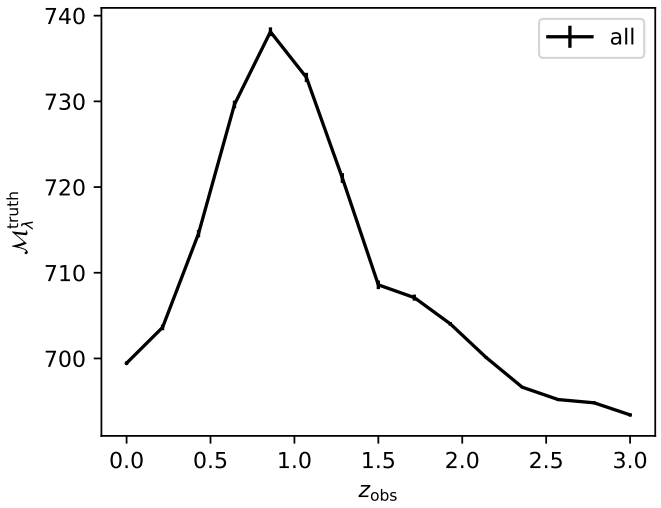


Figure 4.6: The dependence of $\mathcal{M}_\lambda^{\rm truth}$ on $z_{\rm obs}$ in the Flagship 2 mock catalogue. $\mathcal{M}_\lambda^{\rm truth}$ averaged over 1000 SEDs per redshift bin, and error bars show the standard error on the mean.

increasing m-bias at *longer* mean effective wavelengths[2]. This implies a mutual link between magnitude, colour, and shear bias. However, a comparison of the $m(\mathcal{M}_\lambda^{\rm truth})$ relationship shown in fig. 4.4 and the $\mathcal{M}_\lambda^{\rm truth}(m_{\rm VIS})$ relationship shown in fig. 4.7 should not be used to draw conclude that the chromaticity of the m-bias is driven by the $\mathcal{M}_\lambda^{\rm truth}(m_{\rm VIS})$ relationship for two main reasons; firstly, because the overall trend of the m-bias with $m_{\rm VIS}$ shown in fig. 4.1 (a), (b) at magnitudes $m_{\rm VIS} < 24.5$ is weak, such that it likely does not explain the increasing trend present in fig. 4.4 (a), (b); and secondly, because the sample of galaxies represented in fig. 4.4 is dominated by fainter galaxies closer to the magnitude limit, for which the profile present in fig. 4.7 is approximately stationary or decreasing.

The dependence of the additive bias components c_1, c_2 on $\mathcal{M}_\lambda^{\rm truth}$ is shown in panels (c)-(f) of fig. 4.4. The c_1 (panels (c), (d)) component of the additive bias exhibits a stronger dependence on $\mathcal{M}_\lambda^{\rm truth}$ than the c_2 component (panels (e), (f)), likely arising due to anisotropy in the PSF. Unlike the case of the m-bias (panels (a), (b)), the c_1-bias is comparable to the PSF PTO requirement only at the longest values of $\mathcal{M}_\lambda^{\rm truth}$, and is substantially below this requirement for all values of $\mathcal{M}_\lambda^{\rm truth}$ for the c_2-bias.

[2]Note that due to the magnitude cut applied in the galaxy sample represented in fig. 4.4, this should only be compared with the region $m_{\rm VIS} < 24.5$ of fig. 4.7.

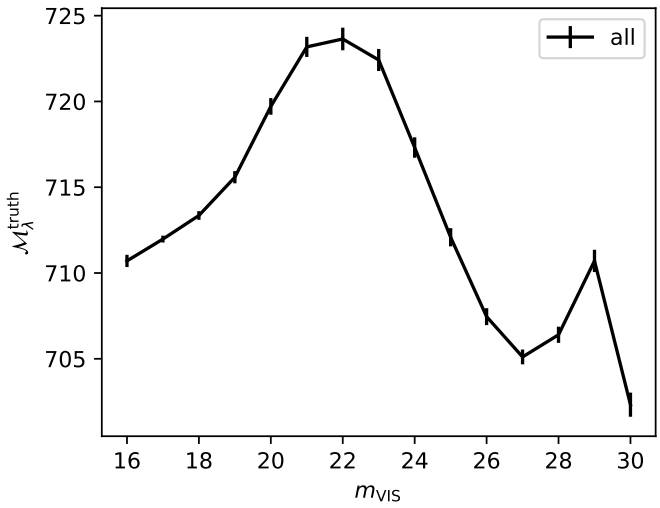


Figure 4.7: The dependence of $\mathcal{M}_\lambda^{\rm truth}$ on $m_{\rm VIS}$ in the Flagship 2 mock catalogue. $\mathcal{M}_\lambda^{\rm truth}$ averaged over 1000 SEDs per magnitude bin, and error bars show the standard error on the mean.

The dependence of the shear biases on the colour index $r-z$ is shown in fig. 4.3. For all components of the shear bias, panels (a)-(f), the shear bias profile with $r-z$ follows closely the corresponding trend with $\mathcal{M}_\lambda^{\rm truth}$ shown in fig. 4.4, indicating a relationship between $\mathcal{M}_\lambda^{\rm truth}$ and $r-z$ that is close to linear, indicating that they contain similar information about the SED.

The dependence of the shear biases on the (noise-averaged) bias in the SED mean effective wavelength, $\delta\mathcal{M}_\lambda = \mathcal{M}_\lambda^{\rm truth} - \langle\mathcal{M}_\lambda^{\rm error}\rangle$ is shown in fig. 4.5. The m-bias (panels (a), (b)) exhibits a very significant linear relationship with $\delta\mathcal{M}_\lambda$, and an increasingly noisy linear (inverse) relationship with c_1, c_2 respectively. The linear relationship can be understood heuristically in terms of Fraunhofer diffraction, in which, for small diffraction angles of order arcseconds, as is relevant to the PSF, for a diffraction-limited telescope with aperture diameter D, the diffraction angle $\alpha \propto \lambda/D$, with λ the wavelength of incoming light. Such a telescope has a PSF given by the Airy disc (Airy, 1835), which in the small-angle approximation is given by:

$$I(\theta) = I_0\left(\frac{2J_1[\pi D\theta/\lambda]}{\pi D\theta/\lambda}\right)^2, \tag{4.3}$$

as a function of diffraction angle θ, where J_1 is the first-order Bessel function of the first kind, and I_0 is the intensity at the centre of the Airy disc. Evaluating the

PSF weighted size-squared $R^2_{\rm PSF}$ using equation (3.1) and (3.2), it may then be shown that, in the limit of a weight function that is large compared to the size of the PSF, the PSF size-squared tends to (Miller et al. *in prep.*):

$$R^2_{\rm PSF} \rightarrow \sqrt{\frac{2}{\pi}}\alpha\sigma_W, \tag{4.4}$$

where σ_W parametrises the size of the weight function present in (3.1), and (4.4) is valid in the regime that $\sigma_W > \alpha$. Given this linearity of $R^2_{\rm PSF}$ in α, and hence in the wavelength λ, it can be seen from equations (3.9) and (3.10) that the multiplicative and additive biases should be roughly linear in the bias in the mean effective wavelength (absent any $\delta\boldsymbol{\chi}_{\rm PSF}$ in (3.10)). Moreover, the increasing error bars on the additive bias terms in fig. 4.5 ((c)-(f)) with increasing $|\delta\mathcal{M}_\lambda|$ indicates increasing $|\delta\mathcal{M}_\lambda|$ at fainter magnitudes (due to larger photometric noise in the SEDs), which is consistent with larger shear biases.

The linearity of the m-bias in $\delta\mathcal{M}_\lambda$ also explains the trends with $r-z$ and $\mathcal{M}^{\rm truth}_\lambda$ shown respectively in fig. 4.3 and fig. 4.4 (a,b), which is probably also the main driver for the redshift dependence shown in fig. 4.1. Figure 4.5 (a,b) shows that galaxies with negative $\delta\mathcal{M}_\lambda$ obtain negative m-bias, and those with positive $\delta\mathcal{M}_\lambda$ obtain positive m-bias; that is, as argued above, galaxies that are interpreted as redder than they are in reality (positive $\delta\mathcal{M}_\lambda$) are assigned a PSF that is larger than it should be, such that the shear measurement pipeline over-compensates for the size of the PSF; since increasing PSF size acts to (multiplicatively) suppress the shear, this will result in a multiplicatively-enhanced shear estimate i.e. positive m-bias (and vice-versa for negative $\delta\mathcal{M}_\lambda$). Since fig. 4.3 and fig. 4.4 (a,b) indicate that bluer galaxies obtain negative m-bias on average, and redder galaxies positive m-bias, this indicates that the SED reconstruction has the mean effect of interpreting blue galaxies as bluer than they are in reality, and red galaxies as redder than they are in reality, i.e. the mean effective wavelengths are exaggerated on average.

The linearity of the shear biases in $\delta\mathcal{M}_\lambda$, a metric summarising the performance of the SED reconstruction, indicates that it may be possible to introduce a correction for the shear biases sourced from SED errors using SED information. This is discussed in section 4.4.

Dependence on galaxy sub-population

In the Flagship 2 mock catalogue, galaxies are assigned labels depending on if they are identified as (i) "central" galaxies, or "satellite" galaxies, and (ii) belonging to the "red sequence", "green valley", or "blue cloud" sub-populations (Euclid Collaboration: Castander et al., 2024). Since these populations have both chromatic dependence (via galaxy type, e.g. star-forming or elliptical, see e.g. Schawinski et al., 2014) as well as differing correlation with the large-scale structure (see e.g. Li et al., 2006; McCullough et al., 2024), any variation of the SED-error-sourced shear biases with these galaxy sub-populations may have cosmological relevance. It should be noted that the samples labelled "all" do not contain equal numbers of each sub-population, but are representative of the catalogue sub-population distribution, and as such the samples labelled "all" are averages of the other samples *weighted* by relative sub-population sizes in the catalogue.

In fig. 4.1–fig. 4.12, the shear biases are shown broken down by sub-population, with the (i) "centrals" vs. "satellites" breakdown shown in the left-hand sub-plots, and (ii) "red sequence" vs. "green valley" vs. "blue cloud" shown in the right-hand sub-plots. In general, the dependence on breakdown (i) is sub-dominant compared with the main shear bias trends, likely due to weaker chromatic dependence of these sub-populations (e.g. both early-type and late-type galaxies may be centrals, see e.g. Laganá et al., 2010), although in general (at VIS magnitudes of interest to the EWS) "satellites" more frequently have higher-magnitude mean shear biases than "centrals", possibly due to their typically smaller sizes.

On the other hand, the dependence of shear biases on breakdown (ii) is more significant than on breakdown (i), due to the explicit chromaticity of these sub-populations. For example, the multiplicative bias for "red sequence" galaxies is in some cases (i.e. parts of the samples binned in $z_{\rm obs}$, $r-z$ and $\mathcal{M}_\lambda^{\rm truth}$, shown in fig. 4.2, fig. 4.3, and fig. 4.4 (a), respectively) substantially lower (more negative) than the other sub-populations. This contrasts with the generally *positive* m-biases on average for redder galaxies seen in fig. 4.3 and fig. 4.4 (a,b); this is probably because the extreme red end of galaxies with $r-z>2.0$, $\mathcal{M}_\lambda^{\rm truth}>$

$770\mathrm{nm}$ and large positive m-bias is not highly-represented in the catalogue, with most galaxies in this sub-population having more intermediate values of $r-z$ and $\mathcal{M}_\lambda^{\mathrm{truth}}$. In general, the dependence on the shear biases with the three sub-populations of breakdown (ii) is highly complex, and varies significantly with the sample selection represented in fig. 4.1–fig. 4.12, and the corresponding impact on cosmological inference is difficult to predict without forward-modelling it. This is discussed further in section 4.4.

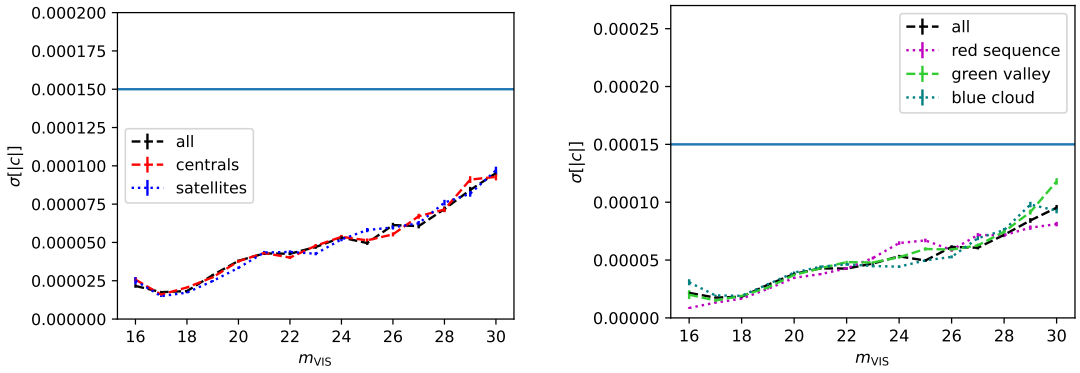
Standard deviation of additive shear bias

The standard deviation of the absolute value of the additive shear bias is also calculated, over the distribution of c-biases for galaxies sampled in 15 bins in each galaxy property described above, with c-biases averaged over the 10 noise realisations for each galaxy, calculated over noise-averaged c-biases for 1000 galaxies in each bin. The standard deviation of the absolute value of the additive bias $\sigma[|\boldsymbol{c}|]$ is calculated for the two sample breakdown schemes described above. $\sigma[|\boldsymbol{c}|]$ is shown as a function of m_{VIS}, z_{obs}, $r-i$, $\mathcal{M}_\lambda^{\mathrm{truth}}$, and $\delta\mathcal{M}_\lambda$ in fig. 4.8, fig. 4.9, fig. 4.10, fig. 4.11, and fig. 4.12, respectively. $\sigma[|\boldsymbol{c}|]$ is compared with the EWS total requirement (see section 3.1.2). The error bars are calculated by assuming that the c-bias estimates are Gaussian-distributed, such that the variance on the sample variance $S^2[|\boldsymbol{c}|]$ may be approximated as $\mathrm{Var}(S^2[|\boldsymbol{c}|]) \approx 2\sigma^4[|\boldsymbol{c}|]/(N_{\mathrm{gal}}-1)$ (O'Neill, 2014); the standard error on the sample variance is therefore the square root of this quantity. The corresponding standard error on the sample standard deviation $S[|\boldsymbol{c}|]$ may be approximated by Taylor expanding $S[|\boldsymbol{c}|] = \sqrt{S^2[|\boldsymbol{c}|]}$ to obtain:

$$\mathrm{SE}(S[|\boldsymbol{c}|]) \approx \frac{\sigma}{\sqrt{2(N_{\mathrm{gal}}-1)}}, \tag{4.5}$$

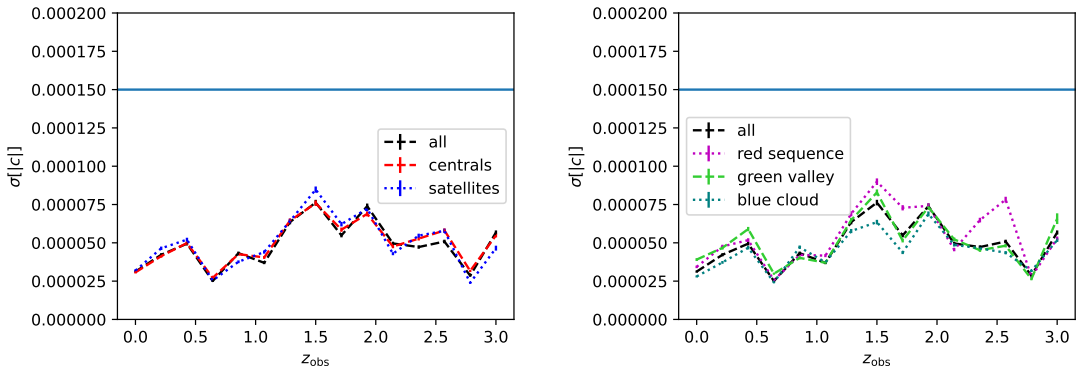
and the population standard deviation has contributions from the noise and from the variation between galaxies as in (4.2), without the factor of N_{gal}^{-1} because we seek the standard deviation.

In general, the size of $\sigma[|\boldsymbol{c}|]$ represent a non-negligible contribution, i.e. $\sim 1/3$, of the total *Euclid* requirement on the additive bias (see section 3.1.2), indicating that it will contribute to the error budget in the cosmological analysis for the



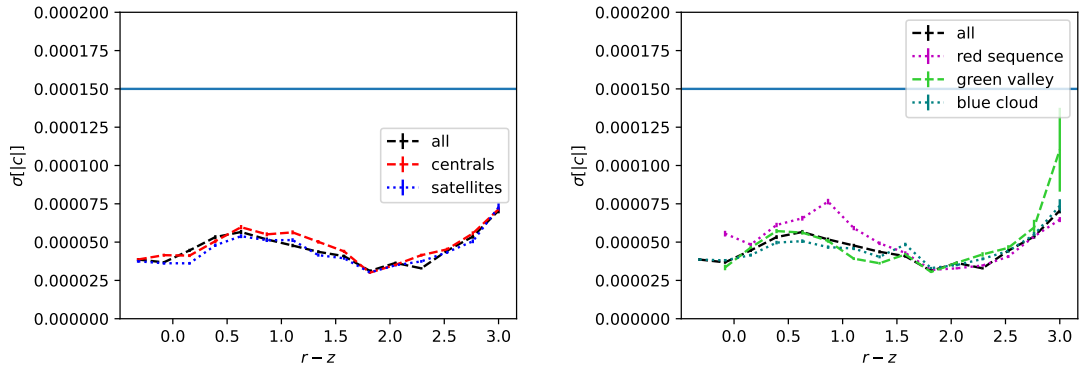
(a) (b)

Figure 4.8: Standard deviation of the absolute magnitude of the additive shear bias $\sigma[|\boldsymbol{c}|]$, as a function of VIS magnitude $m_{\rm VIS}$. Standard deviation calculated over 1000 galaxies sampled from the *Euclid* Flagship 2 mock catalogue in each bin (or the total number of galaxies present in the mock in each bin if fewer); per-galaxy shear biases averaged over 10 noise realisations. (a): galaxy sample broken down into centrals and satellites. (b): galaxy sample broken down into red sequence, green valley, and blue cloud galaxies. Horizontal line corresponds to EWS total requirement (see section 3.1.2).



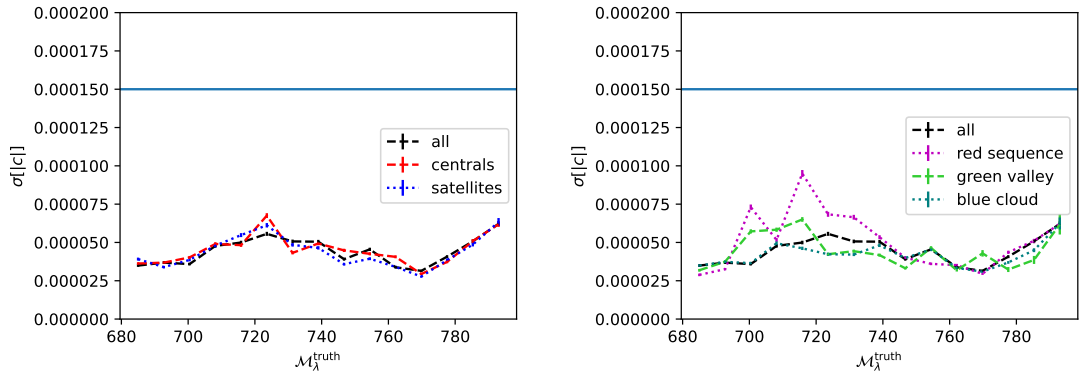
(a) (b)

Figure 4.9: Standard deviation of the absolute magnitude of the additive shear bias $\sigma[|\boldsymbol{c}|]$, as a function of observed redshift $z_{\rm obs}$. Standard deviation calculated over 1000 galaxies sampled from the *Euclid* Flagship 2 mock catalogue in each bin (or the total number of galaxies present in the mock in each bin if fewer); per-galaxy shear biases averaged over 10 noise realisations. (a): galaxy sample broken down into centrals and satellites. (b): galaxy sample broken down into red sequence, green valley, and blue cloud galaxies. Horizontal line corresponds to EWS total requirement (see section 3.1.2).



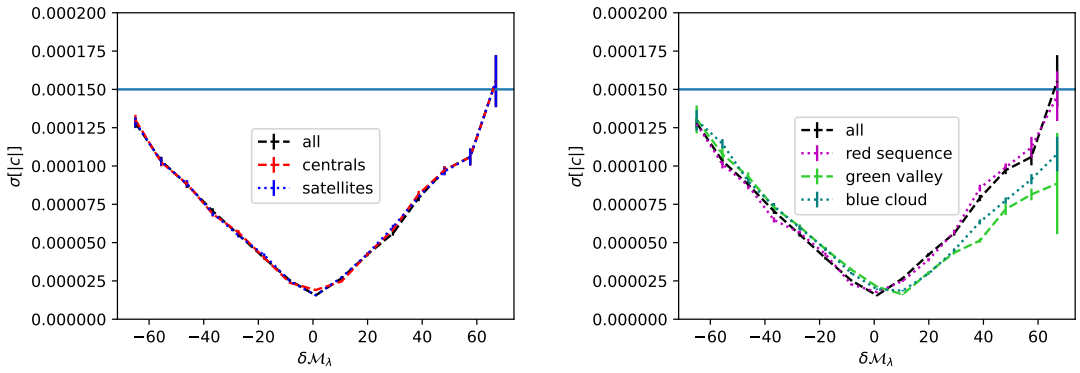
(a) (b)

Figure 4.10: Standard deviation of the absolute magnitude of the additive shear bias $\sigma[|\boldsymbol{c}|]$, as a function of colour index $r - z$. Standard deviation calculated over 1000 galaxies sampled from the *Euclid* Flagship 2 mock catalogue in each bin (or the total number of galaxies present in the mock in each bin if fewer); per-galaxy shear biases averaged over 10 noise realisations. (a): galaxy sample broken down into centrals and satellites. (b): galaxy sample broken down into red sequence, green valley, and blue cloud galaxies. Horizontal line corresponds to EWS total requirement (see section 3.1.2).



(a) (b)

Figure 4.11: Standard deviation of the absolute magnitude of the additive shear bias $\sigma[|\boldsymbol{c}|]$, as a function of truth-channel SED mean effective wavelength $\mathcal{M}_\lambda^{\rm truth}$. Standard deviation calculated over 1000 galaxies sampled from the *Euclid* Flagship 2 mock catalogue in each bin (or the total number of galaxies present in the mock in each bin if fewer); per-galaxy shear biases averaged over 10 noise realisations. (a): galaxy sample broken down into centrals and satellites. (b): galaxy sample broken down into red sequence, green valley, and blue cloud galaxies. Horizontal line corresponds to EWS total requirement (see section 3.1.2).



(a) (b)

Figure 4.12: Standard deviation of the absolute magnitude of the additive shear bias $\sigma[|\boldsymbol{c}|]$, as a function of bias in SED mean effective wavelength $\delta\mathcal{M}_\lambda$. Standard deviation calculated over 1000 galaxies sampled from the *Euclid* Flagship 2 mock catalogue in each bin (or the total number of galaxies present in the mock in each bin if fewer); per-galaxy shear biases averaged over 10 noise realisations. (a): galaxy sample broken down into centrals and satellites. (b): galaxy sample broken down into red sequence, green valley, and blue cloud galaxies. Horizontal line corresponds to EWS total requirement (see section 3.1.2).

EWS by a significant if not mitigated using techniques e.g. Kitching et al., 2021; van Uitert and Schneider, 2016. It should be noted that the standard deviation calculated here includes contributions from galaxy properties (morphology and SED) as well as FoV position; if the shear field is measured in angular pixels which are sufficiently large to contain more than of order one galaxy per pixel (see e.g. Duncan and Brown, 2024), then this will smooth out the FoV contribution somewhat, reducing the $\sigma[|\boldsymbol{c}|]$ of the measured shear field. This is discussed further in section 4.2.3.

The dependence of $\sigma[|\boldsymbol{c}|]$ on $m_{\rm VIS}$ is shown in fig. 4.8. $\sigma[|\boldsymbol{c}|]$ is increasing (roughly linearly) with $m_{\rm VIS}$, with error bars that increase in size with $m_{\rm VIS}$. The dependence of $\sigma[|\boldsymbol{c}|]$ on $z_{\rm obs}$ is shown in fig. 4.9. $\sigma[|\boldsymbol{c}|]$ exhibits high-frequency variation with $z_{\rm obs}$ (similar to the mean m-bias variation with $z_{\rm obs}$ shown in fig. 4.2 (a, b)). As with the variation of the mean m bias with $z_{\rm obs}$, this depends on the chromaticity of the SED-error-source $\sigma[|\boldsymbol{c}|]$ and the colour-redshift relation in the catalogue, and is likely to induce a substantial impact on the cosmological analysis.

The dependence of $\sigma[|\boldsymbol{c}|]$ on $r-z$ is shown in fig. 4.10, and on $\mathcal{M}_\lambda^{\rm truth}$ in fig. 4.11. As with the mean shear biases, there is substantial chromaticity of

$\sigma[||\boldsymbol{c}||]$, and the profile of $\sigma[||\boldsymbol{c}||]$ is similar in both $r-z$ and $\mathcal{M}_\lambda^{\rm truth}$, although (as with the mean shear biases) the breakdown by galaxy population is somewhat different between the two samples.

The dependence of $\sigma[||\boldsymbol{c}||]$ on $\delta\mathcal{M}_\lambda$ is shown in fig. 4.12. $\sigma[||\boldsymbol{c}||]$ is close to linear in $|\delta\mathcal{M}_\lambda|$, and is non-zero even in the case that $\delta\mathcal{M}_\lambda = 0$, indicating a contribution to the additive bias originating from error in the profile of the SED even in the case that the mean effective wavelength is recovered successfully. The linearity of $\sigma[||\boldsymbol{c}||]$ in $\delta\mathcal{M}_\lambda$ is less noisy than that of the mean additive biases as shown in fig. 4.5 (c-f). The implied collinearity of the mean shear biases and $\sigma[||\boldsymbol{c}||]$ implies that they are not linearly independent, and it is possible that this may aid in the development of a correction scheme; this is discussed in section 4.4.

Based on the analysis conducted in chapter 2, it is possible to define a requirement on the equivalent standard deviation of the spatial variations of the multiplicative bias, $\sigma[m]$. As can be seen in fig. 2.8 and fig. 2.9, a stringent requirement that assumes the worst-case would be $\sigma[|m|] < 0.01$. It is verified that in most cases $\sigma[|m|]$ is approximately an order of magnitude below this requirement, and in no case exceeds half of this requirement.

High-frequency variations in $\sigma[||\boldsymbol{c}||]$ that are larger than the scale of the error bars, particularly as a function of $z_{\rm obs}$, fig. 4.9, may indicate a breakdown in the assumptions used to analytically estimate the error bars (4.2) and (4.5), discussed in section 4.2.3. This may also be the case for the variation in m-bias as a function of $z_{\rm obs}$ (fig. 4.2), and for the large error bars estimated for the c-biases at high values of $r-z$, $\mathcal{M}_\lambda^{\rm truth}$, and $\delta\mathcal{M}_\lambda$ (fig. 4.3, fig. 4.4 and fig. 4.5). On the other hand, in the case of the $z_{\rm obs}$ plots, this the high-frequency variations may also be because of complexities of the redshift-colour relation in the mock. This will be investigated further in future work. Future work will also test the validity of the assumptions and formalism used to estimate the error bars in this work, including comparing with error bars estimated using re-sampling methods such as bootstrapping (Efron, 1992).

Field-of-View Dependence

To investigate the FoV-dependence of the shear measurement bias arising due to SED errors, 1000 galaxies are randomly drawn from the Flagship 2 mock catalogue (with the limiting magnitude selection cut of $m_{\rm VIS} \leq 24.5$ applied). For each of these galaxies, the corresponding additive and multiplicative shear biases are calculated on a 10×10 grid on the FoV, and the results are averaged over the 10 error-channel SED noise realisations per galaxy, and 1000 total sampled galaxies. The multiplicative and 2-component additive shear biases as functions of FoV position are shown as a function in fig. 4.13.

The dependence of the FoV-variation profile as a function of both $z_{\rm obs}$ and $\mathcal{M}_{\lambda}^{\rm truth}$ is verified to be subdominant with respect to the amplitude of the $z_{\rm obs}$- and $\mathcal{M}_{\lambda}^{\rm truth}$-averaged variations across the FoV.

What is of principal interest is the contribution to the total variance of the shear biases due to the spatial (FoV) variation. As discussed in section 4.2.3, the spatial variation of the m-bias (parametrised by the standard deviation of the m-bias as a function of FoV-position) in no cases exceeds half of the most stringent requirement on it that may be placed based on the analysis conducted in chapter 2, $\sigma[m] < 0.01$, see section 2.4.3, figs. 2.8 and 2.9. Given that the absolute magnitude of the fractional variations of m-bias relative to the FoV-mean is at most ~ 0.1, and comparing this with typical multiplicative biases shown in fig. 4.1–fig. 4.5 (a, b) $m \sim (1-2) \times 10^{-2}$, it is clear that most of the variance in the m-biases arises due to variation in the galaxy properties (morphology, SED), rather than FoV variation. Therefore, if the shear map is averaged over spatial pixels containing more than of order one galaxy, then the spatial variation of the m-bias arising due to SED errors will be negligible.

On the other hand, the absolute value of the fractional variations in the additive bias components reaches ~ 10 for the c_1 component and ~ 30 or the c_2 component. Whereas the mean additive bias is higher in c_1 than c_2 (fig. 4.1–fig. 4.5 (c-f)), the FoV variation is stronger for the c_2 component. Comparing this with the typical mean additive biases shown in fig. 4.1–fig. 4.5 (c-f), it is apparent that the spatial

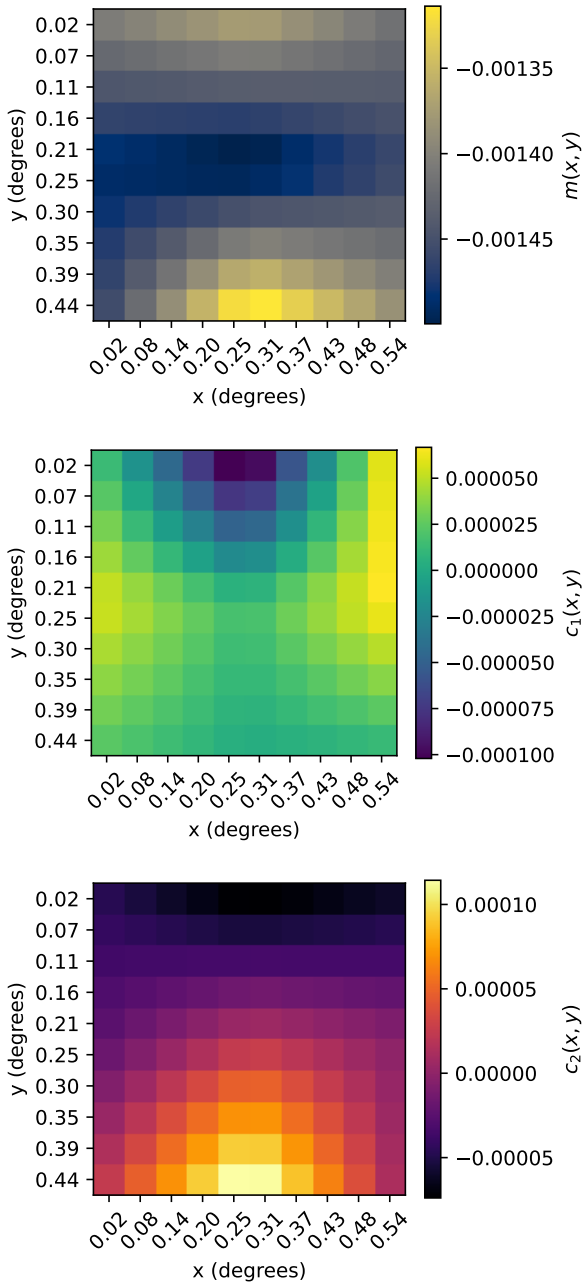


Figure 4.13: Shear biases, as a function of FoV position. Averaged over 1000 galaxies, with shear biases evaluated at each FoV position. Top: Fractional change in m. Middle: Fractional change in c_1. Bottom: Fractional change in c_2. Different colour maps used to represent different scales of variation of fractional change in shear biases.

variation of the additive bias will contribute a significant part of the standard deviation $\sigma[|\boldsymbol{c}|]$ shown in fig. 4.8-fig. 4.12. It is therefore probable that $\sigma[|\boldsymbol{c}|]$ will be represent a substantial contribution to the total EWS requirement, even if the shear field is measured in pixels containing more than of order one galaxy such that the contribution from galaxy properties (morphology, SED) is suppressed, and will therefore have a non-negligible impact on the cosmological analysis for the EWS. This highlights the importance of calibration of the spatial variations of the c-bias in the shear measurement.

In section 4.3, the impact of the SED-error-sourced multiplicative shear bias is propagated to cosmological parameter estimation.

4.3 Propagation of Multiplicative Shear Bias to Cosmological Parameter Estimation

The forecast shear biases arising due to imperfect knowledge of galaxy SEDs presented in section 4.2 are in many cases similar in size to the PTO requirements on the PSF defined in section 3.1.2, and in some cases exceed the total EWS requirements on the shear bias. It is therefore expected that it will be necessary to mitigate the impact of PSF errors sourced by SED errors in the EWS, in order to avoid a significant impact on the cosmological parameter estimation. In this section, the impact of tomographic multiplicative shear biases arising due to SED errors is estimated, in order to further motivate the necessity of mitigating this source of shear bias.

As discussed in section 4.2.3, the amplitude of the spatial variations of the m-bias sourced by SED errors is substantially smaller than the requirement on $\sigma[m]$ defined based on the analysis of chapter 2; hence, in this section, only the mean m-bias per tomographic bin is propagated to biases in cosmological parameter estimates. The mean tomographic m-bias acts multiplicatively on the tomographic cosmic shear angular power spectra, with the measured tomographic cross-correlation power spectra $\widetilde{C}_\ell$ given by (Massey et al., 2013):

$$\widetilde{C}_\ell^{\gamma_i\gamma_j} = (1 + \langle m(z_i)\rangle)(1 + \langle m(z_j)\rangle)C_\ell^{\gamma_i\gamma_j}, \tag{4.6}$$

with $C_\ell^{\gamma_i\gamma_j}$ the shear-shear cross-correlation angular power spectrum between shear fields γ_i, γ_j measured in tomographic redshift bins i, j, $\langle m(z_i)\rangle$ the mean multiplicative shear bias of galaxies in bin i, and covariance between mean tomographic m-biases is neglected.

In section 4.3.1, the estimation of mean tomographic shear biases arising due to SED errors $\langle m(z_i)\rangle$ is described. Biased shear angular power spectra $\widetilde{C}_\ell$ are then calculated using (4.6) and resulting biases in cosmological parameters Ω_c, σ_8, w_0, and w_a are estimated using a Fisher-matrix analysis, as described in chapter 2, with the results presented in section 4.3.2. the results are discussed in section 4.3.3.

In the real cosmological analysis of weak lensing data from the EWS, the cosmological parameter inference will include marginalisation over priors on tomographic mean m-bias nuisance parameters. However, the large values and highly redshift-dependent nature of the m-bias arising due to SED errors seen in section 4.2.3 indicates that marginalising over uninformative priors on the raw m-bias is likely to be insufficient, due to the impact on the figure-of-merit of the resulting parameter constraints (Euclid Collaboration: Mellier et al., 2024). The purpose of the present work is to motivate the development of a correction scheme for the shear biases sourced by SED errors, of which it will be desirable (for example) that the residual m-biases arising from this correction be smaller and less redshift-dependent than the raw m-biases sourced by SED errors, and which may then be marginalised over. The impact of marginalising over mean tomographic shear biases on cosmological parameter estimation is left for future work. The prospect of mitigating the shear bias arising due to SED errors is discussed in more detail in section 4.4.

As shown in section 4.2.3, the standard deviation of the additive shear bias sourced by SED errors $\sigma[|\boldsymbol{c}|]$ is comparable in size with the total EWS requirement, and as discussed in section 4.2.3, the FoV dependence of the additive bias provides a large contribution to this standard deviation. As discussed in e.g. Massey et al., 2013, this results in an additive contribution at the angular power spectrum level. As discussed in section 4.2.3, propagating the impact of the c-bias arising due

to SED errors therefore involves estimating the power spectrum of the additive bias field. Because this is a more complicated task than propagating the mean tomographic m-bias, the propagation of the c-bias to cosmological parameter estimation is left for future work.

As with the analysis of chapter 2, this analysis only considers the impact of bias on the cosmic shear angular power spectra on cosmological parameter estimation, i.e. the additional constraints on cosmological parameters from galaxy clustering and galaxy-galaxy lensing are not considered. The impact of the multiplicative bias sourced by SED errors on such a 3×2-point analysis is left for future work.

4.3.1 Propagation of SED Errors to Tomographic Cosmic Shear Angular Power Spectra

In order to estimate the mean tomographic m-biases arising due to SED errors $\langle m(z_i) \rangle$, it is necessary to sample galaxies in the Flagship 2 mock catalogue belonging to tomographic redshift bin i, and calculate the mean multiplicative shear biases for these galaxies using the methodology described in chapter 3 and section 4.2. To accomplish this, galaxies are sampled from forecast EWS tomographic redshift distributions $n_i(z)$ obtained from OU-PHZ, consisting of redshift distributions for 13 equipopulated tomographic redshift bins with support between $(z_{\rm min} = 0, z_{\rm max} = 3)$ (I. Tutusaus, *priv. comm.*). Flagship 2 mock catalogue galaxies are sampled from these $n_i(z)$ by inverse transform sampling, i.e. by sampling uniformly from the inverse normalised cumulative distribution function of each of the $n_i(z)$ (Robert and Casella, 2004). This is discretised by defining 300 fine redshift bins in the support of the $n_i(z)$, finding the one which corresponds to the sampled redshift, and randomly sampling a catalogue galaxy which exists in this bin.

For each tomographic redshift bin, 1000 Flagship 2 mock galaxies are sampled, and multiplicative shear biases arising due to SED errors are calculated using the methodology described in chapter 3 and section 4.2. In order to obtain multiple realisations of the mean tomographic m-bias $\langle m(z_i) \rangle$, this is repeated for 100

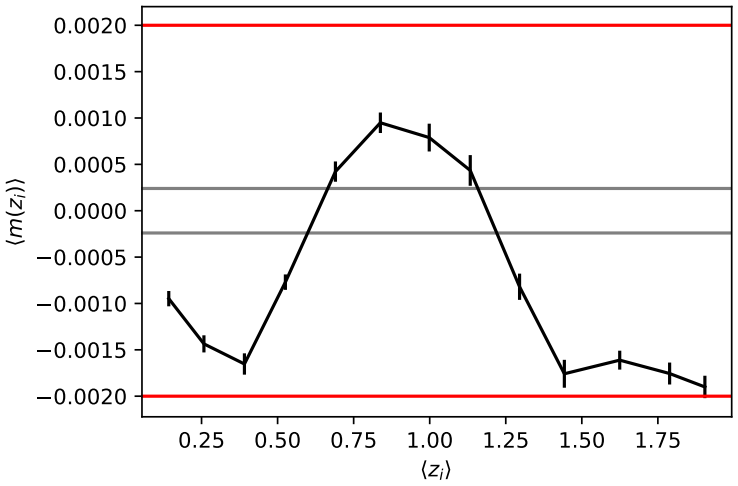


Figure 4.14: Mean tomographic m-bias $\langle m(z_i)\rangle$ as a function of mean bin redshift $\langle z_i\rangle$, averaged over 1000 Flagship 2 mock galaxies in each bin sampled from 13 forecast $n_i(z)$ obtained from OU-PHZ (I. Tutusaus, *priv. comm.*). Red horizontal lines correspond to the EWS total requirement (see section 3.1.2); grey horizontal lines correspond to the PSF PTO requirement (see section 3.1.2).

separate tomographic samples, each with 10 noise realisations per galaxy, as described in section 4.2.1. For each sample, mean m-biases are calculated by averaging over the 1000 galaxies in the sample and 10 noise realisations per galaxy, and the standard error on this mean is calculated as in (4.2). 10 realisations of the $\langle m(z_i)\rangle$ are drawn from the normal distribution defined by this mean and standard error, for a total of 1000 realisations of the $\langle m(z_i)\rangle$ per tomographic bin. Non-Gaussianity of the distribution of the realisations of the $\langle m(z_i)\rangle$ is neglected. m-bias estimates were sampled in this way, rather than by taking the noise realisations directly, because for each galaxy the shear bias estimates corresponding to the noise realisations were regularly clustered, potentially owing to a discretisation effect in the noise sampling in the generation of the OU-PHZ mock photometry; the sampling adopted here was therefore necessary in order to achieve stable cosmological parameter bias estimates when averaging over realisations. The impact of this effect in the mock photometry on the work discussed in this chapter will be further investigated in future work. The mean of the realisations of $\langle m(z_i)\rangle$ are shown in fig. 4.14, where the error bars are the standard deviation of the realisations.

For each realisation of the $\langle m(z_i)\rangle$, corresponding biased shear angular power

spectra $\widetilde{C}_\ell^{\gamma_i\gamma_j}$ are calculated using equation (4.6), neglecting covariance in the mean m-bias between tomographic redshift bins. The fiducial cosmic shear angular power spectra $C_\ell^{\gamma_i\gamma_j}$ and its covariance (including the SSC term (Euclid Collaboration: Sciotti et al., 2024; Krause and Eifler, 2017)) are generated using the same survey configuration settings as are used in chapter 2, except in this case assuming the 13 forecast $n_i(z)$ (I. Tutusaus, *priv. comm.*) used to calculate the $\langle m(z_i)\rangle$, rather than the 10 $n_i(z)$ shown in fig. 2.1.

The mean tomographic m-biases $\langle m(z_i)\rangle$ for forecast $n(z_i)$ for the EWS (I. Tutusaus, *priv. comm.*) are shown as a function of tomographic bin mean redshift $\langle z_i\rangle$ in fig. 4.14. It is noteworthy that the profile of the m-bias as a function of redshift differs from the relationship between the SED-error-sourced m-bias and $z_{\rm obs}$ presented in fig. 4.2 (a, b). This occurs because the sample selection over which the m-biases are averaged differs between fig. 4.2 and fig. 4.14; in particular, the m-bias values shown in fig. 4.2 (a, b) are averaged over galaxies occupying evenly-spaced top-hat bins in redshift, whereas the $\langle m(z_i)\rangle$ values shown in fig. 4.14 are averaged over galaxies in skewed redshift bins with varying widths. This also has the effect of smoothing out the profile of the m-bias-redshift relation, as my be seen by comparing fig. 4.2 (a, b) and fig. 4.14.

The profile of the $\langle m(z_i)\rangle(z_i)$ can be explained by similar arguments to those made in section 4.2.3, based on the colour-redshift relation in the catalogue and the chromaticity of the PSF. fig. 4.4 demonstrates that bluer galaxies result in a more negative m-bias, whereas redder galaxies result in a more positive m-bias. Comparing this with fig. 4.6, which shows the relation between galaxy effective mean wavelength and redshift, with blue galaxies at very low redshifts, redder galaxies at intermediate redshifts $\sim$1, and bluer galaxies again at higher redshifts $\gtrsim$1.5 (which occurs due to the complex of galaxy evolution and redshift), this is qualitatively consistent with the $\langle m(z_i)\rangle(z_i)$ shown in fig. 4.14. As described in section 4.2.3, the fact that bluer galaxies correspond to more negative m-bias and redder galaxies correspond to more positive m-bias implies that the SED reconstruction causes galaxy colours to be exaggerated, a conclusion which is

supported by fig. 4.5.

4.3.2 Bias in Cosmological Parameters

Given biased tomographic cosmic shear angular power spectra $\widetilde{C}_\ell^{\gamma_i\gamma_j}$, a Fisher-matrix analysis similar to the methodology described in chapter 2 is employed to estimate resulting biases in cosmological parameters. As in chapter 2, the Fisher-matrix analysis is conducted for two cosmological models, (i) wCDM, and (ii) w_0w_aCDM (Euclid Collaboration: Mellier et al., 2024); in model (i), biases are estimated in parameters $\{\Omega_c, \sigma_8, w_0\}$, while in model (ii), biases are estimated in parameters $\{\Omega_c, \sigma_8, w_0, w_a\}$. As in chapter 2, the fiducial cosmological parameter values from (Planck Collaboration: Aghanim et al., 2020) are adopted (see table 2.1), and the same differential parameter steps entering the numerical derivatives (2.13) which are used to calculate the Fisher matrix elements (2.12) as in chapter 2.

Cosmological parameter biases are estimated using the Fisher-matrix analysis for each of the 1000 realisations of the $\widetilde{C}_\ell^{\gamma_i\gamma_j}$ described in section 4.3.1, with the Fisher-matrix forecasted conducted separately for each realisation, for three cases in which the angular power spectra are truncated at $\ell_{\rm max} = \{1500, 3000, 5000\}$. Corner plots showing the biased cosmological parameter values for the three values of $\ell_{\rm max}$ considered, compared with fiducial contours, in fig. 4.17 and fig. 4.20 for the wCDM and w_0w_aCDM cosmologies, respectively. The fiducial 65% and 95% confidence-level contours, centred on the fiducial values listed in table 2.1, are obtained from the Fisher matrix of the parameters (2.12) (see e.g. Coe, 2009). The error bars on the parameter bias estimates, indicated by the crosses on the black points fig. 4.17 and fig. 4.20, indicate the standard deviation of the parameter bias estimates obtained from the 1000 $\widetilde{C}_\ell^{\gamma_i\gamma_j}$ realisations described in section 4.3.1. Corner plots are generated using the CHAINCONSUMER python package (Hinton, 2016).

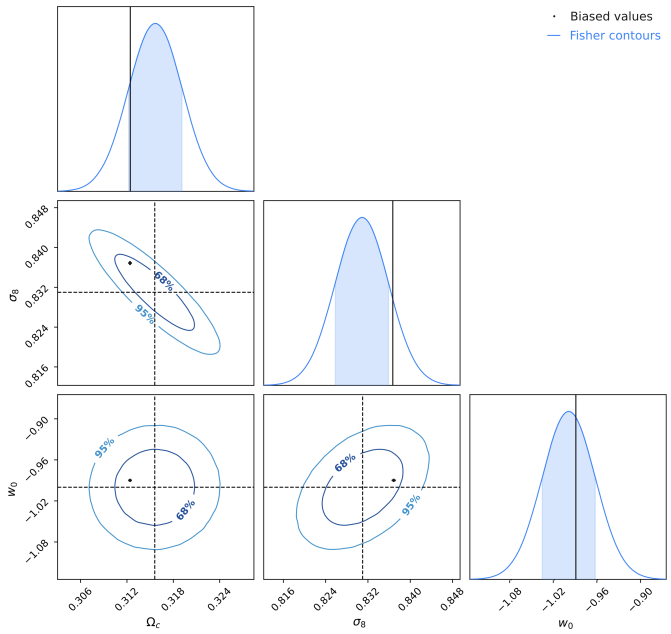


Figure 4.17 (a): Biases in cosmological parameters $\{\Omega_c, \sigma_8, w_0\}$ (black points) due to $\langle m(z_i)\rangle$ sourced by SED errors, compared with fiducial Fisher confidence ellipses, for wCDM cosmology. $\ell_{\max} = 1500$.

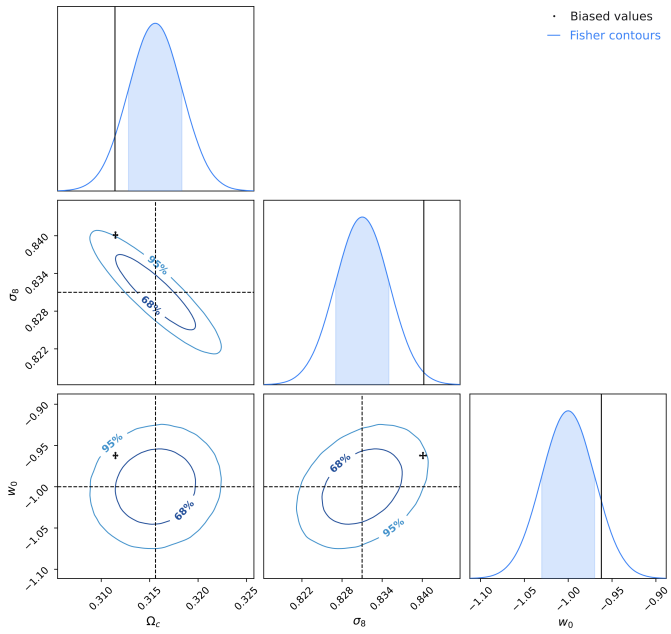


Figure 4.17 (b): Biases in cosmological parameters $\{\Omega_c, \sigma_8, w_0\}$ (black points) due to $\langle m(z_i)\rangle$ sourced by SED errors, compared with fiducial Fisher confidence ellipses, for wCDM cosmology. $\ell_{\max} = 3000$.

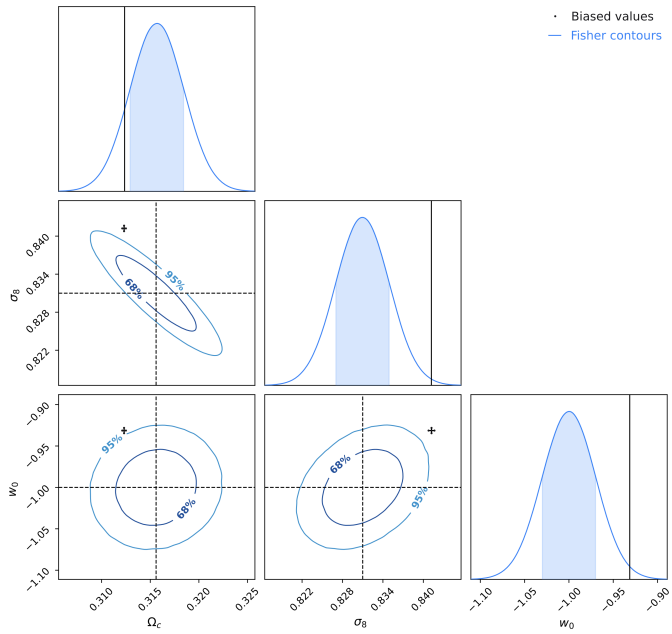


Figure 4.17 (c): Biases in cosmological parameters $\{\Omega_c, \sigma_8, w_0\}$ (black points) due to $\langle m(z_i)\rangle$ sourced by SED errors, compared with fiducial Fisher confidence ellipses, for wCDM cosmology. $\ell_{\max} = 5000$.

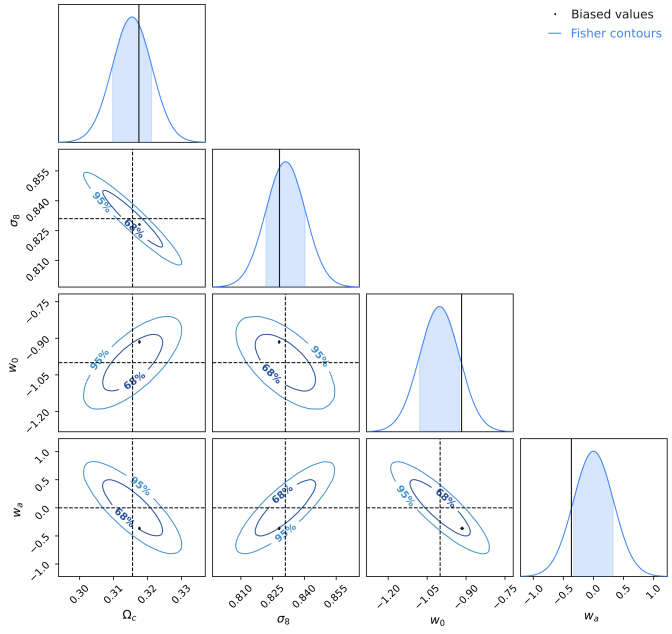


Figure 4.18 (a): Biases in cosmological parameters $\{\Omega_c, \sigma_8, w_0, w_a\}$ (black points) due to $\langle m(z_i)\rangle$ sourced by SED errors, compared with fiducial Fisher confidence ellipses, for wCDM cosmology. $\ell_{\max} = 1500$.

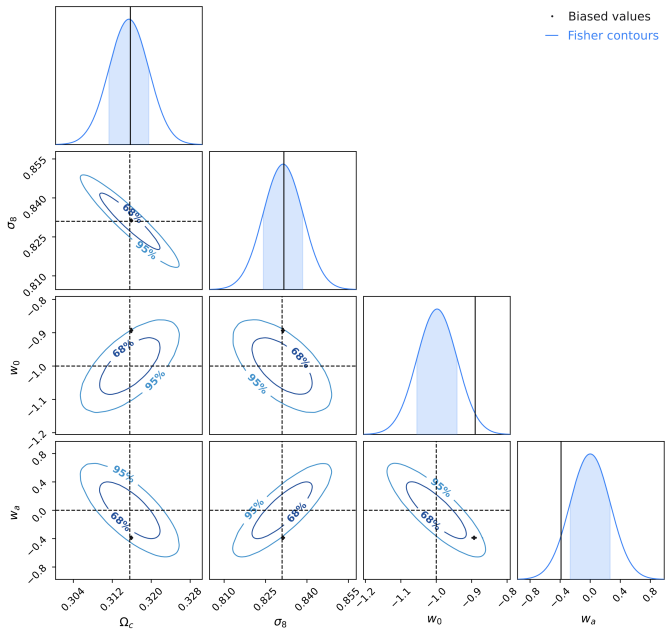


Figure 4.18 (b): Biases in cosmological parameters $\{\Omega_c, \sigma_8, w_0, w_a\}$ (black points) due to $\langle m(z_i)\rangle$ sourced by SED errors, compared with fiducial Fisher confidence ellipses, for wCDM cosmology. $\ell_{\max} = 3000$.

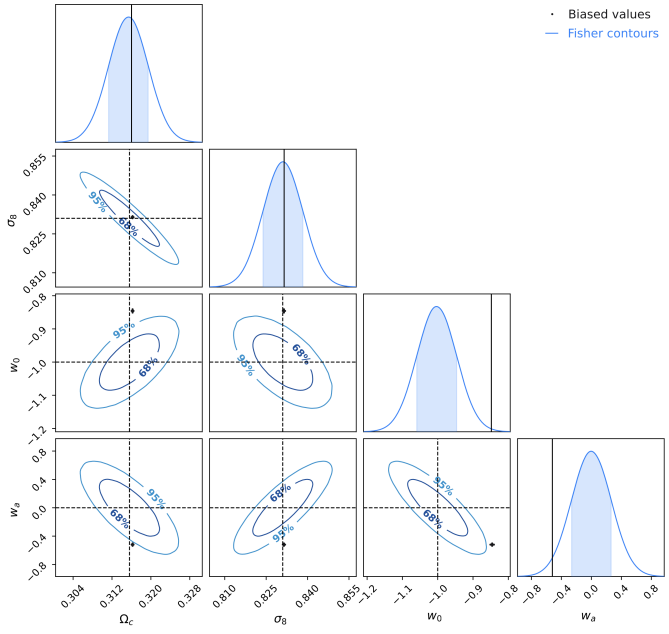


Figure 4.18 (c): Biases in cosmological parameters $\{\Omega_c, \sigma_8, w_0, w_a\}$ (black points) due to $\langle m(z_i)\rangle$ sourced by SED errors, compared with fiducial Fisher confidence ellipses, for wCDM cosmology. $\ell_{\max} = 5000$.

4.3.3 Discussion

The corner plots comparing the biased cosmological parameter values with the fiducial Fisher-matrix confidence ellipses shown in fig. 4.17 and fig. 4.20 demonstrate that if unmitigated and not marginalised over, the mean multiplicative shear bias arising due to imperfect knowledge of galaxy SEDs will result in biases in cosmological parameter estimates that in some cases are larger than the 68% confidence level, and in some cases larger than the 95% confidence level. This is consistent with the comparable sizes of the shear biases with the EWS total mission requirements seen in section 4.2.3. For both cosmological models considered, the size of the biases in cosmological values increase with increasing $\ell_{\rm max}$, both in absolute terms, and fractionally with respect to the fiducial parameter constraints indicated by the Fisher-matrix ellipses.

For the wCDM cosmological model, significant biases are induced in all three parameters considered. For $\ell_{\rm max} = 1500$, biased parameter values lie within the fiducial 68% confidence-level contour for Ω_c, σ_8 and w_0, and are outside the fiducial 95% confidence-level contour for $\ell_{\rm max} = 5000$. The biased point lies approximately along the Ω_c–σ_8 and w_0–σ_8 major degeneracy axes, indicating that the $\langle m(z_i)\rangle$ is largely co-degenerate with these parameter degeneracies.

For the w_0w_aCDM cosmological model, the most obvious difference compared with the wCDM case is that the bias in parameters Ω_c, σ_8 is substantially smaller than in the wCDM case. Comparing with equation (2.15), it is seen that the parameter biases depend on the parameter covariance (i.e. the inverse Fisher matrix), as well as on the (inverse-)covariance between the parameters and the biased C_ℓs, represented by the J, ℓ summation (Thiele et al., 2020), in a scale-dependent way. Therefore the introduction of different parameters and scale-cuts can impact the resulting parameter biases in complex ways. Indeed, in the w_0w_aCDM case, the bias in Ω_c and σ_8 actually decreases slightly with increasing $\ell_{\rm max}$. On the other hand, both w_0 and w_a are very significantly biased, with w_0 substantially more biased at all values of $\ell_{\rm max}$ in the w_0w_aCDM case than

in the wCDM case, and with the biased point lying approximately along the w_0–w_a major degeneracy axis.

The biases in cosmological parameter estimates shown in fig. 4.17 and fig. 4.20 indicate that the shear measurement biases arising due to imperfect knowledge of galaxy SEDs will have a very significant impact on the cosmology analysis for the EWS, if the impact of the shear biases is not mitigated by marginalising over them in the parameter inference, or by applying a correction for them (e.g. from simulations) in the shear measurement. However, as discussed above, due to the large values and highly redshift-dependent nature of the mean tomographic m-biases shown in fig. 4.14, it is likely that marginalising over the uncorrected $\langle m(z_i)\rangle$ with an uninformative prior is likely to have an unacceptably large impact on the dark energy figure-of-merit for the EWS cosmological analysis (Euclid Collaboration: Mellier et al., 2024). It may be possible to mitigate this with redshift-dependent, informative priors on the $\langle m(z_i)\rangle$. Additionally, the additive bias sourced by SED errors is also likely to have a significant impact on the cosmological analysis for the EWS, judging by the large size of its standard deviation $\sigma[|\boldsymbol{c}|]$, as discussed in section 4.2; since this will have a potentially non-trivial impact on the shape of the measured angular power spectra, it may not be straightforward to mitigate this by marginalising over priors on a simple nuisance-parametrisation. The results presented in this chapter therefore motivate the development of a correction scheme for the SED-error-sourced shear measurement biases for the EWS. In particular, in the analysis of shear data for the EWS, shear measurement biases will be calibrated from simulations (Euclid Collaboration: Mellier et al., 2024); the results presented in this chapter highlight the necessity of realistically including the impact of the SED errors on the transfer of the PSF to source galaxies in the shear bias calibration simulations, or of developing an alternative mitigation scheme.

For the w_0w_aCDM case shown in fig. 4.20, the main effect of the SED-sourced tomographic m-bias is to bias the dark energy equation-of-state parameters w_0, w_a. This is because the redshift-dependant m-bias (fig. 4.14) causes the mean shear

per tomographic bin, and hence the observed angular power spectra, and the inferred redshift-evolution of the matter overdensity $\delta_m(z)$, to be biased. It may therefore be expected that a mean m-bias, which is negative at low redshifts, positive at intermediate redshifts $\sim$1, and negative at high redshifts, would lead to an inferred rate of structure growth which is biased low, high, and low in the same respective redshift ranges. As discussed in section 1.1.1, dark energy has the effect of suppressing the growth of structure, with higher dark energy density $\rho_{\rm DE}$ leading to suppressed structure growth (Dodelson, 2003). As a result, an m-bias which is low at high redshift, increases at intermediate redshift, and then decreases at low redshift, is degenerate with a dark energy density $\rho_{\rm DE}$ which is low at high redshift, increases to intermediate redshift, and then decreases to low redshift. Comparing with the equations (1.2) and (1.3), this is consistent with an evolving dark energy model with negative w_0, w_a, as obtained in this work and shown in fig. 4.20. In the restricted wCDM model, this effect cannot be captured with the dark energy model, and results in large biases in Ω_m and σ_8, although this may result in a poor fit to the cosmological model. It should be noted that this effect depends on the bias in the SED reconstruction - as described in section 4.2.3, this m-bias evolution arises because the SED reconstruction interprets blue galaxies as bluer than they actually are, and red galaxies as redder than in reality; an SED reconstruction method that does not have this property would result in a different $\langle m(z_i)\rangle(z_i)$ profile.

The negative biased values of w_0, w_a show in fig. 4.20 is of additional interest, because the obtained values for these parameters are biased in approximately the same direction that the w_0, w_a DESI constraints from BAO+CMB+SNe (DESI Collaboration: Abdul-Karim et al., 2025) depart from ΛCDM (see section 1.1.1). This may result in spurious consistency between w_0, w_a constraints from *Euclid* WL measurements and other cosmological probes if this effect is not corrected for in the EWS analysis.

4.4 Conclusion

4.4.1 Summary

In this chapter, cosmic shear measurement biases arising due to the PSF error that results from imperfect knowledge of galaxy SEDs in the EWS are estimated. By applying the methodology developed in chapter 3, additive and multiplicative shear biases are calculated for galaxies in the *Euclid* Flagship 2 mock catalogue (Euclid Collaboration: Castander et al., 2024), by calculating the PSF error that arises when galaxy SEDs are estimated from noisy, ground-based, broad-band photometric data, as will be the case for the EWS. As discussed in section 4.2, noisy mock photometric SEDs are provided as input to the shear bias estimation pipeline described in chapter 3, and the resulting shear biases are calculated as a function of galaxy properties $m_{\rm VIS}$, $z_{\rm obs}$, and $r-z$; additionally, the mean effective wavelength of the galaxy SED $\mathcal{M}_\lambda$ is defined (equation (4.1)), and shear biases are also estimated as a function of the mean effective wavelength of the true galaxy SED $\mathcal{M}_\lambda^{\rm truth}$, as well as the bias in this metric $\delta\mathcal{M}_\lambda$ arising due to the use of noisy, photometric galaxy SED data. Shear biases are also estimated for galaxies sampled according to two breakdowns provided in the Flagship 2 mock catalogue: (i) into "centrals" and "satellites", and (ii) into galaxies belonging to the "red sequence", "green valley", and "blue cloud". Results are presented and discussed in section 4.2.3.

It is found that shear measurement biases sourced by SED errors are in many cases large, i.e. comparable to the PSF PTO requirements, and in some cases exceeding the total EWS mission requirements (see section 3.1.2). It is found that shear biases depend on VIS magnitude $m_{\rm VIS}$, but remain stable at magnitudes of interest to the EWS, $m_{\rm VIS} \lesssim 24.5$. It is found that the shear measurement biases, in particular the m-bias, have a strong dependence on observed redshift $z_{\rm obs}$, indicating a likely significant degeneracy with the large-scale structure and impact on cosmological parameter influence. This is investigated via the chromaticity of the SED-error-sourced m-bias, which is found to vary strongly with galaxy colour, as quantified by both $r-z$ and $\mathcal{M}_\lambda^{\rm truth}$. Additionally, both the multiplicative and

additive shear biases are found to depend linearly on $\delta\mathcal{M}_\lambda$. The shear biases are found to not depend strongly on breakdown (i) ("centrals" vs "satellites"), and to have a somewhat stronger and complex relationship on breakdown (ii) ("red sequence" vs "green valley" vs "blue cloud").

The standard deviation of the additive bias $\sigma[|\boldsymbol{c}|]$ is also estimated, and found to be comparable in size to the total EWS mission requirement. Like the mean m-bias, $\sigma[|\boldsymbol{c}|]$ is found to vary significantly with $z_{\rm obs}$ and with a complex profile, and to vary linearly with the (magnitude of) $\delta\mathcal{M}_\lambda$. The FoV variation of the additive bias is investigated, and it is concluded that it provides a significant contribution to $\sigma[|\boldsymbol{c}|]$, and that the additive impact of the c-bias on the 2-point statistics is likely to be significant for the EWS cosmological analysis. The standard deviation and spatial variation of the m-bias is also investigated and found to be small compared with a stringent requirement placed on the latter, based on the analysis of chapter 2.

Finally, in section 4.3, the impact of the mean tomographic m-bias, $\langle m(z_i)\rangle$, arising due to SED errors on cosmological parameter estimation is considered. Galaxies from the Flagship 2 mock catalogue are sampled from forecast redshift distributions $n_i(z)$ for the EWS, and resulting mean m-biases per tomographic redshift bin are calculated. These are propagated to bias in cosmic shear angular power spectra using equation (4.6). A Fisher-matrix analysis as described in chapter 2 is carried out to estimate the resulting biases in cosmological parameters for both a wCDM cosmology, and a w_0w_aCDM cosmology, if the $\langle m(z_i)\rangle$ are not marginalised over or otherwise corrected for. As expected from the large sizes and redshift-dependence of the m-bias as presented in section 4.2, it is found that if not mitigated, the SED-error-sourced $\langle m(z_i)\rangle$ will catastrophically bias the cosmological parameter estimation for the EWS. For the wCDM cosmology, Ω_c, σ_8 and w_0 are all significantly biased, whereas for the w_0w_aCDM cosmology, only w_0 and w_a are significantly biased, likely due to degeneracy between the redshift-dependence of the mean m-bias and an evolving dark energy model. Interestingly, w_0, w_a are found to be biased in the same direction that they are found to be discrepant with ΛCDM by DESI Collaboration: Abdul-Karim et al., 2025, which

may result in spurious consistency between WL and other probes if this effect is not corrected for in the EWS analysis. The substantial impact of the SED-error-sourced $\langle m(z_i)\rangle$ on cosmological parameter inference motivates the development of a correction scheme for such shear measurement bias for the EWS.

4.4.2 Future Work

A substantial amount of the work presented in this chapter has consisted of the propagation of mean tomographic $\langle m(z_i)\rangle$ to biases in cosmological parameter inference, via a Fisher matrix analysis. However, this analysis is limited in a number of ways. Firstly, in the real survey analysis for the EWS, tomographic m-bias nuisance parameters will be marginalised over, rather than omitted from the model altogether; the impact of marginalising over priors on the $\langle m(z_i)\rangle$ on cosmological parameter inference is of relevance to the performance of the real survey analysis, and is left for future work. Importantly, this will depend significantly on the choice of priors on the $\langle m(z_i)\rangle$, in particular whether the $\langle m(z_i)\rangle$ are corrected for at the shear-measurement level, with the residual tomographic shear biases marginalised over in the cosmological inference, or if an informative prior on the uncorrected $\langle m(z_i)\rangle$ is marginalised over in the parameter inference; both approaches introduce model-dependence of the SED-sourced shear bias to the cosmological analysis.

Another significant limitation of the propagation to cosmology conducted section 4.3 is the omission of the impact of the additive bias arising due to SED errors. As discussed in section 4.2, the standard deviation of the c-bias $\sigma[|\boldsymbol{c}|]$ sourced by SED errors is comparable to the total EWS mission requirement, with a substantial contribution from the FoV-dependence of the c-bias. The additive impact of the c-bias on the 2-point statistics is therefore likely to have a substantial impact on the cosmological analysis for the EWS. Since estimating the impact of this involves constructing c-bias maps and estimating corresponding c-bias power spectra, it was not considered in this investigation, and is left for future work.

The results of this chapter motivate the development of a scheme to mitigate the impact of shear measurement biases that arise due to SED errors for the EWS, e.g. using shear bias calibration simulations (Euclid Collaboration: Mellier et al., 2024). One possible alternative approach may be similar to the catalogue-level shear bias estimation discussed in section 3.3, i.e. calculating SED-error-sourced shear biases for a calibration sample of galaxies which have been observed both photometrically and spectroscopically, and matching galaxies observed in the Wide Survey to this calibration sample based on broad-band magnitudes and/or colours, and thereby assigning shear bias estimates. In a similar vein, it may be desirable to apply an approach similar to self-organising map (SOM) methods (Yin, 2007) that have been used to estimate photometric redshifts for galaxies in recent photometric galaxy surveys such as DES (Buchs et al., 2019; Campos et al., 2024); such methods also involve assigning a parameter estimate to a galaxy based on its broad-band magnitudes/colours, calibrated with a training sample.

Another possible approach may involve making use of the linearity of the SED-error-sourced shear biases in the bias in the SED mean effective wavelength $\delta\mathcal{M}_\lambda$. In particular, it may be possible to make use of the fact that the SED-error-sourced multiplicative and additive shear biases are not independent, owing to their mutual linearity in $\delta\mathcal{M}_\lambda$. If it is possible to obtain an independent constraint on the additive bias, e.g. using a shear-map smoothing method such as described in van Uitert and Schneider, 2016 or other techniques e.g. Kitching et al., 2021, then this may be used to also constrain the multiplicative bias, particularly if information from the chromatic dependence of the SED-error-sourced shear biases is also folded in. However, this assumes that other sources of additive bias will have already been corrected for, which is likely to be an optimistic assumption; on the other hand, it is possible that colour information may be used to alleviate such degeneracies.

Various physical effects which are likely to impact the shear bias arising due to SED errors have not been considered in this work. Significantly, the effect of the dichroic surface within the *Euclid* spacecraft, which introduces polarisation-

dependence to the PSF error (Euclid Collaboration: Cropper et al., 2024), has been neglected. Additionally, sources of spatial variation of the SED errors, including dependence of the ground-based photometry on airmass, and inhomogeneity of different ground-based survey configurations which provide photometric data for the EWS, have been neglected. Such effects may introduce shear bias variations - including m-bias variations - on large angular scales, which according to the analysis of chapter 2 may have a substantial impact on the cosmological analysis. The impact of such effects is left to future work.

Another observational effect which will introduce errors into the ground-based photometry that will enter the EWS analysis is that of photometric blending, in which ground-based photometric measurements of galaxies may overlap such that they are mutually contaminated (see e.g. MacCrann et al., 2022). This will introduce an additional source of SED error into the PSF estimation, which will propagate to the shear measurement.

Finally, the correlation between the shear bias arising due to SED errors with other weak-lensing systematics which have chromatic dependence may be of interest to the cosmology analysis for the EWS. In particular, if the covariance matrix of nuisance parameters including tomographic shear bias and photometric redshift errors (Eriksen and Hoekstra, 2018) has substantial off-diagonal components which are not accounted for, then this may bias cosmological parameter estimation. The chromaticity of these systematics may cause them to also be correlated with other astrophysical systematics, such as intrinsic alignments. The impact of such correlations between systematic effects on the cosmological analysis of the EWS should be investigated, and is left for future work.

I was sitting on a bench with someone, and they were like, "Wow, the shear measurement in that patch of sky corresponding to a given HEALPIX *pixel within the* Euclid *Wide Survey footprint is so pretty!", and I was like, "And I'm the only PSF scientist in the World who knows what the values of the corresponding forecast additive and multiplicative shear measurement biases arising due to un-modelled spatio-temporal variations of the* Euclid *PSF in that* HEALPIX *pixel are!"*

— Arthur Eddington, after downloading SOURCE EXTRACTOR for the first time; probably attributed to Eddington by Baron Ernst Carl Gerlach Stueckelberg von Breidenbach zu Breidenstein und Melsbach (possibly apocryphal)

5 Tomographic Mapping of Predicted Spatially-Varying Shear Biases for the EWS

Contents

5.1 Introduction 181
5.1.1 Phase-Diversity Calibration Baseline PSF 184
5.2 Forecasting Shear Biases Due to PSF Modelling Errors 187
5.2.1 Sampling PSF Variations Using PCA 187
5.2.2 Propagating PSF Modelling Errors to Shear Biases 193
5.3 Mapping Tomographic Forecast Shear Biases 197
5.3.1 Tomographic Mock Galaxy Sampling 197
5.3.2 Constructing Tomographic Shear Bias Maps 198
5.3.3 Discussion 203
5.4 Conclusion 206
5.4.1 Summary 206
5.4.2 Future Work 208

5.1 Introduction

As discussed in section 1.2.5, there are numerous sources of error in the VIS PSF for the EWS, which can vary spatially, temporally, and spectrally. For example, defects are present on the optical surfaces in the *Euclid*; if these are not accurately characterised in the model of the spacecraft which enters the PSF model, then

there will be error in the PSF that is assumed for the shear measurement. This PSF error may vary spatially, across the FoV. Another example is the error arising in the transfer of the PSF model to target galaxies, which occurs due to imperfect knowledge of the galaxy SEDs, as discussed in chapter 4; this effect results in PSF errors which vary across the FoV, as well as spectrally. However, these effects are temporally stationary - that is, they do not vary between exposures (Euclid Collaboration: Mellier et al., 2024).

Other effects are present which *do* induce such temporal variation of the VIS PSF for *Euclid*. In general, these consist of time-varying characteristics of the telescope state which impact the PSF. While the Lagrange point L2 orbit for *Euclid* was selected to optimise the thermal stability of the spacecraft, and hence of the PSF, the PSF is still subject to temporal variations. It is for this reason that the PSF calibration hierarchy includes observations of calibration fields with a monthly cadence (Euclid Collaboration: Mellier et al., 2024).

One effect which results in a substantial contribution to the temporal variation of the VIS PSF consists of thermal variations in the spacecraft. These arise because the orientation of the spacecraft with respect to the Sun vector varies as the spacecraft makes observations with different pointings. The resulting thermal variations in the spacecraft result in thermal expansion of its components, which result in offsetting and deformation of the components of the optical system. This results in FoV-dependent variations in the optical path length, which in turn results in PSF variations. While the EWS has been designed to minimise the presence of large, rapid slews in order to maximise thermal stability (Euclid Collaboration: Scaramella et al., 2022), some degree of thermal variation in the spacecraft is inevitable, and this effect must be included in the PSF model, at a level that satisfies the shear measurement requirements (Euclid Consortium: Lorenzo Alvarez, 2014). This requires periodic calibration of the Euclid model; because of the finite cadence of such calibration, there will inevitably be some variation in the PSF model on timescales shorter than that of the calibration cadence, which will not be included in the model, and hence result in PSF error that will bias the shear measurement.

Forecasting the shear biases arising due to temporal variations of the PSF, which are not included in the PSF model, is the focus of the present chapter. There are a number of caveats which apply to this work. Firstly, while the temporal variations of the PSF are calibrated with a monthly cadence, the present work considers a PSF model which is calibrated at the beginning of the survey, and considered stationary for the rest of its duration. The purpose of this approach is to estimate the total impact of the PSF variations on the shear measurement, in order to test the importance of the monthly calibration. Additionally, the stationary-model case considered in this work serves as a prototypical proof-of-concept. A further caveat is that the model for thermal variations of the spacecraft, as well as the survey design, that are considered in this work, correspond to pre-launch forecasts. In particular, a model for the PSF variations which is consistent with in-orbit observations is still in development (Miller and Whittam, *in prep.*). Moreover, the in-orbit calibration observations which are used in this work are obtained from preliminary observations during the initial commissioning phase of the *Euclid* mission, rather than the subsequent main calibration campaign. Therefore, the results presented in the present chapter are conditional, in particular pending an updated model of the PSF variations which are consistent with in-orbit observations; again, the method described in the present chapter should be considered prototypical.

Section 5.1.1 describes the in-orbit calibration data which serves as the baseline PSF model, with respect to which thermal variations that are not included in the model induce temporally-varying PSF errors. Section 5.2 describes the estimation of shear biases arising due to these PSF modelling errors. Section 5.3 describes the construction of shear bias maps from the temporally-varying shear biases estimated in section 5.2. The results are summarised and future outlooks are discussed in section 5.4.

5.1.1 Phase-Diversity Calibration Baseline PSF

The optical component of the VIS PSF is modelled for the EWS in terms of the optical wavefront (Euclid Collaboration: Mellier et al., 2024, Duncan et al., *in prep.*, Euclid Consortium: Miller et al., 2020a). In the EWS VIS PSF model, wavefront errors (WFE), i.e. variations in the phase of a light wave at the image plane with respect to a reference surface, arising due to optical path differences, are expressed in terms of *Zernike polynomials* (Zernike, 1934). The Zernike polynomials are a basis set of polynomial functions, which are orthogonal on the unit disc. They are particularly useful in optical contexts, such as in the case of astronomical imaging, because each polynomial corresponds directly to a particular optical aberration, e.g. defocus, astigmatism, coma, trefoil, etc. The WFE in the PSF model is therefore parametrised in terms of the coefficients of the Zernike decomposition. PSF errors arising due to effects which induce optical path differences, including the thermal variations in the spacecraft that are considered in this work, may hence be quantified in terms of bias in the Zernike coefficients.

For the EWS, the VIS PSF model is calibrated before the start of nominal survey operations, in the phase-diversity calibration (PDC) campaign. This provides a baseline model for the telescope state, including the WFE. Thermal variations then induce variations in the Zernike coefficients with respect to the baseline state, which parametrise the PSF error resulting from this effect. In this work, variations in the Fringe sub-set of Zernike modes are considered (Euclid Consortium: Miller et al., 2022; Rimmer et al., 1972).

In the present work, in-orbit PSF calibration data from the preliminary test PDC that was conducted as part of the initial commissioning phase of the *Euclid* mission (Euclid Collaboration: Mellier et al., 2024; Euclid Consortium: Miller et al., 2019) is used to construct the baseline PSF. In the PDC, the Zernike coefficients are measured by making observations of stars in multiple defocussed telescope states. Canonically, the Zernike polynomials are indexed by radial degree n and azimuthal degree m, whereas the Wyant Fringe scheme numbers the Zernike modes using a single index j; the first 15 Zernike modes in the canonical ordering

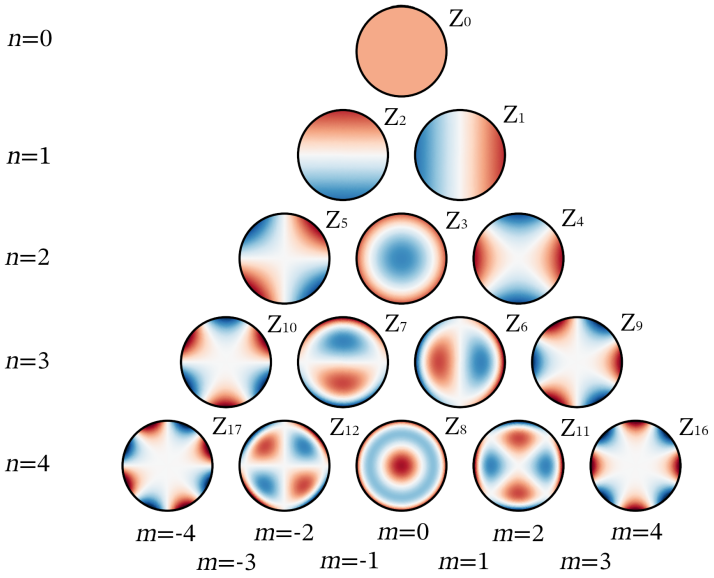


Figure 5.1: First 15 Zernike polynomials in canonical ordering, listed vertically by radial degree n and horizontally by azimuthal degree m, and also labelled with the corresponding Wyant indices (Liaudat et al., 2023; figure adapted from Wikipedia, 2025).

are shown in fig. 5.1, and labelled with the corresponding Wyant indices, where the Wyant index j is given by (Goodwin and Wyant, 2006):

$$j = \left(a + \frac{n + |m|}{2}\right)^2 - 2|m| + \left\lfloor \frac{1 - \mathrm{sgn}(m)}{2} \right\rfloor - 1, \tag{5.1}$$

where $\mathrm{sgn}(m) = \pm 1$ for respectively positive or negative m, or 0 if $m = 0$.

The baseline telescope model assumed in this work is parametrised by the PDC measurements conducted in the preliminary commissioning phase test PDC of 13 Fringe Zernike coefficients, $Z_3, Z_4, Z_5, Z_6, Z_7, Z_8, Z_9, Z_{11}, Z_{12}, Z_{13}, Z_{17}, Z_{18}$, and Z_{24}, numbered according to the Wyant convention. A useful property of the Zernike polynomials is that each one corresponds to a particular optical distortion. For example, Z_3 corresponds to the defocus; Z_4, Z_5 correspond to the vertical and oblique astigmatism, respectively; Z_6, Z_7 correspond to the horizontal and vertical coma, respectively; and Z_8 corresponds to the primary spherical aberration. An offset of the secondary mirror in the z-axis[1] of $0.14\mu\mathrm{m}$, which impacts the focus state of the telescope and is assumed to correspond to the in-orbit telescope state (Euclid Consortium: Miller and Duncan, 2020). The polarisation-dependence

[1] i.e the direction parallel to light beams entering the telescope.

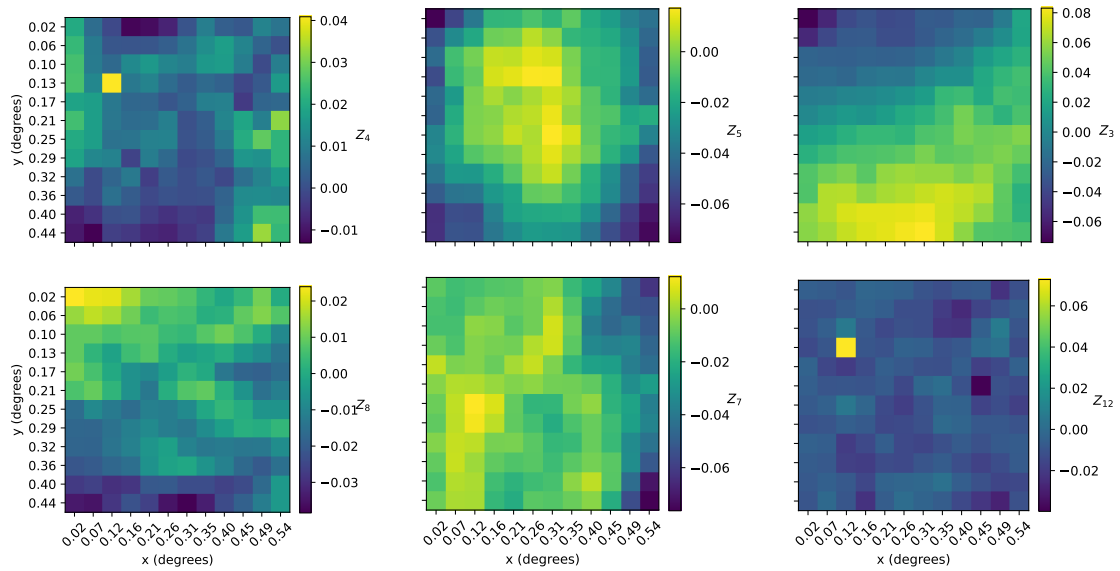


Figure 5.2: Zernike coefficients $Z_3, Z_4, Z_5, Z_7, Z_8, Z_{12}$ as measured in the preliminary test PDC, conducted as part of the *Euclid* commissioning phase, prior to the beginning of the survey. These serve as the baseline parametrisation of the VIS PSF model considered in this work, with respect to which thermal variations in the spacecraft induce temporal variations (Euclid Consortium: Miller et al., 2022).

of the WFE introduced due to reflection from the optical surfaces within the spacecraft, in particular the dichroic plate (Euclid Collaboration: Mellier et al., 2024), is not considered in this work.

PDC measurements of the Zernike coefficients are sampled on a 12×12 grid on the FoV. In this work, temporal variations in 6 Fringe Zernike coefficients, $Z_3, Z_4, Z_5, Z_7, Z_8,$ and Z_{12} are considered. These modes are considered because they are expected to exhibit the most significant temporal variations arising due to the thermo-mechanical behaviour of the spacecraft (Euclid Consortium: Miller et al., 2022). The initial PDC measurements of these Zernike coefficients are shown in fig. 5.2.

5.2 Forecasting Shear Biases Arising Due To PSF Temporal-Variation Modelling Errors

5.2.1 Sampling PSF Temporal Variations Using Principal Component Analysis

Prior to the launch of the *Euclid* spacecraft, the contractor Thales Alenia conducted the structural-thermal-optical (STOP) analysis (Ferrero et al., 2020), which modelled the variations in the 6 Fringe Zernike coefficients which are primarily impacted by thermal variations in the spacecraft listed in section 5.1.1, including the static response of the Zernike modes as a function of its orientation with respect to the Sun vector[2], in addition to the transient response to rapid, i.e. step-function, changes in the spacecraft orientation. Based in the EWS survey design (Euclid Collaboration: Scaramella et al., 2022), corresponding to a mapping between telescope orientation and the time and celestial coordinates of each pointing, Euclid Consortium: Miller et al., 2022 estimated the resulting variations in the 6 STOP Zernike coefficients due to the static response as a function of pointing epoch, ecliptic longitude, ecliptic latitude, and position angle[3], and convolved the time series of the static response with the transient response. Zernike coefficient variations are estimated with a cadence of approximately one hour, with all routine survey operations pointings included. Individual dithers are not included. Zernike variations are estimated with a high spatial resolution on the VIS FoV that is downsampled to a a 3×3 grid on the FoV for the purposes of this work, to make the problem tractable.

The Zernike variations as a function of pointing epoch estimated by Euclid Consortium: Miller et al., 2022; Ferrero et al., 2020 form the PSF error model considered in this work. The aim of this work is therefore to estimate the shear biases that result from the PSF error corresponding to the variation of the Zernikes with respect to the PDC baseline measured prior to the nominal survey operations,

[2]Parametrised by rotation angles about three Cartesian axes, with the x-axis defined as the vector pointing from the spacecraft to the Sun, the z-axis pointing from the spacecraft to the north ecliptic pole, and the y-axis orthogonal to both (Euclid Collaboration: Mellier et al., 2024).

[3]i.e. the orientation of the x-y axes of the FoV with respect to the ecliptic coordinates.

as described in section 5.1.1, as a function of pointing epoch. However, the hourly cadence of the pointings corresponds to ∼26,500 epochs; additionally, when estimating shear biases, it is also necessary to sample the high-dimensional space of galaxy properties, as discussed in chapter 3. The high dimensionality of the joint space of telescope pointing and galaxy properties which must be sampled in order to estimate temporally-varying shear biases thus motivates the construction of a basis set of pointings for which shear biases are estimated. The shear bias estimates for this basis set may then be used to infer the shear bias values for the remaining pointings. The problem of constructing a basis set of points in a high-dimensional space from which shear bias values are constructed is comparable to the problem discussed in chapter 3, and the work presented in this chapter serves as an extension of that work.

The approach adopted in this work is to apply principal component analysis (PCA; Jolliffe and Cadima, 2016) to the ensemble of FoV-dependent Zernike variations, in order to identify a basis set of Zernike variations which is representative of the whole distribution. PCA is a statistical technique which identifies the orthogonal axes (*principal component vectors*) in the distribution of a multivariate population, which are ordered and oriented such that the variance of the population along the first principal component axis is maximised, and such that the variance of the population along the i-th principal component vector is maximised, while being orthogonal to the previous $\{1...i-1\}$-th principal component vectors. This is illustrated schematically in fig. 5.3, in which the principal component vectors of a sample of 2-dimensional Gaussian-distributed data points is shown. The principal component vectors are identified with the eigenvectors of the population covariance matrix, ordered by the magnitudes of the corresponding eigenvalues.

Consider N M-dimensional data vectors $\mathbf{x}_1...\mathbf{x}_N$ which, without loss of generality, have zero mean. If the matrix $\mathbf{X}$ is defined, which is $N \times M$ matrix with columns formed of the vectors $\mathbf{x}_i$, then the $M \times M$ sample covariance matrix

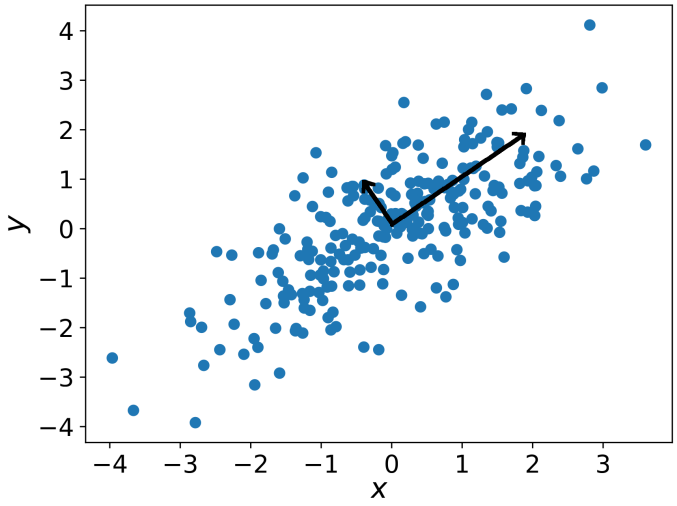


Figure 5.3: Schematic illustration of PCA. 200 points in the space of (x, y) are drawn from a 2D Gaussian distribution, with zero mean and some covariance. Black arrows show the principal component vectors which are given by the eigenvectors of the data covariance matrix, scaled by the corresponding eigenvalues; these correspond to the two orthogonal axes along that maximally explain the variance in the data. The longer arrow corresponds to the first principal component vector, and the shorter arrow to the second principal component vector. In this diagram, arrows are schematically shown for illustrative purposes and do not correspond to the exact principal component vectors).

$\mathbf{C}$ is given by (Joliffe, 2002):

$$\mathbf{C} = \frac{1}{N-1}\mathbf{X}^T\mathbf{X}, \tag{5.2}$$

where T denotes transposition. The principal component vectors are the eigenvectors $\boldsymbol{\alpha}_k$ of $\mathbf{C}$, sorted by the magnitude of its eigenvalues λ_k. The aim, then, is to find the matrix $\mathbf{A}$ with columns formed by the eigenvectors of $\mathbf{C}$, such that it diagonalises $\mathbf{C}$ (Joliffe, 2002):

$$\mathbf{A}^{-1}\mathbf{C}\mathbf{A} = \mathbf{L}, \tag{5.3}$$

where $\mathbf{L}$ is a diagonal matrix with diagonal elements given by the eigenvalues λ_k of $\mathbf{C}$. In practice, for large $\mathbf{C}$, this eigendecomposition may be accomplished numerically using a number of standard libraries. The next aim is to reduce the dimensionality of the data by projecting $\mathbf{X}$ onto a new basis formed by the first $p \leq M$ eigenvectors. If $\mathbf{L}$ is sorted by the magnitude of the eigenvalues λ_k, and the columns of $\mathbf{A}$ are also sorted according to the magnitude of the corresponding

eigenvalues, then the $M \times p$ matrix $\mathbf{P}$ of principal component vectors may be formed from the first p columns of $\mathbf{A}$; then, the $N \times p$ matrix $\mathbf{Y}$ of projected data vectors is given by (Joliffe, 2002):

$$\mathbf{Y} = \mathbf{XP}. \tag{5.4}$$

The fraction of the total variance of the distribution that corresponds to (or is "explained by") each principal component vector is given by the ratio between the corresponding eigenvalue and the trace of the population covariance. PCA therefore serves as a linear data reduction technique, with the principal component vectors constituting a linearly transformed coordinate system with axes ordered according to their contribution to the variation in the population; this allows the most important axes of linear correlation in a population to be identified.

PCA is therefore selected in this work to efficiently sample a basis set from the population of Zernike coefficient variations. This is because it allows the main axes of variation in the correlated population of Zernike variations to be identified, and elements of that population may be efficiently sampled in a way that captures the most important variations, by sampling points projected along the principal component axes. Additionally, while the PSF variations in real space are non-linear, in the wavefront domain, the WFE is linear in the Zernike coefficients; this further justifies the adoption of PCA in this work. In this work, PCA is conducted on the joint 54-dimensional space of STOP analysis Zernike modes and FoV-positions, since the variations in the 6 STOP Zernike modes estimated by Euclid Consortium: Miller et al., 2022 are calculated on a 3×3 grid on the FoV. The purpose of conducting the PCA jointly on the Zernike-FoV-space is to include the effect of the correlations of the Zernike modes across the FoV in the basis set.

In PCA, the input data is mean-subtracted. It is also possible to standardise the input data in each dimension by dividing by the data by its standard deviation. This is used in cases where different dimensions correspond to physical quantities with different units, to factor-out discrepancies in intrinsic scale of each dimension from the covariance that enters the PCA calculation. While the Zernike coefficients are dimensionless, this standardisation is applied in this work because it results

in a PCA basis sample that leads to smaller residuals in the final inferred shear bias estimates; this may because of the presence non-linear correlations in the distribution of FoV-dependent Zernike coefficient variations.

The first 197 hours of the list of survey epochs are discarded due to instability of the PSF in this interval (Euclid Consortium: Miller et al., 2022). The fraction of the variance that is explained by the leading 6 principal components is shown for the un-standardised and standardised cases in table 5.1. A larger number of principal components explains more of the variance of the full distribution, but the distribution will be sampled less efficiently. In the standardised case, 97.6% of the variance is explained by the first four principal components. The population of 54-dimensional FoV-dependent Zernike coefficient variations is projected to the space of the first four principal component vectors. 1000 points constituting the PCA-projected basis set are then sampled, by randomly sampling separately from the marginal distribution of projected Zernike-coefficient variation data points along each principal component axis. The resulting four-dimensional PCA-space basis set is then de-projected back to the original standardised 54-dimensional space of Zernike coefficient variations, lying along the principal component axes. The basis set of Zernike coefficient variations is then obtained by finding the nearest neighbour of each PCA-sampled point in the full population of Zernike coefficient variations, obtained using the `scipy` implementation of the K-D tree algorithm, with distances calculated in the standardised 54-dimensional space. The number of principal components, and the number of basis set points sampled, is selected along with the number of galaxy SEDs for which the shear bias estimation is conducted (see section 5.2.2), to balance accuracy of the final inferred shear bias estimates with computational speed.

In order to estimate shear biases, the points in the full population of FoV-dependant Zernike coefficient variations must be assigned to points in the basis set. A k-nearest-neighbours approach is applied in this work, in which the 5 nearest neighbours of points in the full population in the basis set are identified, with distances calculated in the 4-dimensional standardised space of principal

Table 5.1: Fraction of the variance of the 54-dimensional joint distribution of FoV-dependent Zernike coefficient variations that is explained by the first 6 principal components, along with the cumulative fraction of explained variance including the preceding principal components, for the standardised and un-standardised cases.

Standardised	Cumulative	Un-standardised	Cumulative
0.532	0.532	0.707	0.707
0.310	0.842	0.271	0.978
0.111	0.953	0.0183	0.996
0.0229	0.976	1.85×10^{-3}	0.998
0.0186	0.994	1.23×10^{-3}	0.999
4.33×10^{-3}	0.999	3.07×10^{-4}	0.9997

component vectors. Points in the full population are then assigned shear bias estimates given by the weighted mean of the shear bias estimates for its 5 nearest neighbours in the basis set (see section 5.2.2), with weights given by the inverse-distance of each neighbour, normalised by the sum of inverse-distances of the 5 nearest neighbours.

The PCA-sampled basis set of Zernike variations is plotted along with the full population in fig. 5.4, for the central FoV position, for the first 10000 hours of the survey. As can be seen in fig. 5.4, the PCA-sampled basis set of epochs follows the variations in some Zernike coefficients more than others. For example, variations in the defocus Z_4, the oblique astigmatism Z_3, and the horizontal coma Z_8 are more well-characterised by the PCA-sampled basis set than variations in the vertical coma Z_7 or the vertical astigmatism Z_5. This indicates that the variations in the latter coefficients contribute less to the variations in the joint 54-dimensional distribution of FoV-dependent Zernike coefficient variations, even when the distribution is standardised. If such Zernike coefficient variations which are not well-characterised by the PCA-sampled basis set have a significant impact on the shear measurement, then there will be residual error in the shear bias estimation. For example, if variations in Zernike coefficients which correspond to changes in the size of the PSF are not well-characterised by the PCA-sampled basis set, then the resulting multiplicative bias estimates will be under-estimated. In particular, the vertical astigmatism Z_5 is particularly poorly-sampled, with many large-amplitude spikes which are not captured by the PCA-defined sample

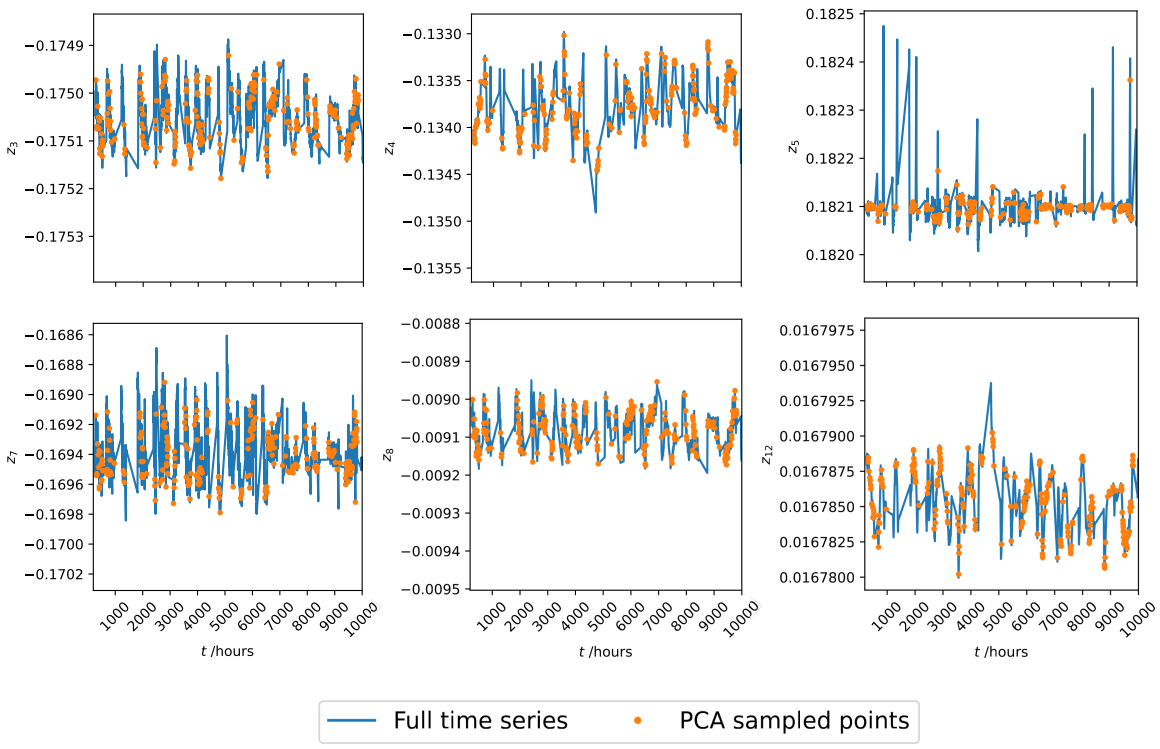


Figure 5.4: Forecast variations in Zernike coefficients $Z_3, Z_4, Z_5, Z_7, Z_8, Z_{12}$ arising due to thermal variations in the *Euclid* spacecraft, as a function of survey epoch, for the first 10,000 hours of the survey, for the central FoV position. Blue: full time series of Zernike variations, as modelled by the STOP analysis (Ferrero et al., 2020), and mapped to survey epoch by Euclid Consortium: Miller et al., 2022. Orange points: PCA-sampled basis set of pointings, sampled as described in section 5.2.1.

(top-right panel of fig. 5.4); comparing with fig. 5.1 shows that this is an anisotropic distortion. As a result, it might be expected that the under-sampling of Z_5 shown in fig. 5.4 may result in residual error in the estimate of the c-bias.

5.2.2 Propagating PSF Temporal-Variation Modelling Errors to Shear Biases

The estimation of shear measurement biases arising due to PSF modelling errors is conducted using an adaptation of the methodology described in chapter 3. For each element of a joint basis set of telescope pointing epochs and galaxy SEDs, truth- and error-channel PSFs are generated using the PSFTOOLKIT software (Duncan et al., *in prep.*, Euclid Consortium: Miller et al., 2020a), with each PSF taking a galaxy SED as input. In this case, the PSF generation also takes in a *telescope state* input, parametrised by a set of Zernike coefficients; this forms the

truth- and error-channel input for this work. For the truth-channel, the baseline set of Zernike coefficients measured in the commissioning-phase test PDC described in section 5.1.1 defines the telescope state. For the error-channel, the telescope state is defined by the baseline set of Zernike coefficients, with the addition of the (baseline-subtracted) set of STOP Zernike coefficient variations corresponding to each element of the basis set of epochs, sampled as described in section 5.2.1. To improve the speed of the PSF generation, the native 12×12 FoV-grid of baseline Zernike coefficients obtained from the PDC are downsampled to a 5×5 FoV-grid. This is accomplished using linear bivariate spline interpolation implemented using the `scipy RectBivariateSpline` routine. This resolution is selected to capture the important FoV variations while maximising computational speed. The temporal variations of the 6 STOP Zernike coefficients with respect to the baseline are calculated by downsampling the 12×12 FoV-grid of baseline coefficients to a 3×3 FoV-grid, and subtracting the downsampled baseline values from the time series of STOP Zernike coefficients.

The basis set of galaxy SEDs used to generate the truth- and error-channel PSFs is sampled from the population of SEDs present in the *Euclid* Flagship 2 mock galaxy catalogue (Euclid Collaboration: Castander et al., 2024), in a similar manner to that described in section 3.3. As mentioned in section 5.2.1, the number of sampled SEDs is balanced with the number of principal components from which the basis set of epochs is sampled, and the number of sampled epochs in the basis set, to balance the accuracy of the shear bias estimation with the computational speed. In this work, a basis set of 500 SEDs is used, sampled in the space of colour indices $(r-i, r-z, i-z)$, on a uniform grid defined by constant $N_{\rm axis} = 10$, with the colour indices defined as in section 3.3. This number of basis SEDs is found to result in shear bias estimate residuals that are sub-dominant with respect to the PSF modelling requirements described in section 3.1.2, which are the pertinent requirements for this work, because of the lower-dimensionality of the space from which the SEDs are sampled, and the relative insensitivity of the thermal-variation-sourced PSF error to spectral variations. Redshift is not included in the

sampling grid, i.e. SEDs are sampled randomly in redshift. In section 5.3, the redshift-dependence of the thermal-variation-sourced shear biases is investigated by sampling mock galaxies explicitly from tomographic redshift distributions $n_i(z)$. For a catalogue-level shear bias forecast as described in chapter 3, including the observed redshift $z_{\rm obs}$ in the sampling grid may result in more accurate per-galaxy ellipticity bias estimates, which would necessitate a larger number of sampled SEDs. For the tomographic, map-level shear bias forecast conducted in this chapter, the approach described here is sufficient.

For each element of the basis set of epochs and galaxy SED, on a 5×3 grid of galaxy scalelength r_s and ellipticity modulus $|\boldsymbol{\chi}|$ as described in section 3.3.3, and on a 3×3 grid on the FoV, the corresponding truth- and error-channel PSFs enter the QE shear bias estimation described in section 3.2 (Euclid Consortium: Miller et al., 2020b). Shear biases are then inferred for mock galaxies using the SED-matching technique described in section 3.3.1, FoV- and morphology-interpolation described in section 3.3.3, and the PCA-space Zernike-coefficient matching technique described in section 5.2.1.

To validate the performance of the PCA sampling of the basis set of epochs, shear biases are estimated directly using the QE method described in section 3.2, for 1000 mock galaxies with random pointing sampled from the full time series of ∼26,000 epochs, for each of the 500 basis-set SEDs and points on the morphology- and FoV-grids described in section 3.3.3. Shear biases for the same sample of galaxies with randomly-selected set of epochs are also inferred from the basis set of epochs, using the matching-based method described in this section and in section 3.3. Histograms of the residual errors in the additive and multiplicative biases, averaged over morphology and FoV-position, are compared with the PSF modelling requirements (see section 3.1.2) in fig. 5.5. As can be seen in fig. 5.5, the residual error in the multiplicative bias inferred using the PCA-matching method described in section 5.2.1 is safely within the corresponding PSF modelling requirement. The same is also true of the c_2 component of the additive bias. On the other hand, the residual error in the c_1 component of the

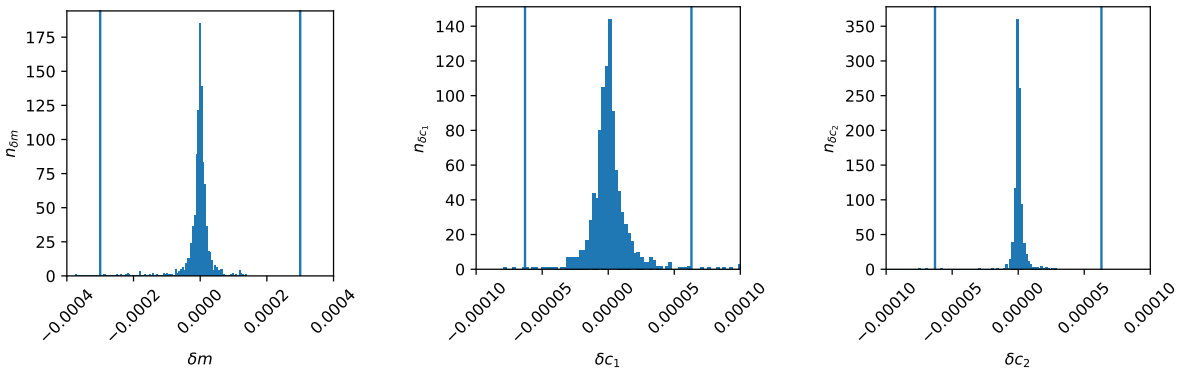


Figure 5.5: Histograms of residual shear bias errors resulting from the estimation of forecast shear biases as a function of survey epoch by matching to the PCA-sampled basis set of survey epochs, as described in section 5.2.1. For a randomly-selected sample of 1000 epochs, residual errors in the forecast shear bias arising due to PSF modelling errors are calculated. Results are averaged over shear biases estimated for the basis set of mock galaxy SEDs and morphologies. Vertical bars show the EWS VIS PSF modelling requirement (see section 3.1.2). Left: residual error in m-bias, δm. Centre: Residual error in c_1 bias component, δc_1. Right: Residual error in c_2 bias component, δc_2.

additive bias is substantially larger with respect to the PSF modelling requirement; this discrepancy arises due to anisotropy in the PSF, since (e.g. by (3.7)) the c-bias depends on the PSF ellipticity. Additionally, it may occur as a result of residual error in the additive bias estimates, for example due to undersampling of the vertical astigmatism variations Z_5, as seen in fig. 5.4. As discussed in section 3.1.2, for sources of PSF error which are a significant contribution to the error budget represented by a particular requirement, then it is sufficient for the purposes of shear bias forecasting that the shear bias estimates be on average sub-dominant with respect to the requirements, rather than negligible. This is because, for shear biases that are large compared to the requirements, the residual errors in the shear bias estimates will be sub-dominant; while for shear biases that are below requirements for which they dominate the error budget, it is sufficient to be satisfied, based on the shear bias estimation, that the size of the shear biases is safely within requirements.This is true of the temporally-varying PSF modelling errors, which are a main contributor to the error budget represented by the PSF modelling requirement. Therefore, the sub-dominance of the c_1 residual errors compared with the PSF modelling requirement is sufficient

for the purposes of this work.

5.3 Mapping Tomographic Forecast Shear Biases

Given the propagation of the temporal variation of the VIS PSF to pointing-dependent shear bias estimates as described in section 5.2, the remainder of this work consist of constructing tomographic maps of the spatial variations of the shear biases. Section 5.3.1 describes the tomographic sampling of mock galaxies and estimation of tomographic shear bias values, as a function of survey epoch. Section 5.3.2 describes the projection of these pointing-dependent shear bias estimates to pixelised tomographic shear bias maps.

5.3.1 Tomographic Mock Galaxy Sampling

In order to estimate tomographic shear biases as a function of survey epoch, Flagship 2 mock galaxies are sampled from the OU-PHZ tomographic redshift distributions $n_i(z)$, supplied by I. Tutusaus (*priv. comm.*), using the inverse transform sampling technique described in section 4.3.1. For each of the 13 tomographic redshift bins, 1000 mock galaxies are randomly sampled. For each sampled galaxy, shear bias values are estimated using the PCA-matching, SED-matching and morphology-interpolation technique described in section 5.2, for every epoch in the list of $\sim$26,000 temporal Zernike coefficient variations described in section 5.2.1. Because the aim of this work is to forecast the spatial variation of the shear biases arising due to PSF modelling error, rather than sampling the FoV-positions of mock galaxies from the Flagship 2 catalogue, the pointing- and galaxy-property-dependent shear bias estimation is conducted separately for each point on the 3×3 FoV grid. The resulting shear bias estimates are averaged over the 1000 mock galaxies sampled from each tomographic redshift bin.

The forecast shear biases in the first year of the survey, as a function of survey epoch, averaged over a timescale of approximately seven days, are shown in fig. 5.6, for the first and last tomographic redshift bins. Error bars are given by the standard deviation of the shear bias estimates for the joint ensemble of

individual epochs and FoV positions, in order to capture the full contribution from the spatial variation of the shear biases; the contribution from the standard error on the mean shear bias estimate per pointing originating from the distribution of galaxy properties is neglected, because of the large number of galaxies over which the shear bias estimates are averaged. It should be noted that these are not error bars on the mean value of the shear biases shown in fig. 5.6, but show the standard deviation of the spatio-temporal variations of the shear biases within the averaging timescale, in order to summarise the distribution of these variations. The standard deviation of the distribution of the absolute value of the additive bias $\sigma[|\boldsymbol{c}|]$ over all pointing-epochs and FoV-positions is plotted as a function of $\langle z_i \rangle$ in fig. 5.7. Error bars for fig. 5.7 are given by the standard error on the standard deviation measurement, estimated as in equation (4.5), with contributions from the variance of the population of spatio-temporal variations of galaxy-averaged $|\boldsymbol{c}|$, and the spatio-temporally-averaged variance of $|\boldsymbol{c}|$ estimates for the galaxies sampled in each tomographic bin.

5.3.2 Constructing Tomographic Shear Bias Maps Using HEALPIX

Given the tomographic epoch-dependent shear bias estimates, the pointings corresponding to each epoch are then projected to pixelised shear bias maps. This is accomplished using the HEALPIX spherical pixelisation scheme (Górski et al., 2005), implemented using the `healpy` Python library (Zonca et al., 2019). Shear bias time series for each tomographic redshift bin, averaged over 1000 galaxies sampled from the corresponding $n_i(z)$, are estimated as described in section 5.3.1. As described in section 5.2.1, the time series of STOP Zernike coefficient variations (Euclid Consortium: Miller et al., 2022) includes the ecliptic longitude, ecliptic latitude, and FoV position angle with respect to the ecliptic latitude corresponding to each survey epoch. These are used to project the tomographic shear bias time series to HEALPIX maps as follows:

(i) Given the resolution of the output HEALPIX map, parametrised by $N_{\rm side}$, calculate the corresponding HEALPIX pixel scale $\theta_{\rm pix}$ in arcminutes;

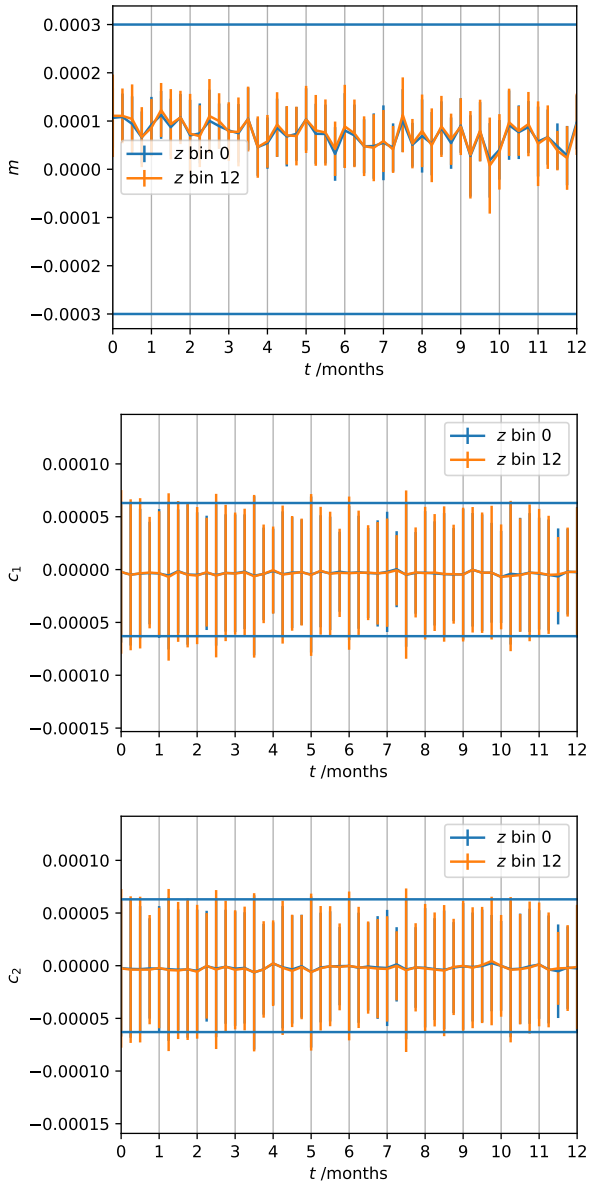


Figure 5.6: Forecast shear bias estimates in the first year of the survey, as a function of survey epoch, in units of 28-day intervals, arising due to PSF thermal-variation modelling errors, for tomographic redshift bins z_0, z_{12}. Shear bias estimates are calculated for each survey pointing epoch and position on a 3×3 FoV-grid, and averaged over values for 1000 mock galaxies sampled from each tomographic bin, and averaged over a seven day interval. Error bars show the standard deviation of the joint spatio-temporal distribution of individual pointing epochs and FoV-positions. Horizontal lines show the EWS VIS PSF modelling requirement (see section 3.1.2). Top: variations in multiplicative shear bias component m. Middle: variations in additive shear bias component c_1. Bottom: variations in additive shear bias component c_2.

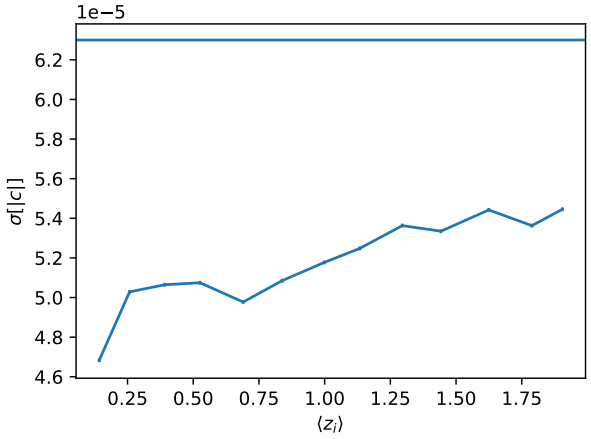


Figure 5.7: Standard deviation of the absolute value of the additive shear bias $\sigma[|\boldsymbol{c}|]$, arising due to PSF spatio-temporal modelling errors, as a function of tomographic bin mean redshift $\langle z_i \rangle$. Error bars are given by the standard error on the standard deviation calculated as described in section 4.2.3. The horizontal line indicates the PSF modelling requirement (section 3.1.2).

(ii) Calculate the resolution of the FoV sampling corresponding to the HEALPIX pixel scale $n_{\rm FoV} \times n_{\rm FoV}$, with $n_{\rm FoV} \equiv \lfloor \theta_{\rm FoV}/\theta_{\rm pix} \rfloor$, and $\theta_{\rm FoV}$ is the mean of the side lengths of the VIS FoV in arcminutes, $\sim 44'$;

(iii) For each survey epoch, the galaxy SED- and morphology-averaged 3×3 FoV grid of shear bias values is upsampled to $n_{\rm FoV} \times n_{\rm FoV}$, using linear bivariate spline interpolation implemented using the `scipy RectBivariateSpline` routine;

(iv) For each pointing, the $n_{\rm FoV} \times n_{\rm FoV}$ grid of upsampled FoV coordinates is rotated by the corresponding position angle, to orient the FoV-grid with respect to the ecliptic coordinate system;

(v) For each pointing and upsampled FoV grid point, the corresponding location in ecliptic coordinates is calculated. Firstly, the distortion of the spherical polar coordinate system as a function of ecliptic latitude is taken into account by dividing the separation in ecliptic longitude between each rotated FoV grid point and the corresponding pointing centre, by the cosine of the ecliptic latitude of the sampled FoV grid point[4]. The resulting distortion-corrected

[4]i.e. the sum of the ecliptic latitude of the pointing centre and the ecliptic-latitude separation

ecliptic-longitude separation between the FoV grid points and pointing centre, and the ecliptic-latitude separation between the FoV grid points and pointing centre, are added to the ecliptic coordinates of the pointing centre, to obtain the ecliptic coordinates of each sampled FoV grid point. Differences in spherical coordinate convention between HEALPIX and that used by Euclid Consortium: Miller et al., 2022 when generating the pointings are also corrected for;

(vi) The four nearest sampled points to each pixel in the output HEALPIX map are then obtained. This is accomplished by converting the ecliptic coordinates of the sampled points, and of the centres of the pixels of the `HEALPix` map with resolution set by $N_{\rm side}$, to Cartesian coordinates on the unit sphere. The four nearest sampled points are then obtained for each pixel, using the K-D tree algorithm, implemented using the `scipy cKDTree` routine. Distances are calculated in three-dimensional Euclidean space, rather than on the sphere using great-circle distances, as an approximation, since on the scale of HEALPIX pixels with angular size of interest, the sky is approximately flat;

(vii) The Euclidean distance in the Cartesian coordinate system corresponding to the width of a HEALPIX pixel is calculated, $r_{\rm pix}$. If the nearest sampled point to a given pixel has distance larger than $r_{\rm pix}$, that pixel is masked out, i.e. its shear bias value is set to zero. If the pixel has neighbours with distance less than $r_{\rm pix}$, then it is assigned a shear bias value equal to the weighted mean of its (up to) four nearest-neighbouring sampled points, with weights given by the inverse Euclidean distances between the pixel centre and each sampled point, normalised by the sum of the (up to) four inverse nearest-neighbour distances.

HEALPIX maps of the m, c_1 and c_2 shear bias components arising due to PSF thermal-variation modelling errors are shown, for the first tomographic redshift bin, in fig. 5.8.

between the pointing centre and sampled FoV grid point

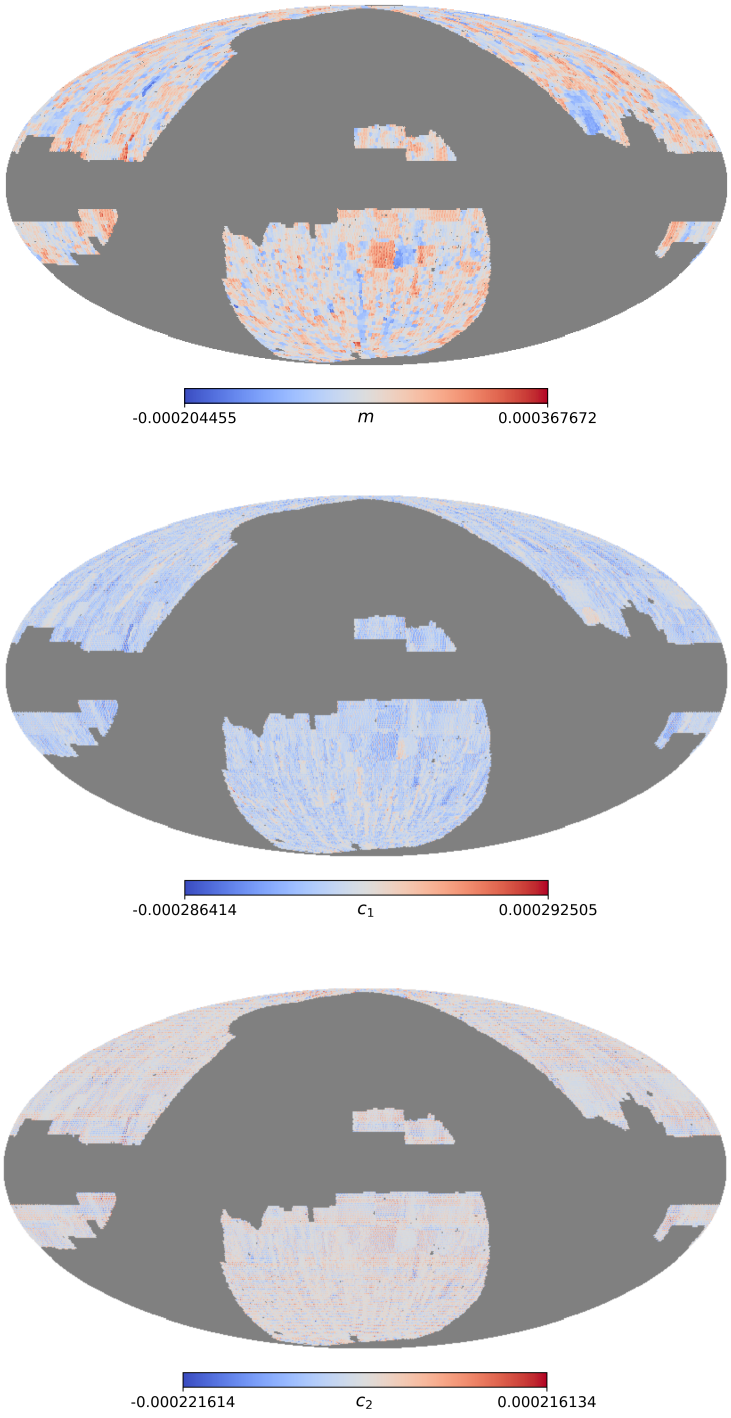


Figure 5.8: HEALPIX maps for the forecast shear biases arising due to PSF thermal-variation modelling errors. Shear bias time series, estimated using the technique described in section 5.2 and section 5.3.1, are projected to HEALPIX maps using the technique described in section 5.3.2, with $N_{\rm side}$ =2048, and plotted in ecliptic coordinates. Top: map of multiplicative m shear bias component. Middle: map of additive c_1 shear bias component. Bottom: map of additive c_2 shear bias component.

5.3.3 Discussion

Figure 5.6 shows the PSF modelling-error-sourced shear biases as a function of survey epoch in units of 28-day intervals, averaged over an interval of approximately seven days, and over shear bias estimates for galaxies sampled from tomographic redshift bins z_0 and z_{12}, the 1^{st} and 13^{th}, respectively. The error bars correspond to the standard deviation of galaxy-averaged shear bias estimates over the FoV and within the time interval over which the shear bias estimates are averaged, neglecting the standard error on the mean shear biases originating from the variation of galaxy properties. Note that these are large compared with the variation in the time-averaged shear bias values because they show the distribution of the spatio-temporal variations, rather than uncertainty on the mean value; that is, the variation in the data points shown in fig. 5.6 only captures the variation in the shear biases *averaged over 28-day* intervals; on the other hand, the error bars are computed from the standard deviation of the sample of shear biases *within each 28-day period*, capturing the variation within that timescale, as well as the FoV variation of the shear bias estimates. This presentation choice was made to illustrate the full variation of the shear bias estimates, in contrast to the standard deviation of the 28-day-averages (i.e. the standard error on the mean), which might give a misleading picture of the amplitude of the full shear bias variations. While for the additive bias components c_1, c_2, the time-averaged bias is well below the PSF modelling requirements, the spatio-temporal variation on timescales shorter than seven days is at the level of requirements for both additive bias components. The amplitude of variations is similar for both additive bias components. The m-bias has a larger time-averaged bias compared with the PSF modelling requirement than the additive bias, but still within the requirement, and with spatio-temporal variations on timescales shorter than seven days that are within the requirement. This indicates that the thermal variations in the spacecraft induce relatively larger errors in the PSF ellipticity than in the PSF size (see section 3.1.2, equations (3.9), (3.10)). However, as seen in fig. 5.4, the PCA epoch sampling characterises the variations in some Zernike coefficients more accurately than others; if variations

in Zernike coefficients which induce PSF size errors, such as focus errors, are not adequately represented in the basis set of pointing epochs, then the resulting multiplicative shear bias may be under-estimated.

The vertical lines present in fig. 5.6 are spaced with an interval of 28 days, approximately corresponding to the cadence of VIS PSF calibration observations. The large additive bias spatio-temporal variations on timescales shorter than this have a substantial contribution from the FoV-variation of the PSF errors; this FoV variation is not temporally stationary, because the shear biases are estimated from the error in the PSF model with respect to the initial telescope state, calibrated prior to the nominal survey operations, and hence a substantial contribution to the shear bias variations from the FoV-variation indicates a departure from this baseline. This can be seen by inspection of the shear bias maps shown in fig. 5.8, which exhibit variation in the shear bias pattern across the FoV across the survey footprint, including variations on small scales, corresponding to a small characteristic timescale of variation. This indicates that there may be shear bias variation on timescales shorter than the monthly calibration cadence, which would not be characterised by monthly PSF calibration, although the amplitude of such shear bias variations depends on the PSF variations with respect to the monthly calibration baseline, which are not considered in this work. The shear bias maps shown in fig. 5.8 also exhibit variations on large angular scales, related to the EWS survey scanning pattern; while large scale shear bias variations have a significant effect on cosmological inference (see e.g. chapter 2), they are more likely to be well-characterised by the regular PSF calibration observations, and as a result are likely to be less important than the small-scale variations.

A suspicious feature of the shear bias maps shown in fig. 5.8 is that the c_1 bias appears to be biased negatively, and the c_2 appears to be biased positively. This may be spurious; for example, as seen in fig. 5.4 and discussed in section 5.2.2, the vertical astigmatism Z_5 is poorly sampled by the PCA sampling technique, with many large-amplitude variations not sampled. Comparing with fig. 5.1, it can be seen that the vertical astigmatism is an anisotropic distortion; bias in the estimate of

the variation of Z_5 may hence result in residual error in the additive bias estimates.

As can be seen in fig. 5.6, the long-timescale temporal variations of the shear bias estimates do not exhibit a significant redshift-dependence. This is verified to be the case for all tomographic redshift bins. Redshift-dependence of the shear bias estimates may enter via the chromaticity of the PSF variations, together with the colour-redshift relation; additionally, there is an inverse relationship between redshift and average galaxy scalelength, that is expected to result in a positive correlation between redshift and shear bias estimates. The shear biases shown in fig. 5.6 are averaged over shear biases calculated for Flagship 2 mock galaxies with SEDs, ellipticity moduli $|\boldsymbol{\chi}|$, and scalelength r_s sampled from the tomographic $n_i(z)$ redshift distributions described in section 4.3.1. On the other hand, the dependence of the standard deviation of the spatio-temporal additive bias variations on tomographic bin mean redshift $\langle z_i \rangle$, shown in fig. 5.7, demonstrates an increasing trend with redshift.

Figure 5.5 shows that the profile of the spatio-temporal shear bias variations has negligible redshift dependence; from the consequent implication that it does not strongly depend on the varying population of SEDs with redshift, this indicates that the profile of the spatio-temporal shear bias variations is not strongly chromatic. However, the increasing tend in $\sigma[|\boldsymbol{c}|]$ with $\langle z_i \rangle$ seen in fig. 5.7 indicates a dependence of the *amplitude* of the (additive) bias variations on galaxy properties. In particular, the redshift dependence of $\sigma[|\boldsymbol{c}|]$ is driven by the inverse relation between redshift and galaxy scalelength. The variation of the trend of $\sigma[|\boldsymbol{c}|](\langle z_i \rangle)$ on scales larger than the (negligible) error bars additionally indicates a dependence on the complicated variation of the population of SEDs with redshift, since the relationship between galaxy scalelength and redshift is expected to be smooth, implying that the amplitude of the PSF-modelling-sourced shear bias is chromatic, even if the profile of the spatio-temporal variations is not. On the other hand, these variations may indicate a breakdown of the assumptions used to estimate the error bars in equation (4.5); in particular, the galaxy samples over which the shear bias estimates are averaged for each FoV-position and epoch are the same, so there

should be a contribution from the covariance in the galaxy-averaged $|\boldsymbol{c}|$ estimates for each spatio-temporal point. Future work will investigate this, including an alternative estimation of the error bars by bootstrapping (Efron, 1992).

5.4 Conclusion

5.4.1 Summary

In this chapter, shear biases arising due to the thermal variations in the *Euclid* spacecraft that are not included in the VIS PSF model are forecast for the EWS. In particular, the test case in which the VIS PSF model is calibrated at the beginning of the survey, and not subsequently updated, is considered, with thermal variations of the spacecraft inducing temporal variations in the PSF with respect to the baseline model. In the real survey, temporal variations of the PSF are calibrated with an approximately monthly cadence, and so the test case considered in this work is not a realistic representation of the true PSF model errors that apply to the EWS. However, it serves to demonstrate the cadence of variations in the PSF that arise due to thermo-mechanical variations in the spacecraft, and is thus indicative of the timescale of the resulting shear bias variations, and therefore of the appropriateness of the monthly calibration cadence. In particular, the additive shear bias arising due to this effect is forecast to vary at the level of the PSF modelling requirement, as shown in fig. 5.6, on timescales shorter than the PSF calibration cadence. While this includes a contribution from the spatial FoV-variation of the additive bias, this can be seen by inspection of the shear bias maps shown in fig. 5.8 to vary on small as well as large angular scales, corresponding to short and long variation timescales, respectively.

It should be stressed that conclusions drawn from the present work regarding the timescale of PSF-modelling-error-sourced shear bias variations and the degree to which the monthly PSF calibration cadence is sufficient should be considered as strictly *indicative*. This is because the case in which the baseline truth-channel PSF model is regularly calibrated is not considered in this work, and so qualitative predictions regarding the amplitude of shear bias variations in that realistic case

can not be made. This work therefore should be considered to serve as a proof of concept, and as motivating further work to forecast the shear biases arising due to PSF variations with respect to the PSF model that is calibrated with a monthly cadence.

In order to forecast the temporally-varying PSF model errors, measurements of the Zernike polynomial coefficients that parametrise the VIS PSF, made during the preliminary in-orbit PDC test observations conducted as part of the pre-survey spacecraft commissioning phase (Euclid Consortium: Miller et al., 2019), enter the baseline PSF model (section 5.1.1). The pre-launch STOP analysis simulation of the Zernike coefficient variations that arise due to thermal variations in the spacecraft (Euclid Consortium: Miller et al., 2022; Ferrero et al., 2020) is then adopted, defining the variation of the PSF with respect to the baseline PDC model.

Variations in 6 Zernike coefficients, downsampled to a 3×3 FoV-grid, as a function of survey epoch, are obtained from Euclid Consortium: Miller et al., 2022. Because it is computationally unfeasible to estimate resulting shear bias values for every survey epoch, a PCA-based method is employed to efficiently sample a basis set of pointings from the 54-dimensional space of FoV-dependent Zernike coefficient variations, while characterising the most important correlated variations in the population (section 5.2.1). Shear biases are estimated for epochs in this basis set, as a function of galaxy SED, morphology, and FoV-position. A k-nearest-neighbours matching technique, together with the SED-matching and morphology/FoV-interpolation methodology described in section 3.3, are then used to infer forecast shear biases for Flagship 2 mock galaxies sampled from tomographic redshift bins (with $n_i(z)$ provided by I. Tutusaus *priv. comm.*), as a function of pointing epoch and FoV-position, as described in section 5.2.2.

Shear biases arising due to spatio-temporal PSF modelling errors are shown as a function of survey epoch in fig. 5.6. The time variation of the shear bias is found to have negligible redshift-dependence, but the standard deviation of the additive bias variations $\sigma[|\boldsymbol{c}|]$ is shown in fig. 5.7 to depend on tomographic bin mean redshift $\langle z_i \rangle$, likely owing to the correlation between redshift and

galaxy scalelength.

The shear bias estimates, computed as a function of survey epoch and FoV position, are then projected onto HEALPIX maps, as described in section 5.3.2. These are generated based on the (pre-launch) survey design (Euclid Collaboration: Scaramella et al., 2022) which relates survey epoch to ecliptic coordinates and position angle of each corresponding pointing; HEALPIX maps for forecast shear bias components m, c_1, c_2 arising due to PSF modelling errors are shown in fig. 5.8.

5.4.2 Future Work

As described in section 5.1, the work presented in the chapter is subject to a number of caveats. One of these is that the model of the Zernike coefficient variations that is adopted in this work, based on the STOP analysis conducted by the contractor Thales Alenia (Ferrero et al., 2020), did not sufficiently predict the actual temporal Zernike mode variations observed in orbit. Indeed, other sources of thermo-mechanical variation in the spacecraft are present which were not anticipated prior to the launch, notably due to variation in the activity of the read-out electronics (ROE) that are part of the VIS instrument resulting in thermal variations in the spacecraft; additionally, other sources of temporal variation of the VIS PSF are present which are not due to thermal variations; as such, a model of the spatio-temporal variations of the PSF as a function of spacecraft orientation, and hence pointing, based on in-orbit PSF calibration observations, is still under development (Miller and Whittam, *in prep.*). The model of PSF variations considered in this work is therefore obsolete, and the methodology and results should be considered as an indicative proof-of-concept. Future work in this area should use a more realistic, empirically-informed model of PSF variations.

Another very important caveat to the work presented in this chapter that has been discussed at length in section 5.1, section 5.3.3, and section 5.4.1, is the fact that this work has considered a single baseline PSF model, defined prior to the start of the nominal survey operations, rather than the realistic case in which the PSF model is calibrated with an approximately monthly cadence. Again, in

this respect, this work should be considered as an indicative proof of concept, demonstrating the timescale and worst-case amplitude of shear biases arising due to spatio-temporally varying PSF model errors. The work presented in this chapter motivates future work considering the more realistic scenario, in which the baseline PSF model is regularly calibrated; assuming a realistic model of PSF variations, this will result in a realistic forecast of the error-budget contribution to the shear measurement arising due to this effect. Monthly calibration was not included in this work because the shear bias estimates are calculated for each element of the PCA-sampled basis set of survey epochs; because the shear bias estimates are calculated with respect to the baseline model, this would increase the dimensionality of the required sampling by a factor of the number of PSF calibrations occurring during the survey. It may be possible to improve this scaling by sampling the distribution of FoV-dependent Zernike coefficient variations more efficiently, e.g. if the PSF only explores a sub-set of the full space during a single inter-calibration period, such that fewer samples are required.

Another potential future direction may involve more efficient methods of sampling the high-dimensional joint space of Zernike coefficient variations and FoV-position. For example, PCA is sensitive only to linear correlations in the population of points; if there are substantial non-linear correlations, then alternative dimensionality-reduction techniques such as kernel PCA (Schölkopf et al., 1998) or self-organising maps (SOMs, e.g. Yin, 2007) may be applicable. In general, the inference of shear bias estimates for a given point in the joint FoV-Zernike coefficient space, based on a training set, in the presence of potentially non-linear correlations, may be accomplished by a large number of machine-learning techniques. Future work may involve investigating whether it is possible to apply such techniques to this problem.

The HEALPIX shear bias maps generated in section 5.3.2 provide a convenient means of propagating the impact of PSF modelling errors to cosmological parameter inference. The impact of shear bias maps on cosmology may be forecast by estimating their impact on summary statistics, e.g. on the angular power

spectra (see e.g. Kitching et al., 2019, chapter 2), which may then be propagated to cosmological parameter biases. This is beneficial in that it allows a realistic forward model of the impact of such systematics on the cosmological aims of *Euclid*, which may be used to obtain or validate requirements or analysis pipelines. For example, Massey et al., 2013 and Cropper et al., 2013 considered the impact of shear measurement biases directly at the level of biases in angular power spectra, and flowed-down the resulting biases in cosmological parameters to requirements on shear measurement e.g. on PSF calibration. As described in section 3.1, such an approach simplifies the complicated impact of measurement biases on the summary statistics. While a full forward model of the impact of shear measurement biases would be conducted from the pixel-level, a map-level forward model is a less computationally-expensive compromise, which allows for more realism than the approach of e.g. Cropper et al., 2013; Massey et al., 2013. Shear bias maps may also be used to forecast the impact of shear measurement biases on observables other than 2-point statistics, such as WL mass maps (Broxterman et al., 2024). Work is currently in preparation to propagate the maps of PSF-modelling-error-sourced shear biases discussed in this chapter to 3×2-point cosmological parameter inference (Tanidis et al., *in prep.*).

Strange enlightenments are vouchsafed to those who seek the higher places.

— Flann O'Brien, *The Third Policeman*

6 Conclusions

Contents

6.1 Overview 211
6.2 Outlook 217

6.1 Overview

As described in chapter 1, the forthcoming cosmological galaxy surveys of the 2020s, including the *Euclid* Wide Survey (Euclid Collaboration: Mellier et al., 2024) and the Rubin Observatory Legacy Survey of Space and Time (Dark Energy Science Collaboration: Mandelbaum et al., 2018) will constrain cosmological parameters with a level of precision that requires meticulous understanding and control of systematic biases (Albrecht et al., 2006). As a space-based observatory, *Euclid* has a diffraction-limited PSF, and the VIS instrument is optimised for precise shape measurement; together with the 14,000 deg^2 survey area and EWS imaging out to magnitude $m_{\mathrm{VIS}} \sim 24.5$, *Euclid*'s constraining power is such that systematics dominate the error budget. A significant source of systematic bias in WL surveys consists of bias in the shear measurement, and it is a crucial task for stage-IV surveys, such as the EWS and the LSST, that shear measurement

biases, and the impact that such biases have on cosmological inference, be well-characterised and mitigated.

The aim of the work presented in this thesis has been to contribute to forecasting the cosmological impact of shear measurement biases for stage-IV WL surveys. Because this is a very large area of research in modern observational cosmology, the work presented here has focused on a small number of specific topics that are relevant to shear measurement for such surveys, which will conduct "precision cosmology". While previous work in placing requirements on shear measurement systematics for WL surveys, such as Cropper et al., 2013; Massey et al., 2013, evaluated the impact of shear measurement biases based on analytic prescriptions, the approach taken in this work has been to forward-model the impact of shear biases with spatial, temporal, and spectral variation. A substantial component of the work presented in this thesis consists of the estimation of shear biases arising due to PSF errors for the EWS, by estimating the ellipticity bias for simple mock images of galaxies sampled from the *Euclid* Flagship 2 simulation (Euclid Collaboration: Castander et al., 2024), forecasting the shear bias and its impact on cosmology from pixels to parameters.

While this is not the first work to propagate the impact of PSF errors at the catalogue-level to the cosmology analysis of Stage-IV WL surveys — in particular, Euclid Collaboration: Paykari et al., 2020 forecast the impact of PSF errors on cosmological inference for the EWS, estimating the shear bias using weighted moments (see section 3.1.2), and propagating to cosmological parameter biases using a Fisher-matrix formalism — the work presented in this thesis has developed an enhanced level of realism. In particular, in chapter 4, a realistic model for the SED-sourced PSF error was propagated through to shear measurement biases, using a more realistic shear bias calculation (Euclid Consortium: Miller et al., 2020b) than has been applied in previous work in this area, with a methodology described in chapter 3 to tractably estimate realistic shear biases that vary with galaxy properties. Additionally, an extension to this methodology is developed in chapter 5 to allow the estimation of shear biases as a function of angular position in

the EWS footprint. Moreover, the propagation of the impact of spatially-varying m-bias to cosmological parameter estimation represents the first requirements placed on the form of the m-bias spatial variations based on the resulting cosmological parameter biases. In general, the characterisation and mitigation of systematics, including shear measurement biases, is a crucial task for Stage-IV WL surveys, and the work presented in this thesis represents a significant development in the former, as well as an important step towards the development of the latter.

In chapter 2, the impact of spatially-varying mutiplicative shear bias on cosmological parameter estimation is estimated, for a general stage-IV WL survey context. This is accomplished by estimating the bias in cosmic shear angular power spectra arising due to the m-bias spatial variations. Spatially-varying m-bias has a convolutional effect on the C_ℓs, via the mode-coupling matrix $\mathsf{M}_{\ell\ell'}$ (2.6). While the impact of spatially-varying m-bias on cosmic shear C_ℓs had been investigated in previous work (e.g. Kitching et al., 2020, 2019), the maximum monopole $\ell_{\rm max}$ to which the impact on the C_ℓs could be calculated had been limited by the high computational cost of calculating $\mathsf{M}_{\ell\ell'}$. In the work presented in chapter 2, a computationally-efficient pseudo-C_ℓ algorith NaMaster (Alonso et al., 2019) was employed to calculate the bias in shear C_ℓs with $\ell_{\rm max} \sim 10^4$. This allowed the propagation of the impact of spatially-varying m-bias to biases in cosmological parameter estimates. Assuming a generic stage-IV WL survey configuration, a Fisher-matrix formalism is employed to estimate resulting biases in cosmological parameters $\{\Omega_{\rm c}, \sigma_8, w_0, w_a\}$, as a function of the properties of the spatial variations of the m-bias, as shown in fig. 2.8 and fig. 2.9. The purpose of this is to allow a requirement to be placed on the amplitude of m-bias spatial variations, which may be flowed-down to requirements on calibration or mitigation of systematics for stage-IV WL surveys. It is found that the spatial variations of the m-bias are likely to be a sub-dominant but potentially non-negligible contribution to the shear measurement error budget for stage-IV WL surveys. The work presented in chapter 2 is based on that described in Cragg et al., 2022.

In chapter 3, a method for forecasting shear measurement biases arising due to PSF errors for the EWS at the catalogue-level is described. This is accomplished by sampling mock galaxies from the *Euclid* Flagship 2 simulation, as a function of galaxy SED and morphology parameters, and FoV-position; given some input PSF error, shear biases are estimated for the sampled galaxies. The shear bias estimates for the sampled galaxies are then used to infer shear bias estimates for the remaining galaxies in the catalogue. PSF errors are estimated using the *Euclid* OU-SHE PSFTOOLKIT, and resulting shear biases are estimated using a model-fitting technique (Euclid Consortium: Miller et al., 2020b), described in section 3.2). The sampling of the basis set of galaxy SEDs is accomplished by defining a regular grid in the space of galaxy colour indices $r-i, r-z, i-z$, observed redshift $z_{\rm obs}$, and VIS magnitude $m_{\rm VIS}$, and sampling galaxies in the cells of the grid, ensuring that all corresponding SED sub-populations present in the catalogue are represented in the sample; this is to avoid potential cosmology-dependent bias in the resulting shear bias estimates. For each sampled SED, shear bias arising due to PSF errors are estimated on a grid of morphology parameters and FoV position. To infer shear biases for galaxies in the catalogue, galaxies are assigned the shear bias estimates of the nearest neighbour in the space of $r-i, r-z, i-z, z_{\rm obs}, m_{\rm VIS}$, interpolated over the grid of morphology parameters and FoV position. The performance of this shear bias inference technique is validated in section 3.3. Chapter 4 and chapter 5 consist of applications of the methodology presented in chapter 3, for two different sources of PSF error for the EWS.

In chapter 4, shear biases arising due to imperfect knowledge of galaxy SEDs, which results in error in the transfer of the VIS PSF model to target galaxies, are forecast for the EWS, and the m-bias is propagated to bias in cosmological parameters $\{\Omega_{\rm c}, \sigma_8, w_0, w_a\}$. Multiplicative and additive biases are calculated for mock galaxies sampled from the Flagship 2 simulation, and are shown as functions of galaxy redshift, VIS magnitude, and spectral properties, broken down by galaxy sub-populations, in section 4.2.3. The SED-error-sourced m-bias is found on average to be around the level of requirements, or exceeding them, and

to have significant redshift variation that depends on the colour-redshift relation in the catalogue. The SED-error-sourced c-bias is found to exhibit variability at or exceeding the level of requirements, which is driven by the FoV-dependence. The m bias is found to be close to linear in the bias in the bias in the mean effective SED wavelength, $\delta\mathcal{M}_\lambda$, which is also approximately the case for the additive bias components; this relation may be useful in applying a correction for the effect of SED errors on shear measurement for the EWS. Multiplicative biases are calculated for mock galaxies sampled from forecast $n_i(z)$ tomographic redshift distributions, and tomographic mean m-biases $\langle m_i(z)\rangle$ are calculated. These are propagated to biases in cosmological parameters using a Fisher-matrix formalism, via the bias induced in the shear angular power spectra, and cosmological parameter biases are found to be large with respect to constraints. w_0, w_a are found to be biased in the same direction as they are found to be discrepant from ΛCDM in DESI Collaboration: Abdul-Karim et al., 2025, which may resuklt in spurious consistency between WL and other probes if the SED-sourced shear bias is not corrected for in the EWS analysis. This further confirms the importance of effectively mitigating the impact of this systematic effect on parameter inference for the cosmological analysis of EWS data.

In chapter 5, shear biases arising due to spatio-temporal variations of the VIS PSF which are not included in the PSF model are forecast for the EWS, as a function of survey epoch. The survey epochs and FoV positions are then projected to sky coordinates, and HEALPIX maps of the spatial variations of the shear biases are generated. A PCA-based method to efficiently sample survey epochs while representing the most important variations in the PSF is developed, as described in section 5.2.1, shear biases are estimated as a function of survey epoch, for Flagship 2 mock galaxies sampled from tomographic redshift distributions. The additive biases arising due to PSF modelling errors are found to exhibit spatio-temporal variability which is at the level of PSF modelling requirements. The spatio-temporal variation of the shear biases is found to have negligible redshift variation, but the time-averaged standard deviation of the additive bias is found to

increase with redshift, because of the dependence of galaxy scalelength on redshift. As described in section 5.4, this work is subject to a number of caveats, and should be considered as an indicative proof-of-concept. In particular, the HEALPIX maps presented in section 5.3.2 may in future work be used to propagate the impact of this source of shear measurement bias to bias in summary statistics, and to cosmological inference, and a similar approach may be applied to propagate the cosmological impact of other sources of shear measurement bias which exhibit spatial variation.

Overall, the work presented in this thesis demonstrates the value of forward-modelling the impact of shear measurement biases for stage-IV WL surveys. In this work, based on the methodology described in chapter 3, this approach has allowed the realistic estimation of shear biases arising for galaxies at the catalogue-level. This in turn has allowed the estimation of tomographic biases in angular power spectra, as in chapter 4, and HEALPIX maps of shear bias variations, as in chapter 5, which may in future work be propagated to forecast biases in various summary statistics, e.g. using the methods described in chapter 2. In principle, the estimation of shear measurement systematics at the catalogue-level allows the impact of these systematics on cosmological inference to be realistically characterised, which represents a significant contribution to efforts to mitigate their impact, a central task for stage-IV weak lensing surveys.

The methods developed in this thesis have allowed for a realistic characterisation of the impact of highly complex systematic biases affecting shear measurement, advancing on previous work that has been conducted in this area (Eriksen and Hoekstra, 2018; Euclid Collaboration: Paykari et al., 2020; Massey et al., 2013), resulting in a realistic forecast of the performance of the *Euclid* WL measurement, subject to certain important systematics. The level of realism to which the shear measurement biases discussed in this thesis have been estimated has been informed by the stringent requirements of stage-IV WL surveys, and represents an important step towards ensuring the level of systematics control

that will be vital to the realisation of their core scientific aims.

6.2 Outlook

The work presented in this thesis admits a number of avenues for future work. The most immediate of these consist of developments with respect to the limitations of the work described in chapter 2–chapter 5. For example, in chapter 2 and chapter 4, the propagation of the impact of the shear biases to cosmology was done by estimating the resulting bias in cosmic shear angular power spectra. However, in stage-IV WL surveys, the cosmological analysis will be conducted using 3×2 point statistics, i.e. including the constraints from photometric galaxy clustering and the cross-correlation with shear, the galaxy-galaxy lensing, along side the cosmic shear. Such an analysis has more constraining power than the cosmic shear two-point statistics alone, and for *Euclid* is required to meet the top-level mission requirement on the dark energy figure of merit (Euclid Collaboration: Mellier et al., 2024). Future work in this area should therefore consider the impact of shear measurement biases on the 3×2-point statistics, rather than the cosmic shear alone. In addition to the different sensitivity to cosmological parameters of the 3×2-point statistics compared with the cosmic shear alone, the galaxy-galaxy lensing is also sensitive to the multiplicative shear biases considered here (Prat et al., 2022).

Another limitation in the cosmology propagation carried out in chapter 2 and chapter 4 is that the biases in cosmological parameters arising due to the bias in angular power spectra is computed using a Fisher-matrix formalism. This is an analytic formalism that assumes that the joint parameter posterior distribution is a multivariate Gaussian. In modern cosmological inference, posterior distributions of cosmological parameters are typically inferred numerically, using Bayesian Monte-Carlo Markov Chain (MCMC)-based techniques (Heymans et al., 2021; Planck Collaboration: Aghanim et al., 2020; The DES Collaboration: Abbott et al., 2022); MCMC may also be used for cosmological forecasts (Wolz et al., 2012). While more computationally expensive than conducting a Fisher-matrix forecast, MCMC allows for more realism in the parameter posterior distributions. Because

of this, while marginalisation over the prior probability distributions of nuisance parameters is possible using the Fisher-matrix formalism (Coe, 2009), the impact on the cosmological parameter constraints of marginalisation over priors on nuisance parameters may be estimated more realistically in an MCMC-based forecast. This is highly pertinent in the case of shear measurement biases; for example, if the impact of multiplicative shear bias on angular power spectra is parametrised by a mean m-bias per tomographic redshift bin $\langle m_i(z) \rangle$, which has some informative prior estimated e.g. from simulations, then the impact of marginalising over this prior on cosmological inference may be estimated. Realistically forecasting the impact of this is of substantial interest for stage-IV WL surveys.

As discussed in section 5.4, the work conducted in chapter 5 is subject to a number of caveats, and should therefore be considered an indicative proof-of-concept. Future work in this area should consider the shear biases for the EWS that arise due to modelling errors with respect to the VIS PSF model calibrated with regular cadence, in order to result in a realistic forecast. Moreover, future work in this area should consider a realistic model of the PSF variations as a function of the orientation of the spacecraft, based on in-orbit data, rather than the pre-launch model, that has been found to be inconsistent with PSF variation measurements made in orbit (L. Miller, *priv. comm.*); such a model is currently under development (Miller and Whittam, *in prep.*). Work is currently ongoing to propagate the shear bias HEALPIX maps described in section 5.3.2 to biases in cosmological parameter constraints, using a 3×2-point analysis (Tanidis et al., *in prep.*).

There are a number of other future research directions which may be pursued, that relate to the work presented in this thesis. For example, to a good approximation, B-modes are expected to be negligible in the cosmic shear signal (Kilbinger, 2015), although they may be introduced due to source clustering (Schneider et al., 2002). Measurements of B-modes in shear data may therefore indicate the presence of unmitigated systematics. In chapter 2, the BB auto-correlation cosmic shear angular power spectra that are induced due to the m-bias spatial variations are

measured, and found to be closely related to the bias in the EE angular power spectra induced by the m-bias spatial variations. This suggests that observations of the BB angular power spectra from shear data may be used to diagnose the presence of shear measurement systematics, as well as indicate the level to which such systematics bias the EE angular power spectra. Future work may involve estimating the signature B-modes induced in shear measurements arising due to specific realistic spatially varying shear measurement systematics, such as the PSF modelling errors discussed in chapter 5. Furthermore, the separation of E- and B-modes present in shear data may be estimated using *Complete Orthogonal Sets of E-/B-mode Integrals* (COSEBIs, Schneider et al., 2010), which separate the shear E- and B-mode signal into discrete orthogonal modes; systematic effects, such as spatially-dependent shear measurement biases, may excite specific modes which may not be excited in the cosmological shear signal (Asgari et al., 2019). This provides a convenient discrete quantification of the E- and B-mode contribution from shear measurement systematics, and different systematics may induce different signature excitations in the COSEBIs. A forecast of the impact of the shear measurement biases considered in this thesis on COSEBIs is therefore of interest.

Apart from the level of summary statistics, techniques have been presented in the literature to detect the presence of systematics at the map level. For example, van Uitert and Schneider, 2016 presents a technique to detect the presence of spatially-varying additive c-biases, by stacking pointings and averaging the ellipticity measurements, and identifying the mean component with a residual additive shear measurement systematic. Kitching et al., 2021 presents a method to map the additive shear measurement bias present in shear data by measuring discrepancies in the statistical distribution of the measured shear compared with the fiducial expectation. The performance of such methods may be validated in future work, by testing them on realistic forecast shear bias maps generated using the methodology described in chapter 5. An evaluation of the performance of the empirical c-bias mapping technique presented in Kitching et al., 2021 by testing on the shear bias maps presented in chapter 5 is currently in preparation.

As discussed in section 4.4.2, it is of interest in future work to investigate the impact of cosmological parameter inference of marginalising over priors on mean tomographic m-bias, $\langle m_i(z) \rangle$. As seen in chapter 4, the $\langle m_i(z) \rangle$ arising due to SED errors varies substantially with redshift, and informative priors on these nuisance parameters may be estimated from simulations, e.g. by bootstrapping the $\langle m_i(z) \rangle$ estimates presented in chapter 4. Additionally, because of the mutual dependence of SED-error-sourced shear bias and photometric redshift errors on the galaxy SEDs, these systematics are likely to be correlated (Eriksen and Hoekstra, 2018); there will therefore be non-zero off-diagonal elements in the covariance matrix of the corresponding nuisance parameters that, if not included in cosmological parameter inference, will result in biased cosmological parameter estimates when the priors on these nuisance parameters are marginalised over. Future work should therefore involve the propagation of the impact of the correlation between photometric redshift errors and SED-error-sourced shear biases, for example by forecasting the impact of marginalising over their joint prior on cosmological parameter inference, with an estimate of their joint prior potentially obtained by bootstrapping estimates from simulations.

Future work should also be conducted to develop methods to correct for the SED-error-sourced shear bias at the level of galaxies, potentially making use of photometric or spectroscopic data, along with the linearity of the shear bias in $\delta\mathcal{M}_\lambda$, as discussed in section 4.4.2. Additionally, space-based multi-band imaging data, in particular such as will be measured with the *Roman* space telescope (Green et al., 2012), is not subject to the atmospheric contribution to the photometric noise, and hence may offer more precise SED data for galaxies that, in areas in which the EWS and *Roman* HLIS (Doré et al., 2018) overlap, may be synergistically used to obtain less-biased propagation of the VIS PSF model to source galaxies in potential future re-analyses of EWS data.

Another effect which impacts the SED errors for the EWS is blending of the ground-based photometry (MacCrann et al., 2022); unrecognised blended

galaxy images results in biased SED estimates for the blended source galaxies, even if they are not blended in the VIS imaging, that comprises an additional source of PSF error. If images are also blended in the VIS photometry, then this results in an additional correlation between the PSF error and blending-induced shear measurement bias, although blending is less of a problem for space-based shear measurement than ground-based observations, due to the smaller PSF. This correlation will be more relevant to the WL measurement for the LSST, for which the shear measurement will be conducted on the deep ground-based imaging that will be conducted by *Rubin*.

Spatial variations of the SED-error-sourced shear biases may also be investigated in future work. For example, the significant FoV-dependent contribution to the SED-error-sourced c-bias shown in section 4.2.3 may be propagated to additive bias maps using the HEALPIX map construction method described in section 5.3.2, which may then allow its impact to be propagated to cosmology as described in section 5.4.2. Additionally, further contributions to the spatial variation of the SED-error-sources shear bias may be investigated, including inhomogeneity of the ground-based survey configurations which provide the galaxy SED data, as well as variations in noise in ground-based photometry as a function of spatial coordinates due to dependence on airmass. In particular, these effects may induce multiplicative bias with large characteristic angular scales of variation; as seen in chapter 2, large-scale m-bias variations have the largest impact on cosmological parameter estimation.

Bibliography

Abbott, T. M. C. et al. (2021). In: *The Astrophysical Journal Supplement Series* 255.2, p. 20.

Ade, P. et al. (2019). In: *Journal of Cosmology and Astroparticle Physics* 2019.2, 056, p. 056.

Ahlberg, J. H., Nilson, E. N., and Walsh, J. L., eds. (1967). *The Theory of Splines and Their Applications*. Elsevier.

Aihara, H. et al. (2022). In: *Publications of the Astronomical Society of Japan* 74.2, pp. 247–272.

Airy, G. B. (1835). In: *Transactions of the Cambridge Philosophical Society* 5, p. 283.

Alam, S. et al. (2017). In: *Monthly Notices of the Royal Astronomical Society* 470.3, pp. 2617–2652.

Albrecht, A. et al. (2006). In: *arXiv e-prints*, astro-ph/0609591, astro–ph/0609591.

Alonso, D. et al. (2019). In: *Monthly Notices of the Royal Astronomical Society* 484.3, pp. 4127–4151.

Amara, A. and Réfrégier, A. (2008). In: *Monthly Notices of the Royal Astronomical Society* 391.1, pp. 228–236.

Amon, A. et al. (2023). In: *Monthly Notices of the Royal Astronomical Society* 518.1, pp. 477–503.

Antilogus, P. et al. (2014). In: *Journal of Instrumentation* 9.3, C03048, p. C03048.

Asgari, M. et al. (2019). In: *Astronomy & Astrophysics* 624, A134, A134.

Asgari, M. et al. (2021). In: *Astronomy &; Astrophysics* 645, A104, A104.

Bartelmann, M. and Schneider, P. (2001). In: *Physics Reports* 340.4-5, pp. 291–472.

Benítez, N. (2000). In: *The Astrophysical Journal* 536.2, pp. 571–583.

Bennett, C. L. et al. (1996). In: *The Astrophysical Journal Letters* 464, p. L1.

Bernardeau, F. (1998). In: *Astronomy & Astrophysics* 338, pp. 375–382.

Bernstein, G. M. and Jarvis, M. (2002). In: *The Astronomical Journal* 123.2, p. 583.

Bernstein, G. M. (2010). In: *Monthly Notices of the Royal Astronomical Society* 406.4, pp. 2793–2804.

Blazek, J. et al. (2012). In: *Journal of Cosmology and Astroparticle Physics* 2012.5, 041, p. 041.

Blumenthal, G. R. et al. (1984). In: *Nature* 311, pp. 517–525.

Bond, J. R. et al. (1991). In: *Physics Review Letters* 66.17, pp. 2179–2182.

Bracewell, R. (1965). *The Fourier Transform and its Applications*. Stanford, USA: McGraw-Hill Higher Education.

Brout, D. et al. (2022). In: *The Astrophysical Journal* 938.2, 110, p. 110.

Brown, M. L., Castro, P. G., and Taylor, A. N. (2005). In: *Monthly Notices of the Royal Astronomical Society* 360.4, pp. 1262–1280.

Broxterman, J. C. et al. (2024). In: *arXiv e-prints*, arXiv:2412.02736, arXiv:2412.02736.

Buchs, R. et al. (2019). In: *Monthly Notices of the Royal Astronomical Society* 489.1, pp. 820–841.

Campos, A. et al. (2024). In: *arXiv e-prints*, arXiv:2408.00922, arXiv:2408.00922.

Cardone, V. F. et al. (2014). In: *Monthly Notices of the Royal Astronomical Society* 439.1, pp. 202–220.

Chambers, K., Unions Team Including Pan-Starrs Team, and Cfis Team (2020). In: *American Astronomical Society Meeting Abstracts #235*. Vol. 235. American Astronomical Society Meeting Abstracts, 154.04, p. 154.04.

Chang, C. et al. (2012). In: *Monthly Notices of the Royal Astronomical Society* 428.3, pp. 2695–2713.

Chevallier, M. and Polarski, D. (2001). In: *International Journal of Modern Physics D* 10.2, pp. 213–223.

Chisari, N. E. et al. (2019). In: *The Astrophysical Journal* 242.1, 2, p. 2.

Coe, D. (2009). In: *arXiv e-prints*, arXiv:0906.4123, arXiv:0906.4123.

Coupon, J. et al. (2009). In: *Astronomy &; Astrophysics* 500.3, pp. 981–998.

Cragg, C. et al. (2022). In: *Monthly Notices of the Royal Astronomical Society* 518.4, pp. 4909–4920.

Crittenden, R. G. et al. (2002). In: *The Astrophysical Journal* 568.1, pp. 20–27.

Cropper, M. et al. (2013). In: *Monthly Notices of the Royal Astronomical Society* 431.4, pp. 3103–3126.

Cypriano, E. S. et al. (2010). In: *Monthly Notices of the Royal Astronomical Society* 405.1, pp. 494–502.

Dalal, R. et al. (2023). In: *Physics Review D* 108.12, 123519, p. 123519.

Dark Energy Science Collaboration: Mandelbaum, R. et al. (2018). In: *arXiv e-prints*, arXiv:1809.01669, arXiv:1809.01669.

de Bernardis, P. et al. (2001). In: *Cosmology and Particle Physics*. Ed. by R. Durrer, J. Garcia-Bellido, and M. Shaposhnikov. Vol. 555. American Institute of Physics Conference Series. AIP, pp. 85–94.

DES and KiDS Collaboration: Abbott, T. M. C. et al. (2023). In: *The Open Journal of Astrophysics* 6, 36, p. 36.

DESI Collaboration: Abdul-Karim, M. et al. (2025). In: *arXiv e-prints*, arXiv:2503.14738, arXiv:2503.14738.

DESI Collaboration: Adame, A. G. et al. (2024). In: *arXiv e-prints*, arXiv:2404.03001, arXiv:2404.03001.

Dodelson, S. (2003). *Modern Cosmology*.

Doré, O. et al. (2018). In: *arXiv e-prints*, arXiv:1804.03628, arXiv:1804.03628.

Duncan, C. A. J. and Brown, M. L. (2024). In: *arXiv e-prints*, arXiv:2411.15063, arXiv:2411.15063.

Duncan, C. A. J. et al. (2014). In: *Monthly Notices of the Royal Astronomical Society* 437.3, pp. 2471–2487.

Duncan, C. A. J. et al. (2022). In: *Monthly Notices of the Royal Astronomical Society* 515.1, pp. 1130–1145.

Edmonds, A. R. (1957). *Angular Momentum in Quantum Mechanics*. Princeton: Princeton Univ. Press.

Efron, B. (1992). "Bootstrap Methods: Another Look at the Jackknife". In: *Breakthroughs in Statistics: Methodology and Distribution*. Ed. by S. Kotz and N. L. Johnson. Springer New York, pp. 569–593.

Efstathiou, G., Sutherland, W. J., and Maddox, S. J. (1990). In: *Nature* 348.6303, pp. 705–707.

Efstathiou, G. (2025a). In: *Monthly Notices of the Royal Astronomical Society*.

Efstathiou, G. (2025b). In: *Monthly Notices of the Royal Astronomical Society* 538.2, pp. 875–882.

Endicott, J. et al. (2012). In: *High Energy, Optical, and Infrared Detectors for Astronomy V*. Ed. by A. D. Holland and J. W. Beletic. Vol. 8453. Society of Photo-Optical Instrumentation Engineers (SPIE) Conference Series, 845304, p. 845304.

Erben, T. et al. (2013). In: *Monthly Notices of the Royal Astronomical Society* 433.3, pp. 2545–2563.

Eriksen, M. and Hoekstra, H. (2018). In: *Monthly Notices of the Royal Astronomical Society* 477.3, pp. 3433–3448.

Euclid Collaboration: Ajani, V. et al. (2023). In: *Astronomy &; Astrophysics* 675, A120.

Euclid Collaboration: Blanchard, A. et al. (2020). In: *Astronomy & Astrophysics* 642, A191, A191.

Euclid Collaboration: Castander, F. J. et al. (2024). In: *arXiv e-prints*, arXiv:2405.13495, arXiv:2405.13495.

Euclid Collaboration: Congedo, G. et al. (2024). In: *Astronomy & Astrophysics* 691, A319, A319.

Euclid Collaboration: Cropper, M. S. et al. (2024). In: *arXiv e-prints*, arXiv:2405.13492, arXiv:2405.13492.

Euclid Collaboration: Deshpande, A. C. et al. (2020). In: *Astronomy & Astrophysics* 636, A95, A95.

Euclid Collaboration: Deshpande, A. C. et al. (2024). In: *Astronomy & Astrophysics* 684, A138, A138.

Euclid Collaboration: Desprez, G. et al. (2020). In: *Astronomy &; Astrophysics* 644, A31.

Euclid Collaboration: Jahnke, K. et al. (2024). In: *arXiv e-prints*, arXiv:2405.13493, arXiv:2405.13493.

Euclid Collaboration: Laureijs, R. et al. (2011). In: *arXiv e-prints*, arXiv:1110.3193, arXiv:1110.3193.

Euclid Collaboration: Martinet, N. et al. (2019). In: *Astronomy & Astrophysics* 627, A59, A59.

Euclid Collaboration: Mellier, Y. et al. (2024). In: *arXiv e-prints*, arXiv:2405.13491, arXiv:2405.13491.

Euclid Collaboration: Paykari, P. et al. (2020). In: *Astronomy & Astrophysics* 635, A139, A139.

Euclid Collaboration: Pires, S. et al. (2020). In: *Astronomy &; Astrophysics* 638, A141.

Euclid Collaboration: Racca, G. D. et al. (2016). In: *Space Telescopes and Instrumentation 2016: Optical, Infrared, and Millimeter Wave*. Ed. by H. A. MacEwen et al. SPIE.

Euclid Collaboration: Scaramella, R. et al. (2022). In: *Astronomy & Astrophysics* 662, A112, A112.

Euclid Collaboration: Sciotti, D. et al. (2024). In: *Astronomy & Astrophysics* 691, A318, A318.

Euclid Collaboration: Tutusaus, I. et al. (2020). In: *Astronomy & Astrophysics* 643, A70, A70.

Euclid Consortium: Lorenzo Alvarez, J. (2014). *Euclid Ground Data Processing Requirements Document*. Tech. rep. EUCL-EST-RS-8-001. ESA and Euclid Consortium.

Euclid Consortium: Miller, L. and Duncan, C. A. J. (2020). *VIS Phase Diversity Defocus Amount*. Tech. rep. EUCL-OXF-TN-8-005. Euclid Consortium.

Euclid Consortium: Miller, L., Duncan, C. A. J., and Amiaux, J. (2022). *VIS PSF Variations from the STOP Analysis*. Tech. rep. EUCL-OXF-TN-8-006. Euclid Consortium.

Euclid Consortium: Miller, L. et al. (2019). *VIS PSF Phase Diversity Calibration Observations Definition*. Tech. rep. EUCL-OXF-TN-8-005. Euclid Consortium.

Euclid Consortium: Miller, L. et al. (2020a). *Science Ground Segement VIS PSF Generation*. Tech. rep. EUCL-OXF-TN-8-001. Euclid Consortium.

Euclid Consortium: Miller, L. et al. (2020b). *Science Ground Segement VIS PSF Model Optimisaton*. Tech. rep. EUCL-OXF-TN-8-009. Euclid Consortium.

Faber, S. M. and Jackson, R. E. (1976). In: *The Astrophysical Journal* 204, pp. 668–683.

Fenech Conti, I. et al. (2017). In: *Monthly Notices of the Royal Astronomical Society* 467.2, pp. 1627–1651.

The Thermal Testing of Euclid STM (2020). 2020 International Conference on Environmental Systems.

Flaugher, B. et al. (2015). In: *The Astrophysical Journal* 150.5, 150, p. 150.

Flewelling, H. A. et al. (2020). In: *The Astrophysical Journal Supplement Series* 251.1, p. 7.

Freudenburg, J. K. C., Huff, E. M., and Hirata, C. M. (2020). In: *Monthly Notices of the Royal Astronomical Society* 496.3, pp. 2998–3014.

Friedmann, A. (1922). In: *Zeitschrift fur Physik* 10, pp. 377–386.

Gatti, M. et al. (2021). In: *Monthly Notices of the Royal Astronomical Society* 504.3, pp. 4312–4336.

Gentile, M., Courbin, F., and Meylan, G. (2012). In: *arXiv e-prints*, arXiv:1211.4847, arXiv:1211.4847.

Giblin, B. et al. (2021). In: *Astronomy & Astrophysics* 645, A105, A105.

Gillis, B. R. and Taylor, A. N. (2016). In: *Monthly Notices of the Royal Astronomical Society* 456.3, pp. 2518–2536.

Good, I. J. (1960). In: *Journal of the Royal Statistical Society: Series B (Methodological)* 22.2, pp. 372–375.

Goodwin, E. P. and Wyant, J. C. (2006). *Field guide to interferometric optical testing*. SPIE Press.

Górski, K. M. et al. (2005). In: *The Astrophysical Journal* 622.2, pp. 759–771.

Green, J. et al. (2012). In: *arXiv e-prints*, arXiv:1208.4012, arXiv:1208.4012.

Guy, L. P. et al. (2022). In: *Zenodo id. 5836022*. Vol. 58, 5836022, p. 5836022.

Hamimeche, S. and Lewis, A. (2008). In: *Physical Review D* 77.10, 103013, p. 103013.

Hanany, S. et al. (2000). In: *The Astrophysical Journal Letters* 545.1, pp. L5–L9.

Heymans, C. et al. (2006). In: *Monthly Notices of the Royal Astronomical Society* 368.3, pp. 1323–1339.

Heymans, C. et al. (2021). In: *Astronomy & Astrophysics* 646, A140, A140.

Hinton, S. R. (2016). In: *The Journal of Open Source Software* 1, 00045, p. 00045.

Hirata, C. M. and Seljak, U. (2004). In: *Physics Review D* 70.6, 063526, p. 063526.

Hirata, C. M. et al. (2004). In: *Monthly Notices of the Royal Astronomical Society* 353.2, pp. 529–549.

Hivon, E. et al. (2002). In: *The Astrophysical Journal* 567.1, pp. 2–17.

Hoekstra, H. et al. (1998). In: *The Astrophysical Journal* 504.2, pp. 636–660.

Hubble, E. (1929). In: *Proceedings of the National Academy of Science* 15.3, pp. 168–173.

Huff, E. and Mandelbaum, R. (2017). In: *arXiv e-prints*, arXiv:1702.02600, arXiv:1702.02600.

Huff, E. et al. (2014). In: *Monthly Notices of the Royal Astronomical Society* 440.2, pp. 1296–1321.

Huterer, D. et al. (2006). In: *Monthly Notices of the Royal Astronomical Society* 366.1, pp. 101–114.

Ilbert, O. et al. (2008). In: *The Astrophysical Journal* 690.2, pp. 1236–1249.

Jarvis, M. and Jain, B. (2008). In: *Journal of Cosmology and Astroparticle Physics* 2008.01, p. 003.

Jarvis, M. et al. (2016). In: *Monthly Notices of the Royal Astronomical Society* 460.2, pp. 2245–2281.

Joachimi, B. and Bridle, S. L. (2010). In: *Astronomy &; Astrophysics* 523, A1, A1.

Joliffe, I. (2002). *Principal Component Analysis*. Second. New York, USA: Springer.

Jolliffe, I. T. and Cadima, J. (2016). In: *Philosophical Transactions of the Royal Society A: Mathematical, Physical and Engineering Sciences* 374.

Kacprzak, T. et al. (2012). In: *Monthly Notices of the Royal Astronomical Society* 427.4, pp. 2711–2722.

Kaiser, N., Squires, G., and Broadhurst, T. (1995). In: *The Astrophysical Journal* 449, p. 460.

Kannawadi, A., Rosenberg, E., and Hoekstra, H. (2021). In: *Monthly Notices of the Royal Astronomical Society* 502.3, pp. 4048–4063.

Kannawadi, A. et al. (2019). In: *Astronomy &; Astrophysics* 624, A92, A92.

Khaire, V. et al. (2019). In: *Monthly Notices of the Royal Astronomical Society* 486.1, pp. 769–782.

Kilbinger, M. (2015). In: *Reports on Progress in Physics* 78.8, 086901, p. 086901.

Kitching, T. D., Deshpande, A. C., and Taylor, P. L. (2021). In: *The Open Journal of Astrophysics* 4.1.

Kitching, T. D. et al. (2016). In: *Monthly Notices of the Royal Astronomical Society* 455.3, pp. 3319–3332.

Kitching, T. D. and Deshpande, A. C. (2022). In: *The Open Journal of Astrophysics* 5.1, 6, p. 6.

Kitching, T. D., Deshpande, A. C., and Taylor, P. L. (2020). In: *The Open Journal of Astrophysics* 3.1, 14, p. 14.

Kitching, T. D. et al. (2019). In: *The Open Journal of Astrophysics* 2.1, 5, p. 5.

Kogut, A. et al. (2003). In: *The Astrophysical Journal* 148.1, pp. 161–173.

Korsch, D. (1977). In: *Applied Optics* 16, pp. 2074–2077.

Krause, E., Eifler, T., and Blazek, J. (2015). In: *Monthly Notices of the Royal Astronomical Society* 456.1, pp. 207–222.

Krause, E. and Eifler, T. (2017). In: *Monthly Notices of the Royal Astronomical Society* 470.2, pp. 2100–2112.

Laganá, T. F., Andrade-Santos, F., and Lima Neto, G. B. (2010). In: *Astronomy & Astrophysics* 511, A15, A15.

Lemaître, G. (1927). In: *Publications du Laboratoire d'Astronomie et de Geodesie de l'Universite de Louvain* 4, pp. 101–111.

Lewis, A. and Chamberlain, E. (2025). In: *Journal of Cosmology and Astroparticle Physics* 2025.5, 065, p. 065.

Li, C. et al. (2006). In: *Monthly Notices of the Royal Astronomical Society* 368.1, pp. 21–36.

Li, S.-S. et al. (2023). In: *Astronomy & Astrophysics* 670, A100, A100.

Liaudat, T. et al. (2023). In: *Inverse Problems* 39.3, 035008, p. 035008.

Linde, A. (2005). In: *arXiv e-prints*, hep-th/0503203, hep–th/0503203.

Linder, E. V. (2003). In: *Physics Review Letters* 90.9, 091301, p. 091301.

LSST Science Collaboration: Abell, P. A. et al. (2009). In: *arXiv e-prints*, arXiv:0912.0201, arXiv:0912.0201.

Ma, Z., Hu, W., and Huterer, D. (2006). In: *The Astrophysical Journal* 636.1, pp. 21–29.

MacCrann, N. et al. (2022). In: *Monthly Notices of the Royal Astronomical Society* 509.3, pp. 3371–3394.

Maddox, S. J. et al. (1990). In: *Monthly Notices of the Royal Astronomical Society* 242, p. 43.

Mandelbaum, R. (2018). In: *Annual Review of Astronomy and Astrophysics* 56, pp. 393–433.

Mandelbaum, R. et al. (2006). In: *Monthly Notices of the Royal Astronomical Society* 368.2, pp. 715–731.

Massey, R. et al. (2007). In: *The Astrophysical Journal Supplement Series* 172.1, pp. 239–253.

Massey, R. et al. (2013). In: *Monthly Notices of the Royal Astronomical Society* 429.1, pp. 661–678.

McCullough, J. et al. (2024). In: *arXiv e-prints*, arXiv:2410.22272, arXiv:2410.22272.

McDonald, P. et al. (2006). In: *The Astrophysical Journal Supplement Series* 163.1, pp. 80–109.

McGillem, C. D. and Cooper, G. R. (1984). *Continuous and Discrete Signal and System Analysis (2nd ed.)* Princeton, NJ: Princeton University Press.

Meinhold, P. and Lubin, P. (1991). In: *the Astrophysical Journal Letters* 370, p. L11.

Melchior, P. and Viola, M. (2012). In: *Monthly Notices of the Royal Astronomical Society* 424.4, pp. 2757–2769.

Melchior, P. et al. (2011). In: *Monthly Notices of the Royal Astronomical Society* 412.3, pp. 1552–1558.

Meyers, J. E. and Burchat, P. R. (2015). In: *The Astrophysical Journal* 807.2, 182, p. 182.

Miller, L. et al. (2007). In: *Monthly Notices of the Royal Astronomical Society* 382.1, pp. 315–324.

Miller, L. et al. (2013). In: *Monthly Notices of the Royal Astronomical Society* 429.4, pp. 2858–2880.

Miralda-Escude, J. (1991). In: *The Astrophysical Journal* 380, p. 1.

Montgomery, D. C. (2019). *Design and Analysis of Experiments*. Tenth. Wiley.

Myles, J. et al. (2021). In: *Monthly Notices of the Royal Astronomical Society* 505.3, pp. 4249–4277.

Niemi, S.-M. et al. (2015). In: *Experimental Astronomy* 39.2, pp. 207–231.

O'Neill, B. (2014). In: *The American Statistician* 68(4), pp. 282–296.

Oke, J. B. and Gunn, J. E. (1983). In: *The Astrophysical Journal* 266, pp. 713–717.

Pandey, S. et al. (2022). In: *Physics Review D* 106.4, 043520, p. 043520.

Paulin-Henriksson, S. et al. (2008). In: *Astronomy &; Astrophysics* 484.1, pp. 67–77.

Peacock, J. A. (1999). *Cosmological Physics*. Cambridge University Press.

Peebles, P. J. E. (1980). *The large-scale structure of the universe*. Princeton University Press.

Perlmutter, S. et al. (1999). In: *The Astrophysical Journal* 517.2, pp. 565–586.

Phillips Longley, E. (2021). In: *American Astronomical Society Meeting Abstracts*. Vol. 237. American Astronomical Society Meeting Abstracts, 443.03, p. 443.03.

Planck Collaboration: Aghanim, N. et al. (2020). In: *Astronomy & Astrophysics* 641, A6, A6.

Plazas, A. A. et al. (2016). In: *Publications of the Astronomical Society of the Pacific* 128.968, p. 104001.

Postman, M. et al. (2012). In: *The Astrophysical Journal Supplement* 199.2, 25, p. 25.

Prat, J. et al. (2022). In: *Physics Review D* 105.8, 083528, p. 083528.

Press, W. H. et al. (2007). *Numerical Recipes: The Art of Scientific Computing (3rd ed.)* Cambridge, UK: Cambridge University Press.

Pujol, A. et al. (2019). In: *Astronomy &; Astrophysics* 621, A2, A2.

Rahman, M. et al. (2015). In: *Monthly Notices of the Royal Astronomical Society* 447.4, pp. 3500–3511.

Refregier, A. et al. (2012). In: *Monthly Notices of the Royal Astronomical Society* 425.3, pp. 1951–1957.

Rhodes, J. et al. (2010). In: *Publications of the Astronomical Society of the Pacific* 122.890, p. 439.

Riess, A. G. et al. (1998). In: *The Astronomical Journal* 116.3, pp. 1009–1038.

Riess, A. G. et al. (2022). In: *The Astrophysical Journal Letters* 934.1, L7, p. L7.

Rimmer, M. P., King, C. M., and Fox, D. G. (1972). In: *Applied Optics Information Photonics* 11.12, p. 2790.

Robert, C. P. and Casella, G. (2004). *Monte Carlo Statistical Methods*. Second. Springer New York.

Robertson, H. P. (1935). In: *The Astrophysical Journal* 82, p. 284.

Ross, N. P. et al. (2007). In: *Monthly Notices of the Royal Astronomical Society* 381.2, pp. 573–588.

Rowe, B. (2010). In: *Monthly Notices of the Royal Astronomical Society* 404.1, pp. 350–366.

Rowe, B. et al. (2015). In: *Astronomy and Computing* 10, pp. 121–150.

Rubin, V. C. and Ford Jr., W. K. (1970). In: *The Astrophysical Journal* 159, p. 379.

Sánchez, C. et al. (2022). In: *Physics Review D* 105.8, 083529, p. 083529.

Schawinski, K. et al. (2014). In: *Monthly Notices of the Royal Astronomical Society* 440.1, pp. 889–907.

Schmidt, F. et al. (2012). In: *The Astrophysical Journal Letters* 744.2, L22, p. L22.

Schneider, P. (2006). "Weak Gravitational Lensing". In: *Gravitational Lensing: Strong, Weak and Micro*. Springer Berlin Heidelberg, pp. 269–451.

Schneider, P., Eifler, T., and Krause, E. (2010). In: *Astronomy & Astrophysics* 520, A116, A116.

Schneider, P., van Waerbeke, L., and Mellier, Y. (2002). In: *Astronomy &; Astrophysics* 389, pp. 729–741.

Schölkopf, B., Smola, A., and Müller, K.-R. (1998). In: *Neural Computation* 10.5, pp. 1299–1319.

Schutz, B. (2009). *A First Course in General Relativity*. Second. Cambridge University Press.

Seitz, C. and Schneider, P. (1997). In: *Astronomy & Astrophysics* 318, pp. 687–699.

Seljak, U. et al. (2005). In: *Physics Review D* 71.10, 103515, p. 103515.

Sérsic, J. L. (1963). In: *Boletin de la Asociacion Argentina de Astronomia La Plata Argentina* 6, pp. 41–43.

Sheldon, E. S. and Huff, E. (2017). In: *The Astrophysical Journal* 841.1, 24, p. 24.

Sheldon, E. S. et al. (2020). In: *The Astrophysical Journal* 902.2, 138, p. 138.

Simard, L. et al. (2002). In: *The Astrophysical Journal Supplement Series* 142.1, pp. 1–33.

Slipher, V. M. (1914). In: *Popular Astronomy* 22, pp. 19–21.

Slipher, V. M. (1918). In: *Publications of the American Astronomical Society*. Vol. 3. Publications of the American Astronomical Society, p. 98.

Smail, I., Ellis, R. S., and Fitchett, M. J. (1994). In: *Monthly Notices of the Royal Astronomical Society* 270, pp. 245–270.

Spergel, D. N. et al. (2003). In: *The Astrophysical Journal Supplement Series* 148.1, pp. 175–194.

Taylor, A. N. and Kitching, T. D. (2018). In: *Monthly Notices of the Royal Astronomical Society* 477.3, pp. 3397–3405.

Taylor, P. L. et al. (2018). In: *Physical Review D* 98.2, 023522, p. 023522.

Tegmark, M., Taylor, A. N., and Heavens, A. F. (1997). In: *The Astrophysical Journal* 480.1, pp. 22–35.

The DES Collaboration: Abbott, T. M. C. et al. (2022). In: *Physics Review D* 105.2, 023520, p. 023520.

Thiele, L., Duncan, C. A. J., and Alonso, D. (2020). In: *Monthly Notices of the Royal Astronomical Society* 491.2, pp. 1746–1758.

Treu, T. (2010). In: *Annual Review of Astronomy and Astrophysics* 48, pp. 87–125.

Tröster, T. et al. (2022). In: *Astronomy & Atrophysics* 660, A27, A27.

Troxel, M. A. et al. (2021). In: *Monthly Notices of the Royal Astronomical Society* 501.2, pp. 2044–2070.

van Uitert, E. and Schneider, P. (2016). In: *Astronomy &; Astrophysics* 595, A93, A93.

Voigt, L. M. and Bridle, S. L. (2010). In: *Monthly Notices of the Royal Astronomical Society* 404.1, pp. 458–467.

Voigt, L. M. et al. (2012). In: *Monthly Notices of the Royal Astronomical Society* 421.2, pp. 1385–1398.

Walker, A. G. (1937). In: *Proceedings of the London Mathematical Society* 42, pp. 90–127.

Weiss, N. A., Holmes, P. T., and Hardy, M. (2005). *A Course in Probability*. Pearson Addison Wesley.

Wikipedia (2025). *Zernike polynomials — Wikipedia, The Free Encyclopedia*. http://en.wikipedia.org/w/index.php?title=Zernike%20polynomials&oldid=1292513141. [Online; accessed 12-June-2025].

Wolz, L. et al. (2012). In: *Journal of Cosmology and Astroparticle Physics* 2012.9, 009, p. 009.

Wong, K. C. et al. (2020). In: *Monthly Notices of the Royal Astronomical Society* 498.1, pp. 1420–1439.

Wright, A. H. et al. (2025). In: *arXiv e-prints*, arXiv:2503.19441, arXiv:2503.19441.

Yin, H. (2007). "Learning Nonlinear Principal Manifolds by Self-Organising Maps". In: vol. 60, pp. 68–95.

Yu, Y. et al. (2015). In: *The Astrophysical Journal* 803.1, 46, p. 46.

Zaldarriaga, M. and Seljak, U. (1997). In: *Physical Review D* 55.4, pp. 1830–1840.

Zernike, v. F. (1934). In: *Physica* 1.7, pp. 689–704.

Zhang, T. et al. (2021). In: *Monthly Notices of the Royal Astronomical Society* 510.2, pp. 1978–1993.

Zhang, T. et al. (2022). In: *Monthly Notices of the Royal Astronomical Society* 520.2, pp. 2328–2350.

Zonca, A. et al. (2019). In: *The Journal of Open Source Software* 4.35, 1298, p. 1298.

Zuntz, J. et al. (2013). In: *Monthly Notices of the Royal Astronomical Society* 434.2, pp. 1604–1618.